



**Finite Element Modelling and Evaluation of Welding
Procedures in High Strength (450 MPa : 65 ksi) W-
shape Column Assemblies**

By

Violetta Nikolaidou

Department of Civil Engineering and Applied Mechanics

McGill University, Montreal, Canada

October 2013

**A thesis submitted to McGill University in partial fulfillment of the
requirements of the degree of Master of Engineering**

©Violetta Nikolaidou, 2013

Abstract

The use of high strength steel has become more frequent in modern steel construction due to the increasing demand for taller buildings and longer spans. High strength stocky steel columns are often used as part of a building's primary lateral load resisting system. During the fabrication of welded steel subassemblies that utilize high strength columns, there exists the potential for crack initiation related to the welding process. The likelihood of cracking necessitates the evaluation of current welding guidelines and techniques used in practice related to welding performed on high strength steel so that failures occurring during or soon after fabrication can be avoided.

This research focuses on the development of an advanced 2D finite element model that can accurately simulate multi-pass welding processes and provide a good estimate for crack initiation, occurring during or soon after fabrication. A specific case study was used involving a prequalified beam-to-column connection with welded thick doubler plates on a high strength steel column. When columns of this type are used as part of prequalified beam-to-column connections, thick doubler plates are typically welded to the column web in order to provide sufficient panel zone shear strength to prevent excessive yielding during an earthquake. The necessity to simulate the welding procedures performed in the panel zone area became evident after cracks were discovered post fabrication in the flanges of the case study column near the k-area. The FE model was relied on to simulate the complete joint penetration flare bevel groove welds on the web of an A913 Gr. 65 W-shape using a multi-pass flux cored arc welding process with CO₂ gas shield. The results are presented for the heat transfer and stress analyses that replicate the welding sequence

that is currently used in practice. High residual stress values are illustrated in the affected flange regions due to the welding. Additionally, an extended testing program for material characterization was employed involving tensile testing, Charpy V-Notch testing and scanning electron microscopy. It is demonstrated that the material exhibited good behaviour, suggesting that the cracking of the high strength steel column occurred due to the welding process. The measured material properties of the steel column were subsequently used in the finite element simulation. Through the use of linear elastic fracture mechanics crack propagation due to the welding was investigated, the quality of the W-shape material and the weld was evaluated and conclusions were drawn regarding the cause of the observed cracks during fabrication.

Résumé

Les aciers à haute résistance sont de plus en plus usités dans les constructions modernes en raison de la demande croissante pour des bâtiments plus grands et des portées plus longues. Les colonnes trapues à haute résistance sont souvent utilisées dans le système principal de résistance aux efforts latéraux. Lors de la fabrication de sous-ensembles en acier soudé utilisant des colonnes à haute résistance, il peut y avoir apparition de fissures à cause du procédé de soudage. La fissuration potentielle impose une évaluation des procédés et des directives actuelles de soudage pour les aciers à haute résistance afin que les défaillances survenant pendant ou peu de temps après fabrication puissent être évitées.

Cette recherche se concentre sur le développement d'un modèle avancé d'éléments finis 2D simulant de manière précise le soudage multi-passage et fournissant une bonne estimation pour la formation de fissure survenant pendant ou peu de temps après fabrication. Une étude de cas spécifique a été utilisée impliquant un assemblage poutre - colonne pré-qualifié avec d'épaisses plaques de renfort soudées sur une colonne en acier à haute résistance. Lorsque des colonnes de ce type sont utilisées dans le cadre de connexions poutre-colonne pré-qualifiées, les épaisses plaques de renfort sont généralement soudées à l'âme de la colonne afin de fournir une résistance en cisaillement suffisante au niveau de la "panel zone" pour éviter des déformations plastiques excessives durant les séismes. La nécessité de modéliser le procédé de soudage effectué dans la "panel zone" est devenu évidente lorsque des fissures ont été découvertes, après fabrication, dans les semelles de la colonne étudiée près de la zone k. Le modèle EF a été utilisé pour modéliser la pénétration complète de la soudure sur chanfrein sur l'âme d'un

profilé W A913 Gr.65 effectuée par un processus de soudage à l'arc à file fourré avec un enrobage en CO₂ avec multi-passage. Les résultats sont présentés pour le transfert de chaleur et l'analyse de contraintes qui reproduisent la séquence de soudage qui est actuellement utilisée. Des valeurs de contraintes résiduelles élevées dues à la soudure sont présentées dans les zones où les semelles sont affectées. De plus, un programme d'essais pour la caractérisation des matériaux a été employé impliquant essai de traction, essai Charpy V- Notch et microscopie électronique à balayage. Il est démontré que le matériau présente de bonnes caractéristiques, ce qui implique que la fissuration de la colonne en acier haute résistance a lieu en raison du procédé de soudage. Les propriétés du matériau de la colonne en acier obtenues par mesures ont ensuite été utilisées dans la simulation par éléments finis. La propagation des fissures dues au soudage a été étudiée selon la théorie des fissures mécaniques élastiques linéaires. Les qualités du matériau du profilé W et du soudage sont évaluées et des conclusions sont tirées concernant les causes des fissures observées pendant la fabrication.

Acknowledgements

First and foremost, I would like to express my sincere gratitude to my advisors Professor Colin Rogers and Professor Dimitrios Lignos for their continuous support during my Master's study and research, for their patience, motivation, enthusiasm, and, above all, their immense knowledge. This thesis would not have been possible without their guidance and support and I can sincerely say that I could not have imagined having better advisors and mentors. I am looking forward to working with you again in the near future.

I would, also, like to thank ADF Group Inc. and DPHV Structural Consultants for their generous technical and financial support as well as the Natural Sciences and Engineering Research Council of Canada. Your support is greatly appreciated.

My sincere thanks also goes to my research colleagues and good friends, Ahmed Elkady, Zaid Gouleh, Omar Ibrahim, Samy Albardaweel, Erwan Lrigoleur, Sarven Akcelyan, Nasser Al Shawwa, Yusuke Suzuki, Omar Shaikhon, Emre Karamanci and Andrew Komar for their help with my research, their friendship and for making the office the best place for someone to work in.

I would also like to thank all my friends in Montreal and in Athens for their support throughout the duration of this research. Thank you for everything.

Last, but not least, I would like to thank my family for supporting me, for believing in me and giving me the strength to pursue my goals. I love you more than words can say and thank you from the bottom of my heart.

Table of Contents

Abstract	i
Résumé	iii
Acknowledgements.....	v
List of Tables	xi
List of Figures.....	xii
Chapter 1 – Introduction.....	1
1.1 General Overview	1
1.2 Research Objectives	5
1.3 Scope.....	6
1.4 Outline.....	7
Chapter 2 – Literature Review	9
2.1 Introduction.....	9
2.2 Theoretical Background.....	9
2.2.1 Welding Parameters	9
2.2.2 Welding Defects	12
2.2.3 Welding Inspection	17
2.2.4 Residual Stresses.....	26
2.2.5 Heat Affected Zone.....	34
2.2.6 Material Properties of A913 Gr. 65 Steel	39

2.2.6.1	Material Parameters	40
2.2.6.2	Mechanical Characterisation of Steel Materials	46
2.2.6.3	Fracture Criteria.....	49
2.2.6.4	Microscopy	54
2.3	Summary	57

Chapter 3 – Testing Program for High Strength Steel ...

Material Characterization.....	59
3.1 Introduction.....	59
3.2 Fracture Toughness and Failure Type.....	62
3.2.1 Charpy V-Notch Tests	62
3.2.1.1 Specimen Preparation	70
3.2.1.2 CVN Specimen Test Results.....	72
3.2.2 Fracture Surface (SEM)	80
3.3 Chemical Composition and Microstructure Examination.....	84
3.3.1 Specimen Preparation	85
3.3.2 EDS Results and Observations	87
3.4 Tensile Material Properties	91
3.4.1 Specimens: Dimensions and Selected Locations.....	92
3.4.2 Results and Evaluation.....	102
3.4.2.1 Standard and Special Coupons Testing Results.....	102
3.4.2.2 Special K-area Coupons Testing Results.....	108
3.4.2.3 Small Coupons Testing Results	110
3.5 Summary of Testing Program and Results	117

3.5.1 Charpy V-Notch Tests	117
3.5.2 Scanning Electron Microscopy	118
3.5.3 Tensile Testing.....	119
 Chapter 4 – Simulation of Welding Procedures Through Finite Element...	
Modelling	121
4.1 Introduction.....	121
4.2 Welded Column Assembly Geometry and FE Meshing.....	123
4.3 Material Properties	130
4.3.1 Expected Material Properties	130
4.3.2 Measured Material Properties	133
4.4 Element Birth and Death Technique	136
4.5 Heat Transfer Analysis	138
4.5.1 Welding Sequence and Modelling Parameters	139
4.6 Stress Analysis	144
4.6.1 Modelling Parameters	144
4.7 Summary of the Results	146
4.7.1 Heat Transfer Analysis Results.....	146
4.7.2 Stress Analysis Results	149
4.8 Critical Crack Length.....	157
4.9 Summary	159
 Chapter 5 – Summary and Conclusions.....	161
5.1 Material Characterisation: Testing Program	161

5.2 Finite Element Modelling of Welding Procedures on High Strength Steel W-shape	
Columns	164
5.3 Suggestions for Future Work	165
List of References	167
A Summary of Tensile Coupon Testing Results.....	177

List of Tables

Table 2.1	Acceptance criteria for visual inspection (AWS 2010, Table 6.1)	22
Table 2.2	Acceptance criteria for visual inspection (AWS 2010, Table 6.2)	25
Table 2.3	Chemical composition of ASTM A913 steel (2007b)	40
Table 2.4	Mechanical Properties of ASTM A913 steel (2007b)	41
Table 2.5	Filler weld metal mechanical properties (AWS D1.8 2009).....	41
Table 2.6	Reduction factors based on Eurocode 3 (2005)	42
Table 2.7	Mechanical properties of four steel grades (Outinen et al. 2002).....	43
Table 3.1	High strength steel column groups	60
Table 3.2	Summary of CVN specimen groups from repaired flange	63
Table 3.3	Summary of CVN specimen groups from gouged flange.....	64
Table 3.4	Repaired flange: CVN test results.....	76
Table 3.5	Gouged flange: CVN test results	77
Table 3.6	Chemical composition of A913 Gr. 65 steel provided by the industrial partner	85
Table 3.7	Chemical composition of developed steels (Banerjee 2013).....	90
Table 3.8	Standard tensile coupon specimens	94
Table 3.9	K-area tensile coupon specimens.....	94
Table 3.10	Small tensile coupon specimens	94
Table 3.11	Mean values for groups close to the weld regions	103
Table 3.12	Mean values for groups away from the weld regions	104
Table 3.13	Mean values from small coupons	113
Table 3.14	SD and COV for small coupon results.....	113
Table 4.1	Average values for the measured engineering stress-strain curves	134
Table 4.2	Welding sequence and procedures.....	142
Table 4.3	Expected material properties case, a_{cr} calculation.....	158
Table 4.4	Measured material properties case, a_{cr} calculation	158
Table A.1	Standard coupon test results.....	199
Table A.2	K-area coupon test results	201
Table A.3	Small coupon test results	202

List of Figures

Figure 1.1	Cracks occurring at groove welded web splice (Fisher 1987).....	3
Figure 1.2	Real life examples of prequalified connections with doubler plates (courtesy of Prof. M. Engelhardt, University of Texas Austin).....	4
Figure 1.3	Examples of a prequalified connection (AISC 2010b).....	4
Figure 2.1	FCAW process (Jefferson’s Welding Encyclopedia 1997)	11
Figure 2.2	Flare bevel groove weld for CJP using FCAW-G (CSA W59 2008)	12
Figure 2.3	Different weld imperfections in a butt joint (Maddox 1994).....	13
Figure 2.4	Centerline cracking (Blodgett et al. 1999).....	14
Figure 2.5	Heat affected zone cracking (Blodgett et al. 1999).....	15
Figure 2.6	Transverse cracking (Blodgett et al. 1999)	16
Figure 2.7	Visual inspection with direct approach (API 2010).....	18
Figure 2.8	Magnetic particle inspection (API 2010).....	19
Figure 2.9	Ultrasonic inspection (Coffey and Whittle 1981).....	20
Figure 2.10	Principle of ultrasonic flaw detection (Coffey and Whittle 1981).....	20
Figure 2.11	Diagram of interaction of ultrasonic beam with crack (Coffey and Whittle 1981)	21
Figure 2.12	Probe movement for testing of butt joint welds (DVN 2012)	21
Figure 2.13	Requirements of groove weld profiles in corner joints (AWS 2010)	23
Figure 2.14	Residual stresses from fabrication (James 2010).....	26
Figure 2.15	Residual stress distribution for a W-shape (Szalai et al. 2005)	27
Figure 2.16	Stress distribution for heavier W-shape (Ziemian 2009, Tall 1964)	28
Figure 2.17	Stress distribution (Ziemian 2009, Hubert 1956)	28
Figure 2.18	Three zones created by one weld bead (Blodgett et al. 1999)	34
Figure 2.19	Reduction factors for yield strength of S460M steel (Outinen et al. 2000) .	44
Figure 2.20	Reduction factors for Young’s modulus of S460M steel (Outinen et al. 2000)	44
Figure 2.21	Three loading modes (Zehnder 2012, Rooke and Cartwright 1976, Tada et al. 2000)	50

Figure 2.22	Two types of crack for K_I (Zehnder 2012, Rooke and Cartwright 1976, Tada et al. 2000)	51
Figure 2.23	Temperature shift between K_{Ic} and K_{Id} (Barsom and Rolfe 1970).....	53
Figure 3.1	Prequalified beam-to-column connection in 65 ksi (450 MPa) W-shape....	60
Figure 3.2	Efforts to repair columns at crack locations	61
Figure 3.3	Schematic drawing of W-shape column with the detected crack location ..	61
Figure 3.4	Plan view and cross sections of repaired column flange / web showing locations of CVN specimens	64
Figure 3.5	Plan view and cross sections of gouged column flange / web showing locations of CVN specimens	67
Figure 3.6	Standard CVN specimen dimensions (ASTM A370 2007a)	70
Figure 3.7	CVN specimens and equipment.....	71
Figure 3.8	Impact energy vs. temperature theoretical curve for 0.06wt.% carbon content	74
Figure 3.9	Evaluation of CVN test results for repaired flange.....	74
Figure 3.10	Evaluation of CVN test results for gouged flange	75
Figure 3.11	Shear surface percentage measurement of C11, C12 & C13 group	81
Figure 3.12	Lateral expansion measurements of C11, C12 & C13 group	81
Figure 3.13	Fracture surface for low, intermediate and high temperature	82
Figure 3.14	SE and BSE images for C1-3 specimen.....	83
Figure 3.15	SE images for C2-6 specimen.....	84
Figure 3.16	Prepared surfaces of C1-3 specimen for SEM.....	86
Figure 3.17	Chemical analysis using EDS	87
Figure 3.18	MnS sulphide inclusions	88
Figure 3.19	Microstructure for different carbon contents (Johnson and Storey 2008) ...	89
Figure 3.20	Comparison of C1-3 and Heat No.14 microstructure	91
Figure 3.21	Dimensions of coupons	92
Figure 3.22	Plan view and cross sections of the repaired column flange / web showing locations of standard\special coupon specimens	95
Figure 3.23	Plan view and cross sections of gouged column flange / web showing locations of standard\special coupon specimens	97

Figure 3.24	Plan view and cross sections of gouged and repaired column flange / web showing locations of small coupon specimens	99
Figure 3.25	Standard coupons engineering stress-strain curves.....	102
Figure 3.26	Standard & special coupon results for various W-shape locations	104
Figure 3.27	Testing of k-area specimens.....	108
Figure 3.28	Stress-strain results for k-area coupon specimens	109
Figure 3.29	Small coupon testing process.....	111
Figure 3.30	Small coupon engineering stress-strain curve.....	112
Figure 3.31	Small coupon results	114
Figure 3.32	Comparison between small and standard coupon results	116
Figure 4.1	Isometric drawing of welded column assembly.....	124
Figure 4.2	2D model geometry of the welded column assembly... (Cross-section A-A)	125
Figure 4.3	FE mesh of the W-shape, the doubler plates and the welds.....	128
Figure 4.4	Material properties variation with temperature (Eurocode 3 2005).....	131
Figure 4.5	True stress-strain curves	135
Figure 4.6	Measured material properties vs. temperature	136
Figure 4.7	Time periods of basic welding procedures	143
Figure 4.8	Snapshots of the activation of welding passes from... heat transfer analysis ($^{\circ}\text{C}$)	147
Figure 4.9	Temperature distribution in two different analysis phases	148
Figure 4.10	Snapshots from stress analysis results for U_x displacements (mm)	149
Figure 4.11	Snapshots from stress analysis results for von Mises stresses (MPa).....	150
Figure 4.12	Results from final step of the stress analysis	151
Figure 4.13	Maximum S22 stress diagrams in the critical crack region	154
Figure 4.14	Comparison of results for SA1 with and without initial residual stresses from fabrication.....	156
Figure A.1	Standard coupon test results.....	178
Figure A.2	K-area coupon test results.....	187
Figure A.3	Small coupon test results	188

CHAPTER 1

Introduction

1.1 General Overview

Over the years, there has been an ever-growing demand for taller buildings and longer spans. Early high rise buildings reached heights of 40 floors and more, while the new generation of skyscrapers involves structures with up to 160 floors and a structural height of over 800m. In order to satisfy the construction demands associated with taller and larger buildings new design methodologies and technologies were introduced to the steel industry. One such innovation is the implementation of high strength steel in modern steel construction. High strength steels have a yield stress in the range of $F_y = 450$ to 500 MPa (i.e. A913 Gr. 65, $F_y = 450$ MPa) versus typical strength steels with $F_y = 300$ to 350 MPa (i.e. A992 Gr. 50, $F_y = 350$ MPa) and super high strength steels with $F_y > 700$ MPa. Increased strength, adequate fracture toughness and weldability are some of the properties that have made high strength steels popular for construction; for example ASTM A913 (2007) steel members with $F_y = 450$ MPa. The use of common steels, such as ASTM A572 (2007) and A992 (2006), in these high-rise buildings would lead to the overall increase of the structural weight since large column sections would have to be used in the construction in order for the steel members to carry the applied loading. Therefore, another advantage of the use of high strength steels that explains their increased popularity is the reduction of the total weight of the structure.

All the aforementioned benefits, entailing high strength steel, have led to the increased use of high strength steel shapes as part of the construction process (Okazaki et al. 2011). However, the use of this material has given rise to problems encountered in practice involving the conduction of welding processes on high strength steel shapes. Typically, a steel construction includes the welding of steel subassemblies either in the shop or, directly, on site. Despite of the fact that in modern steel construction welding procedures are commonly performed in high strength steel shapes, the present American and Canadian welding codes (AWS 2005, D1.8/D1.8M 2009, D1.1/D1.1M 2010 and CSA W59-03 2008) appear not to be updated in order to provide more concrete welding guidelines for subassemblies that involve structural components made of high strength steel.

One of the main concerns in welded connections is the resultant residual stresses, produced mainly by the weld shrinkage that occurs upon completion of the welding process as the steel cools. These stresses can cause defects (i.e. cracking) both at the weld and in the base metal. The adequacy of a welded connection can be ensured through a variety of measures such as increasing the preheat temperature, minimizing the weld volume, using the proper welding technique, applying a proper post heating temperature and procedure, as well as conducting various inspection procedures. However, fabrication related fractures of the welded connection cannot always be avoided. Figure 1.1a illustrates a case where cracking occurred in the column web that originated from the groove-welded web splice termination while Figure 1.1b depicts cracking that occurred through the groove weld (Fisher 1987).



(a) Crack originating at groove weld termination (b) Crack originating at groove weld

Figure 1.1: Cracks occurring at groove welded web splice (Fisher 1987)

The quality of the resulting weld depends on many parameters such as the electrode used and corresponding machine settings, the experience of the weld operator, the chosen welding procedure (including pre- and post-heating), the welding sequence, as well as, the material properties of the welded section and base metal, among others. Therefore, given the difficulties accompanying a welding connection, the lack of welding guidelines with respect to high strength steel is further underlined.

The motivation for this research was generated because of problems related to the welding process of welds conducted in the panel zone area that occurred during the fabrication of high strength steel prequalified beam-to-column connections. Prequalified beam-to-column connections are widely used in modern steel construction as parts of a structure's seismic force resisting system. It is common to reinforce these connections in the panel zone area by welding doubler plates to the web of the column, as illustrated with real-life examples in Figure 1.2.



Figure 1.2: Real life examples of prequalified connections with doubler plates (courtesy of Prof. M. Engelhardt, University of Texas Austin)

Figure 1.3a and b illustrates schematically two common types of fully restrained beam-to-column moment connections; reduced beam section (RBS) and welded unreinforced flange-welded web (WUF-W) as per AISC-358-10 (AISC 2010b). The panel zone area is reinforced such that its shear resistance satisfies the seismic design requirements for controlled panel zone yielding during an earthquake (AISC 2010a, CSA S16 2009).

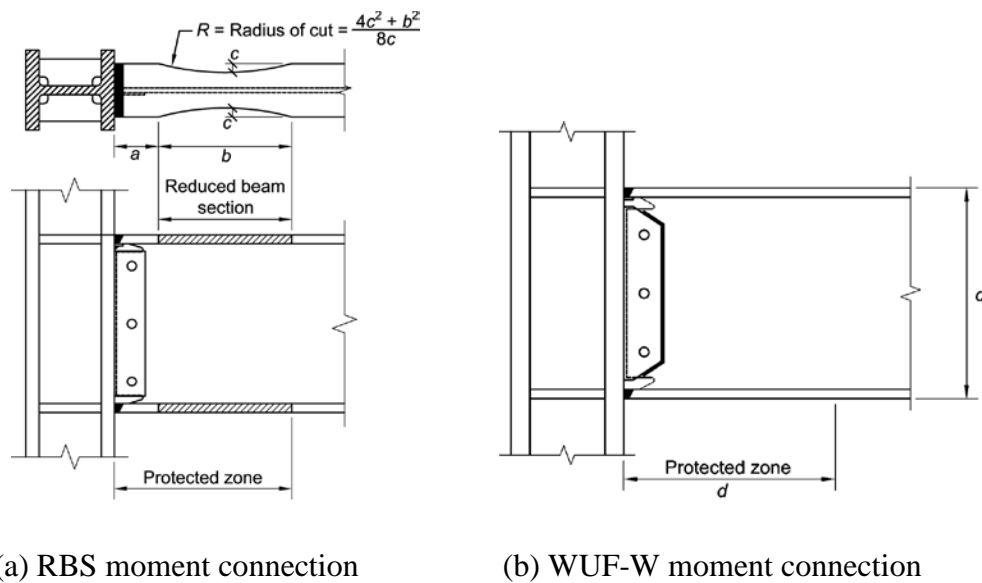


Figure 1.3: Examples of a prequalified connection (AISC 2010b)

Based on information provided by the industrial partner of this project, cracking occurred in the flanges of the high strength W-shape columns near the flange-to-web junction directly after all welding procedures of the prequalified connections in the panel zone area had been completed. The welding procedures involved welding in the k-area. Based on AISC-360-10 (AISC 2010a), welding at highly restrained joints is not recommended and it should be avoided, given that cracking had occurred in the past in these locations. However, in practice welding in the k-area is often unavoidable (Figure 1.2). Addressing this problem through testing different welding techniques in the shop would prove costly with respect to labour and material expenses and time. An alternative approach would be to opt for the use of advanced finite element (FE) modelling tools in order to ensure structural robustness for these connections.

Although the cracking problem discussed is a localized issue, the limitation of the welding codes with respect to welding in high strength steel and the various cracking induced issues related to multi-pass welded connections emphasise the importance of investigating the behaviour of these welded connections. In addition, the regular use of prequalified beam-to-column connections with welded doubler plates on high strength steel columns underlines the necessity to evaluate the commonly used welding techniques in the panel zone area of these members in order for future failures to be avoided.

1.2 Research Objectives

The main objectives of this thesis are to evaluate (1) the applicability of the current welding codes for high strength steel shapes and (2) the current welding procedures used in practice for high strength steel subassemblies. This evaluation is achieved through the

development of a finite element (FE) analysis approach that can successfully simulate multi-pass welding procedures in the panel zone area of a prequalified beam-to-column connection; with which an explanation of how the welding process influences the initiation of cracks may be expressed.

1.3 Scope

To be able to achieve the research goals of this thesis (Section 1.2), a case study was used, which involved the formation of cracks in a prequalified beam-to-column connection in the flanges, near the flange to web junction, of a high strength W-shape column after all welding procedures of the welding of thick doubler plates on the web of the column had been completed. To investigate the cause of the cracking, a two-dimensional (2D) FE model was developed. This model was able to simulate a multi-pass flux core arc welding process with a CO₂ gas shield (FCAW-G) of thick doubler plates on an ASTM A913 Gr. 65 (450 MPa) W-shape with complete joint penetration (CJP) flare bevel groove welds on the sides of the plates and two plug welds in the middle. Two types of analyses were conducted, a heat transfer analysis and a stress analysis. These analyses were performed in order to explicitly model numerically the welding sequence used currently in fabrication practice. Temperature, stress and strain distributions were obtained for the FE model of the beam-to-column connection under investigation. Material testing, consisting of tensile coupon testing, Charpy V-Notch (CVN) testing and scanning electron microscopy (SEM), was also conducted in order to update the FE model. The measured material properties of the cross section, where cracking was originally observed, were utilized to update the FE model. Moreover, using linear elastic

fracture mechanics principles, the probability for crack initiation was computed, the quality of the steel material of the W-shape and the welds performed were investigated and conclusions were drawn regarding the cause of the cracks.

The FE model described in this thesis can be adjusted to any welding process used in current fabrication practice. This model can provide stresses and strains for every welding sequence, number of welding passes and electrode speed by simply changing these parameters in the model while the main principles of the analysis remain the same.

1.4 Outline

Chapter 2 contains a literature review involving previous studies of various welding processes, as well as, a theoretical background involving material testing procedures, residual stresses and linear elastic fracture mechanics theory. Emphasis is placed on the various FE simulations of welding processes performed in the past, which are closely related to this research.

Chapter 3 focuses on the testing program conducted in order to acquire precise material properties for the W-shape column in question. A description of the tensile, CVN and SEM testing includes information regarding the number and the dimensions of the samples tested and the procedures followed to conduct the tests. This chapter also includes information on the particular case study under investigation in this research.

A detailed description of the developed FE model is provided in Chapter 4, which consists of (a) the geometry and meshing of the numerical model; (b) the definition of material properties; (c) the various interaction properties inserted to the surfaces to ensure

the interaction of in-contact surface between themselves and with the environment; (d) constraints and boundary conditions in the two types of analyses conducted; and (e) the “Element Birth and Death” technique used to simulate the welding process. Finally, linear elastic fracture mechanics criteria are employed to examine the possibility of crack initiation and provide a critical crack length for the W-shape section in question based on its material properties, obtained in Chapter 3. Chapter 4 concludes with the results summarised from both analyses for the current welding sequence used in practice.

Chapter 5 provides a summary of the most significant findings of this research. Appendix A contains the results from the tensile coupon testing.

CHAPTER 2

Literature Review

2.1 Introduction

This chapter summarises the basic theoretical background employed for the realisation of this research and presents previous studies involving finite element modelling simulations carried out over the last two decades, relative to the work in question. Welding parameters, inspection and defects are discussed, as well as topics related to changes of the material properties and microstructure from the welding process.

2.2 Theoretical Background

This section discusses the theoretical framework on which this research was based by providing information on the welding process and profile of the simulated weld, the possible welding defects, residual stresses, the heat affected zone (HAZ), material variation and fracture.

2.2.1 Welding Parameters

There are various welding processes and profiles available to conduct a welded joint. However, in this subsection, only the flux cored arc welding (FCAW) process and complete joint penetration (CJP) flare bevel groove weld profile are presented in detail in order to facilitate the understanding of the finite element simulation, discussed in Chapter 4.

- **Welding Process**

Based on the American Welding Society (AWS) D1.1 D1.1M Standard (2010) shielded metal arc welding (SMAW), submerged arc welding (SAW), gas metal arc welding (GMAW) and flux cored arc welding (FCAW) are prequalified processes; thus, processes approved for use without performing any additional welding procedures specifications tests (WPS).

FCAW is most commonly used among these processes. Based on the Fabricator's and Erector's Guide provided by Blodgett et al. (1999) the main component of this method is "the use of an arc between the continuous filler metal electrode and the weld pool". An important advantage of this process is that the use of a continuous electrode minimises the possibility of discontinuities or material accumulation in the weld and, thus, imparts a cost-effective value to the process.

There are two types of FCAW, self-shielded and gas-shielded (FCAW-G). The second type is not suitable for field welding since the weld need to be protected from wind during the process. However, higher strength gas shielding FCAW-G electrodes are available, which increase the speed and the productivity of the welding procedure if used in a fabrication shop setting. An important issue is the selection of the shielding gas, as it affects the mechanical properties of the material (yield stress F_y , ultimate stress F_u , elongation, notch toughness). This is attributed to the fact that depending on the gas chosen different amounts of alloy are transferred from the filler metal to the weld deposit. For example carbon dioxide, as a reactive gas, would most likely oxidize alloys contained in the electrode and, as a consequence, less amount of alloy would result in the weld

deposit. Table 1.2 of AWS A5.20 (2005) summarises the suitable filler metals for this procedure and there are special requirements regarding the storage of the electrodes, given that this is a low hydrogen welding process. This process is generally considered ideal for the conduction of out-of-position welding. Figure 2.1 illustrates the flux cored gas shielded welding process in a butt joint.

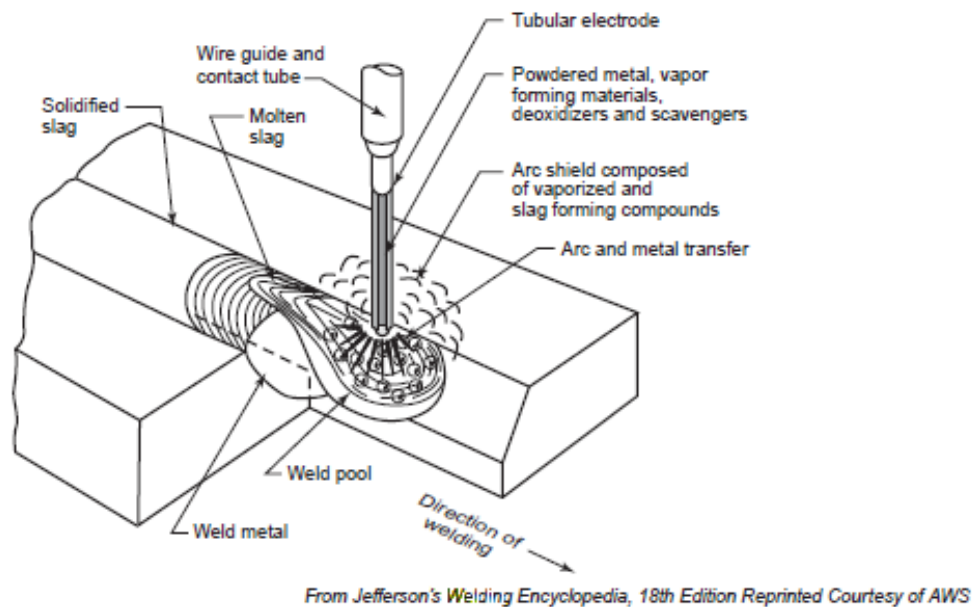


Figure 2.1: FCAW process (Jefferson's Welding Encyclopedia 1997)

- **Welding Profile**

Based on the CSA W59-03 (R2008) Standard (2008) the complete joint penetration weld is defined as “one having fusion of weld and base metal throughout the thickness of the joint”. Welding performed between a curved surface and a planar surface of two members is referred to as a flare bevel groove weld in a T-joint. Figure 2.2 illustrates a typical prequalified joint configuration of this type, conducted with FCAW-G. Groove welds are continuous throughout the length of the joint and their use involves the

transmission of several different types of stresses. Provisions referring mainly to the effective throat of the weld ensure the adequacy of the weld (AWS 2010, AISC 2010a and CSA 2008).

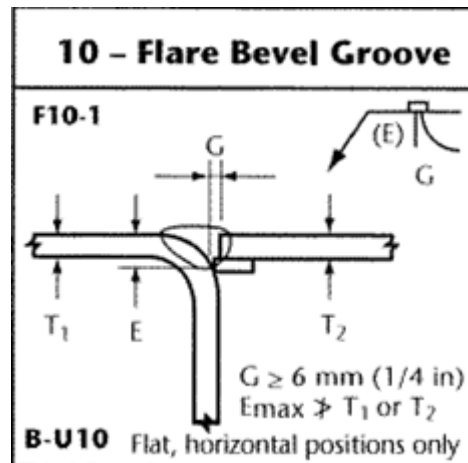


Figure 2.2: Flare bevel groove weld for CJP using FCAW-G (CSA W59 2008)

Plug welds involve drilling a hole in the planar surface of the member overlapping a second member with a diameter that is at least the thickness of the member in question plus 8mm and filling it with weld metal following an ellipsoidal motion. Plug welds are mostly used in order to transfer shear between members, prevent buckling or, in some cases, ensure the fixity between members being connected along their edges with fillet or groove welds.

2.2.2 Welding Defects

During the welding process, melting and cooling of the weld and base metal take place by applying locally a considerable concentrated amount of heat through the use of a transient heat source (electrode). The base metal being in the vicinity of the weld is mostly affected because its properties change due to the increase of temperature (increased level of hardness). This region is referred to as the heat-affected zone (HAZ). The performance

of the resulting weld depends on many parameters such as the electrode used and the experience of the operator, with the most significant parameters being the welding procedure (including pre- and post-heating) and the welding sequence. Discontinuities and cracking may occur both in the weld metal and the heat-affected zone of the base metal. Two main reasons exist for the occurrence of discontinuities after the completion of the welding process; poor weld design and residual stresses. The former refers to discontinuities such as undercut, lack of fusion and incomplete penetration, while the latter to cracking introduced through solidification, cooling and weld shrinkage (Blodgett et al. 1999). Figure 2.3 illustrates some of these defects, as described by Maddox (1994). The non-uniform cooling process occurs inside the weld metal while the welding is in progress, where parts of the metal cool at a slower rate than others. Tensile residual stresses result in the adjacent parts that have cooled faster, which can lead to the initiation of cracks.

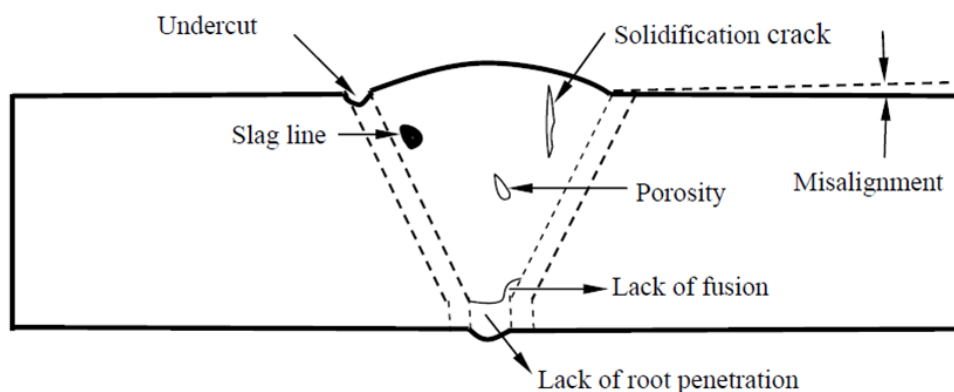


Figure 2.3: Different weld imperfections in a butt joint (Maddox 1994)

The existence of cracking in or near the weld is most alarming and, when observed, careful analysis of the crack's characteristics is necessary to identify the cause and to

select corrective action. The following are types of cracks that can be encountered in and adjacent to a weld soon after fabrication:

- *Centerline cracking*: occurs in the middle of a particular weld bead. It may or may not be in the centre of the weld, when referring to multi-pass welding process (Figure 2.4). It is caused by segregation induced cracking, bead shape induced cracking or surface profile induced cracking (Blodgett et al., 1999). The first cause refers to elements with low melting point such as phosphorus that are unable to be incorporated successfully inside the weld due to the fact that they are the last to solidify. As a result, they are forced to the middle of the weld bead. The second cause refers to the geometry of the weld. For deep penetration processes such as FCAW-G, if the weld depth is much larger than the weld width then newly formed grains during the cooling of certain parts of the weld that develop in a direction perpendicular to the steel surface are unable to merge with the rest of the material. The third cause refers to the weld profile. If high arc voltage is used during welding a concave instead of a convex exterior surface will form. In this case, the interior shrinkage stresses will end up as tension stresses in the outer surface leading to cracking.

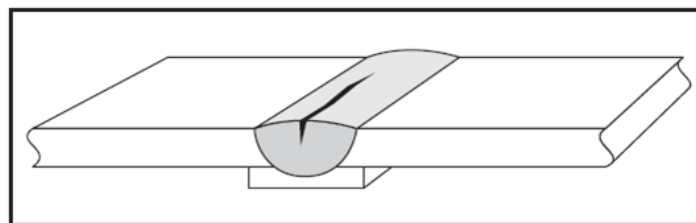


Figure 2.4: Centerline cracking (Blodgett et al. 1999)

- *Heat affected zone cracking*: refers to cracking that occurs in the area of the base metal being the closest to the weld and directly affected by the process (Figure 2.5). This cracking is often referred to as cold cracking as it occurs after the steel has cooled to 204°C (400°F). Three parameters lead to the cause of this type of crack; material sensitivity, high residual or applied stress and increased level of hydrogen. In order for migration of metal to take place due to the hydrogen, enough time must pass; to this end AWS D1.1 (2010) refers to ASTM A514 (2009a), A517 (2010), A709 Gr. 100 and 100W (2009b) standards, which require a minimum of 48 hours post fabrication before an inspection of the weld is conducted, especially when dealing with these steel types, which are known to be sensitive to this type of cracking.

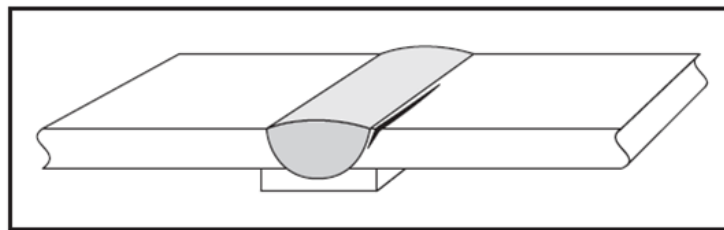


Figure 2.5: Heat affected zone cracking (Blodgett et al. 1999)

- *Transverse cracking*: also called cross cracking, is a crack within the weld metal but perpendicular to the direction of the electrode travel (Figure 2.6). It is a rare case, which mostly occurs when the weld metal significantly exceeds the base metal in strength. The same conditions mentioned above for the heat affected zone cracking can apply for this type of crack; the difference lies in the fact that transverse cracks occur due to the longitudinal residual stresses, caused by the

high restraint of the surrounding material due to the shrinkage of the weld in this direction.

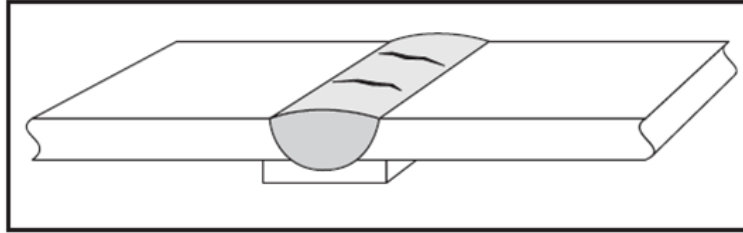


Figure 2.6: Transverse cracking (Blodgett et al. 1999)

Discontinuities are almost always inevitable after a weld is performed; whether they are acceptable or not depends on the applicable code (e.g. AWS D 1.1/D1.1M 2010 and CSA W59 2008) or the project quality level requirements. Examples of these discontinuities are summarised below:

- *Undercut*: is part of the base metal being melted near the weld toe without additional filler metal covering after the void was created. Human errors involving the way the welding is conducted, such as the manner with which the electrode is placed, can lead to this type of discontinuity.
- *Incomplete penetration*: is a problem in the case where the strength of the weld depends also on the melting of the base metal. Failings involving the welding process such as low amperage level and very slow travel speed can lead to inadequate penetration.
- *Lack of fusion*: refers to the case where the base and the weld metal exhibit a certain weakness in creating the appropriate metallurgical bonds that take place during merging of the two materials. This can be caused due to poor selection of filler

metal, of welding procedure or inadequate preparation of the surface before the welding is conducted.

- *Slag inclusions*: refers mostly to non-metallic material that is trapped between weld passes for the case of multi-pass procedures. Inadequate removal of the slag after the completion of a welding pass can lead to these inclusions in the weld. It should be noted that removing the slag can be challenging for even experienced welders since slag can be trapped in notches or small cavities. Proper weld design minimises this effect.
- *Porosity*: refers to the development of small voids of gases inside the weld while it changes phase from molten to solid. These are attributed to poor shielding or the weld from external factors such as oxygen that can contaminate the weld joint.

Cracking constitutes the most serious type of weld discontinuity. It should be pointed out that the failures described above occur during or soon after fabrication and are not due to in-service loading.

2.2.3 Welding Inspection

Five major non-destructive methods exist with which a weld can be examined and discontinuities can be traced and evaluated; visual inspection, penetrant testing, magnetic particle inspection, radiographic inspection and ultrasonic inspection. Following is a brief summary for three of these methods:

- **Type of inspection:**

- *Visual inspection*: is the simplest method as no advanced equipment is required to conduct it. In spite of its simplicity, visual inspection is not to be disregarded as it

can immediately provide a first indication for the quality of the weld but also of the material welded even before the welding procedure has begun. It involves checking the quality, size and cleanness of the material before the weld, verification of the procedures followed based on the Welding Procedures Specifications (WPS), such as preheat, and interpass temperatures and observing the size, the appearance and the bead profile of the weld after completion of the process. For this type of inspection good lighting is of the outmost importance. There are two main approaches; direct and indirect observation. In the case where accessibility to examine the weld surface is provided direct inspection is possible. Based on the API 5 77 Standard (2010) the eye must be placed “within 6 in. – 24 in. (150 mm – 600 mm) of the surface to be examined and at an angle not less than 30 degrees to the surface” (Figure 2.7). In the case where accessibility to the surfaces is not easy indirect observation includes certain tools that can provide the same quality of information as the direct inspection such as telescopes, fiberscopes and cameras.

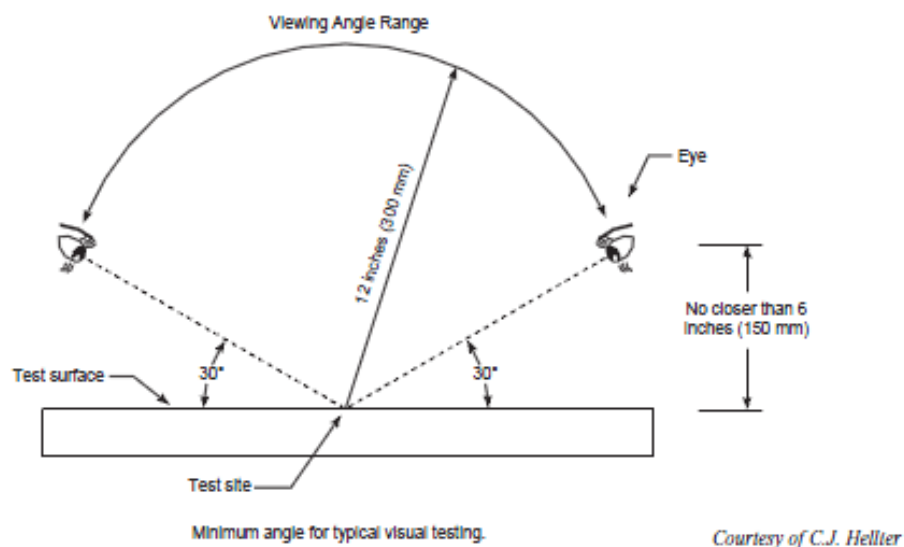
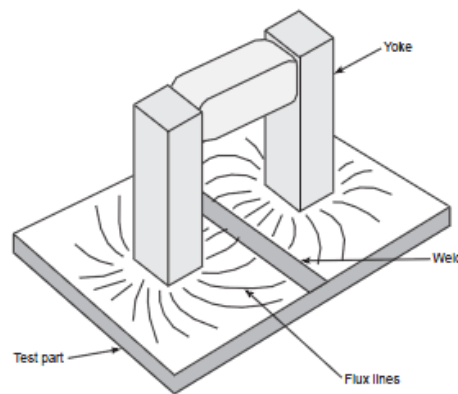


Figure 2.7: Visual inspection with direct approach (API 2010)

- *Magnetic particle inspection:* with this method discontinuities are traced using the magnetic field that is present in their location when the surface is magnetized. In particular, when magnetic powders are placed on the surface the difference in magnetic flux density around the discontinuity region is translated as a different pattern (Figure 2.8). The pattern created by the particles is an indication of the size and shape of the discontinuity. This method is considered to be very effective in locating cracks near the surface, slag inclusion and porosity.



Courtesy of C.J. Hellier

Figure 2.8: Magnetic particle inspection (API 2010)

- *Ultrasonic inspection:* high frequency sound waves are transmitted to the surface under examination. If the surface has discontinuities the sound will be reflected off of the back surface of the part to the receiver in an interrupted fashion. There is a proportional relationship between the magnitude of the signal and the amount of the reflected sound that offers indirectly information about the size, type and orientation of the discontinuity. The relationship of the signal with the back surface of the part being inspected will indicate the location of the discontinuity. Ultrasonic testing is particularly effective in tracing surface and subsurface planar discontinuities in

comparison to cylindrical ones (because of the way the sound is reflected from the surface) and is preferred in CJP groove welds compared to other methods. The signal received is displayed on a screen (Figure 2.9). There are various types of displays and methods to choose from depending on the type of crack being located (A-Scan Display, B-Scan Display etc.). Figure 2.10 illustrates the basic principle of this method, which is the pulse moving in the direction of the crack and being reflected by the crack in a scattered manner towards the receiver. Figure 2.11 demonstrates the different type of waves reflected by the crack while Figure 2.12 illustrates the movement of the probe when examining a butt joint weld.

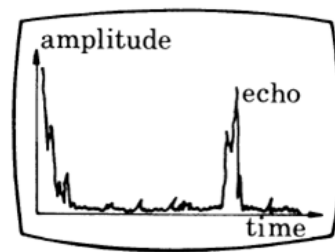


Figure 2.9: Ultrasonic inspection (Coffey and Whittle 1981)

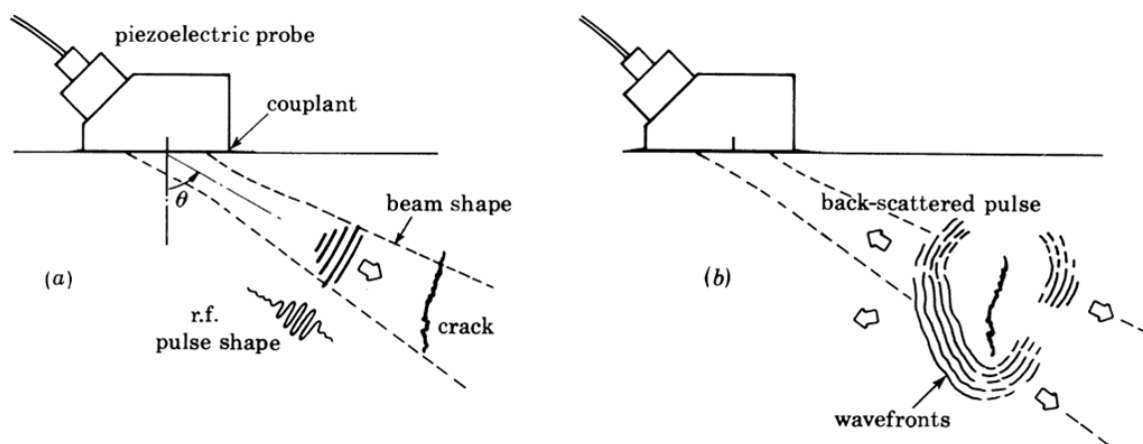


Figure 2.10: Principle of ultrasonic flaw detection (Coffey and Whittle 1981)

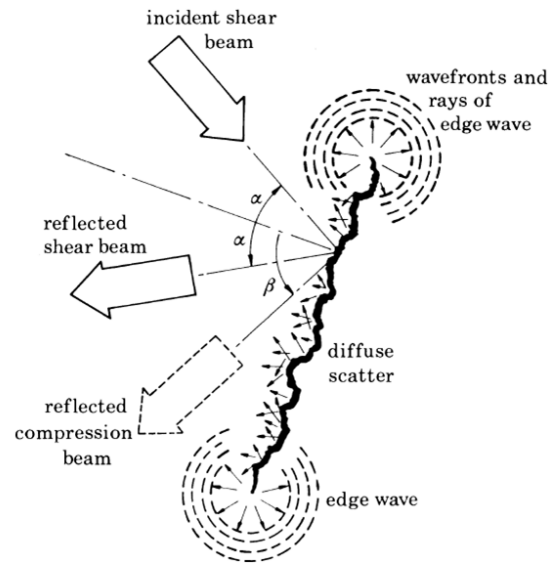


Figure 2.11: Diagram of interaction of ultrasonic beam with crack (Coffey and Whittle 1981)

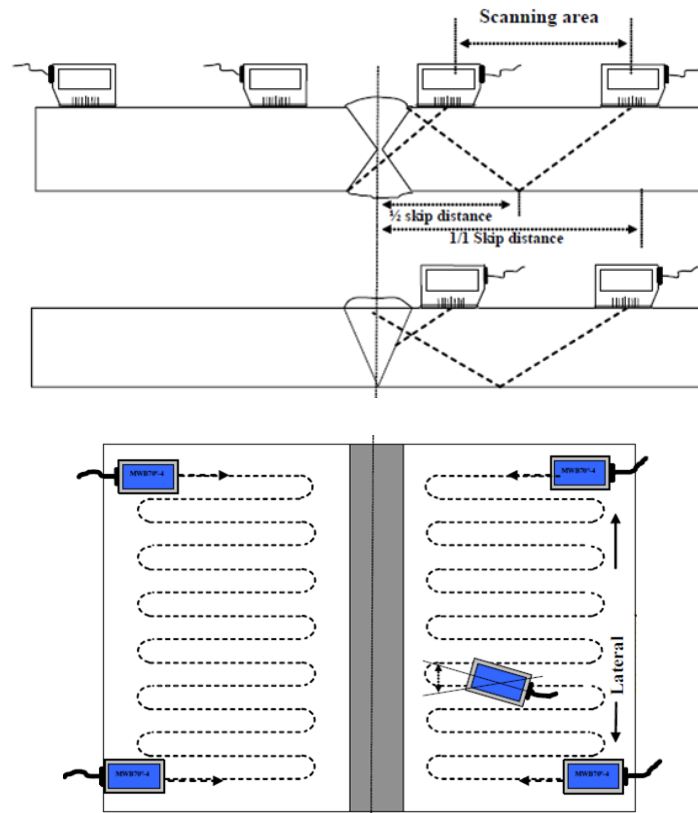


Figure 2.12: Probe movement for testing of butt joint welds (DVN 2012)

- **Acceptance criteria for statically loaded non-tubular connections:**
 - *Visual inspection:* Table 6.1 from AWS D1.1 (2010) summarises the acceptance criteria for visual inspection (Table 2.1), which are in agreement with the acceptance criteria offered in CSA W59 (2008).

Table 2.1: Acceptance criteria for visual inspection (AWS 2010, Table 6.1)

Table 6.1
Visual Inspection Acceptance Criteria (see 6.9)

Discontinuity Category and Inspection Criteria	Statically Loaded Nontubular Connections	Cyclically Loaded Nontubular Connections	Tubular Connections (All Loads)								
1) Crack Prohibition Any crack shall be unacceptable, regardless of size or location.	X	X	X								
2) Weld/Base-Metal Fusion Complete fusion shall exist between adjacent layers of weld metal and between weld metal and base metal.	X	X	X								
3) Crater Cross Section All craters shall be filled to provide the specified weld size, except for the ends of intermittent fillet welds outside of their effective length.	X	X	X								
4) Weld Profiles Weld profiles shall be in conformance with 5.24.	X	X	X								
5) Time of Inspection Visual inspection of welds in all steels may begin immediately after the completed welds have cooled to ambient temperature. Acceptance criteria for ASTM A 514, A 517, and A 709 Grade 100 and 100 W steels shall be based on visual inspection performed not less than 48 hours after completion of the weld.	X	X	X								
(6) Undersized Welds The size of a fillet weld in any continuous weld may be less than the specified nominal size (L) without correction by the following amounts (U): <table><tr><td>L, specified nominal weld size, in [mm]</td><td>U, allowable decrease from L, in [mm]</td></tr><tr><td>≤ 3/16 [5]</td><td>≤ 1/16 [2]</td></tr><tr><td>1/4 [6]</td><td>≤ 3/32 [2.5]</td></tr><tr><td>≥ 5/16 [8]</td><td>≤ 1/8 [3]</td></tr></table> In all cases, the undersize portion of the weld shall not exceed 10% of the weld length. On web-to-flange welds on girders, underrun shall be prohibited at the ends for a length equal to twice the width of the flange.	L, specified nominal weld size, in [mm]	U, allowable decrease from L, in [mm]	≤ 3/16 [5]	≤ 1/16 [2]	1/4 [6]	≤ 3/32 [2.5]	≥ 5/16 [8]	≤ 1/8 [3]	X	X	X
L, specified nominal weld size, in [mm]	U, allowable decrease from L, in [mm]										
≤ 3/16 [5]	≤ 1/16 [2]										
1/4 [6]	≤ 3/32 [2.5]										
≥ 5/16 [8]	≤ 1/8 [3]										
(7) Undercut (A) For material less than 1 in [25 mm] thick, undercut shall not exceed 1/32 in [1 mm], with the following exception: undercut shall not exceed 1/16 in [2 mm] for any accumulated length up to 2 in [50 mm] in any 12 in [300 mm]. For material equal to or greater than 1 in [25 mm] thick, undercut shall not exceed 1/16 in [2 mm] for any length of weld. (B) In primary members, undercut shall be no more than 0.01 in [0.25 mm] deep when the weld is transverse to tensile stress under any design loading condition. Undercut shall be no more than 1/32 in [1 mm] deep for all other cases.	X										
(8) Porosity (A) CJP groove welds in butt joints transverse to the direction of computed tensile stress shall have no visible piping porosity. For all other groove welds and for fillet welds, the sum of the visible piping porosity 1/32 in [1 mm] or greater in diameter shall not exceed 3/8 in [10 mm] in any linear inch of weld and shall not exceed 3/4 in [20 mm] in any 12 in [300 mm] length of weld. (B) The frequency of piping porosity in fillet welds shall not exceed one in each 4 in [100 mm] of weld length and the maximum diameter shall not exceed 3/32 in [2.5 mm]. Exception: for fillet welds connecting stiffeners to web, the sum of the diameters of piping porosity shall not exceed 3/8 in [10 mm] in any linear inch of weld and shall not exceed 3/4 in [20 mm] in any 12 in [300 mm] length of weld. (C) CJP groove welds in butt joints transverse to the direction of computed tensile stress shall have no piping porosity. For all other groove welds, the frequency of piping porosity shall not exceed one in 4 in [100 mm] of length and the maximum diameter shall not exceed 3/32 in [2.5 mm].	X										
		X	X								
		X	X								

Note: An "X" indicates applicability for the connection type; a shaded area indicates non-applicability.

For the case of highly restrained joints of quenched and tempered steels CSA W59 advises a time interval of 48 hours between the completion of the weld and the conduction of the visual inspection. Any crack detected with this method will be considered unacceptable. Certain criteria exist also with respect to the profile of the weld. Figure 2.13 summarises the basic requirements for groove welds.

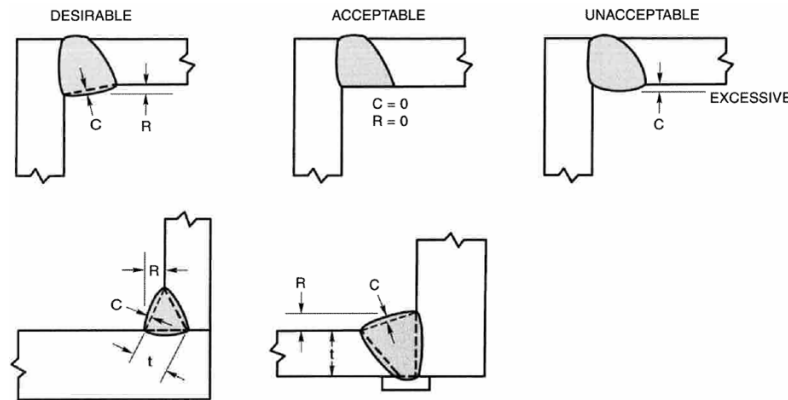


Figure 2.13: Requirements of groove weld profiles in corner joints (AWS 2010)

- *Magnetic particle inspection (MT)*: is considered an additional inspection to visual inspection. Based on AWS D1.8 (2009) cracking or lack of fusion indications traced by this method will be considered unacceptable regardless of their length. In addition, visual inspection criteria apply also for this method. CSA W59 (2008) considers unacceptable porosity of fusion related discontinuities that are 2.5mm (3/32in) or more in length and belong to the following categories:

- Their larger dimension exceeding $\frac{2}{3}$ of the joint or weld throat thickness, with 20mm (3/4in) being the maximum allowable value of this dimension in any case.
- In the case of a group of discontinuities in line, with each discontinuity being in a distance less than 3 times the larger dimension of each adjacent one

(comparing this for each pair of discontinuities), and the sum of their larger dimension exceeding the weld throat thickness in a weld length of 6 times this thickness (or else this rule does not apply).

-For a groove welded joint, discontinuity, designed to receive tensile stress, positioned less than 3 times each larger dimension from each end or at the edge in the case of a transverse weld.

-In general, for porosity or fusion discontinuities arbitrarily distributed over the volume of the weld with the sum of their larger dimension being less than 2.5mm (3/32in) but exceeding 10mm (3/8in) in any 25mm (1in) linear weld length.

MT inspection is required before welding and, also, after welding in the case of a prequalified connection. The member web must be inspected after welding of doubler plates, continuity plates or stiffeners in the k-area. The area to be tested for cracks will include the base metal k-area within 75mm (3in) of the weld and must be conducted not less than 48 hours after the completion of weld.

- *Ultrasonic inspection (UT)*: Table 6.2 (Table 2.2) of AWS D1.1 (2010) and D1.8 (2009) summarises the acceptance criteria. For example, if a class B discontinuity is assumed for a weld thickness of no more than 203mm (8in) the critical discontinuity length is 21mm (0.83in), which gives a critical discontinuity length of $acr=21/2=10.5\text{mm}$ (0.415in). In the case of CJP web-to-flange welds “acceptance (for discontinuities detected from scanning movements other than scanning pattern “E”) may be based on weld thickness equal to the actual web thickness plus 1in (25mm) while discontinuities detected by scanning pattern E shall be evaluated

based on Table 6.2 for the actual web thickness” (AWS 2010). UT is typically performed after the welding procedure is completed. Table 6.2 (Table 2.2) of AWS D1.1 (2010) indicates whether discontinuities found in the base metal within $t/4$ of the steel surface adjacent to the fusion line should be accepted or rejected. Based on this approach any unacceptable welds must be repaired. Additionally, it should be mentioned that the above criteria refer mainly to the weld metal, not base metal, for members of the Seismic Force Resisting Systems (SFRS). Table 11.3 of CSA W59 (2008) is in agreement with Table 6.2 of AWS D1.1 (2010) illustrated in Table 2.2 of this thesis.

Table 2.2: Acceptance criteria for visual inspection (AWS 2010, Table 6.2)

Table 6.2 UT Acceptance-Rejection Criteria (Statically Loaded Nontubular Connections) (see 6.13.1 and C-6.26.6)											
Discontinuity Severity Class	Weld Size ^a in inches [mm] and Search Unit Angle										
	5/16 through 3/4 [8–20]	> 3/4 through 1-1/2 [20–38]	> 1-1/2 through 2-1/2 [38–65]			> 2-1/2 through 4 [65–100]			> 4 through 8 [100–200]		
	70°	70°	70°	60°	45°	70°	60°	45°	70°	60°	45°
Class A	+5 & lower	+2 & lower	-2 & lower	+1 & lower	+3 & lower	-5 & lower	-2 & lower	0 & lower	-7 & lower	-4 & lower	-1 & lower
Class B	+6	+3	-1 0	+2 +3	+4 +5	-4 -3	-1 0	+1 +2	-6 -5	-3 -2	0 +1
Class C	+7	+4	+1 +2	+4 +5	+6 +7	-2 to +2	+1 +2	+3 +4	-4 to +2	-1 to +2	+2 +3
Class D	+8 & up	+5 & up	+3 & up	+6 & up	+8 & up	+3 & up	+3 & up	+5 & up	+3 & up	+3 & up	+4 & up

Class A (large discontinuities) Any indication in this category shall be rejected (regardless of length).	Scanning Levels	
Class B (medium discontinuities) Any indication in this category having a length greater than 3/4 in [20 mm] shall be rejected.	Sound path ^b in inches [mm]	Above Zero Reference, dB
Class C (small discontinuities) Any indication in this category having a length greater than 2 in [50 mm] shall be rejected.	through 2-1/2 [65 mm]	14
Class D (minor discontinuities) Any indication in this category shall be accepted regardless of length or location in the weld.	> 2-1/2 through 5 [65–125 mm]	19
	> 5 through 10 [125–250 mm]	29
	> 10 through 15 [250–380 mm]	39

^b This column refers to sound path distance; NOT material thickness.

2.2.4 Residual Stresses

Residual stresses are induced in a steel section during the fabrication process and their contribution to the total residual stresses being present in a W-shape member after a welding process may be significant (Alpsten 1968, Nyashin 1982). Non-uniform plastic deformations, thermal contractions and phase transformations cause these stresses. No external loading is involved. There are two kinds and three types of residual stresses (Figure 2.14), micro stresses (Type II and III) and macro stresses (Type I). Micro stresses are caused from differences in the microstructure of the material (“different phases or constituents in a material, dislocations and crystallite defects”, James 2010). Their magnitude alternates along the size of the grain. Type II stresses vary at the grain size level while Type III stresses exist within a grain. Macro stresses are developed along the size of the component, Type I. All three types of residual stresses can be present in a structural member. (James 2010).

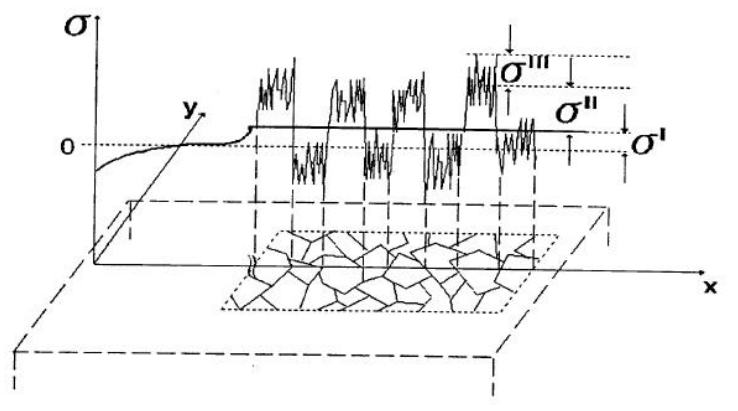


Figure 2.14: Residual stresses from fabrication (James 2010)

The level of influence residual stresses exert on a structural member is directly related to the controlling length, area or volume of the material referring to a particular mode of failure. For a wide flange (W) section the typical stress distribution is parabolic or linear.

The size of the section plates and the thickness of the flange influence the maximum stress value expected. In the case of W-shaped sections there is always pressure at the tip of the flanges, and generally tension at the connection of web and flange with a maximum compressive stress varying between 0.3 - 0.75 times the yield stress (Bjorhovde 1988, Klopper et al. 2011). In Figure 2.15 three common residual stress distributions for a W-shape are presented (Szalai et al. 2005).

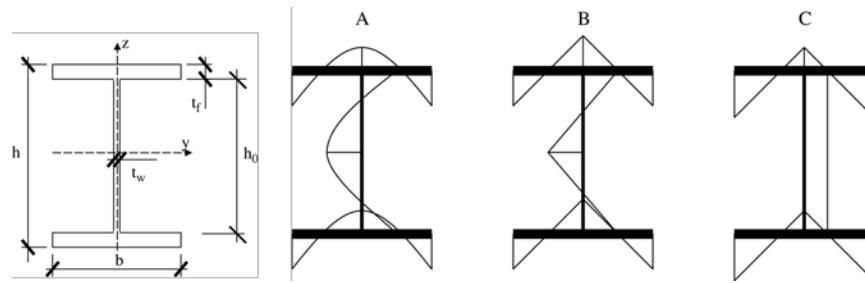


Figure 2.15: Residual stress distribution for a W-shape (Szalai et al. 2005)

However for heavier shapes, residual stress distribution in various thickness levels demonstrates significant differences in magnitude and is not uniform (Ziemian 2009, Brozzetti et al. 1970a, Tall 1964). These differences between the surface and interior residual stresses become more pronounced with the increase of thickness, therefore it is important to be taken into account when dealing with sections with considerable web or flange thicknesses. Figure 2.16 shows a stress distribution of a heavy W-shape where tensile residual stresses from fabrication are developed along the entire length of the web (Ziemian 2009, Tall 1964). Another possible distribution involving hot rolled wide flange shapes with increased web and flange thicknesses also discussed by Ziemian (2009) and presented by Hubert (1956) is shown in Figure 2.17. Hubert investigated the residual stress distribution found in hot-rolled wide flange shapes for various thicknesses that had undergone cold-straightening during the fabrication process. Cold-straightening is

typically performed in most hot-rolled columns leading to the decrease of the initial residual stresses caused by earlier fabrication processes (Ziemian 2009, Brockenbrough 1992, Bjorhovde 2006).

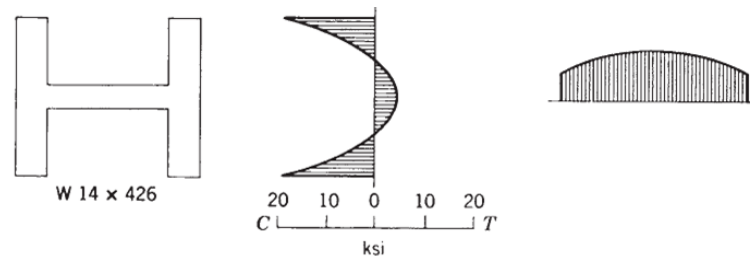


Figure 2.16: Stress distribution for heavier W-shape (Ziemian 2009, Tall 1964)

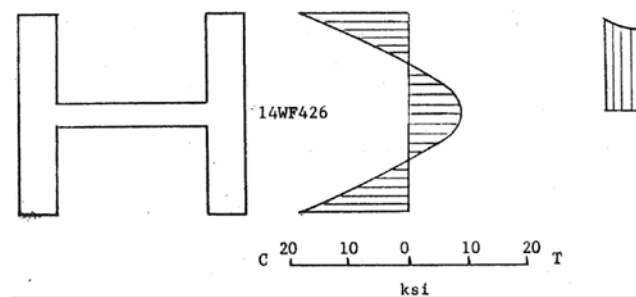


Figure 2.17: Stress distribution (Ziemian 2009, Hubert 1956)

Residual stresses can cause fatigue crack initiation in a component, a change in buckling load and load for welded columns, an increased possibility of brittle fracture in service as well as higher corrosion rates, e.g. in HAZ of welds in marine environment, referring to a microstructure level (James 2010, Alpsten 1968).

Welding influences the residual stress distribution already existing in the section from fabrication processes such as cooling after rolling (Ziemian 2009). Most cracks occur due to shrinkage of the weld metal while cooling; a non-uniform process that takes place inside the weld. Tensile residual stresses are introduced both inside the weld bead and

between the weld bead and the heat-affected zone. The sequence of welding and the number of welding passes are the factors that influence mostly the resulting distribution of residual stresses compared to other welding parameters such as voltage, temperature and areas of preheating (Ziemian 2009, Brozzetti et al. 1970b). The larger the weld the larger the shrinkage and the stresses introduced to the weld location and the areas adjacent to it. Therefore this issue is magnified in multi-pass welding. Tensile residual stresses can influence greatly the global behaviour of the welded structure as they soften the material, making it susceptible to early yielding and even fracture failure.

- **Previous studies:**

Many studies of the last two decades were carried out to better understand and predict the residual stress distribution in T-joint fillet welds and pipe flange welded joints (Ma et al. 1995, Teng et al. 2001, Siddique et al. 2005). Because of the complexity of the welding process due to the various parameters that it involves, accurate prediction of residual stresses raised many difficulties, which led to the use of advanced finite element modelling of the welding procedures. Recent studies involve finite element modelling in thick-walled ship structures, T-joint fillet welds, butt-welded plates and high strength steel plate to plate joints (Pilipenko 2001, Vakili-Tahami et al. 2008 and 2010, Chang et al. 2009, Jin et al. 2011). In all the aforementioned studies the “Element Birth and Death” technique was employed in order to simulate the movement of the electrode for various types of welding processes and welding joints (Brickstad and Josefson 1998). In these studies accurate results were obtained through the use of this technique, which is discussed in further detail in Chapter 4.

Pilipenko (2001) focused on the development of a simulation system, based both on analytical and numerical methods, that could replicate the welding conditions, the temperature fields and the stress and strain distribution during the conduction of a multi-pass submerged arc butt welding process of thick-walled steel panels, referring to the exterior wall structure of ships. Two basic welding techniques were simulated using the finite element program Abaqus; the three-electrode one-pass welding process and the one-electrode multi-pass process, which were then compared in terms of stresses and deformations. Several techniques, such as mechanical straightening and thermal tensioning, were investigated in order to reduce the residual stresses induced from welding using 3D finite element mechanical and sequentially coupled thermal stress models. The temperature interval considered was between 500°C and 1500°C. The 2D simulation revealed that cooling occurs at a much faster rate in the conventional one-electrode welding technique than in the three-electrode. Moreover, another interesting point involves the microstructure of the HAZ. The two welding techniques examined differ in the chemical composition of the HAZ. In the one-electrode case pearlite is not present in the material while it forms 20% of the material in the three-electrode case, leading to a less brittle material and softer HAZ. Referring to residual stresses, the 3D simulations revealed high residual stresses (over the yielding point) in the longitudinal direction, which were attributed primarily to material hardening, while in the transverse through-thickness direction the values were smaller due to the relatively wide plasticity deformation zone developed due to the high heat input applied locally. It was shown that multi-electrode welding causes a wider plasticity zone but also an increased shrinkage in the longitudinal direction than the multi-pass welding. Another important observation

was that inherent residual strains exhibit a noticeable non-linear behaviour. Finally, among other conclusions, it is worth mentioning that mitigation techniques like thermal tensioning lead to a significant reduction of peak residual stresses.

The 2008 study by Vakili-Tahami et al. aimed at the development of a 3D transient finite element simulation of a butt joint weld. Two 2.25Cr1Mo (low-alloy-ferritic steel) welded plates were examined using a coupled thermo-mechanical analysis in order to obtain temperature and stress and strain distributions. The influence of the electrode speed as a welding parameter in the results was investigated. Material variation with respect to temperature was taken into account. The authors of this study concluded that the maximum stresses develop in the HAZ with values varying along the length of the weld and through the thickness of the plate. The longitudinal stresses decrease considerably at a distance 6 times the thickness of the plate away from the weld axis. Comparison with experimental data showed that through the 3D transient simulation in Abaqus accurate results can be obtained.

Vakili-Tahami et al. (2010) investigated the effect of burn-through risk during in-service welding in pipe connection. The main parameters examined were the pipe thickness and the amount of heat input. A 3D finite element model was employed in order to simulate this AISI-316 pipe connection. The material inserted was temperature dependent. Thermal-mechanical analysis was conducted for two different wall thicknesses, for welding sequences involving 4 and 8 weld passes and for two different electrode diameters (direct influence to the heat input) at a T-joint welding connection, taking into account the pressure applied to the main wall of the pipe when under use. Temperature and stress levels obtained were compared to the critical temperature level (980°C) and the

yield stress at certain temperature levels, respectively. The results indicated that pipe thickness is the most important parameter as an increase in thickness can prevent burn-through failure. Moreover, it was discovered that when conducting the welding passes the end position of the electrode has a significant effect in preventing or provoking this type of failure. Finally, the heat input plays also an important role as high heat applied locally can deteriorate the weld quality.

Chang and Lee (2009) developed a 3D finite element model simulating 1-pass fillet welds in T-joints (between two plates) for similar and dissimilar steel welds using the FCAW process. Uncoupled thermo-mechanical analysis was conducted targeting the accurate prediction of residual stresses for the two cases and comparison of the results. This type of analysis is performed in two steps, a thermal and, separately, a stress analysis. Temperature dependent material and mechanical properties were inserted in the model. The data obtained showed that the sharp drop of temperature with the increase of the distance from the welded area leads to a significant variation of the residual stress components through the thickness. An interesting observation was that by increasing the yield stress of the welded material there is an increase in the peak value of the longitudinal residual stresses, located at the weld toe for the similar steel welds case. Finally, between dissimilar and similar steels no significant difference was noted with respect to the magnitude and profile of the residual stresses in both flange and web, only a small difference in the web-to-flange contact locations. Since this was a continuing study from butt joints to T-joints the authors concluded that using this analysis approach enables the acquisition of accurate results.

Jin et al. (2011) focused their study on the finite element modelling of T and Y high strength steel plate-to-plate joints using Abaqus. Various skewed angles and plate thicknesses were examined through the conduction of 2D sequentially coupled thermal-mechanical analysis. The results obtained were compared with experimental data. The authors concluded that the element birth and death technique can be used to successfully simulate the case of multiple welding passes, where welding material is added as the welding process is in progress. Additionally, the sequentially coupled thermal-stress analysis provides reasonable results for the cases tested. Two important observations explain that when welding is performed under ambient temperature the principle residual stress gradually decreases with the increase of the distance from the weld, as observed also in the previous studies, while transverse stress reaches critical value near the weld toe. Lastly, in this study it was shown that although the preheat treatment reduces the maximum value of the principle residual stress and transverse stress in the weld toe it leads to an increase of the transverse stresses in the bottom part of the joint.

In all the aforementioned studies, successful finite element approaches were presented for various types of welding joints, processes and welded steel material types. Most studies were focused in butt or T-joints and involved typically one to three welding passes procedures. Therefore, it is evident that there appears to be a lack of information concerning finite element modelling of multi-pass welding procedures on high strength sections involving real life structural components and problems encountered in practice related to residual stresses due to the welding processes.

2.2.5 Heat Affected Zone

The HAZ is the area of the base metal adjacent to the weld that is mostly affected by the welding process. During the welding process of the doubler plate to the web of a column, for example, the melting and cooling of the weld and base metal take place by applying locally a considerable concentrated amount of heat through the use of a transient heat source. The base metal being in the vicinity of the weld is mostly affected because its properties change due to the increase of temperature. The most important change is the increase of hardness of the material in that region. As a result, the material exhibits more brittle behaviour, which can lead to the appearance of cracks in that location. Therefore, it is important to be able to predict the exact width and depth of the heat affected zone near the weld so as to know how far to expand methods like preheat to eliminate the possibility of cracks, and also the welding inspection in order for a crack to be traced around the weld region. Figure 2.18 depicts three zones developed under the weld bead. After the molten metal is deposited, a fusion zone is created under the weld consisting of molten metal and base metal. Under the fusion zone lies the HAZ referring to the region where the microstructure and mechanical properties of the base metal have been altered due to the increasing heat without melting of the material in that location. The rest of the material that is not greatly affected by the welding process constitutes the third zone (Blodgett et al. 1999).

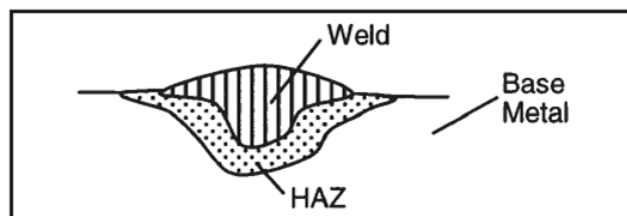


Figure 2.18: Three zones created by one weld bead (Blodgett et al. 1999)

In the case of multi-pass welding, the HAZ created by the first layer of weld beads is reheated and the grains refined by the layer conducted on top of it. With each layer this process is repeated; therefore, in the end, mechanical properties in the HAZ around and in the material inside the final weld product are altered to a certain extent, regardless of the typically small difference between the chemical composition of filler and base metal. Because of the uncertainty of the impact of this process in the ultimate strength, yield strength and hardness, tensile testing and Charpy V-Notch testing (CVN) are typically required to obtain accurate values for the mechanical properties of the welded material. These tests will be explained in further detail in Section 2.2.6.2.

- **Previous studies:**

In order to be able to predict the HAZ width many studies have been conducted in the past 10 years. In most of these studies, the effect of the weld bead on the material properties of the base metal for different welding processes was examined using micrographs (Gunaraj & Murugan 2002, Aloraier et al. 2006, Aloraiera et al. 2010, Lee et al. 2007, Mark et al. 2012). The range of the width of the heat-affected zone for one welding pass was found to be approximately from 4 to 6mm under the weld and 2mm to 4mm near the weld.

In the study by Gunaraj & Murugan (2002) the three aforementioned zones were mentioned as subcritical, intercritical and supercritical, with the supercritical zone being divided in two subzones, grain growth and grain refinement region. The supercritical zone is the one that influences the most the weld joint properties. The size of the HAZ depends on the amount of heat input and the various welding parameters of the welding process under examination. In this paper a mathematical model was developed that could

establish values of welding parameters for the submerged arc welding (SAW) process in order to obtain the desirable weld bead with respect to material mechanical properties and predict HAZ dimensions. Experiments were conducted with 300x150x6mm steel plates using semiautomatic welding. The welding was conducted each time changing welding parameters such as the arc voltage and the welding speed. One weld bead was deposited in the steel plate each time. After obtaining the limit values for these parameters, mathematical models were developed yielding the heat input and the width of each subzone of the HAZ. Preheating was not performed before welding was conducted on the plates. The HAZ width for a typical weld bead was found approximately in total 1.28mm for the SAW process.

Aloraier et al. (2006) investigated the possibility of using temper bead welding to repair the weld (relieve residual stresses and decrease hardness) instead of post weld heat treatment (PWHT) after performing fully automated FCAW. The percentage of the weld that should be covered by the weld bead in order to be successfully treated was also investigated. Welding of 200x100x12mm steel plates was performed. Two weld beads were conducted with 12 to 14mm width and 165mm length as follows; one in the middle of the plate and the other in such a way that it completely overlapped the ending point of the first weld bead but was covering only a part of it at the starting point. This was done so that different percentages of the first weld bead area were covered by the second weld bead along the length of the plate. The plate was then sectioned in the transverse direction and optical microscopy was used to investigate the HAZ width around the welded area. The hardness was measured for different percentages of overlap. The authors concluded that where the percentage of overlap is less the hardness is increased. Also, the bigger the

area covered by the second weld bead the bigger the area of the HAZ refined (heat treated). Therefore, the authors concluded that best percentage of overlap with respect to hardness and microstructure is 50-70%. Moreover, from microscopy, using the scale provided in the figures, it was shown that for welding conducted with the FCAW process the width of HAZ under the weld is approximately 3 to 5mm while near the weld is 2mm.

Aloraier et al. (2010) subsequently conducted an investigation of 200x100x12mm mild steel plates and the Tempered Bead Welding technique to decrease the HAZ in the weld and the base metal without applying PWHT. Four weld beads were deposited, each heat treating the underlying one; a 3D model was employed in the finite element program VrWeld in order to obtain accurate information about the microstructure, the hardness and the HAZ width. After obtaining data for the FE model, the hardness was measured in three vertical lines of the plate using the Vickers hardness test. Using the Vickers hardness tester force is applied to the sample through a diamond indenter and the level of hardness is identified using Vickers Pyramid Number (*HV*). *HV* is determined through the F/A ratio, where F is the force in kilograms-force and A is the area of the indentation imprinted on the sample in millimeters square. The results indicated that there is a big improvement of the microstructure and decrease of hardness after the subsequent weld beads are deposited on top of the first weld bead. In addition, from the subsequent pictures obtained from microscopy with the deposition of every weld bead it was shown that for one weld bead the HAZ width near the weld is 2mm and under the weld bead is 2 to 3mm.

Lee et al. (2007) investigated the effect that various welding parameters had on the size of the weld bead and the HAZ for the SAW process. Weld beads were deposited on the

surface of ASTM A36 low carbon steel plates 300x150x38mm in size. Sectioning was performed after the welding and a Reichart microscope was used to measure the deposition area, fusion area and penetration area. Using Chandel equations (Chandel 1990) the heating process efficiencies were calculated and a ratio between HAZ and bead size was found by correlating the HAZ with the plate melting efficiency. Basic conclusions are that every parameter of the welding process influences the size of the HAZ but in a different level with the welding current being the most important factor as higher current leads to smaller HAZ and HAZ to weld bead ratio. It was shown that the HAZ/bead size ratio varies from 0.35 to 0.70 depending on the welding parameters of the SAW process.

Mark et al. (2012) investigated the resultant residual stresses and local material properties of the weld metal, base metal and HAZ after welding of a three-pass 6mm deep groove weld on two 200x150x20mm ferritic steel plates using a Gas-tungsten arc welding process. Through the neutron diffraction method stresses were measured for the one pass and the three pass case. Local hardness was measured and tensile testing (coupons) was conducted in order to evaluate the properties of the material. Interpass and preheat temperature of 150°C was applied. A 2D transient welding simulation was also included in this research using the FE program SYSWELD. A total of 45 and 53 locations were examined using neutron diffraction method and 6 and 8 coupons were tested at the one-pass and three-pass weld, respectively. Hardness was also measured in sections subtracted from the welded plates at the starting points. First observations referred to the microstructure. From a macrostructure point of view, microscopy revealed that the HAZ around the one weld bead is symmetric (the same near and under it) while in the three-

pass weld it is not. At the microstructure level, the maximum hardness measurements are reduced with the addition of a second weld bead and even more when a third one is added as re-austenitization occurs and the grains are refined. However, the same reduction is not observed in the part of the base metal under the weld, which is attributed to the multiple strain cycles involved in the three-pass welding process. As far as residual stresses are concerned, the data obtained showed a reduction of the peak residual stress in the three-pass compared to the one-pass weld and their presence is further away from the specimen surface. However, the stresses are higher from either side of the specimen leading to the conclusion that residual stresses remain a concern for the three-pass case too. From this paper, it was shown that for one weld bead for this method the HAZ width can be assumed to be 4mm symmetrically distributed around the weld. Moreover, each pass added to the weld did not seem to cause considerable expansion of the HAZ width near the weld (4-5mm) while under the weld the increase is approximately 2mm leading to a 6mm under the weld.

The aforementioned studies offer a good indication of the microstructural changes that take place during a welding process. The influence of welding parameters was investigated and accurate measurements for the hardness, HAZ and residual stresses were obtained through experimental and analytical work.

2.2.6 Material Properties of A913 Gr. 65 Steel

In this section extended reference is made to the properties and fabrication process of ASTM A913 Gr. 65 high strength steel. Information is provided regarding the variation of the material properties with the increase of temperature, the conducted program testing, the fracture criteria and the microscopy.

2.2.6.1 Material Parameters

The ASTM A913 Specification (2007) addresses high strength low-alloy steels. The manufacturing process involves quenching with cold water and self-tempering. The basic advantage of Gr. 65 (450MPa) steel that distinguishes it from other hot rolled steels such as ASTM A572 (2007c) and A992 (2006a) is that it combines high strength, good weldability due to its low carbon equivalent (0.43%) and good toughness in low temperatures. ASTM A913 (2007b) includes strengths from Grade 50 (345MPa) to Grade 70 (485MPa). Its nominal chemical composition and mechanical properties are summarised in Tables 2.3 and 2.4. For Gr. 65 one basic requirement is an average Charpy V-Notch toughness of 54 Joules (40ft.lbs) at 21°C (70°F) while for lower yield strength steels AISC 360 (2010a) requires a minimum average value of 27 Joules (20ft.lbs) at 21°C (70°F).

Table 2.3: Chemical composition of ASTM A913 steel (2007b)

TABLE 1 Chemical Requirements (Heat Analysis)				
Element	Maximum content in %			
	Grade 50 [345]	Grade 60 [415]	Grade 65 [450]	Grade 70 [485]
Carbon	0.12	0.14	0.16	0.16
Manganese	1.60	1.60	1.60	1.60
Phosphorus	0.040	0.030	0.030	0.040
Sulfur	0.030	0.030	0.030	0.030
Silicon	0.40	0.40	0.40	0.40
Copper	0.45	0.35	0.35	0.45
Nickel	0.25	0.25	0.25	0.25
Chromium	0.25	0.25	0.25	0.25
Molybdenum	0.07	0.07	0.07	0.07
Columbium	0.05	0.04	0.05	0.05
Vanadium	0.06	0.06	0.06	0.09

Table 2.4: Mechanical Properties of ASTM A913 steel (2007b)

TABLE 2 Tensile Requirements							
Grade		Yield Point, min.		Tensile Strength, min.		Elongation, min	
		ksi	[MPa]	ksi	[MPa]	8 in. [200 mm], %	2 in. [50 mm], %
50	[345]	50	[345]	65	[450]	18	21
60	[415]	60	[415]	75	[520]	16	18
65	[450]	65	[450]	80	[550]	15	17
70	[485]	70	[485]	90	[620]	14	16

Moreover, referring to a welding connection, AWS D1.8 (2009) summarises CVN requirements in Table A2 (Table 2.5) for E70 and E80 matching filler weld metals for a Gr. 65 base metal that are in agreement with the CVN value discussed above for this base metal.

Table 2.5: Filler weld metal mechanical properties (AWS D1.8 2009)

Table A.2 All Weld Metal Mechanical Properties; Yield Strength, Tensile Strength, Elongation, and CVN Toughness Requirements (see A7.1, A7.2)		
Nominal Electrode Classification Strength	E70	E80
Minimum Yield Strength, ksi [MPa]	58 [400] min.	68 [470] min.
Minimum Tensile Strength, ksi [MPa]	70 [480] min.	80 [550] min.
Minimum Elongation (%), measured in a 2 in [50 mm] gage length	22 min.	19 min.
Minimum CVN Toughness when LAST is greater than or equal to +50°F [10°C]	40 ft·lbf [54 J] @ +70°F [21°C]	40 ft·lbf [54 J] @ +70°F [21°C]
Minimum CVN Toughness when LAST is less than +50°F [10°C]	40 ft·lbf [54 J] @ LAST + 20°F [10°C]	40 ft·lbf [54 J] @ LAST + 20°F [10°C]

- **Yield strength and Young's modulus**

As far as mechanical properties of steel at elevated temperatures are concerned, Eurocode 3 (Part1-2: Structural Fire Design 2005) offers suitable reduction factors for the yield stress (K_y), proportional stress (K_p) and Young's modulus (K_E) (Tables 2.6):

Table 2.6: Reduction factors based on Eurocode 3 (2005)

Temp C	K_E	K_p	K_y
20°C	1	1	1
100°C	1	1	1
200°C	0.900	0.807	1
300°C	0.8	0.613	1
400°C	0.7	0.42	1
500°C	0.6	0.36	0.78
600°C	0.31	0.18	0.47
700°C	0.13	0.075	0.23
800°C	0.09	0.05	0.11
900°C	0.0675	0.0375	0.06
1000°C	0.045	0.025	0.04
1100°C	0.0225	0.0125	0.02
1200°C	0	0	0

Similar reduction factors can be found also in AISC 360 (2010a) and CSA S16 (2009). However, due to the fact that these reduction factors refer to fire design conditions and apply for all types of steels, further research has been realised in order to obtain a more accurate variation of the material properties with the increase of temperature. Outinen et al. (2000) published a paper summarising the results of an experimental study conducted from 1994 to 2000 in the Laboratory of Steel Structures at the Helsinki University of Technology. Results were published in 2001 and 2002 as the program was under progress. This research program involved verification of the mechanical properties and acquisition of stress-strain curves with the increase of temperature for the following steel grades, cold-rolled S350GD+Z steel (2mm thick steel sheet tested, SFS-EN 10 147 1992), hot-rolled S355 steel (cold-rolled 4mm thick steel sheets tested, SFS-EN 10 025 1993), S460M (20mm thick steel plate tested, SFS-EN 10 113-3 1993) and S350J2H cold formed steel (3mm thick tubes tested, SFS-EN 10219-1 1998).

Specimens were tested up to 950°C temperature using two methods, transient and steady state tensile test, with the first being the main method used. The reduction factors

obtained by the test results for each steel grade were compared with the respective ones of Eurocode 3 (2005) for yield stress and Young's modulus as shown in Table 2.6. The main purpose of the research was to provide the variation of material properties for each steel grade with the increase of temperature in such a manner that it could easily be used by researchers in order to insert accurate material properties in a finite element modelling simulation. The results showed that for the S355 and S460 steels the Eurocode reduction factors were close to those obtained from the tests, while for the S350 steel a new approach was suggested since there was significant difference between the experimental result and the Eurocode curve (Outinen et al. 2000, 2004). Table 2.7 illustrates the mechanical properties of these steels at ambient temperature.

Table 2.7: Mechanical properties of four steel grades (Outinen et al. 2004)

Table I. Studied steel grades.			
Steel grade	Nominal f_y (N/mm ²)	Measured f_y (N/mm ²)	Material standard
S350GD + Z	350	402	SFS-EN 10 147
S355	355	406	SFS-EN 10 025
S460M	460*	445*	SFS-EN 10 113
S355J2H	355	539–566 [†]	SFS-EN 10 219-1

In particular, for the high strength S460 steel, tests were carried out in specimens of 20mm thick plates, which were cut out longitudinally to the rolling direction. In total, 60 specimens were tested using both methods mentioned for temperatures up to 900°C. The results demonstrated that the yield strength decreases in a different manner than that proposed by the Eurocode 3 (2005) until a temperature of 500°C is reached. However, at higher temperatures the reduction of the yield strength is similar to that provided by the Eurocode. For the Young's modulus, the opposite applies. The two curves, experimental and from Eurocode, are in agreement until 500°C but for higher temperatures there is a

noticeable difference between the two. Figures 2.19 and 2.20 summarise the reduction factors proposed by Outinen et al. for high strength steel S460.

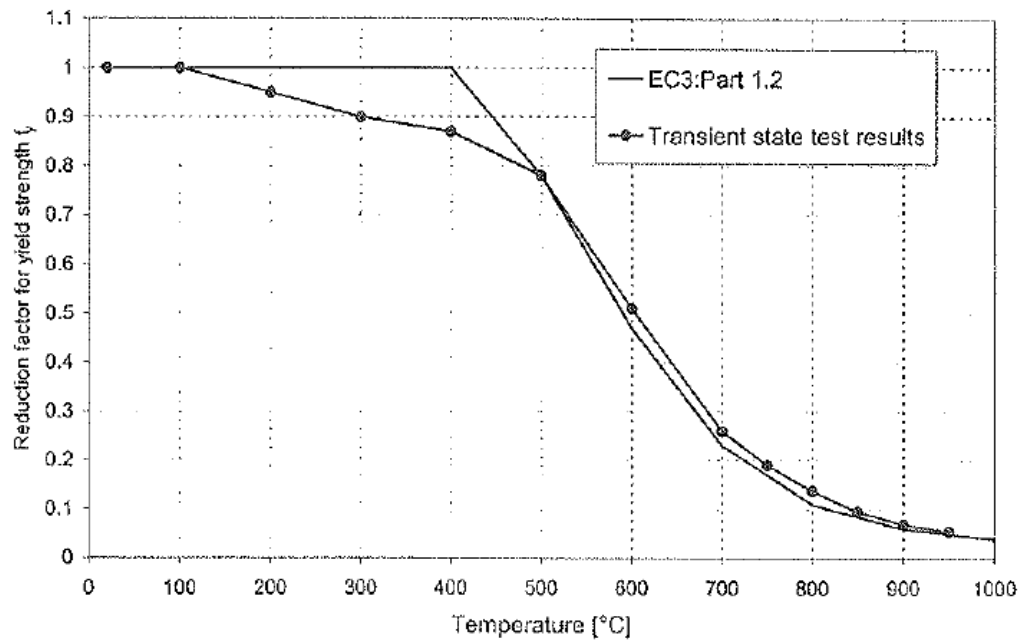


Figure 2.19: Reduction factors for yield strength of S460M steel (Outinen et al. 2000)

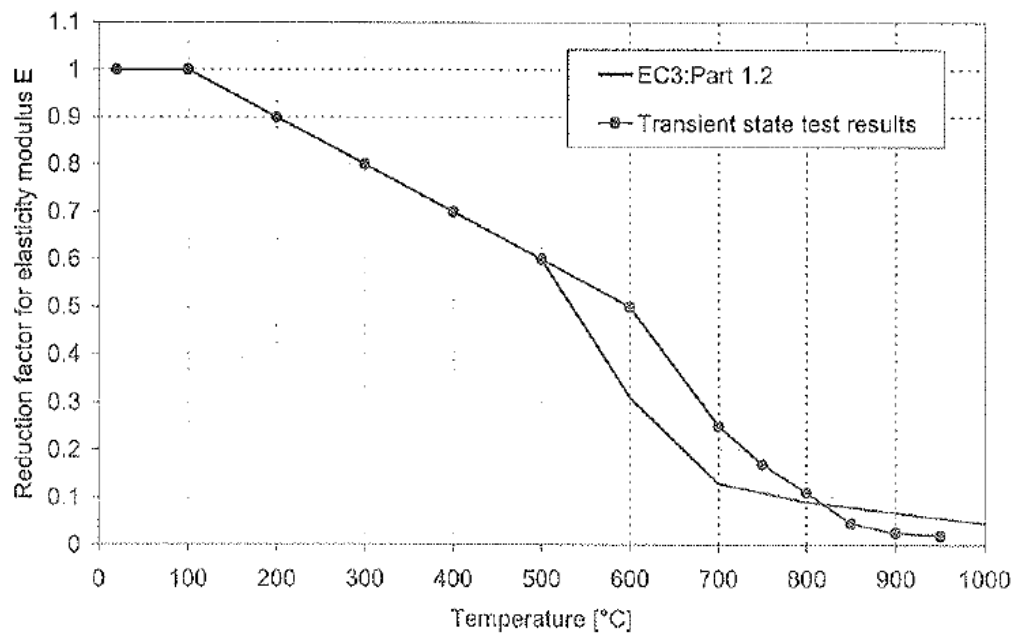


Figure 2.20: Reduction factors for Young's modulus of S460M steel (Outinen et al. 2000)

Apart from the yield strength and Young's modulus, certain thermal properties such as thermal elongation and thermal conductivity are also influenced by the increase of temperature.

- **Thermal elongation**

Thermal elongation ε is defined as the elongation in a member per unit temperature increase (cm/cm/°C). Its value for steel at ambient temperature is 12.6×10^{-6} cm/cm/°C. The AISC 360 Specification (2010a) provides for calculations the value of 14×10^{-6} cm/cm/°C for thermal elongation for temperatures higher than 65°C, which remains constant with the change in temperature. The CSA S16 Standard (2009) provides constant thermal elongation value 11.7×10^{-6} cm/cm/°C for structural steel for a temperature range from 0°C to 100°C. Bletzacker (1966) performed tests on the thermal expansion of steel at elevated temperatures from which were produced Equations 2.1, 2.2 and 2.3:

$$\varepsilon_{th} = (-2.416 \times 10^{-4}) + (1.2 \times 10^{-5} T) + (0.4 \times 10^{-8} T^2), \text{ for } 20 \leq T < 750^\circ C \quad (2.1)$$

$$\varepsilon_{th} = 0.011, \quad \text{for } 750^\circ C \leq T \leq 860^\circ C \quad (2.2)$$

$$\varepsilon_{th} = 0.0062 + (2 \times 10^{-3} T), \quad \text{for } T > 860^\circ C \quad (2.3)$$

These equations are also found in Eurocode 3 (2005).

- **Thermal conductivity**

Thermal conductivity k is defined as the amount of heat flux that would pass through a material according to the temperature gradient over that material. Its unit is W/mK or W/m°C. The thermal conductivity for steel is 54 W/mK at ambient temperature. Eurocode 3 (2005) proposes a variation model with the change of temperature for k as follows in Equations 2.4 and 2.5:

$$k_s = 54 - 3.33 \times 10^{-2} T, \quad \text{for } 20^\circ C \leq T < 800^\circ C \quad (2.4)$$

$$k_s = 27.3, \quad \text{for } 800^\circ C \leq T \leq 1200^\circ C \quad (2.5)$$

- **Specific heat coefficient**

Specific heat C_p is defined as the amount of heat required to raise the temperature of a unit mass of a material by one degree. It is given in J/KgK or J/Kg°C. Eurocode 3 (2005) gives the following equations (Equations 2.6, 2.7, 2.8 and 2.9) to calculate the specific heat of steel with temperature variation:

$$C_p = 425 + 0.773T + 1.69 \times 10^{-3} T^2 + 2.22 \times 10^{-6} T^3, \quad \text{for } 20^\circ C \leq T < 600^\circ C \quad (2.6)$$

$$C_p = 666 + \left[\frac{13002}{738 - T} \right], \quad \text{for } 600^\circ C \leq T < 735^\circ C \quad (2.7)$$

$$C_p = 545 + \left[\frac{17820}{T - 731} \right], \quad \text{for } 735^\circ C \leq T < 900^\circ C \quad (2.8)$$

$$C_p = 650, \quad \text{for } 900^\circ C \leq T < 1200^\circ C \quad (2.9)$$

2.2.6.2 Mechanical Characterisation of Steel Materials

In this section the basic material test methods are summarised based on the ASTM 370 Standard (2007a).

- **Tensile testing**

Tensile testing is a process during which a machined or full-section specimen is subjected to tensile loading until failure occurs. The load is applied with controlled displacement or strain rates through a mechanical or hydraulic means. The main objective is to obtain

accurate values of the Young's modulus and yield, ultimate and fracture stress and strain. In other words, engineering stress-strain curves are acquired for the specific material under examination, which can later be converted to true stress-strain curves and be inserted in the FE model in order to ensure the accuracy of the results, given that nominal material property values are known to differ significantly from the actual values of the material used.

The basic concern in this type of testing is that the load is applied uniaxially. To this end, the specimen is gripped to both ends in such a way as for the centre of the action of the grips to be as much as possible in alignment. Moreover, bending or twisting of the specimen during the test should be restricted to the minimum possible level. For this purpose, specimen dimension requirements specify certain areas of the specimen as grip regions. The A370 (2007a) Standard provides two tables with dimension specifications for rectangular and round coupon specimens of standard and small-size. Typically, coupons are obtained from the structural element in the longitudinal direction but there can also be removed from the transverse or tangential direction if the size of the element allows it. To calculate the elongation a gauge length is clearly indicated on the specimens and typically strain gauges are placed in the centre of that area to measure directly the strain. As an additional measurement of displacement, an extensometer can also be placed in that region. The Standard includes certain methods that can be used to obtain the desired material properties from the results of the test.

- **Charpy impact testing**

During the Charpy Impact test a specially notched specimen is broken in two by a single blow of a swinging pendulum. The specimen notch (either a V or U shape) and

dimensions are specified in ASTM A370 (2007a). The Charpy V-Notch (CVN) test performed under dynamic conditions and at different temperatures. Basic temperatures are the ambient temperature ($23\text{ }^{\circ}\text{C} \pm 5\text{ }^{\circ}\text{C}$) and the 0°C based on requirements with respect to the CVN value for different steel grades tested (BS-EN 10045-1-1990 and A370 2007a). The test does not provide a direct measure of fracture toughness. From the CVN test the absorbed impact energy (related to the height differential before and after impact) is first obtained, through which the fracture toughness of the material can be calculated, as will be explained in further detail in Section 2.2.6.3. In particular, impact energy vs. temperature curve is obtained (Figure 2.22). From this curve, the lower shelf energy, the upper shelf energy and the transition temperature are obtained. After a certain low temperature value decreasing the temperature further does not change the impact energy value obtained; this is the lower shelf energy (minimum energy), where the specimens behave in a fully brittle manner. Respectively, after a certain elevated temperature value the specimens provide the same impact energy while increasing the temperatures; thus this is the upper shelf energy (maximum energy), where the specimens behave in a fully ductile manner. The transition temperature is defined in many ways, such as the temperature below which the material behaves in a purely brittle manner or below which the fracture surface exhibits a percentage of cleavage higher than 50%. ASTM A370 (2007a) defines the transition temperature as “the temperature at which the designated material test value equals or exceeds a specified minimum test value”. Between the transition and the upper shelf energies the specimens are expected to behave in an in-between brittle-ductile manner.

Moreover, by examining the surfaces of the specimens a good indication of the shear area percentage is obtained using tables provided by the A370 Standard (2007a), and lateral expansion is measured using a lateral expansion gauge. From these measurements, the brittle or ductile behaviour of the specimen is determined, expecting the material to behave in a more brittle manner in low temperatures and in more ductile manner as the temperature increases. When testing in different temperatures the difficulty of the test lies on the 5sec time limitation between removing the specimen from the gas or liquid medium used to cool it down or heat it up and performing the test (hit the specimen with the pendulum). The A370 (2007a) requires a minimum of 3 specimens representing one location in the structural element so that an average CVN value can be obtained.

2.2.6.3 Fracture Criteria

Fracture mechanics can simply be described as mechanics for solids with notches, cracks or defects. In linear elastic fracture mechanics the stress intensity factor K is used in order to predict or assess fracture due to applied stress at the location of the crack ($\text{ksi}\cdot\sqrt{\text{in}}$ or $\text{MPa}\cdot\sqrt{\text{m}}$). The stress intensity factor K depends on the size of the crack and the nominal stress away from the crack. Around the crack tip the stress components can be divided in three major modes, Mode I (opening mode), Mode II (sliding/shear mode) and Mode III (tearing mode), as illustrated in Figure 2.21, referring to three intensity factors K_I , K_{II} , K_{III} . For Modes I and II, the solution can be easily found through a plane stress or strain problem using certain boundary conditions such as an infinite plate with an edge of middle finite crack.

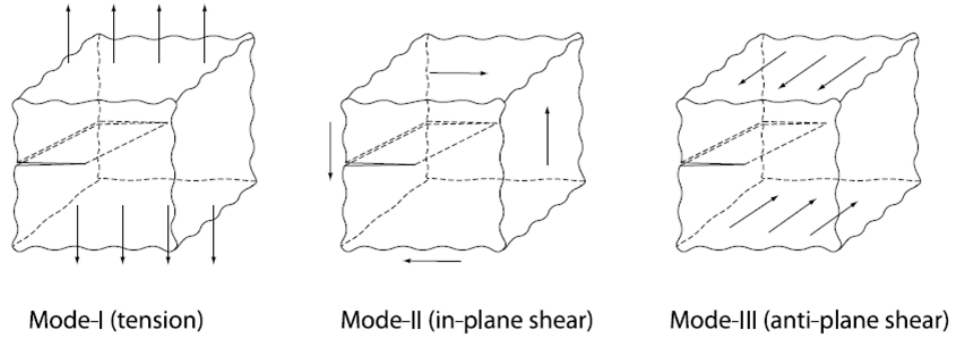


Figure 2.21: Three loading modes (Zehnder 2012, Rooke and Cartwright 1976, Tada et al. 2000)

In elasticity theory it is assumed that the material behaves linear elastically up to the point of the fracture and that very small plastic deformation occurs in the region around the crack (Small Scale Yielding Model). The stress intensity factor K_I is given below for two simple cases (Equations 2.10 to 2.13):

- Single Edge Notch Tension (Figure 2.22 (a)):

$$h/W > 1$$

$$K_I = \sigma \sqrt{\pi a} F\left(\frac{a}{w}\right) \quad (2.10)$$

$$F\left(\frac{a}{w}\right) = 0.265 \left(1 - \frac{a}{w}\right)^4 + \frac{0.865 + 0.265 \frac{a}{w}}{\left(1 - \frac{a}{w}\right)^{3/2}} \quad (2.11)$$

where h is the length of the plate, σ is the average stress applied perpendicular to the crack, a is half the crack length and W is the width of the plate.

- Centre Crack Tension (Figure 2.22 (b)):

$$h/W > 3$$

$$K_I = \sigma \sqrt{\pi \alpha} F\left(\frac{a}{w}\right) \quad (2.12)$$

$$F\left(\frac{a}{w}\right) = \sqrt{\sec\left(\frac{\pi \alpha}{2w}\right)} \left(1 - 0.025\left(\frac{a}{w}\right)^2 + 0.06\left(\frac{a}{w}\right)^4\right) \quad (2.13)$$

where h is the length of the plate, σ is the average stress applied perpendicular to the crack, a is the crack length and W is the width of the plate.

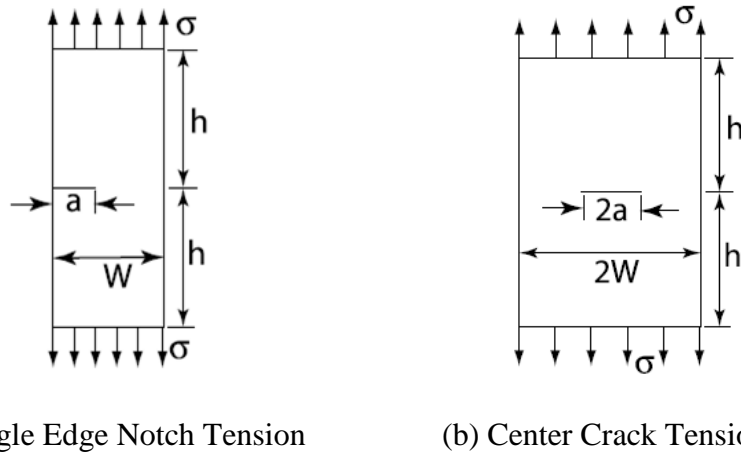


Figure 2.22: Two types of crack for K_I (Zehnder 2012, Rooke and Cartwright 1976, Tada et al. 2000)

The material resistance to fracture is characterised through the fracture toughness K_c or K_d . In particular, K_c refers to the case of static loading while K_d to the case of dynamic loading. These factors are material properties, which are compared with the stress intensity factor K for the particular loading case under examination. If K is equal or exceeds the fracture toughness of the material for the particular loading conditions examined then fracture may occur in the material. There are several methods to calculate fracture toughness; the three-point bend test, the compact tension test and the Charpy impact tests. Through the Charpy V-Notch method, described in the previous section,

CVN values (impact energy values) are obtained for certain locations and temperature conditions. As mentioned before, this is a dynamic test therefore empirical formulas were developed by Barsom and Rolfe (1987) to provide a correlation between K_{Id} and CVN (Equation 2.14):

$$K_{Id} = \sqrt{0.64CVN \times E}, kpa - \sqrt{m} \text{ or } K_{Id} = \sqrt{5CVN \times E}, psi - \sqrt{in} \quad (2.14)$$

where E is the Young's modulus for steel.

In order to obtain the K_{Ic} value for static or slow load conditions for low shelf energies a temperature shift exists between K_{Ic} and K_{Id} illustrated in Figure 2.23. Equations 2.15 to 2.18 are empirical formulas that connect the yield stress F_y of the material and the temperature shift T_s (U.S. Army Corps of Engineers 2001):

$$T_s = 102 - 0.12F_y, \quad \text{for } 250MPa < F_y < 965MPa \quad (2.15)$$

$$T_s = 0, \quad \text{for } F_y > 965MPa \quad (2.16)$$

Or

$$T_s = 215 - 1.5F_y^{\circ F}, \quad \text{for } 36ksi < F_y < 140ksi \quad (2.17)$$

$$T_s = 0^{\circ F}, \quad \text{for } F_y > 140ksi \quad (2.18)$$

For upper shelf energies there is no temperature shift and the K_{Ic} values are obtained using Equation 2.19.

$$\left(\frac{K_{Ic}}{F_y} \right)^2 = 0.646 \left(\frac{CVN}{F_y} - 0.0098 \right) \quad (2.19)$$

Therefore, having obtained a CVN-T curve for a material, a K_{Id} - T curve can be developed and be converted to a K_{Ic} - T curve in case the problem examined involves static and not dynamic loading.

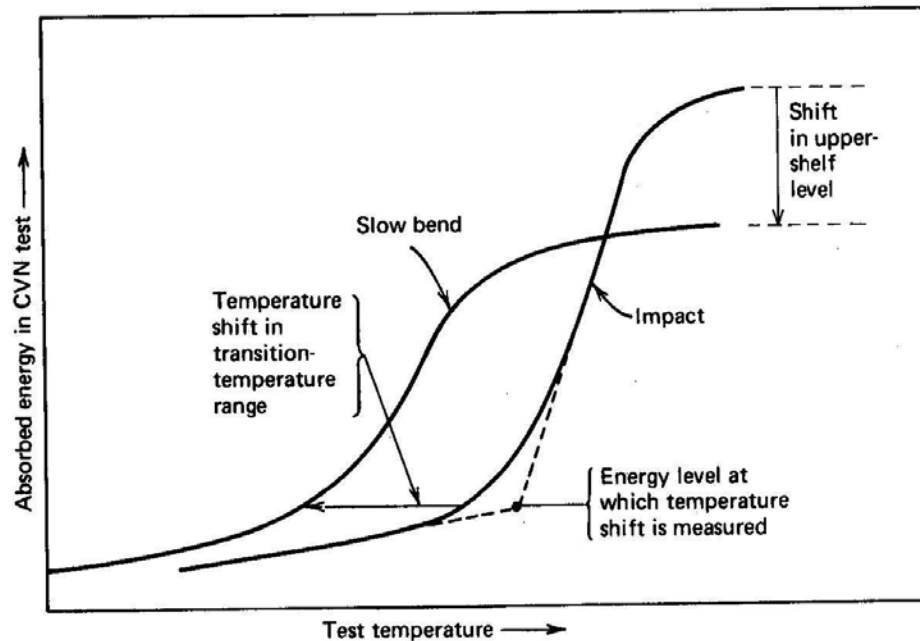


Figure 2.23: Temperature shift between K_{Ic} and K_{Id} (Barsom and Rolfe 1970)

The importance of fracture mechanics lies not only in the fact that estimation can be made for the probability of fracture of a specific material under specific loading conditions but also in the development of acceptance criteria when discontinuities are discovered after inspection of the structural element for cracks and defects (Whittaker 1972). For a specific material, environmental conditions (temperature) and a given set of loads, critical discontinuity sizes can be established through fracture mechanics. Discovered crack sizes can be compared with those limits based on which the structural engineer will decide whether corrective action must be taken or not.

2.2.6.4 Microscopy

In order for the variation of material properties to be better understood one should investigate the microstructural changes that occur inside the material with the increase or decrease of temperature. In this section information about the phase changes of steel are discussed (by Jefferson 1990) as well as the use of scanning electron microscope as a mean to identify them.

- **Microstructure**

In general, it is known that when a material reaches its melting point and is still undergoing heating the temperature of the material stays constant until the entire specimen is melted. This is attributed to the absorption of heat by the elements. For metals that cool slowly there are certain temperatures where phase change occurs. At these temperatures the temperature of the material remains the same for a certain period of time due to the absorption of energy by the metal.

Steels are divided into three categories according to their carbon content; carbon content less than, equal to or greater than 0.83%. As the carbon content of steel increases the freezing point decreases. At high temperatures the iron structure is arranged as face centered cubic, called austenite (carbon atoms soluble in iron). With the decrease of temperature austenite starts to convert to body centered cubic. For steel carbon alloys, during cooling, the temperature does not flatten until the entire element is frozen. Instead grain growth starts taking place. The formed grains freeze while others remain in the liquid stage. The process continues until all grains are frozen (“Mushy stage”). Next is the “white hot stage” where the iron structure, reaching room temperature, becomes body centered and has no longer space for carbon atoms. At this point, the “white hot stage at

room temperature” takes place where the changes happening in the microstructure are dependent on the carbon content as follows:

- *Carbon content equal to 0.83%:* The process of solidification takes place from the moment that temperature is lowered to 1466°C. At 1371°C the process is complete and until 723°C is reached the iron structure is still face centered allowing enough space for the carbon atoms to remain between them. After 723°C body centered arrangements are beginning to form in austenite. Carbon atoms are forced outside the solution by the growing crystals leading to the formation of ferrite (pure iron atoms). Austenite is saturated with carbon atoms. During this transformation process heat is released by the atoms. A new structure appears as free carbon atoms unite with 3 iron atoms to produce Fe₃C iron carbide which is called cementite. The final structure is called pearlite and consists of cementite and ferrite
- *Carbon content less than 0.83%:* At this percentage the transformation of austenite to body centered structure occurs at 816°C. As described previously, carbon atoms are released from the structural arrangement leaving formations of only iron atoms (ferrite). The freed carbon atoms unite with unsaturated austenite that is going to be frozen only when its carbon content reaches 0.83%. At 723°C pearlite is formed. The final mixture will contain pearlite and ferrite.
- *Carbon content greater than 0.83%:* At 1315°C freezing is complete. Austenite grains become larger as temperature drops. Austenite starts rejecting carbon atoms leading to the formation of cementite. Carbon atoms are continuously squeezed out of austenite until the carbon content reaches 0.83%. Then at 723°C pearlite is formed. The final structure will be composed from pearlite and cementite.

For the case of quenched steel, the rapid and abrupt cooling of the metal does not allow enough time for grain growth or segregation of carbon with other elements to take place leading to a structure arrangement called martensite (needle-like crystals). Body centered structures occur at 149°C, where carbon atoms are pushed out of the crystals, imparting high strength and hardness to the material while at the same time the behaviour of the material becomes more brittle. In high cooling rates the structure may be composed only from martensite and in relatively high rates martensite and pearlite.

- **Scanning electron microscopy**

Through microscopy, engineers can gain valuable information about the particular material used in their project or research. Advanced instruments, such as a scanning electron microscope (SEM), provide an accurate description of the material, chemical composition and crystal structure. This can be seen in Chapter 3 for the testing program that was conducted as part of the present study. In the case of a fractured surface, the type of fracture and the crack initiation can be detected through the use of a SEM. This instrument uses a focused beam of electrons to scan the surface of a specimen. The surface can either be cleaned and polished to reveal more about the chemical composition and the structural arrangement or fractured to offer information about the fracture type and crack propagation. SEM achieves a resolution better than 1 nanometre.

There are four methods that can be used to examine the specimen: secondary electrons (SE), backscattered electrons (BSE), energy dispersive spectroscopy (EDS) and electron backscattered diffraction (EBSD). The first two methods provide information about topography, surface morphology and indications about the elements existing in the surface and the grain boundaries. EDS involves the use of X-rays with which a full

analysis of the sample is obtained, all elements present in the material are registered with their molecular and atomic weight in whole regions or certain points of the surface examined, specified manually by the user. Finally, EBSD offers a clear view of the grain boundaries and their orientation.

From all the above information, it can be concluded that through tensile testing, Charpy V-Notch testing and microscopy, a comprehensive investigation of the material properties is achieved leading to definite answers concerning its quality and integrity.

2.3 Summary

In this chapter an extensive summary of the theoretical background of this research is presented. Reference is made to welding processes, profiles, defects and inspection methods. Previous studies involving finite element modelling and residual stress results are discussed and important findings are emphasised related to the heat affected zone through the use of micrographs. The material dependency on temperature changes as well as the microstructural changes taking place inside steel is described with an extended reference on Eurocode 3. Finally, program testing, fracture criteria and scanning electron microscopy are discussed as tools to ensure the suitability of the material.

CHAPTER 3

Testing Program for High Strength Steel Material Characterization

3.1 Introduction

A particular case study involving prequalified beam-to-column connections with welded thick doubler plates on high strength steel columns was incorporated in this research in order for the research objectives to be achieved (Chapter 1, Section 1.2 and 1.3). Discontinuities were found in the flanges of high strength (i.e., nominal yield stress, $F_{y,n} = 450$ MPa) steel W-shape columns near the flange-to-web junction directly after all welding procedures in the panel zone area were completed. These welding procedures consisted of complete joint penetration (CJP) flare bevel welds between the edges of the doubler plate and the k-area of the W-shape and two plug welds in the middle of the plate. A total of 28 high strength steel columns had to be checked for cracks after discontinuities were observed in two of the columns in the flange locations after the removal of misplaced shear tabs. The main focus of this research lies in identifying the cause of the fractures in these flange locations. Table 3.1 summarizes the 28 columns in 4 groups; already on site (not re-checked), to be checked for cracks, cracks discovered in flange locations and columns checked with ultrasonic testing and no cracks were found. In Table 3.1 the sizes of the columns and doubler plates used are included. Figure 3.1 demonstrates the prequalified connection assembly with the doubler plates and the CJP welds of one of the ASTM A913 (2007b) Gr. 65 (450 MPa) wide flange W360x237 (W14x159) 8131mm long columns where cracks were discovered.

Table 3.1: High strength steel column groups

Groups of columns	Size of column (in)	Size of column (mm)	Size of doubler plate (in)**	Size of doubler plate (mm)
Already on site (4)*	W14x193	W360x287	7/8" to 2"	22 to 51
To be checked (7)	W14x193	W360x287	3/4", 7/8"	19, 22
	W14x109	W360x162	3/4"	19
	W14x311	W360x463	1-1/2", 7/8"	38, 22
Cracks discovered (4)	W14x159	W360x237	1"	25
Checked and no cracks were found (13)	W14x120	W360x179	3/4"	19
	W14x193	W360x287	3/4" to 7/8"	19 to 22
	W14x159	W360x237	1"	25
Comments:	* The numbers in parenthesis indicate the number of columns in each group			
	** In some groups different sizes of doubler plates were used for the same size of column			



Figure 3.1: Prequalified beam-to-column connection in 65 ksi (450 MPa) W-shape

Action was taken to trace and remove the defects in two of the columns (Table 3.1 “cracks discovered” group) through gouging of the flange, but attempts to repair the columns were unsuccessful. Figure 3.2a illustrates the gouged flange of one column and Figure 3.2b shows the flange after the attempted repair procedure. Since the repair attempts were unsuccessful one of the columns was discarded along with a part of the other column. One of these two discarded members was available for further examination; and thus was used in this study (Figure 3.2). The crack found in this column had a length of 25.4mm and a depth of 12.7mm through the flange thickness. Figure 3.3a

and b illustrates an indicative schematic drawing of the column with the detected crack location.

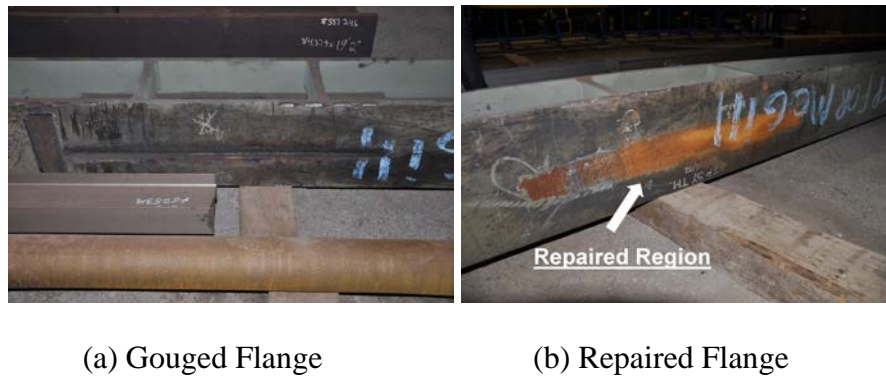


Figure 3.2: Efforts to repair columns at crack locations

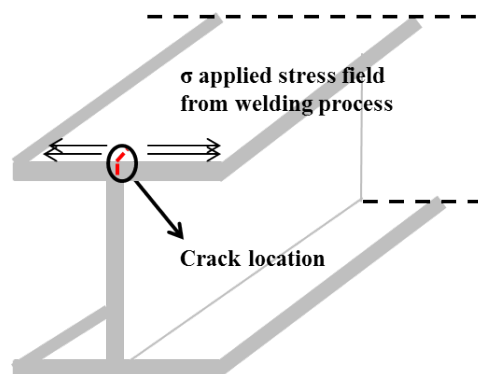
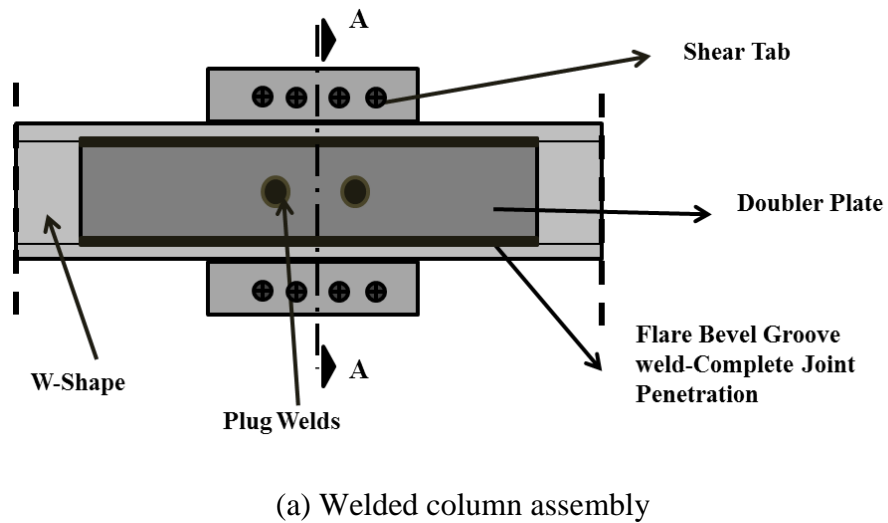


Figure 3.3: Schematic drawing of W-shape column with the detected crack location

A thorough examination of the steel material of the particular column and of the welding procedures performed needed to be conducted. First, the adequacy of the material was verified. Second, a finite element (FE) model simulating the welding procedures was developed to examine whether these fabrication procedures were the primary cause of the cracks, described in detail in Chapter 4.

In this chapter, the detailed material examination is discussed. Results are presented from the scanning electron microscopy (SEM) study, as well as, the tensile coupon testing and Charpy V-Notch testing (CVN). Specimens were milled from the steel column, in order to obtain the chemical composition and mechanical properties of the ASTM A913 Gr. 65 (450 MPa) steel material.

3.2 Fracture Toughness and Failure Type

In this section the CVN testing is described and basic conclusions are drawn, referring to the different groups of specimens obtained from the steel column. Moreover, results from SEM using both secondary electrodes (SE) and backscattered electrodes (BSE) methods are presented for the fracture surface of representative CVN samples, with which a complete evaluation of the material with respect to fracture toughness and specimen failure modes is achieved.

3.2.1 Charpy V-Notch Tests

A total of 16 groups of CVN specimens were tested with each group representing a different location and orientation in the column flange. The specimen groups were obtained from locations near the beam-to-column connection region as well as from regions away from the weld in both the short and long orientations of the column. Tables

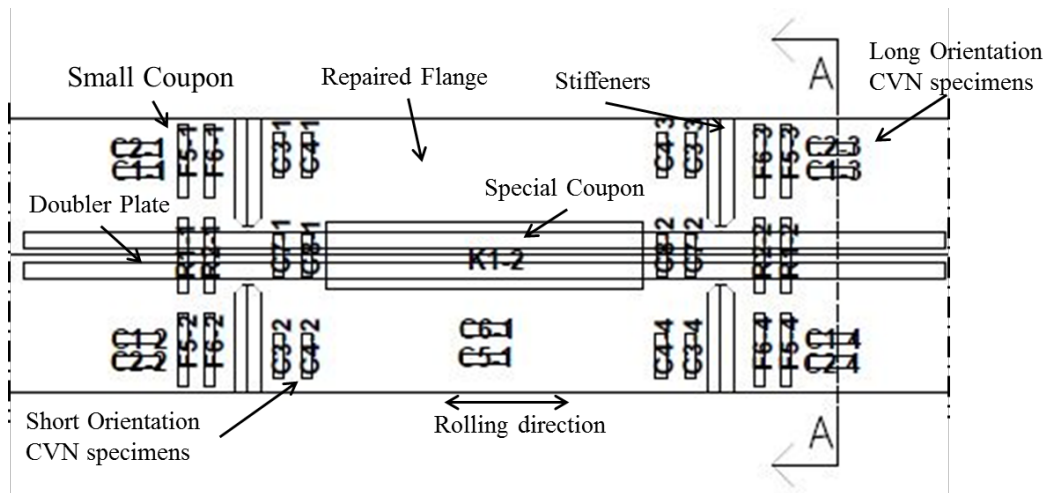
3.2 and 3.3 summarise the CVN specimen groups by number and location while Figures 3.4 & 3.5 include plan views and cross sections with the exact locations of the specimens for the repaired and gouged flange, respectively. The unique notation for the CVN specimens starts with the letter C followed by two numbers separated by a dash. The first number is that of the group while the second number is that of the particular specimen in the group. For example, the C1-3 notation refers to a CVN specimen, which belongs to Group 1 and is the third one in order. In addition, the thicknesses are depicted, T1 and T2. The different flange regions considered are the flange edge, the flange region on top of the k-area (“up flange” area) and the k-area. The column has two locations with doubler plates welded on its web, which are referred to in the figures as welded locations 1 and 2.

Table 3.2: Summary of CVN specimen groups from repaired flange

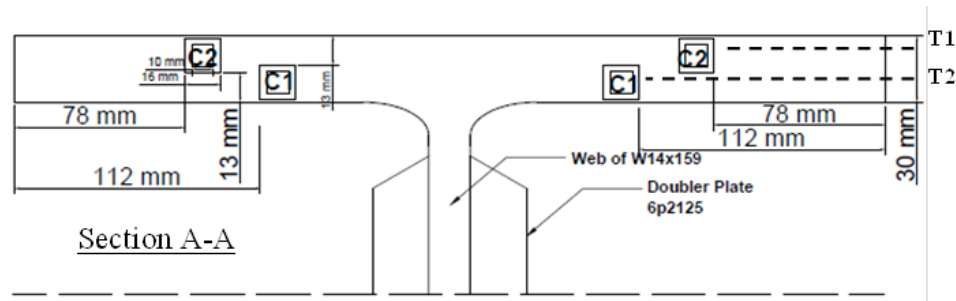
Repaired Flange	Location	Number of specimens
Group		
C1-1 to C1-6	Welded area, long orientation, edge flange	6
C2-1 to C2-6	Welded area, long orientation, edge flange	6
C6-1	Welded area, long orientation, edge flange	1
C5-1	Welded area, long orientation, edge flange	1
C3-1 to C3-8	Welded area, short orientation, edge flange	8
C4-1 to C4-8	Welded area, short orientation, edge flange	8
C7-1 to C7-3	Welded area, short orientation, up flange	3
C8-1 to C8-3	Welded area, short orientation, up flange	3
C14-1 to C14-12	Away from weld, short orientation, edge flange	12
C15-1 to C15-12	Away from weld, short orientation, edge flange	12
C16-1 to C16-12	Away from weld, short orientation, up flange	12
C11-1 to C11-8	Away from weld, long orientation, edge flange	8
C12-1 to C12-8	Away from weld, long orientation, edge flange	8
C13-1 to C13-6	Away from weld, long orientation, k-area	6
Total		94

Table 3.3: Summary of CVN specimen groups from gouged flange

Gouged Flange Group	Location	Number of specimens
C1-7 to C1-12	Welded area, long orientation, edge flange	6
C2-7 to C2-12	Welded area, long orientation, edge flange	6
C6-2, C6-3	Welded area, long orientation, edge flange	2
C5-2, C5-3	Welded area, long orientation, edge flange	2
C3-9 to C3-12	Welded area, short orientation, edge flange	4
C4-9 to C4-12	Welded area, short orientation, edge flange	4
C9-1 to C9-3	Welded area, short orientation, up flange	3
C10-1 to C10-3	Welded area, short orientation, up flange	3
C11-9 to C11-12	Away from weld, long orientation, edge flange	4
C12-9 to C12-12	Away from weld, long orientation, edge flange	4
C13-7 to C13-12	Away from weld, long orientation, k-area	6
Total		44



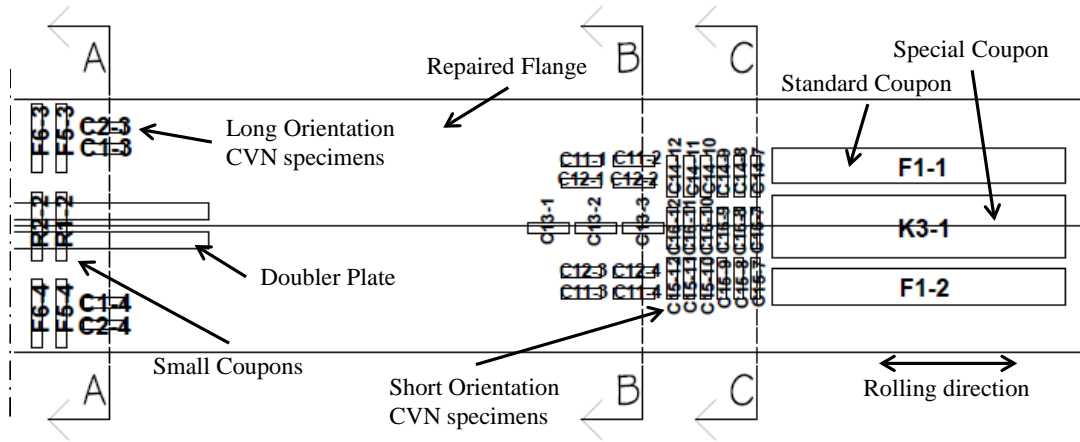
(a) Plan view of welded location 1



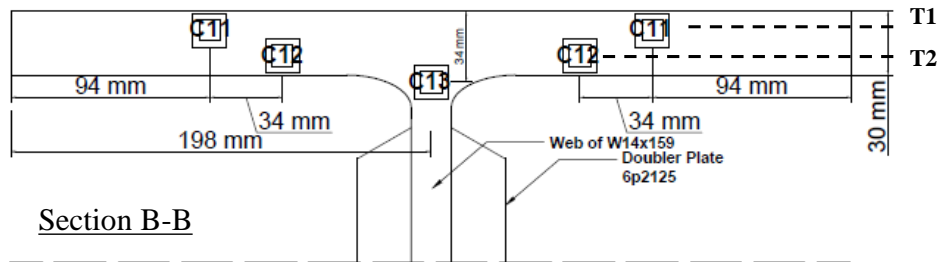
(b) Cross section for specimen groups C1 and C2

Figure 3.4: Plan view and cross sections of repaired column flange / web showing

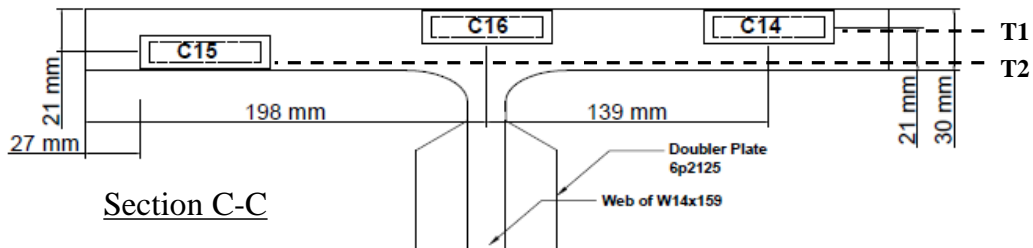
locations of CVN specimens



(c) Plan view of flange region away from welded location 1

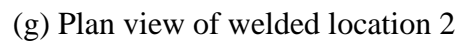


(d) Cross section for specimen group C11, C12 and C13

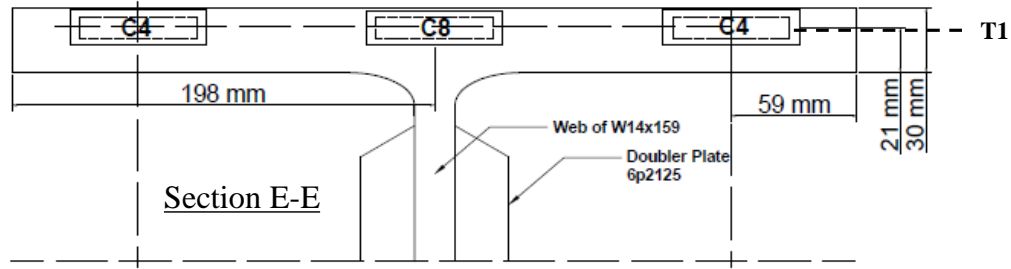


(e) Cross section for specimen group C14, C15 and C16

Figure 3.4 (Continued): Plan view and cross sections of repaired column flange / web showing locations of CVN specimens

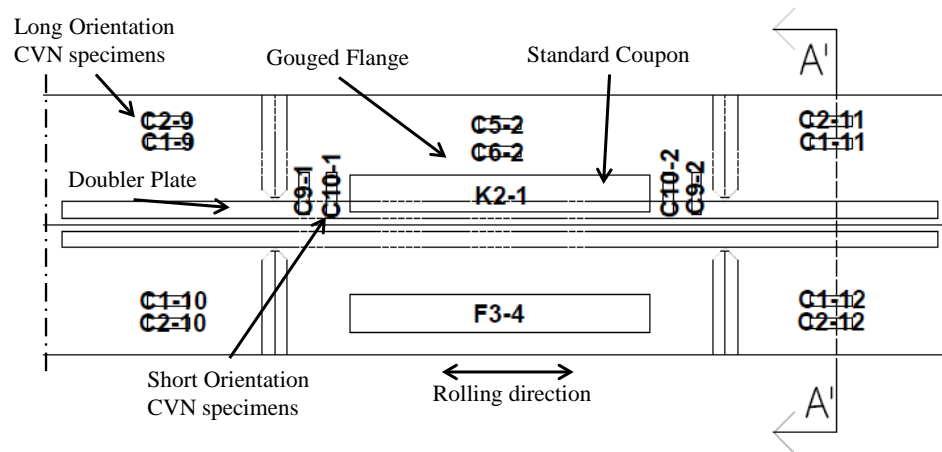


66

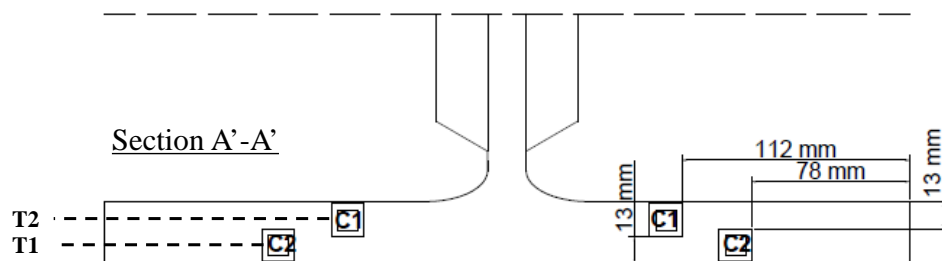


(i) Cross section for groups C4 and C8 (groups C3 and C7 are in the same locations but with T2 thickness)

Figure 3.4 (Continued): Plan view and cross sections of repaired column flange / web showing locations of CVN specimens

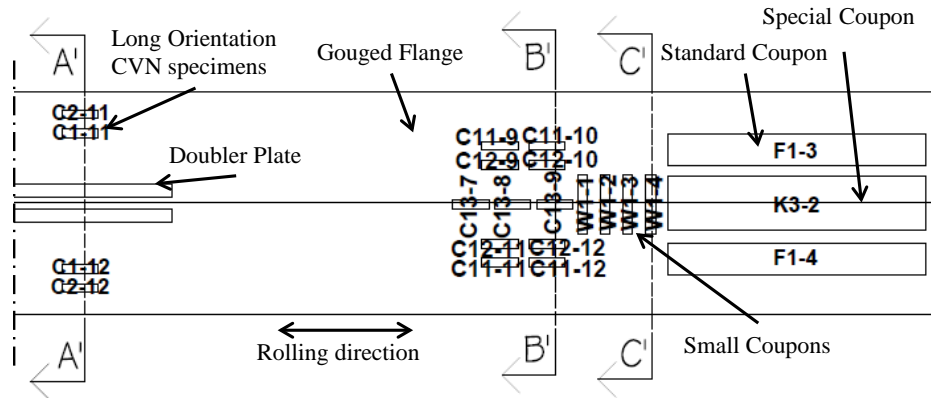


(a) Plan view of welded location 1

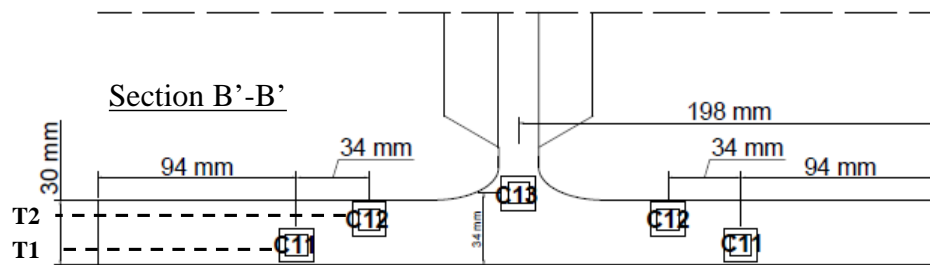


(b) Cross section for groups C1 and C2

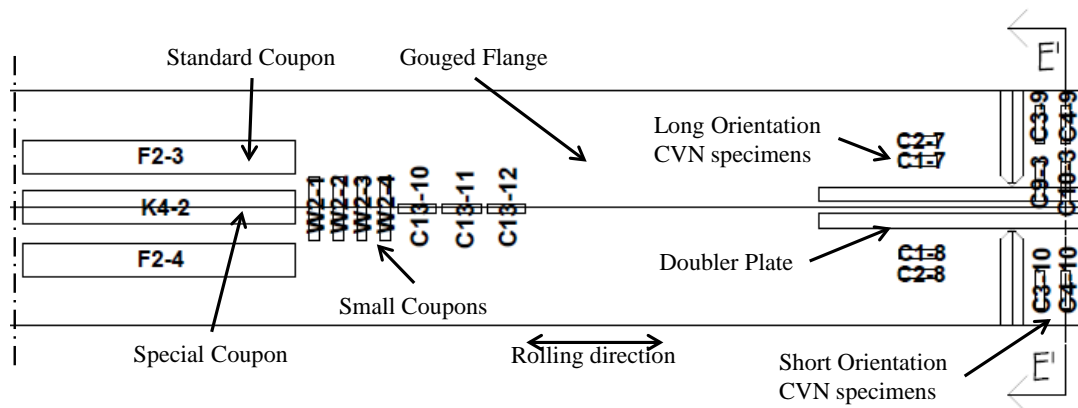
Figure 3.5: Plan view and cross sections of gouged column flange / web showing locations of CVN specimens



(c) Plan view of area away from welded location 1

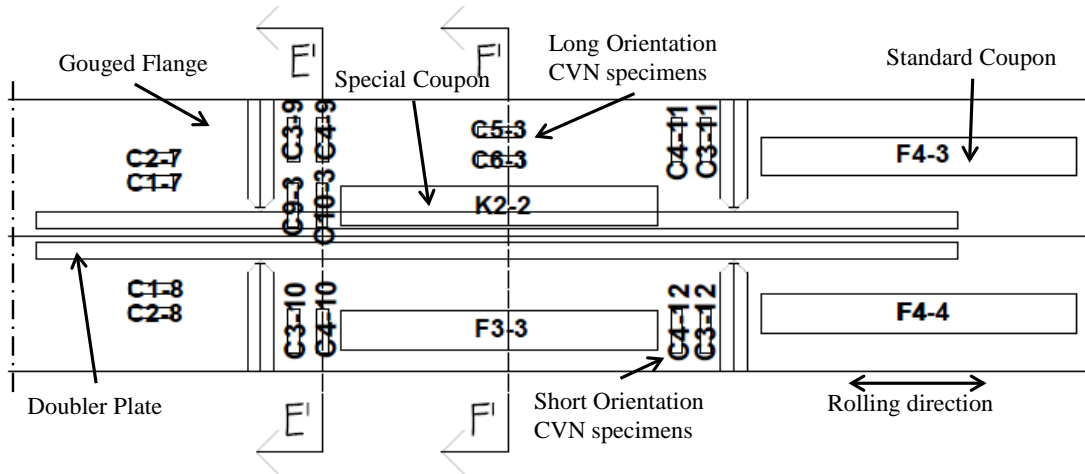


(d) Cross section for groups C11, C12 and C13

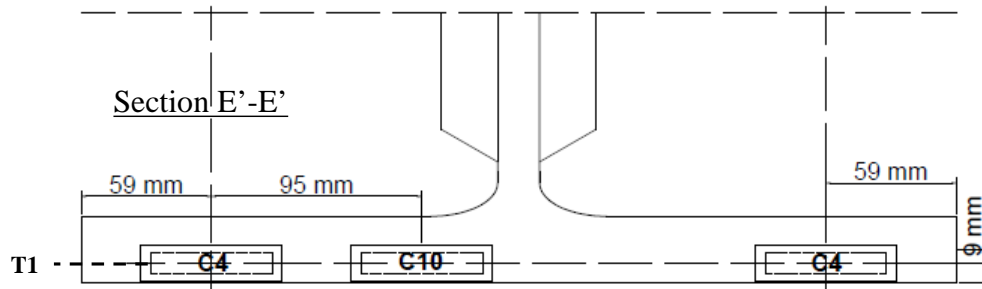


(e) Plan view of area away from welded location 2

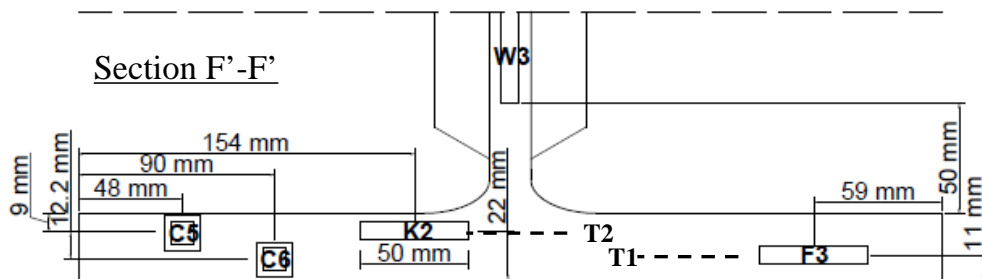
Figure 3.5 (Continued): Plan view and cross sections of gouged column flange / web showing locations of CVN specimens



(f) Plan view of welded location 2



(g) Cross section for groups C4 and C10 (C9 is in the same location as C10 but at T2 thickness)



(h) Cross section for groups C5 and C6

Figure 3.5 (Continued): Plan view and cross sections of gouged column flange / web showing locations of CVN specimens

As depicted in Figure 3.4 & 3.5, CVN specimens were removed from the column in both orientations (grain-short and grain-long). However, the orientation that is of higher importance is the long orientation, given that the observed cracks were deemed to belong to the fracture mode I-tension only case, as described in Chapter 2 (Figure 2.21). Based on this fracture mode, the fracture toughness of the long orientation specimens was used to evaluate the ability of the material to resist fracture, given that the crack caused by impact of the hammer on these CVN specimens propagates perpendicular to the fibre alignment (as the cracks observed in the columns discussed in Section 3.1). Nonetheless, in order for a complete investigation of the material to be realised, specimens were extracted in both orientations.

3.2.1.1 Specimen Preparation

Figure 3.6 shows the dimensions and the notch detail based on ASTM A370 (2007a).

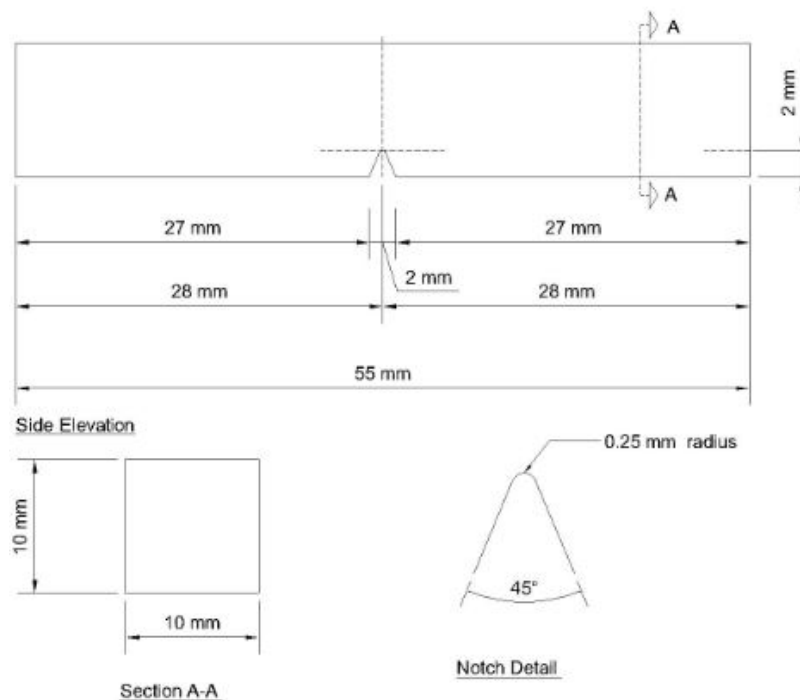


Figure 3.6: Standard CVN specimen dimensions (ASTM A370 2007)

Figure 3.7 shows a selection of the specimens prior to testing as well as the pendulum hammer machine that was used to conduct the CVN tests, located in the Wong Building materials laboratory at McGill University. The tests were performed for various temperatures ranging from -70°C to 160°C . The goal was not only to be able to obtain the upper shelf, the lower shelf and the transition temperature (described in Chapter 2) for each group but also to verify that the material satisfied the 54 Joules (40 ft.lbs) at 21°C (70°F) ASTM A913 (2007b) requirement.



Figure 3.7: CVN specimens and equipment

An oven was used to heat the CVN specimens for the elevated temperature tests. The specimens were placed in the oven for at least 30min while a special pair of pliers, used to move them from the oven to the pendulum hammer machine, was placed inside a boiler with the temperature being kept manually constant to the desired level. In the oven, the temperature level was controlled through the use of a thermometer placed in the top of the oven. Cool air entered into the oven each time it was opened for a specimen to be taken and tested. Depending on the drop of temperature, a minimum waiting time of 5 to

10 min was applied before the next specimen was tested to ensure that all specimens inside the oven remained at the required temperature. The oven was placed as close as possible to the CVN machine so that the minimum possible time elapsed between removing and testing a specimen. With this placing arrangement the estimated “lost” time between removing and breaking a specimen for the elevated temperatures was 10 to 15 sec.

Dry ice and acetone were used to cool the CVN specimens for the low temperature tests. The specimens were kept inside the liquid environment for at least 5min from the moment the required temperature was reached. Specimens were cooled in pairs, as the basin space was small. After the required 5 min cooling period the basin was moved near to the hammer to reduce the “lost” time period, which was estimated to be nearly 5sec. A thermocouple was used to monitor the temperature inside the liquid environment.

3.2.1.2 CVN Specimen Test Results

In order to be able to evaluate the obtained experimental points and resulting transition curves a theoretical reference curve was developed based on Johnson’s and Storey’s paper (2008). They developed a correlation between impact energy, carbon content and temperature referring to simple normalized irons and steels with manganese, carbon and silicon chemical components. They separated iron-based steels into three categories; low, medium and high carbon content based on the fact that for each category the microstructure of steel changes with respect to ferrite and pearlite percentages.

Relationships were developed connecting the upper shelf energy for ferrite with the carbon content, as well as, separate relationships for the transition curve for pearlite and

ferrite. All the relationships were then combined to obtain the transition curve and impact energy values for the material for a given temperature and carbon content. It was observed that as the carbon content increases the transition temperature increases. Moreover, the transition curve becomes steeper as the carbon content decreases but with higher upper shelf energy. Therefore for very low carbon content a steep transition curve is expected with high upper shelf energy. In addition, based on their extracted curves it was observed that for very low carbon content the ferrite equations only provide accurate results leading to the conclusion that for these cases the pearlite contribution is negligible.

The theoretical curve developed for the processing of the results from the CVN testing described in this thesis was based only on the contribution of ferrite, given the low carbon content (0.06%) and presence of pearlite in the microstructure of the A913 Gr. 65 steel in question, as is demonstrated thoroughly in Section 3.3. In the theoretical transition curve for 0.06wt.% carbon, the lower shelf energy and the transition temperature was assumed to be 4 Joules and 0°C, respectively, based on the lower shelf energies and transition temperatures included in Johnson's and Storey's paper. The upper shelf energy was found to be 362 Joules while the width factor had a value of 10.

Figure 3.8 illustrates the constructed impact energy versus temperature theoretical curve for 0.06wt.% carbon content steel. Figures 3.9 and 3.10 illustrate the CVN results for the repaired and gouged flange of the steel column, respectively.

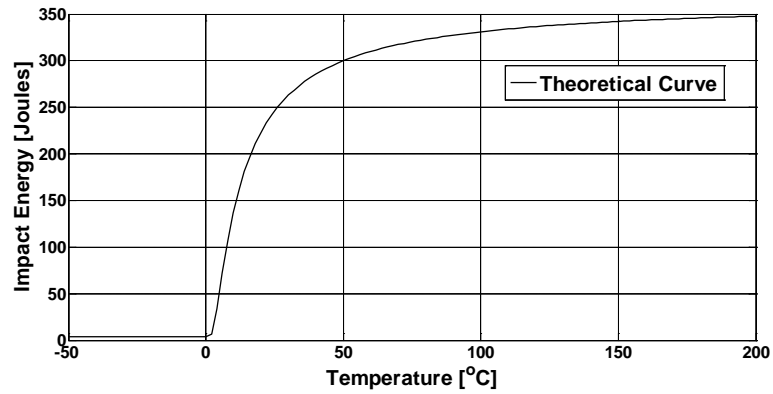
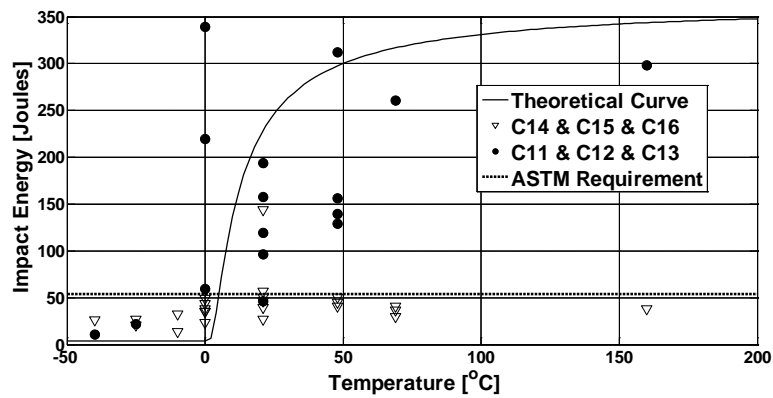
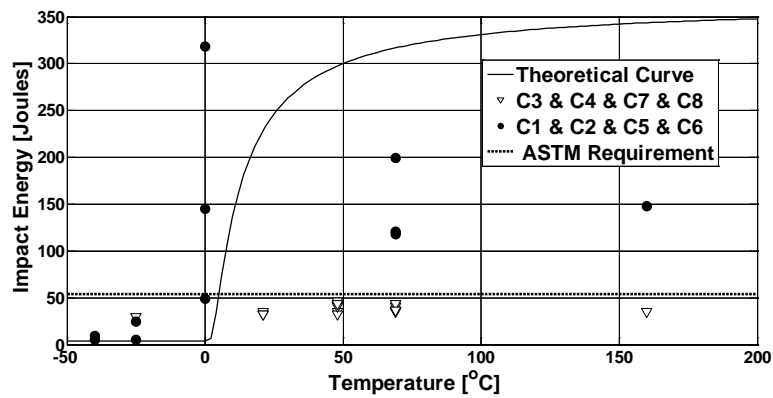


Figure 3.8: Impact energy vs. temperature theoretical curve for 0.06wt.% carbon content

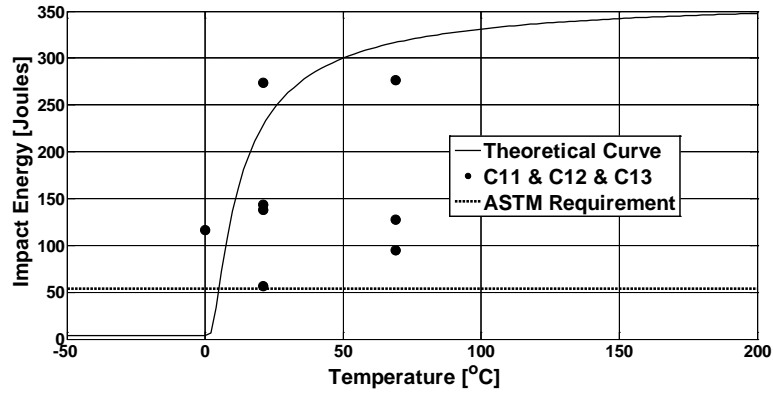


(a) Flange region away from welded locations

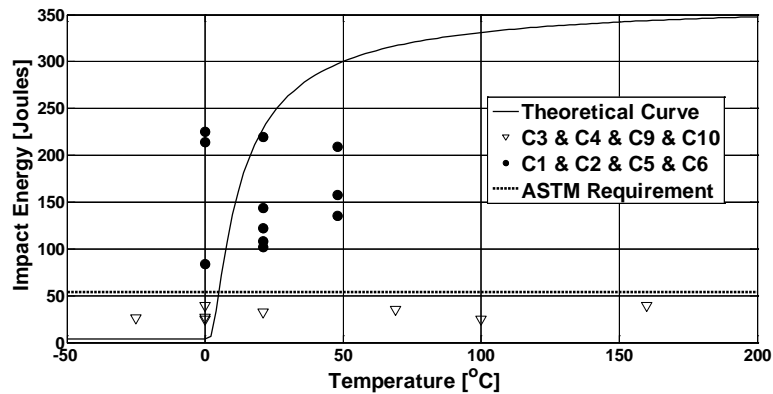


(b) Flange region in the welded locations

Figure 3.9: Evaluation of CVN test results for repaired flange



(a) Flange region away from the welded locations



(b) Flange region in the welded locations

Figure 3.10: Evaluation of CVN test results for gouged flange

In Figures 3.9 and 3.10, it is shown that the CVN values from the long orientation specimens were, as expected, higher than the short orientation values. The long orientation values followed the theoretical curve while the short orientation values remain fairly low over the entire range of temperatures in all the examined locations. The long orientation specimens were expected to absorb more energy while cracking due to the fact that the crack propagates transverse to the direction of the fibre alignment. Similarly, the short orientation specimens exhibited very low energy values due to the fact that the crack propagates parallel to the rolling direction. From the same figures, the CVN values

at ambient temperature (21°C) satisfied the 54 Joules requirement as per ASTM A913 (2007b) for both flange thicknesses in all the examined locations. Note that the requirement refers to the dynamic loading case; hence the temperatures that correspond to this case are shown in Figures 3.9 and 3.10.

Tables 3.4 and 3.5 summarise the mean energy measurement for all the CVN groups, along with the standard deviation (SD) and coefficient of variation (COV) when sufficient test data were available, and separately for the two flange thicknesses for the repaired and gouged flange, respectively.

Table 3.4: Repaired flange: CVN test results

Repaired Flange		Temperature (°C)	Mean (Joules)	SD (Joules)	COV (%)	No. Specimens
Long Orientation						
Away from weld						
Edge Flange	T1	0	220	-	-	1
		21	123	57	46	5
		48	156	-	-	1
		69	260	-	-	1
	T2	-40	11	-	-	1
		-25	22	-	-	1
		0	199	-	-	2
		48	193	103	53	3
		160	298	-	-	1
K-Area		0	14	-	-	1
		21	35	-	-	1
		48	187	-	-	1
		69	175	27	15	3
Repaired Flange		Temperature (°C)	Mean (Joules)	SD (Joules)	COV (%)	No. Specimens
Long Orientation						
Near the weld						
Edge Flange	T1	-60	15	-	-	1
		-40	9	-	-	1
		48	87	-	-	1
		69	146	46	32	3
		160	148	-		1
	T2	-40	5	-	-	1
		-25	15	-	-	2
		0	171	137	80	3
		48	289	-	-	1

Repaired Flange		Temperature (°C)	Mean (Joules)	SD (Joules)	COV (%)	No. Specimens
Short Orientation						
Near the weld						
Edge Flange	T1	21	33	2	5	3
		48	43	3	6	3
		69	40	-	-	2
	T2	-25	30	-	-	1
		48	37	5	13	3
		69	38	3	8	3
		160	35	-	-	1
Flange Up	T1	21	43	-	-	2
		48	35	-	-	1
K-Area	T2	0	58	-	-	2
		48	39	-	-	1

Table 3.4 (Continued): Repaired flange: CVN test results

Repaired Flange		Temperature (°C)	Mean (Joules)	SD (Joules)	COV (%)	No. Specimens
Short Orientation						
Away from weld						
Edge Flange	T1	-25	24	-	-	2
		0	42	7	16	3
		21	78	57	74	3
		48	45	5	11	3
		160	38	-	-	1
	T2	-40	26	-	-	1
		-10	23	-	-	2
		0	32	8	25	3
		21	43	15	35	3
		69	36	5	15	3
Up Flange	T1	-40	4	-	-	1
		-25	16	-	-	1
		0	25	5	22	3
		48	40	10	26	3
		69	42	2	5	3
		160	43	-	-	1

Table 3.5: Gouged flange: CVN test results

Gouged Flange		Temperature (°C)	Mean (Joules)	SD (Joules)	COV (%)	No. Specimens
Long Orientation						
Away from weld						
Edge Flange	T1	21	57	-	-	1
		69	166	97	58	3
	T2	0	117	-	-	1
		21	185	77	41	3
K-Area		0	22	3	13	3
		48	101	10	10	3

Table 3.5 (Continued): Gouged flange: CVN test results

Gouged Flange		Temperature (°C)	Mean (Joules)	SD (Joules)	COV (%)	No. Specimens
Long Orientation						
Near the weld						
Edge Flange	T1	0	174	78	45	3
		21	148	55	37	4
	T2	0	98	-	-	2
		21	162	51	32	3
		48	167	38	22	3
Gouged Flange		Temperature (°C)	Mean (Joules)	SD (Joules)	COV (%)	No. Specimens
Short Orientation						
Near the weld						
Edge Flange	T1	-25	35	-	-	1
		21	33	-	-	1
		69	26	-	-	1
		100	24	-	-	1
	T2	0	30	8	26	3
		160	39	-	-	1
Up Flange	T1	21	42	8	18	3
	T2	69	43	7	17	3

In Tables 3.4 and 3.5 it is shown that for 21°C the CVN values for the long orientation specimens were higher than 54 Joules, with the exception of one k-area specimen away from the weld location. This specimen was located in the repaired flange that exhibited a lower value. However, that is expected since it is known that the k-area exhibits typically lower toughness due to the cold working that this region undergoes during the fabrication process of the cross section (Brockenbrough et al. 1999). In particular, the Flange Edge group with T2 thickness in the gouged flange represents precisely the one third of the flange width position per ASTM A913 (2007b). The same group satisfied the 54 Joules limit of the ASTM A913 standard. Moreover, for both flanges in all the locations the short orientation groups exhibited very low values. The CVN values for the short orientation groups were nearly 30 to 40 Joules for all temperatures. It is noted that the short orientation groups had also low SD and COV values compared to the long

orientation specimens; an indication that most of the short orientation specimens provided similar low toughness values while there was a greater variation observed in the long orientation specimens' values. However, it should be acknowledged that part of this variability comes from the small number of the available specimens.

Referring to the long orientation specimens, away from the weld the absorbed energy was higher than for specimens near the weld. This is to be expected given that near the weld the elevated temperatures achieved during the welding process and subsequent rapid cooling increase the hardness of the material, and as such its behaviour became brittle. For example, for the case of the edge repaired flange T2 (Table 3.4) group, an increase of the CVN value with the increase of temperature for both near and away from the weld locations was observed with the values near the weld being slightly lower than those of away from the weld. In addition, in most cases the SD and COV for near the weld energy values were lower than the respective values for material away from the welding location (in example gouged edge flange group with T2 thickness near and away from the weld Table 3.5). Thus, the specimens near the weld appear to be more consistent with respect to their values in the particular sample, which can be attributed to the fact that all specimens were exposed to welding temperatures in those locations. Moreover, as expected, the gouged flange groups (Table 3.5) seem to exhibit a larger variation in values compared to the repaired flange (Table 3.4) based on the SD and COV indications for the various location. Lastly, based on Figures 3.8 and 3.9 and the corresponding tables, it can be assumed that the upper shelf energy starts from 48°C temperature.

It should be noted that for each location the maximum number of specimens in each group is 3 (Tables 3.4 and 3.5). This should be taken into careful consideration before

one tries to interpret the variability of the material properties based on the SD and COV. However, the material satisfies the ASTM 913 (2007b) requirements.

3.2.2 Fracture Surface (SEM)

In this section the fracture surface of the tested CVN specimens is examined. The percentage of shear area and lateral expansion were measured based on guidelines provided by the ASTM A370 Standard (2007a). For lateral expansion a digital caliper micrometer gauge was used following the guidelines of Section 25.4.3 of ASTM A370. All the SEM examinations presented in this section took place at the Ecole de Technologie Supérieure facilities.

Measurements for the long orientation repaired edge flange away from weld group of Table 3.4 are presented in this section (C11, C12 & C13 group, as described in Section 3.2.1). Figure 3.11 shows the results for the shear surface percentage while Figure 3.12 refers to the lateral expansion values, calculated based on the empirical approach provided by ASTM A370 (2007a). In Figures 3.11 and 3.12 it is illustrated that with the increase of temperature there was an increase of shear surface percentage and lateral expansion, as expected. This is due to the fact that as the temperature increased the specimen is expected to break in a more ductile manner and absorb more energy during the impact.

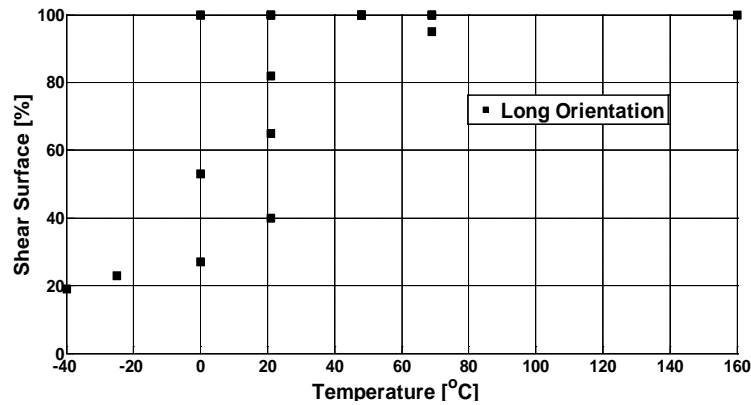


Figure 3.11: Shear surface percentage measurement of C11, C12 & C13 group

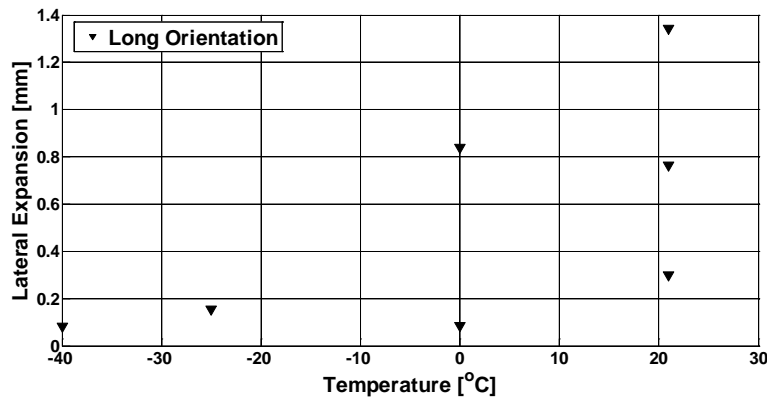
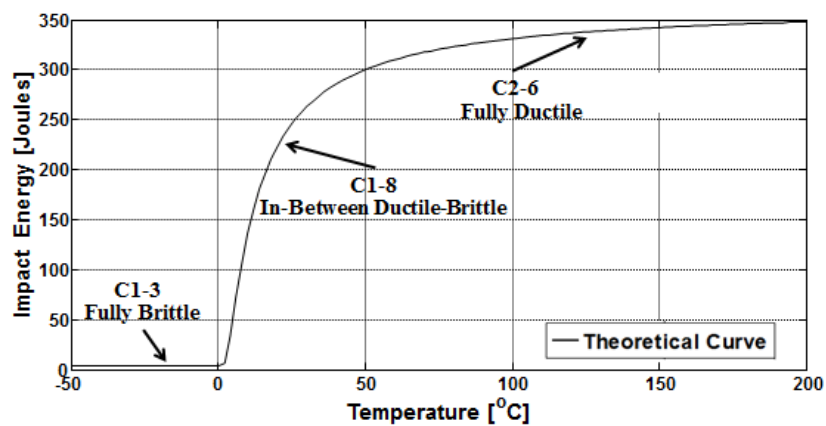


Figure 3.12: Lateral expansion measurements of C11, C12 & C13 group

Thus, CVN specimens at elevated temperatures exhibited a reduced cleavage percentage on the fracture surface and an increase in the lateral expansion, referring to the width of the specimen at the point of impact. Figures 3.13a and b illustrate the different fracture surface conditions for the case of low (specimen C1-3), intermediate (specimen C1-8) and high temperature (specimen C2-6) tested specimens. Specimens C1-3 and C2-6 were taken from a long orientation location of the flange near the welded location, while specimen C1-8 was taken from a long orientation location of the flange away from the weld (as explained in Section 3.2.1). These specimens were chosen to indicate the different surface characteristics encountered for the three temperature cases.



(a) Fracture surfaces for fully brittle, fully ductile and partly brittle-ductile specimen

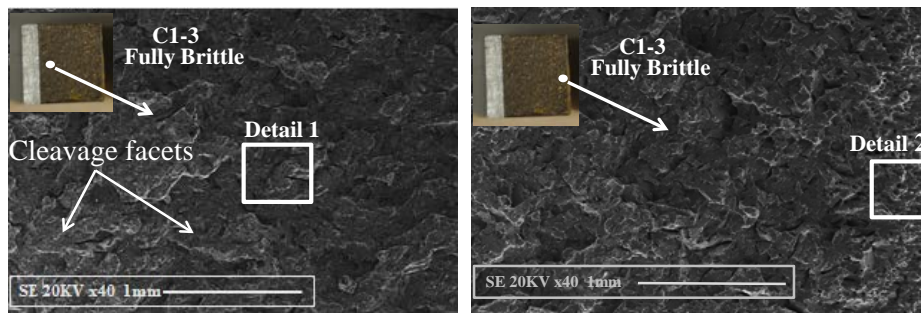


(b) Different fracture surface conditions related to temperature and impact energy

Figure 3.13: Fracture surface for low, intermediate and high temperature

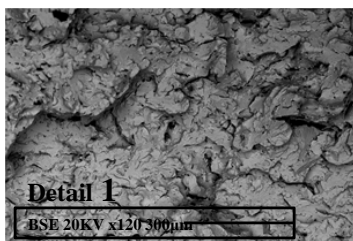
At -40°C specimen C1-3 had a CVN value of 5Joules. At 21°C specimen C1-8 provided 144Joules CVN value, while C2-6 had a CVN value of 148Joules at 160°C . As depicted in Figure 3.13, specimen C1-3 exhibited fully brittle behaviour and its fracture surface was characterised by 100% cleavage, based on Table 8 of ASTM A370 (2007a). Specimen C1-8 exhibited an intermediate situation leaning towards a more ductile behaviour since on its fracture surface the shear surface percentage was 85%. This is in agreement with its CVN value, which is fairly high. Specimen C2-6 fractured in a fully ductile manner with 100% shear surface illustrated in Figure 3.13. Lastly, in order to complete the evaluation of the steel material properties under investigation, as acquired

from these CVN tests, SEM was employed for the examination of the fully brittle and fully ductile specimens shown in Table 3.5. The fracture surfaces of specimens C1-3 and C2-6 were scanned with secondary and backscattered electrons and are shown in Figures 3.14 and 3.15. Figure 3.14 demonstrates images from two different locations of the C1-3 fully brittle specimen. The first location is near the notch (Figure 3.14a) while the second location is near the other end, at the impact point (Figure 3.14b). Detail 1 illustrates a dominant granular fracture in this specimen, indicating the cleavage region. Detail 2 reveals a small fibrous region near the end of the specimen at the second location. Thus, the fracture surface of specimen C1-3 is not 100% cleavage, as found using Table 8 from ASTM A370 (2007a). However, the shear area is negligible since the human eye cannot see it without the aid of magnification.

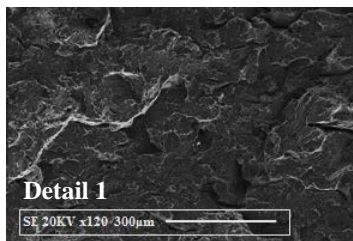


(a) Detail 1: Near the notch

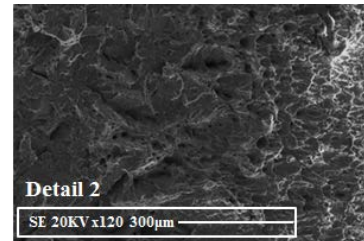
(b) Detail 2: Near the impact point



(c) Detail 1: BSE



(d) Detail 1: SE



(e) Detail 2: SE

Figure 3.14: SE and BSE images for C1-3 specimen

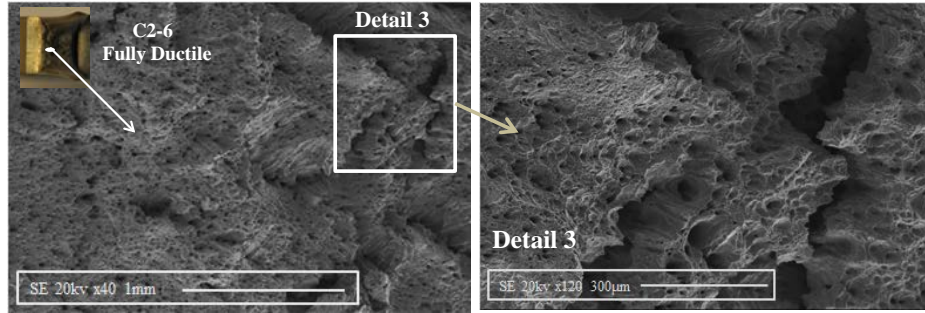


Figure 3.15: SE images for C2-6 specimen

The BSE method is able to capture the depth change in Figure 3.14c, which clearly illustrates the morphology of the surface. Transgranular fracture is depicted in both details, meaning the occurrence of crack branching inside the grains and not in the grain boundaries. Cleavage facets (flat facets) are visible at the first location near the notch while approaching the second location dimples start to appear along the cleavage facets leading to a purely dimpled fracture surface, which is an indication for ductile fracture. Figure 3.15 illustrates the ductile fracture surface case. Dimples (microvoids) are depicted clearly in Detail 3, which shows a purely ductile mode of fracture, as expected for a fine grain surface heated to high temperatures. From the aforementioned information, it is clearly shown that the material meets the ASTM 913 (2007) requirements.

3.3 Chemical Composition and Microstructure Examination

A mill test report provided by the industrial partner of this project demonstrates the chemical composition of the material obtained through heat analysis based on ASTM A913 (2007b) as well as the tensile properties of the material (yield stress 516MPa). Table 3.6 lists the chemical composition of the material for the column in question where

0.06% of carbon content is depicted among other elements (as mentioned in Section 3.2.1).

Table 3.6: Chemical composition of A913 Gr. 65 steel provided by the industrial partner

Heat No 63868	Heat Analysis (%)											
	C	Mn	P	S	Si	Cu	Ni	Cr	V	Nb	No	CEV
Min	-	-	-	-	0.10	-	-	-	-	-	-	-
Max	0.16	1.60	0.030	0.030	0.40	0.35	0.25	0.25	0.06	0.050	0.07	0.43
Test values	0.06	1.15	0.026	0.024	0.20	0.22	0.24	0.17	0.02	0.037	0.04	0.32

The chemical components of this steel were also obtained through SEM using energy dispersive spectroscopy (EDS). This method is described in detail in Chapter 2, Section 2.2.6.4. The C1-3 specimen, used in CVN testing, was prepared, polished and etched in order for EDS to be conducted. A description of the specimen dimensions and location is given in Section 3.2. The specimen was removed from the column at a position located nearly 1/3 from the flange edge (as per ASTM A913 (2007b) referring to the CVN requirement location) in a welded location along the long orientation of the column (Figure 3.4h). EDS was used to verify the various chemical components and to give their relative intensity, focusing on specific areas of the specimen. An effort was made to identify the microstructural phase changes due to the heating and cooling process from the weld and fabrication (Section 3.3.2).

3.3.1 Specimen Preparation

The C1-3 long orientation specimen selected for scanning electron microscopy exhibited a very low CVN value in the Charpy V-Notch test (Section 3.2.1), and hence was considered to have behaved in a brittle manner. This selection was based on the fact that nearly 100% brittle fracture provides a less irregular and rough surface; thus, the

polishing process becomes easier and less time-consuming than in the case of a ductile specimen. The specimen was cut in two pieces. The upper fractured surface of one piece was mounted and polished while for the other piece a side surface was prepared. During preparation, the specimen pieces were first mounted in a hot mounting press. The grinding process followed this where 240, 320, 400 and 800 grit silicon carbide sandpapers were used. Finally, for the polishing process, 3mm diamond suspension and 0.05µm colloidal silica was used to accomplish a near-mirror surface finishing. Additionally, the side surface was etched with 5% Nital for 10sec in order for the grain boundaries to become visible. These processes took place at the Department of Materials Engineering in the Wong Building laboratories at McGill University. Figure 3.16 illustrates the two prepared pieces. It should be mentioned that carbon tape was used as a conductive material in order to connect the specimen to the special base inside the SEM machine to avoid “charging”, since the material used for mounting was not conductive.

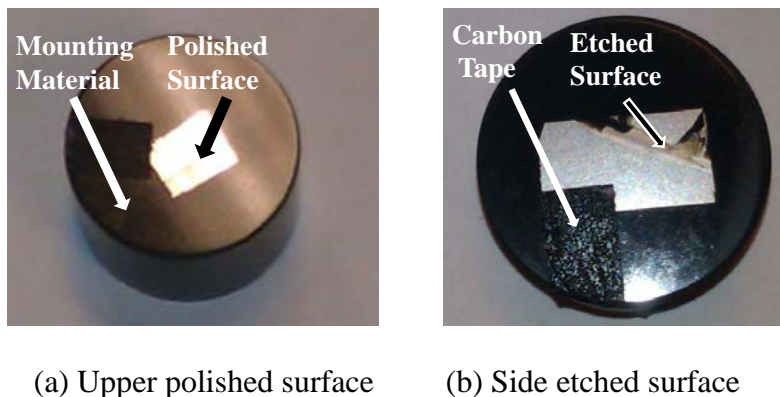


Figure 3.16: Prepared surfaces of C1-3 specimen for SEM

The upper polished surface did not add any significant information to this research; therefore only the results of the etched one are discussed. For EDS the etched surface is preferable due to the clear illustration of the grain boundaries, which facilitates the selection of areas of interest in the surface to be examined.

3.3.2 EDS Results and Observations

Various areas and magnifications of the specimen were examined in an effort to better capture the morphology of the etched surface. Figure 3.17 illustrates an area of the etched surface in x600 magnification. The photograph was acquired using secondary electrons. Below the figure is the corresponding spectrum with the basic chemical elements. From Figure 3.17, the iron level is much higher compared with the other elements while the carbon level is fairly low. This is in agreement with the chemical composition acquired through heat analysis where the carbon level is only 0.06% (Table 3.6).

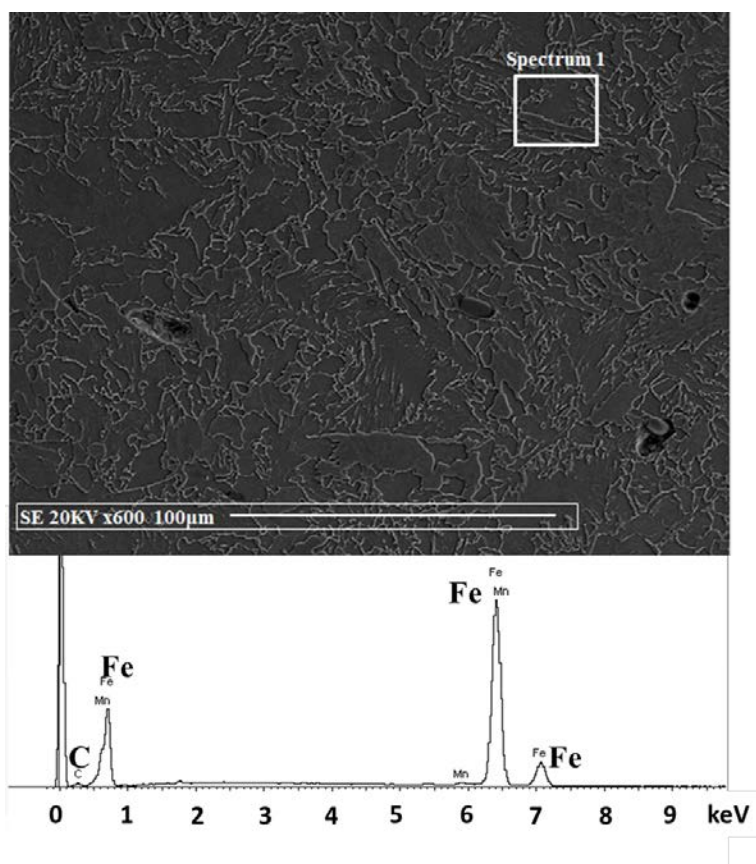


Figure 3.17: Chemical analysis using EDS

In general, most of the chemical elements from the heat analysis were detected in this graph but are not shown due to their low relative intensity and in order to avoid

complexity of the graph. Moreover, increased magnification in a different area of the surface revealed sulphide inclusions in the material. One such inclusion is illustrated in Figure 3.18 along with the corresponding spectrum. Non-metallic inclusions are to be expected in steel. Manganese sulfide inclusions belong to the sulphide inclusions category (Vander Voort 1984). Non-metallic inclusions are extraneous elements and can influence the mechanical properties of the material depending on factors such as their size, distribution or chemical characteristics. In this particular steel, their presence was not frequent and their size was fairly small leading to the assumption that the material properties would not be greatly influenced.

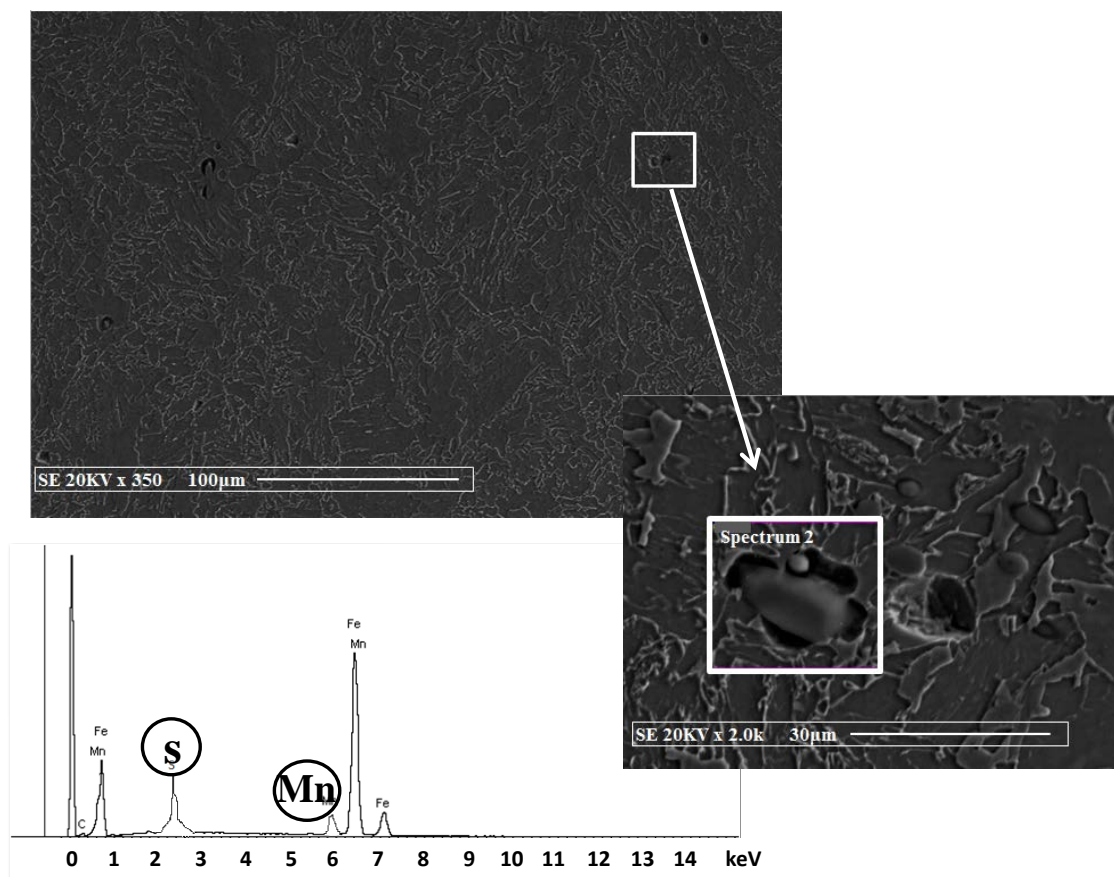


Figure 3.18: MnS sulphide inclusions

Regarding the morphology of the material, the small grain size, as expected for high strength steel, was the first observation (Figures 3.17 & 3.18). A nearly pure ferritic matrix with indications of pearlite and martensite was expected, given the small carbon content and the fabrication process of A913 Gr. 65 steel (quenching and tempering), as well as the fact that the C1-3 specimen was exposed to high temperatures and fast cooling rates through the welding process. Johnson and Storey (2008) investigated the carbon content influence on the ductile-brittle transition curve. In this study, the surface of the material was examined using light microscopy for the cases of a very low, a medium and high carbon content (Figure 3.19). The percentage of pearlite in the microstructure increases as the carbon content increases. Figure 3.18 illustrates the three cases presented by Johnson and Storey (2008). The middle case refers to 0.25% carbon content where some small “islands” of pearlite (dark regions) are detected in a “sea” of ferrite (light regions). This figure is representative of the microstructure observed for the column specimen depicted in Figures 3.17 and 3.18.

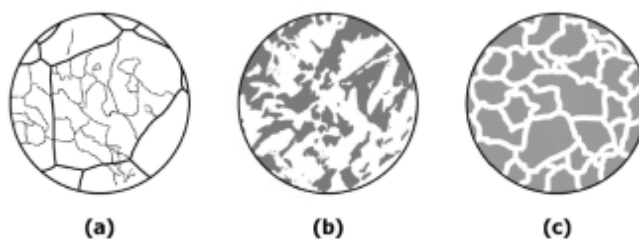


Figure 3.19: Microstructure for different carbon contents (Johnson and Storey 2008)

Moreover, a recent study by Banerjee (2013) addresses issues related to microstructural phases, their source of formation and their influence on mechanical properties such as tensile strength. The main focus of this paper was on advanced high strength steels (AHSS), which refers to steels that include in their microstructure ferrite along with

martensite and bainite as a result of fabrication processes that involve various heating and cooling conditions.

In Banerjee's study, high strength steel samples were fabricated through hot-rolling and cold-rolling followed by continuous annealing. The samples were then welded with an arc-spot weld. The effect of cooling rate and bainite content on the weldability and tensile properties of the steels was examined. Table 3.7 summarises the chemical composition of the developed steels.

Table 3.7: Chemical composition of developed steels (Banerjee 2013)

Heat No.	C	Mn	Si	Al	Mo	Ti	Nb	Cr	P	S	CE
9	0.12	1.52	0.37	0.15	0.29	0.009	0.004	0.021	0.008	0.013	0.27
14	0.09	1.55	0.41	0.27	0.21	0.031	0.009	0.036	0.008	0.008	0.24

The chemical composition of Heat No.14 sample with a carbon content of 0.09% is fairly close to the A913 Gr.65 steel, given that the carbon content influences mostly the type of phase transformations that are taking place in the microstructure. One important part of Banerjee's study was the thorough examination of the microstructure using high resolution scanning electron microscopy. Sections of the samples were polished and etched with a 2% Nital solution.

Figure 3.20 illustrates the microstructure of this sample at the top right corner. As explained by Banerjee, the microstructure consists of ferrite, pearlite, bainite and martensite, where ferrite is depicted by the darker regions with pearlite along with bainite and martensite forming in the boundaries of the grains (brighter dendroid regions). It was observed that with slower cooling rates the microstructure was characterised by mostly

ferrite, while with the increase of the cooling rate bainite and martensite appeared in the microstructure.

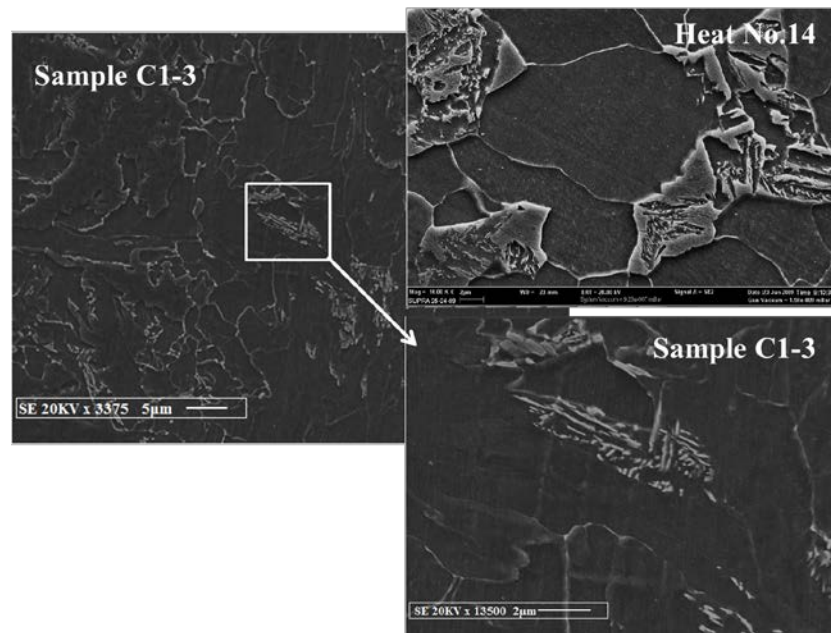


Figure 3.20: Comparison of C1-3 and Heat No.14 microstructure

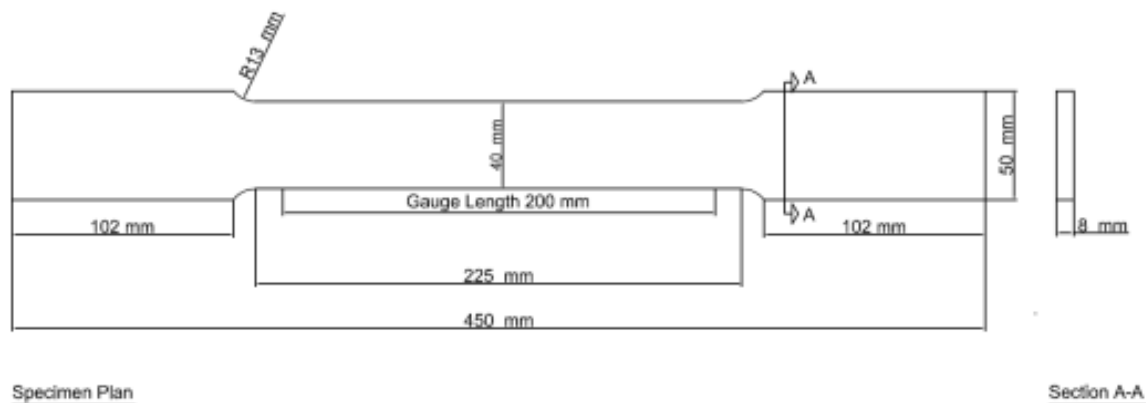
In the bottom right part of Figure 3.20 the microstructure of C1-3 is depicted using a magnification of 13500x. It can be seen that the two microstructures (top and bottom) demonstrate some similarities. Therefore, following Banerjee's paper a better understating of the microstructure of sample C1-3 is achieved.

3.4 Tensile Material Properties

In this section, the tensile coupon testing is described and the results are presented for a selection of the coupon specimen groups. Due to the repetitive nature of the results, all graphs and tensile properties for all the groups are provided in Appendix A, while in this section only representative results are included. The material yield, F_y , and tensile, F_u , stresses are examined as well as the Young's modulus, E and the tensile-stress-to-yield-point ratio F_u/F_y ratio.

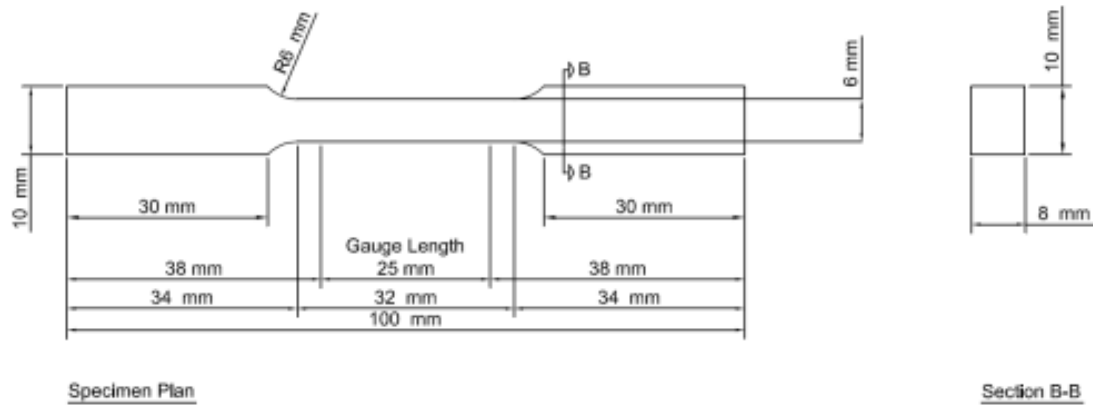
3.4.1 Specimens: Dimensions and Selected Locations

Tensile coupon testing was performed for 45 small and standard coupons sized based on the ASTM A370 Standard (2007a), and 3 special k-area coupons, sized based on the profile of the k-area of the W-shape section. The specimens were extracted from different positions over the thicknesses of the column flange and web and in different orientations with respect to the rolling direction of the column. Figures 3.21a, b and c show the dimensions of the tensile coupons. All specimens' information is summarised in Tables 3.8, 3.9 and 3.10. Groups of specimens were selected based on the location of the specimens in the W-shape column, similarly as for the CVN specimens. One specimen from each group was instrumented with strain gauges in order to obtain an accurate measure of Young's modulus, E . Strain gauges were installed only for the small and standard coupons. For the special coupons the cross section was not constant; thus, E measurements could not be obtained for those specimens using strain gauges, only localised yielding.

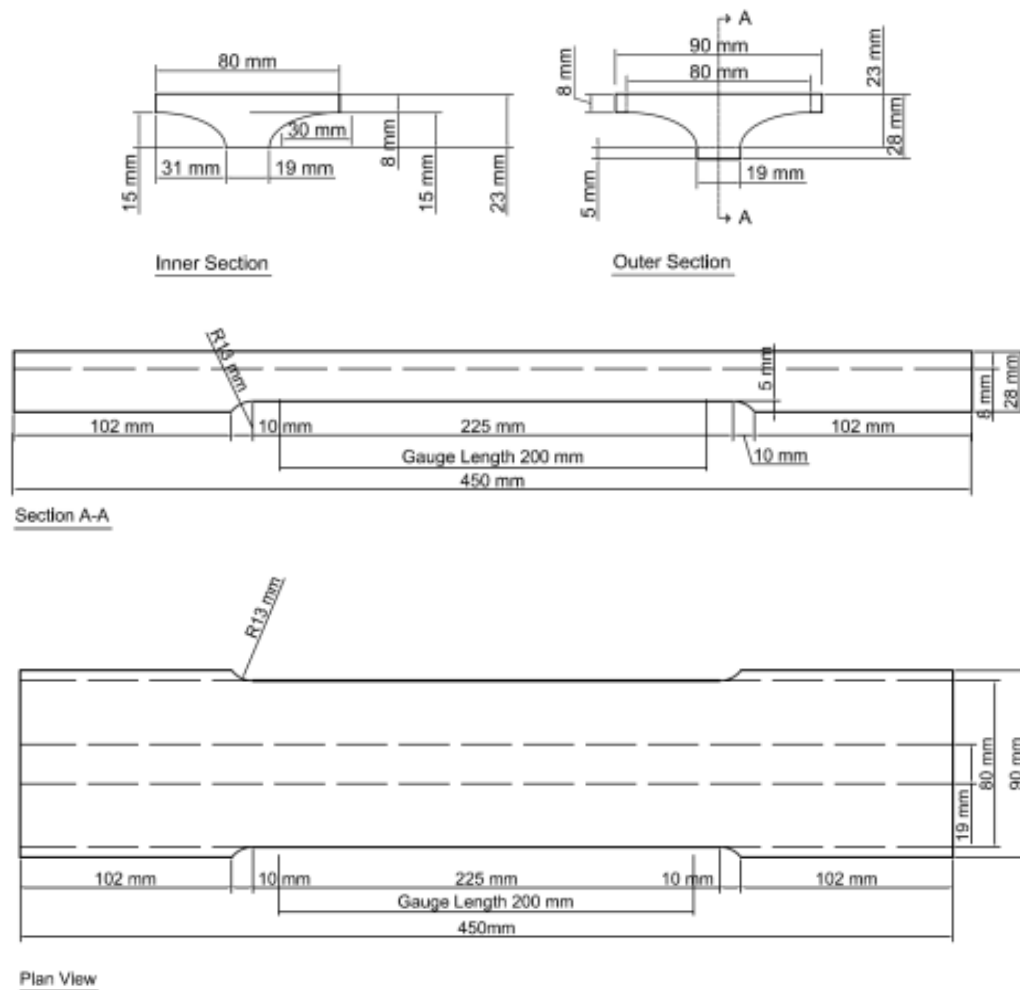


(a) Standard coupon

Figure 3.21: Dimensions of coupons

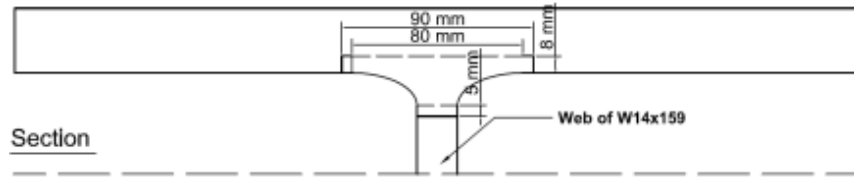


(b) Small coupon



(c) Special k-area coupon

Figure 3.21 (Continued): Dimensions of coupons



(c) Special k-area coupon (Continued)

Figure 3.21 (Continued): Dimensions of coupons

Table 3.8: Standard tensile coupon specimens

Standard Rectangular Coupon Group Notation	Location	Number
F1	Away from welded area, flange edge	4
F2	Away from welded area, flange edge	4
F3	Welded area, flange edge	3
F4	Welded area, flange edge	4
W3	Web area	3
K2	Welded area, flange up	2
K4	Away from welded area, flange up	2
Total	-	22

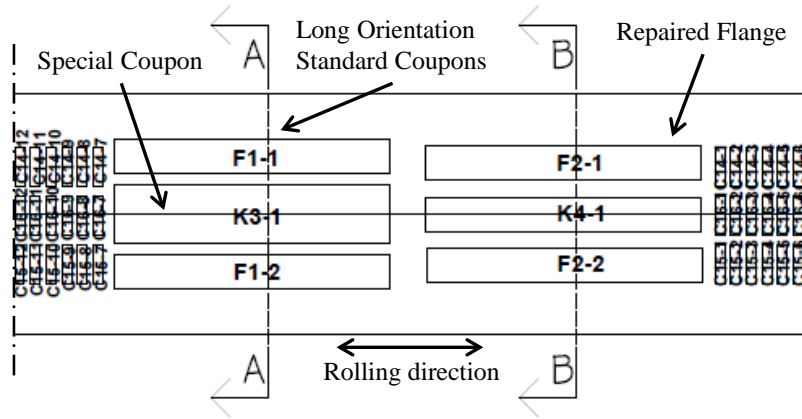
Table 3.9: K-area tensile coupon specimens

Special K-Area Coupons	Location	Number
K1	Welded area, k-area	1
K3	Away from weld, k-area	2
Total	-	3

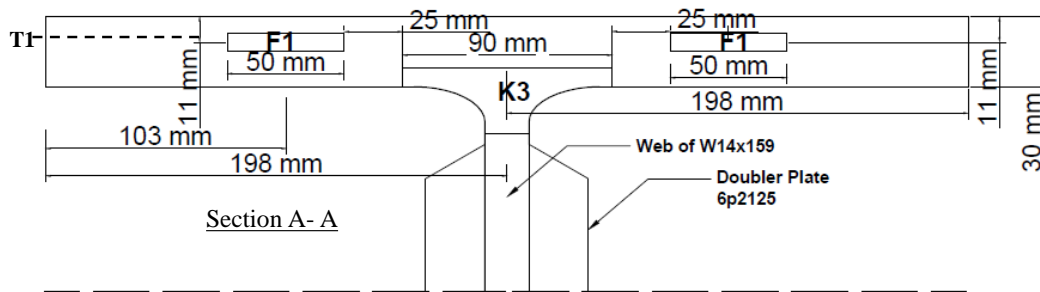
Table 3.10: Small tensile coupon specimens

Small Rectangular Coupon Groups	Location	Number
R1	Welded area, flange up	3
R2	Welded area, flange up	3
W1	Away from welded area, flange up	4
W2	Away from welded area, flange up	4
U4	Welded area, k-area	1
F5	Welded area, flange edge	4
F6	Welded area, flange edge	4
Total	-	23

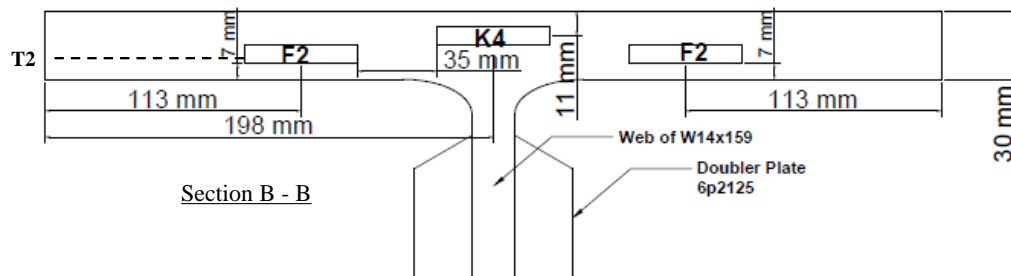
Figures 3.22 and 3.23 illustrate the standard and special coupons locations in the repaired and gouged flange width respectively; Figure 3.24 depicts the small coupon locations.



(a) Plan view of flange region away from welded location 1

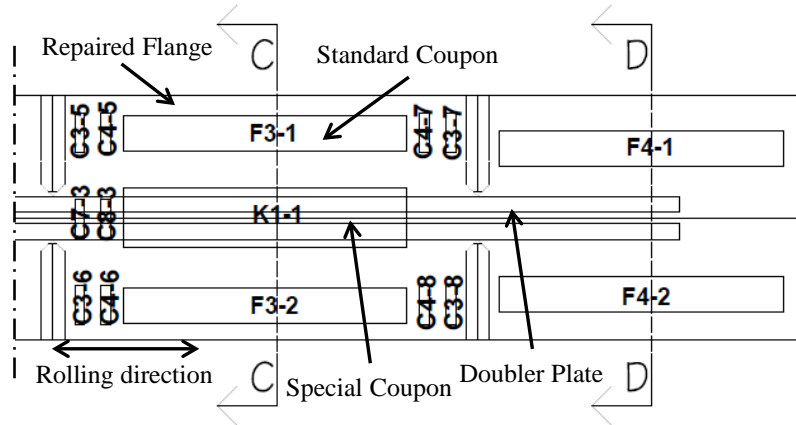


(b) Cross section for specimen groups F1 and K3

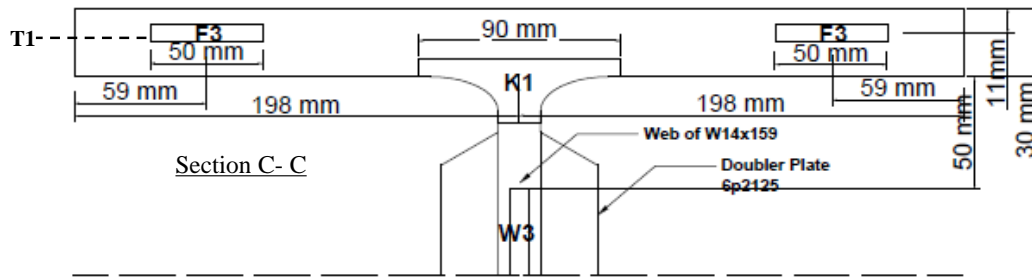


(c) Cross section for specimen groups F2 and K4

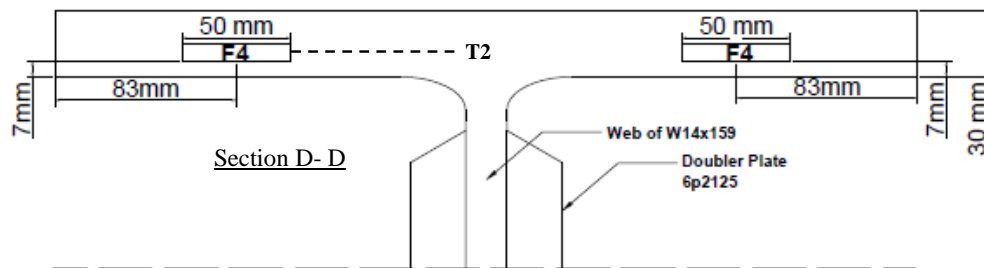
Figure 3.22: Plan view and cross sections of the repaired column flange / web showing locations of standard\special coupon specimens



(d) Plan view of flange region in the welded location 2

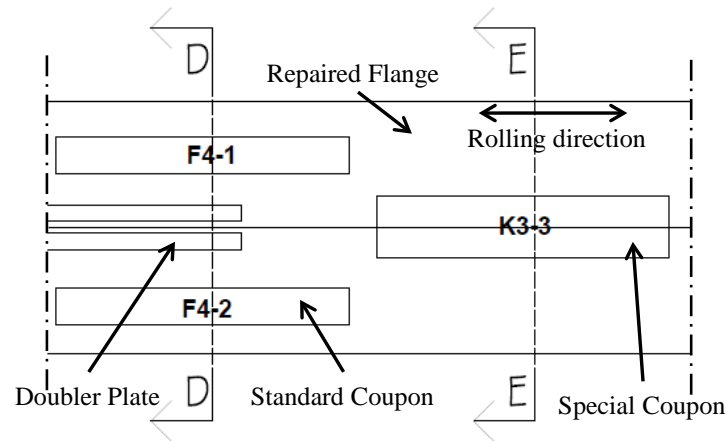


(e) Cross section for specimen groups K1 and F3

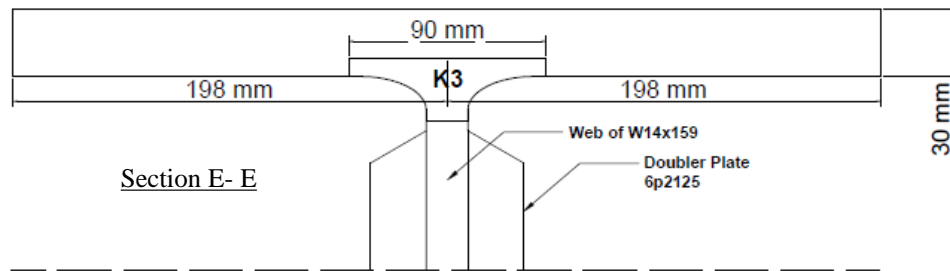


(f) Cross section for specimen group F4

Figure 3.22 (Continued): Plan views and cross sections of the repaired column flange / web showing locations of standard\special coupon specimens

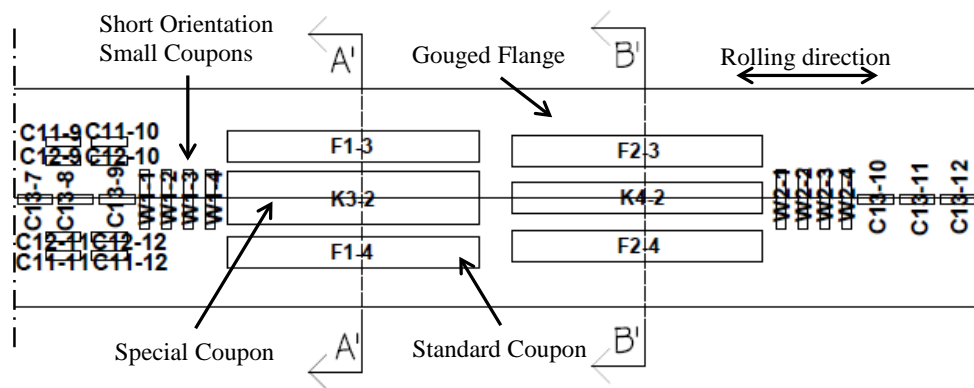


(g) Plan view of flange region in the welded location 2



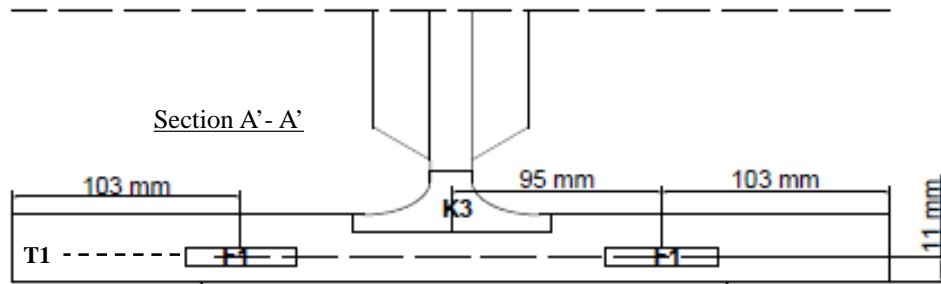
(h) Cross section for specimen group K3

Figure 3.22 (Continued): Plan views and cross sections of the repaired column flange / web showing locations of standard\special coupon specimens

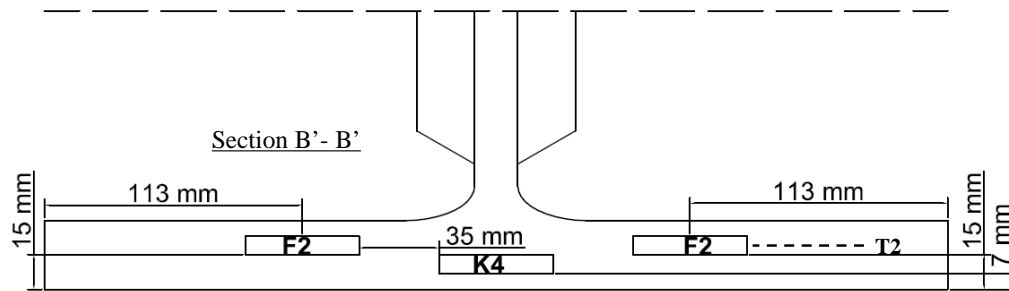


(a) Plan view of flange region away from welded location 1

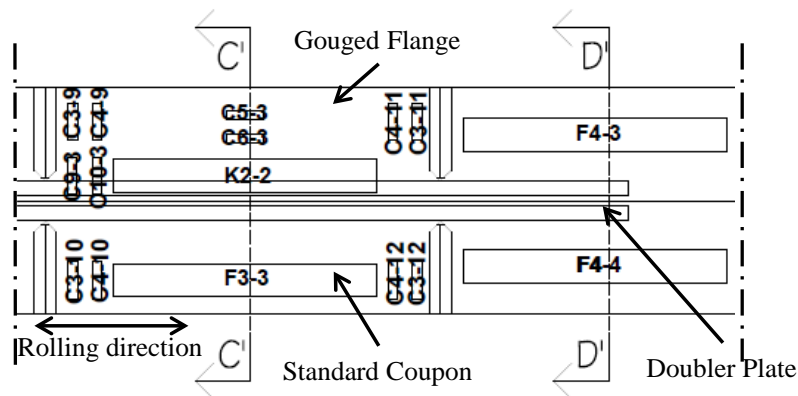
Figure 3.23: Plan view and cross sections of gouged column flange / web showing locations of standard\special coupon specimens



(b) Cross section for specimen groups K3 and F1

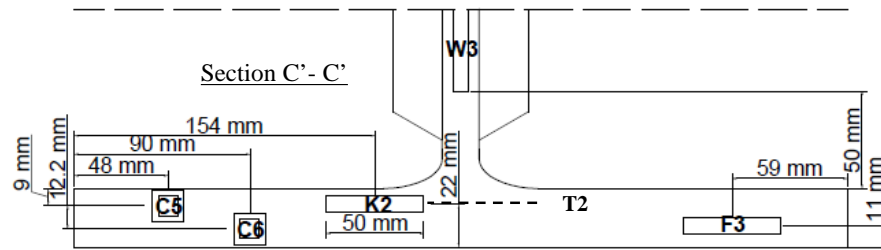


(c) Cross section for specimen groups K4 and F2

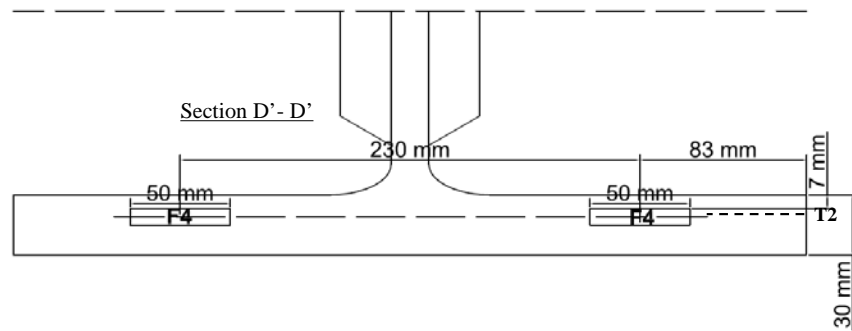


(d) Plan view of flange region in welded location 2

Figure 3.23 (Continued): Plan view and cross sections of gouged column flange / web showing locations of standard\special coupon specimens

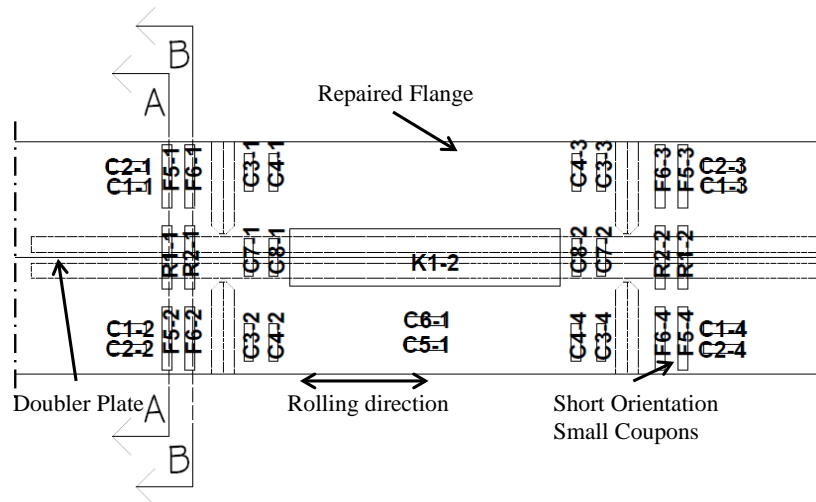


(e) Cross section for specimen group K2 and F3



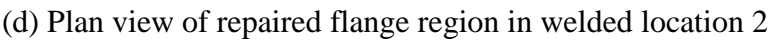
(f) Cross section for specimen group F4

Figure 3.23 (Continued): Plan view and cross sections of gouged column flange / web showing locations of standard\special coupon specimens

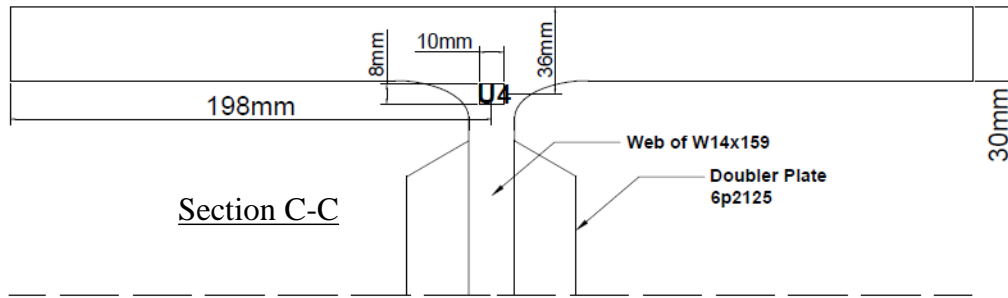


(a) Plan view of repaired flange region in welded location 1

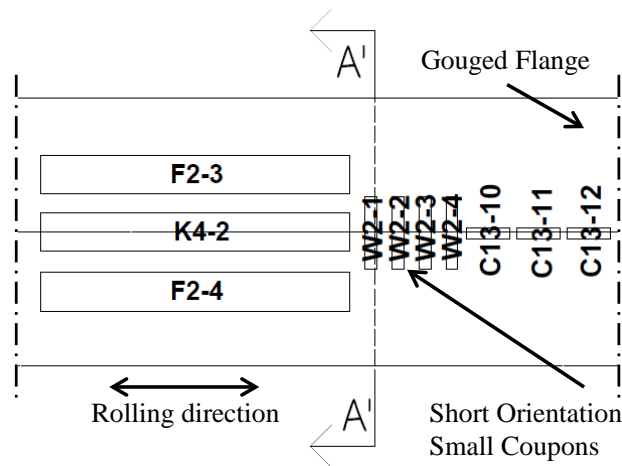
Figure 3.24: Plan view and cross sections of gouged and repaired column flange / web showing locations of small coupon specimens



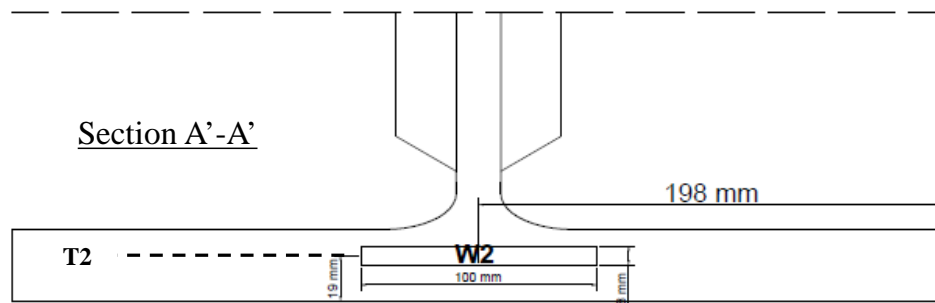
flange / web showing locations of small coupon specimens



(e) Cross section for specimen U4



(f) Plan view of gouged flange away from welded locations



(g) Cross section for specimen group W2 (W1 is in the same location with thickness T1)

Figure 3.24(Continued): Plan view and cross sections of gouged and repaired column flange / web showing locations of small coupon specimens

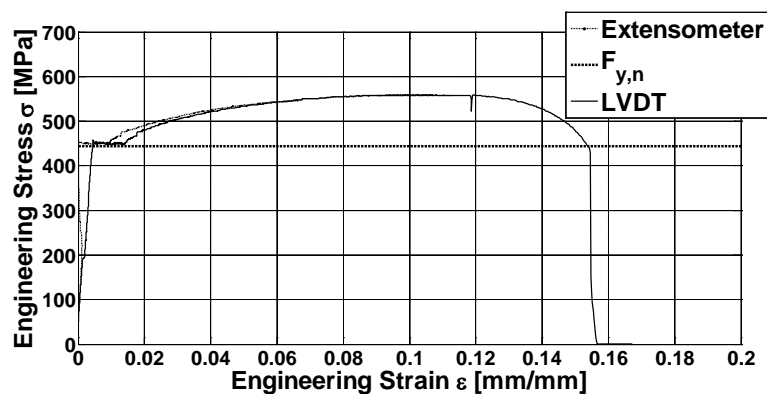
Thus, areas near the welded and not welded regions were tested using specimens located at the flange edge at two thickness locations, at the flange region on top of the k-area using two thickness locations for the small coupons (“flange up”), at the k-area and at the web. The tensile tests were conducted in the facilities of the structural and materials laboratories in the Macdonald Engineering Building at McGill University.

3.4.2 Results and Evaluation

In this section the results for each coupon type are presented.

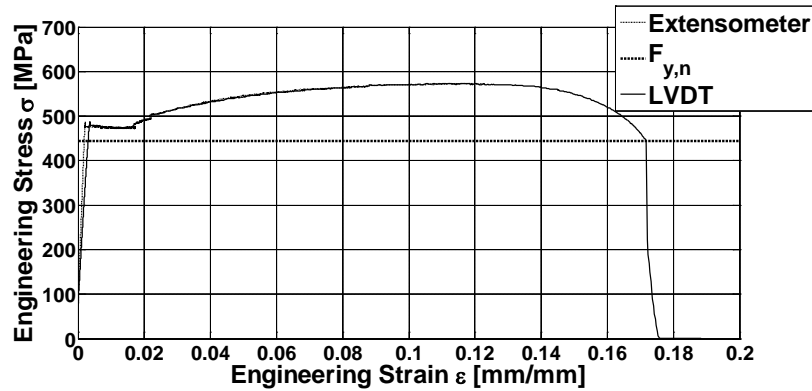
3.4.2.1 Standard and Special Coupons Testing Results

Figure 3.25a and b illustrate the typical engineering stress-strain curves of the A913 Gr. 65 steel as they were obtained from the tensile tests of coupons from the welded region (specimen F33) and the region that was not welded (specimen F11). These figures show the engineering stress - strain curves obtained from the extensometer and the internal actuator piston LVDT (MTS machine), as well as the nominal (minimum specified) yield stress for A913 Gr. 65 steel, $F_{y,n}$.



(a) Specimen F11 away from welded locations

Figure 3.25: Standard coupons engineering stress-strain curves



(b) Specimen close to welded locations (F33)

Figure 3.25 (Continued): Standard coupons engineering stress-strain curves

The curves obtained were in agreement with the stress-strain curve expected for this type of steel. During the manufacturing process, rapid cooling of the material by quenching increases the yield stress and tensile strength but decreases the ductility. Thus, the plateau in the inelastic range is reduced and fracture occurs earlier (at 0.15%-0.2%) for this type of steel compared, for example, to A992 Gr. 50 steel (ASTM A992 2006a). Tables 3.11 and 3.12 summarise the results for all specimen groups. The 0.2% offset method was used to determine the yielding point.

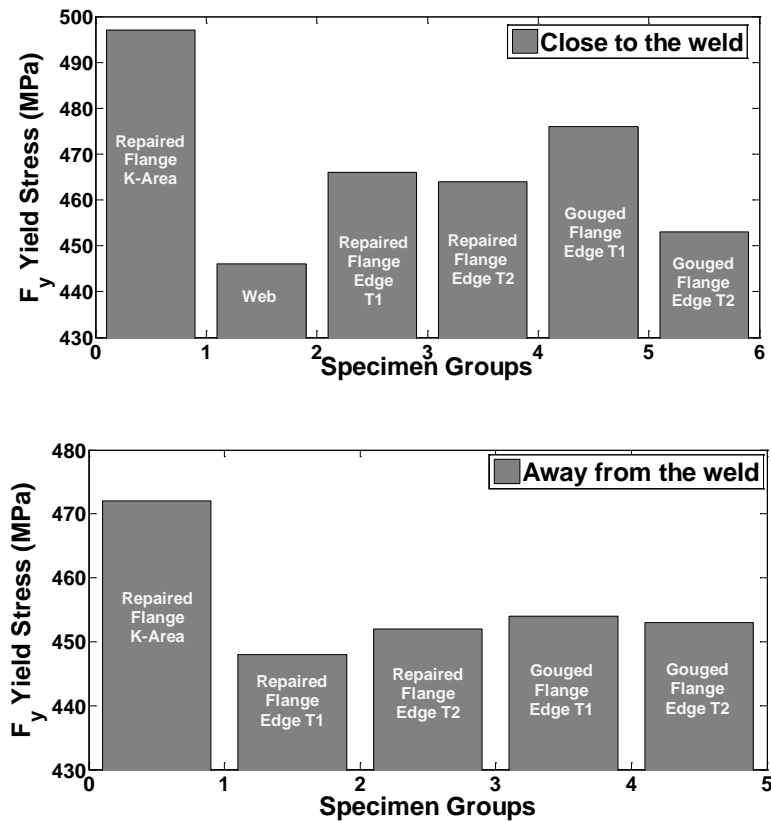
Table 3.11: Mean values for groups close to the weld regions

Close to the Weld		Mean Values						No.
Standard/Special Coupons		F_y (MPa)	ϵ_y (mm/mm)	F_u (MPa)	F_u/F_y	ϵ_u (mm/mm)	E (MPa)	
Repaired Flange K-Area		497	0.0145	563	1.13	0.0872		1
Web		446	0.0042	546	1.22	0.1229	207923	3
Repaired Flange Edge	T1	466	0.0043	559	1.20	0.1233	203546	2
	T2	464	0.0043	562	1.21	0.1050	202812	2
Gouged Flange Edge	T1	476	0.0044	573	1.20	0.1156	-	1
	T2	453	0.0046	563	1.24	0.1073	-	2
Gouged Flange Up	T2	477	0.0043	564	1.00	0.1192	203846	2

Table 3.12: Mean values for groups away from the weld regions

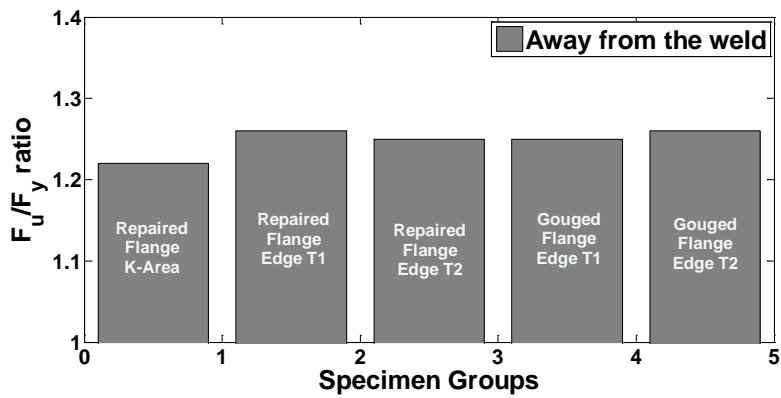
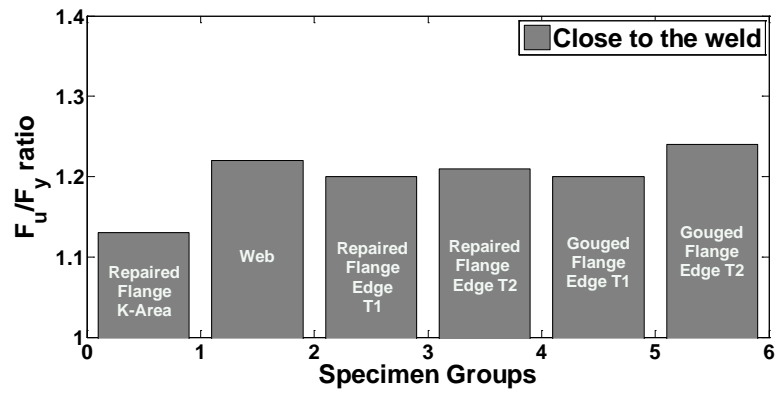
Away from Weld		Mean Values						No.
Standard/Special	Coupons	F_y (MPa)	ϵ_y (mm/mm)	F_u (MPa)	F_u/F_y	ϵ_u (mm/mm)	E (MPa)	
Repaired Flange K-Area		472	0.0157	574	1.22	0.1358	-	2
Repaired Flange Edge	T1	448	0.0055	563	1.26	0.1175	203159	2
	T2	452	0.0042	567	1.25	0.1214	204246	2
Gouged Flange Edge	T1	454	0.0052	569	1.25	0.1203	-	2
	T2	453	0.0043	569	1.26	0.1217	-	2
Repaired Flange Up		449	0.0042	550	1.22	0.1254	206764	1

Figure 3.26a, b, c and d show the results of the Tables 3.11 and 3.12 from the tensile tests in terms of stress, strain and Young's modulus using comparative histograms.

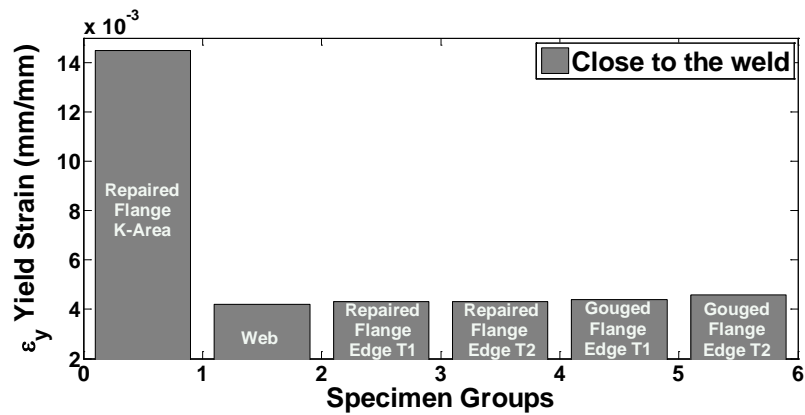


(a) Yield Stress

Figure 3.26: Standard & special coupon results for various W-shape locations

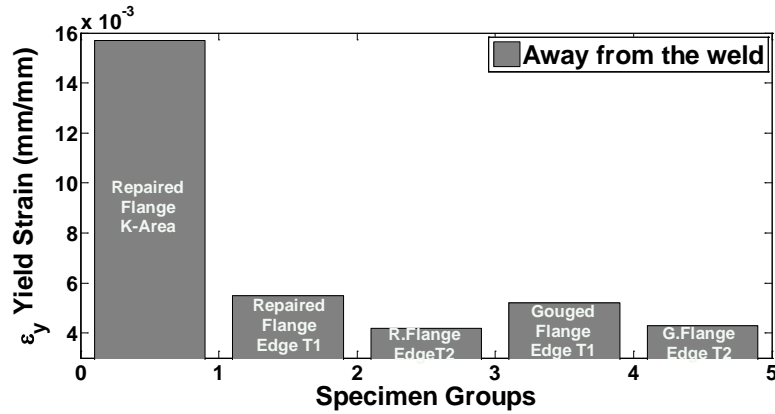


(b) F_u/F_y ratio

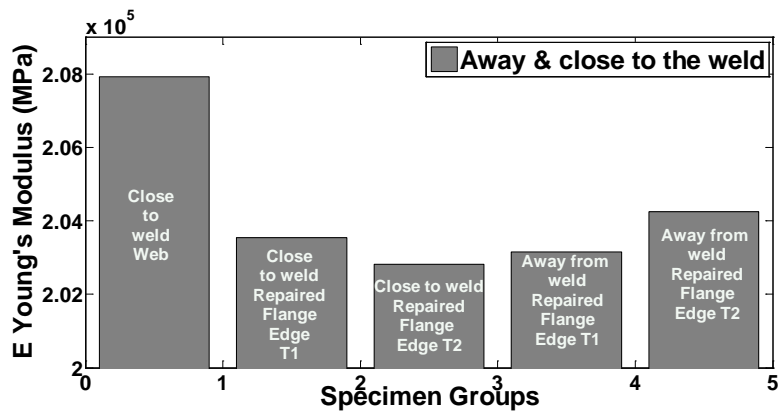


(c) Yield Strain

Figure 3.26 (Continued): Standard & special coupon results for various W-shape locations



(c) Yield Strain (Continued)



(d) Young's modulus

Figure 3.26 (Continued): Standard & special coupon results for various W-shape locations

From Figure 3.26a, it can be seen that the average yield stress for the groups that were near the welded regions was slightly higher compared to the groups that were away from the weld. This can be attributed to the fact that residual stresses may have been introduced to these specimens from the welding process (Chapter 2, Section 2.2.4). However, in this case the web specimens exhibited lower stress values than those in the flange; the opposite is usually expected. In addition, typically the F_y values for the coupons from the two locations over the flange thickness for the repaired and gouged

flange were close, while the values of the special coupons for the k-area were increased, as it will be explained further on.

Figure 3.26b demonstrates that the F_u/F_y ratios were close to 1.22, which is the nominal ratio expected for A913 Gr.65 steel (2007b), except for the K11 special coupon extracted near the welded region, which exhibited a different behaviour compared to the other special coupons as demonstrated in Subsection 3.4.2.2.

Figure 3.25c shows that for most groups away and near the weld the yield strain values were similar with a slightly increased value for the T1 thickness group for the away from the weld case compared to the T2 ones. As the thickness of the flange increases, the difference in the surface and interior residual stresses can vary significantly.

Figure 3.26d depicts that for the two locations close to and away from the weld, the web had a greater stiffness (higher Young's modulus value) than the flange specimens, which all demonstrated similar values. Nonetheless, the difference was fairly small (nearly 2%).

Given the internal actuator piston LVDT (MTS machine) error and the fact that average stresses and strains included in these graphs were derived from 2 to 3 specimens or even 1 specimen for each group, one could conclude that the values do not vary significantly for flange and web for this wide-flange section. Small differences are attributed due to the variability of the material and the errors accompanying this type of testing. It should be noted that, referring to the ultimate stress and strain, the specimens exhibited similar behaviour as observed for the yield stress and strain.

3.4.2.2 Special K-area Coupons Testing Results

These coupons were taken from the k-area region at a location near and away from the weld. Figure 3.27 illustrates the testing process and fracture of these specimens.



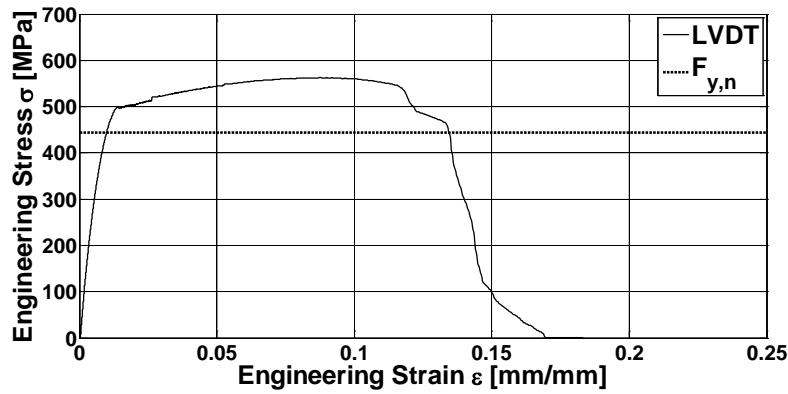
(a) K31 & K33 specimen fracture (away from the weld)



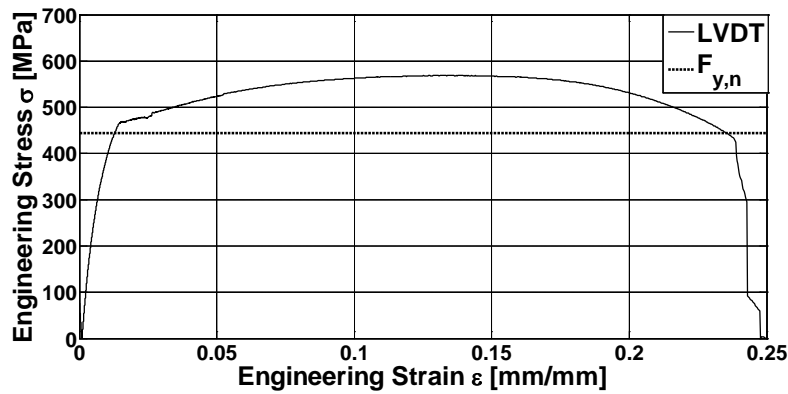
(b) K11 specimen fracture (near the weld)

Figure 3.27: Testing of k-area specimens

In Figure 3.28a & 3.28b the results for specimen K11 and K31 are presented, respectively.



(a) Specimen K11 near the welded area



(b) Specimen K31 away from the welded area

Figure 3.28: Stress-strain results for k-area coupon specimens

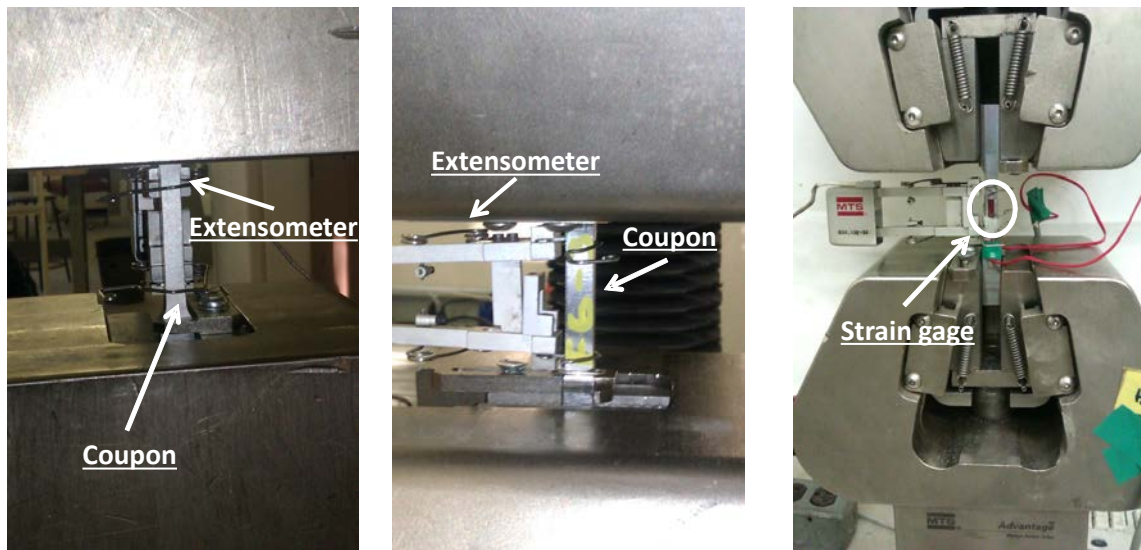
As shown in Figure 3.27, both the K31 and K33 specimens fractured in shear in the middle of the web while specimen K11 fractured almost vertically in the middle of the web. Upon removing the K11 specimen, there was evidence of a possible pre-existing crack, which could have propagated during the test, resulting in the earlier fracture (lower F_u/F_y ratio) for this specimen. This was a specimen obtained from a column that exhibited cracking near the weld. Thus, it is reasonable to assume that the crack may have existed prior to coupon testing, and may have been caused by the welding process induced stresses in consideration of the low toughness of the k-area. During the tensile

test, due to the eccentricity of the k-area special coupon, torque-twisting action was applied to the coupon because of its non-standard shape and the gripping apparatus, which may have led to the propagation of the crack. It should be noted that defects were also identified in specimen K11 prior to testing (Figure 3.27b), which could have been trigger points that led to the illustrated fracture behaviour (Figure 3.27b). It is also noted that specimen K11 being near the weld had a higher yield stress due to residual stresses than the other two specimens. Moreover, while for the first two specimens the fracture was brittle, for the K11 fracture occurred but not in a brittle manner. Finally, from Figure 3.28 it is demonstrated that for all specimens the elastic range of the stress-strain plot is slightly curved; a phenomenon that is attributed mostly to the special dimensions and cross-section of this coupon. It should be noted that given the gradual yielding behavior of the graph for the special k-area coupons the 0.2% offset method cannot be applied with absolute precision, which may explain the elevated yield stresses observed for these specimens.

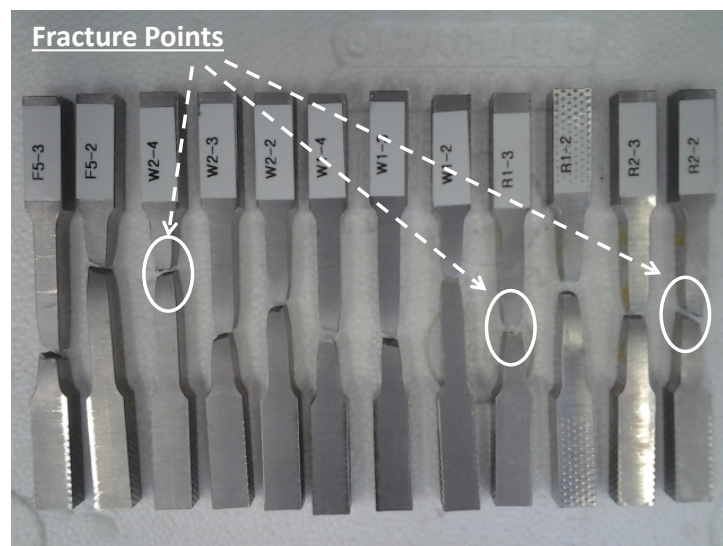
3.4.2.3 Small Coupons Testing Results

Following are the results as obtained from the testing of the small coupons. These coupons were extracted from the column mostly in the short orientation. Figure 3.29a and b include photographs taken during and after the testing. The configuration of the experiment and the installation of the specimen, the strain gauges and the extensometer are visible as well as the fracture points for each specimen (indicatively three of the fracture points are pointed out in Figure 3.29b).

Figure 3.30a and b present two stress-strain curves referring to two specimens near and away from the welded regions.



(a) Specimen placed in the MTS machine

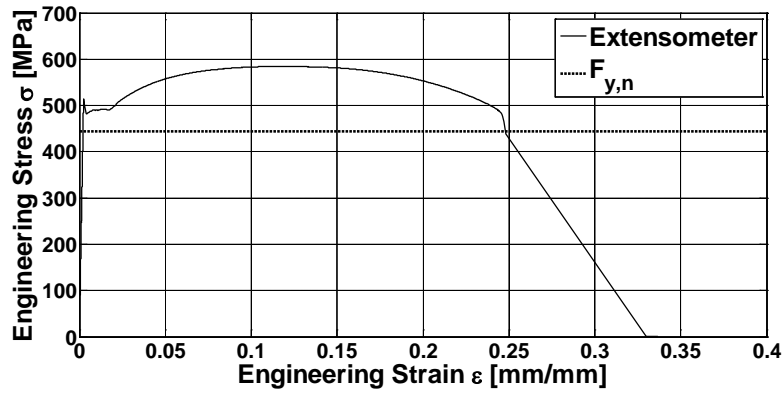


(b) Tested specimens

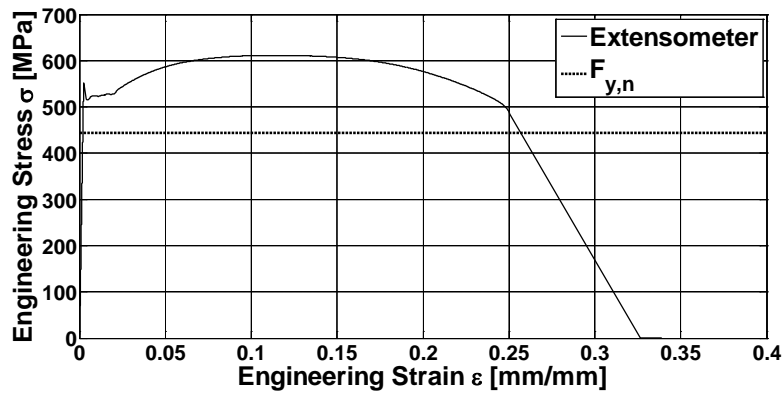
Figure 3.29: Small coupon testing process

Due to the fact that the specimens were significantly smaller compared to the machine used to test them only the measurements of the extensometer were used to determine the strain. For the Young's modulus value, strain gauge measurements were considered more reliable than then extensometer measurements mainly because the gauges' size and physical operation allowed them to capture even the smallest deformation of the area that

they were locally placed on. Moreover, these instruments measure strain directly at the local level. Therefore, any errors related to division of displacement with a certain strain gauge length and the flexibility of the machine applying the load is avoided.



(a) Specimen R11 near the welded area



(b) Specimens W11 away from the welded area

Figure 3.30: Small coupon engineering stress-strain curve

The curves obtained for the small coupons exhibit similar characteristics to those described for the standard coupons in Section 3.4.2.1. However, a considerable difference in the fracture point is observed. The fracture strain is now at 0.25%. This difference can be attributed to the smaller strain gauge length considered for the small coupons than the standard ones, as well as the fact that small coupons are in the transverse orientation.

Tables 3.13 and 3.14 summarize the mean, standard deviation and the coefficient of variation for the engineering stress and strain results for the different location groups.

Figures 3.31a, b, c and d provide comparative histograms for the same values.

Table 3.13: Mean values from small coupons

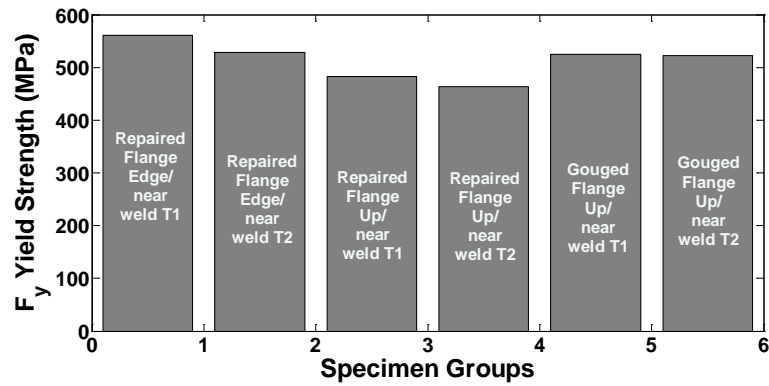
Short Orientation		Mean Values						No.
Small Coupons		F_y (MPa)	ϵ_y (mm/mm)	F_u (MPa)	F_u/F_y	ϵ_u (mm/mm)	E (MPa)	
Repaired Flange Edge/Near Weld	T1	561	0.0044	635	1.15	0.1119	216666	4
	T2	528	0.0043	591	1.15	0.1029	219767	4
Repaired Flange Up/Near Weld	T1	483	0.0043	580	1.21	0.1187	220523	3
	T2	463	0.0037	576	1.24	0.1330	216412	3
Gouged Flange Up/Away from Weld	T1	525	0.0043	618	1.18	0.1315	215656	4
	T2	522	0.0040	611	1.17	0.1333	216146	4

Table 3.14: SD and COV for small coupon results

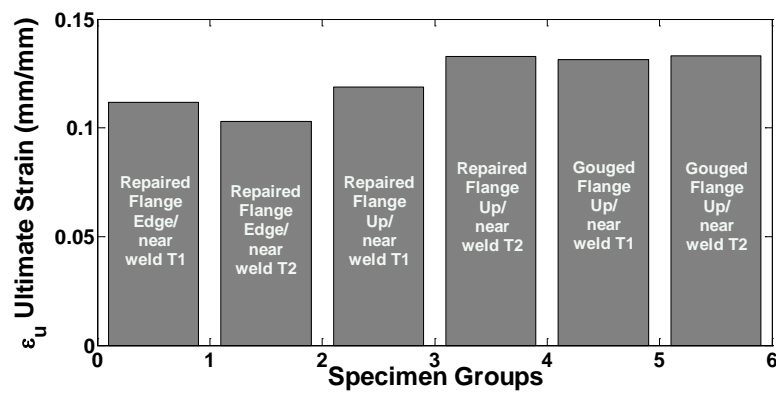
Short Orientation		SD			
Small Coupons		F_y (MPa)	ϵ_y (mm/mm)	F_u (MPa)	ϵ_u (mm/mm)
Repaired Flange Edge/Near Weld	T1	24	0.0001	22	0.0108
	T2	60	0.0003	56	0.0364
Repaired Flange Up/Near Weld	T1	11	0.0003	10	0.0205
	T2	10	0.0005	12	0.0040
Gouged Flange Up/Away from Weld	T1	8	0.0003	11	0.0079
	T2	6	0.0005	6	0.0069
Short Orientation		COV (%)			
Small Coupons		F_y	ϵ_y	F_u	ϵ_u
Repaired Flange Edge/Near Weld	T1	4	2	3	10
	T2	11	6	9	35
Repaired Flange Up/Near Weld	T1	2	8	2	17
	T2	2	13	2	3
Gouged Flange Up/Away from Weld	T1	1	7	2	6
	T2	1	12	1	5

In Table 3.13 and 3.14 it is shown that the yield strain values were very close for each group. The differences in yield stress and ultimate stress were similar while the difference in values for the Young's modulus was nearly 1%. The ultimate strain values seemed to

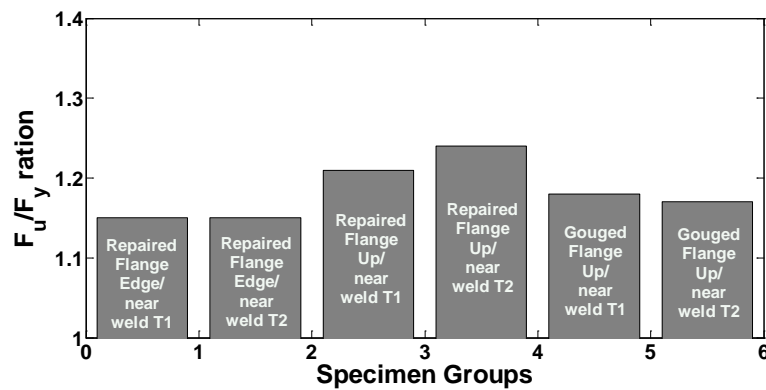
differ to a greater extent among the different groups. Thus, comparative histograms are presented for the yield stress, the ultimate strain and the F_u/F_y ratio.



(a) Yield Stress



(b) Ultimate Strain



(c) F_u/F_y ratio

Figure 3.31: Small coupon results

It is demonstrated that the yield stress values for all groups were close to 500MPa. In Figure 3.31a, the yield stress for the flange edge area was higher than the respective one for the flange up region for the near the weld case. However, the flange up region away from the weld exhibited similar yield stress values as the flange edge region near the weld, thus, higher than the respective flange up region near the weld. The opposite is typically expected, as explained in the standard coupons section. Nonetheless, it should be noted that the near the weld region had been repaired. Moreover, the SD for the group near the weld was higher than the group away from the weld while COV values are close. Thus, it can be concluded that the specimen group away from the weld was more consistent referring to the separate values of the specimens for that group; although, given the small number of specimens this is mentioned only for comparison reasons between the different W-shape regions.

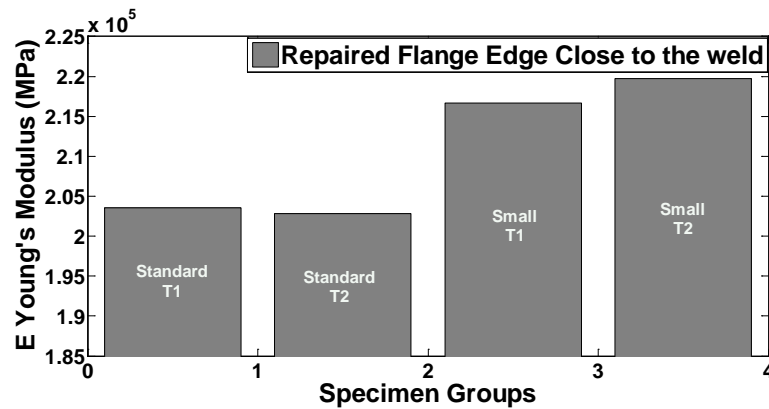
In terms of ultimate strain, Figure 3.31b shows that the flange edge near weld region experienced earlier fracture than the rest of the groups. However, the SD and COV values for this group were fairly high revealing a considerable variation of the values obtained for this location compared with the other group SD and COV values.

Figure 3.31c demonstrates a F_u/F_y ratio for all groups less than the 1.22 expected value with the exception of the flange up near weld group, which had lower yield strength. However, the difference was small (nearly 6%).

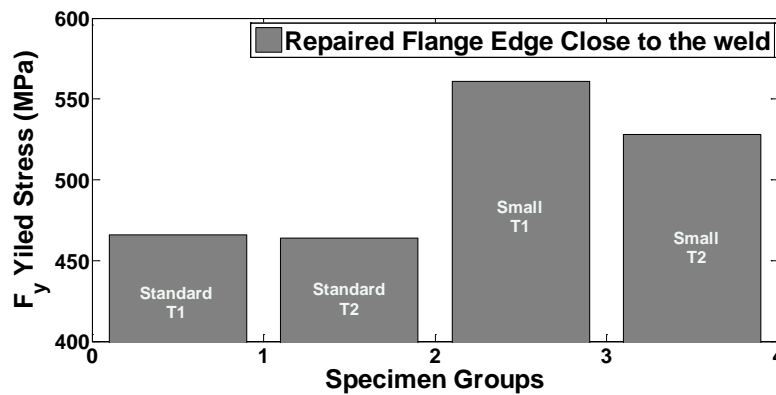
In general, for the properties obtained no significant differences were observed, as the values of the material properties of the specimens (Young's modulus, ultimate stress & strain etc.) were close in magnitude (12% to 20% max difference).

- Small coupons compared to standard coupons

Focusing on the same locations for the small and standard coupons two basic differences stand out, the difference in yield stress and in Young's modulus. Figure 3.32 depicts these differences for the repaired flange edge close to the weld location.



(a) Young's modulus



(b) Yield Stress

Figure 3.32: Comparison between small and standard coupon results

The yield stress values of the small coupons (about 520MPa) were close to those obtained from mill tests, provided by the industrial partner of this project (516MPa). The shorter gauge length of the small coupons and the smaller strain gauges installed on them can lead to more accurate results (10mm and 5mm strain gauges used for standard and small

coupons, respectively); the smaller the strain-gauge the better the strain measurement resolution. In addition, the small coupon measurements are more reliable in terms of stresses and strains, given the larger number of specimens available for each group and the consistency of the values based on the SD and COV. In addition, torque, introduced during the gripping of specimens in the machine (misalignment in some cases), is considered as one of the reasons why earlier yielding (in terms of stress) was observed in the standard coupon test results and was corrected accordingly before inserting the material stress-strain curves to the finite element model, although its contribution to the final results was negligible (Chapter 4).

3.5 Summary of Testing Program and Results

In this chapter, the material properties of one of the columns that experienced cracking during welding of doubler plates and shear tab plates were examined using Charpy V-Notch testing, tensile testing and scanning electron microscopy.

3.5.1 Charpy V-Notch Tests

Charpy V-notch testing was used to calculate the fracture toughness of the material in different environment conditions. The basic conclusions drawn after testing 138 specimens are as follows:

- The material met the 54Joules (40 ft.lb) requirement at 21°C (ASTM A913 2007b).
- Specimens in the long orientation exhibited higher CVN values than in the short orientation, as expected.
- The long orientation samples followed the theoretical curve constructed using Johnson's and Storey's paper (2008) characterising the specific material in question

for 0.06wt.% carbon content. The lower shelf energy was 4Joules while the upper shelf reached an average of 200Joules starting at 48°C. Transition temperature was estimated at 0°C.

- Long orientation specimens close to the k-area provided lower CVN values, complying with the low fracture toughness values observed in that location.
- Lateral expansion and shear surface percentage measurements, based on the empirical method provided by ASTM A370 (2007a), showed an increase with the increase of temperature for the long orientation specimens. This is in accordance with the fact that as the temperature increases the specimen absorbs more energy and behaves in more ductile manner.
- SD and COV calculations for different specimen groups revealed a more consistent in measurements sample near the weld than away from the weld, with CVN values of the first being lower. This is to be expected given the welding processes (elevated temperatures) that took place in those locations.
- The variability observed for some specimen groups was partly attributed to the small number of specimens available for each location and one should take this into account in the interpretation of the results.

3.5.2 Scanning Electron Microscopy

From scanning electron microscopy the chemical composition was verified, as well as the following expected microstructural phase changes connected to the carbon content of the material and the exposure to elevated temperatures and fast cooling rates:

- The chemical composition obtained through EDS indicated very low carbon content in accordance with the mill test report provided by the industrial partner.

- Small grain sizes were observed in the polished surface of one specimen, as expected due to the fabrication processes of quenching and self-tempering for the A913 Gr. 65 high strength steel.
- Manganese sulphide inclusions were discovered in the surface but their size and frequency indicated that they do not have great influence on the material properties.
- Examination of a fully brittle specimen revealed transgranular fracture and cleavage facets were clearly visible in the fractured surface.
- A purely dimpled surface characterised the fracture surface of the fully ductile specimen.
- Examination of the fracture surface of these specimens with SEM revealed a microstructure being in accordance to the fully brittle or ductile manner that each specimen provided during the test.

3.5.3 Tensile Testing

Finally, the tensile testing conducted for standard, non-standard and small coupons provided the following information about the material:

- The tests showed acceptable stress, strain and Young's modulus values for the high strength steel in question, based on the nominal values given in the ASTM A913 (2007b) standard.
- Standard coupon stress-strain curves indicated a reduced plateau in the inelastic range and earlier fracture (at 0.15%-0.2%). Small coupons provided higher fracture strain values along with higher stress values compared to the standard coupons; these

differences are attributed to the smaller gauge length and transverse orientation in the column of the small coupons compared to the standard ones.

- Comparative histograms highlighted higher average yield stresses for the standard coupon groups near the weld than for those in the non-welded regions due to residual stresses present in the welding locations.
- The variation in the stress and strain values for the standard coupon results was very small (differences of approximately 2%).
- Special k-area coupons fractured in shear during the test. They presented curved elastic range attributed mostly to their special dimensions and cross-section, while their yielding stress was slightly increased possibly due to torque applied in the specimen during the gripping process.
- One special coupon specimen near the weld exhibited earlier fracture (nearly 0.12%) and fractured vertically in the middle of the web in a more ductile manner. A pre-existing crack could have been the cause for this specimen's fracture manner.
- The variability of the material observed for certain specimen groups through SD and COV calculations is attributed to the number of specimens available for each location and the errors accompanying this type of testing.

It is concluded that the material satisfies the ASTM A913 requirements. Thus, having excluded the material as the cause for the cracking observed in the column the next step is the thorough investigation of the welding sequence used in the welding procedures (Chapter 4).

CHAPTER 4

Simulation of Welding Procedures Through Finite Element Modelling

4.1 Introduction

In Chapter 3, it was shown that the steel material of the W-shape column was not accountable for the observed cracking in the case study discussed. Thus, the next step was to evaluate the welding processes and sequence that were used to establish the weld of the doubler plate at the panel zone of the beam-to-column connection. To this end, a 2D finite element (FE) approach was developed in order to simulate with accuracy the conditions of the welding processes taking place on the web of the high strength steel W-shape column discussed in Chapter 3 and to obtain the stress distributions due to the welding of the doubler plate. It should be noted that although it was the removal of the shear tabs due to a fabrication error that led to the discovery of the cracks in the column (Chapter 3), it was assumed for this research that the cracking was caused by the doubler plate welding and did not have anything to do with the shear tab itself. Therefore, the shear tabs were not simulated and are not part of the FE modelling approach presented in this thesis (Figure 4.1).

Within the context of this thesis two types of analyses are discussed, an uncoupled heat transfer and a stress analysis, conducted in the finite element program Abaqus (Abaqus FEA/CAE 2011, Version 6.11-3). A heat transfer analysis allows modelling of the internal energy (thermal energy) of a solid body as it receives from and transfers energy

to other bodies and the environment. The conduction of a heat transfer analysis is achieved through the insertion of temperature-dependent thermal material properties (such as thermal conductivity and thermal expansion) and the application of boundary conduction and boundary radiation (Abaqus FEA/CAE 2011, Version 6.11-3). In this way, all effects on material properties due to the change of temperature are included and the interaction of the solid body/model in question with its surroundings is ensured. The exact thermal loading applied on a model can be acquired through the conduction of a heat transfer analysis.

Subsequently, a stress analysis can be conducted, which provides the stresses and strains that a solid body or structure undergoes. This is achieved by inserting in the model mechanical material properties and the loading conditions that are applied to the simulated body/structure. Boundary conditions ensuring the stability of the model are of the utmost importance. In the case of thermal loading, temperature-dependent mechanical properties are inserted so that the change in yield stress or Young's modulus with the change in temperature is taken into account. The results from the heat transfer analysis can be imported as input (thermal loading) to the stress analysis, which will provide the stresses and strains of the simulated model due to thermal loading.

The separate execution of the heat transfer and stress analyses constitutes an uncoupled modelling approach, which was the case in the current research, and is referred to in Abaqus as “sequentially coupled thermal-stress analysis” (Abaqus FEA/CAE 2011, Version 6.11-3). Coupling of mechanical and thermal effects in the heat transfer analysis was neglected, meaning that the temperature distribution of the steel material adjacent to the weld was calculated without considering stresses and deformations in the model. This

was based on the assumption that in the simulation of the welding process the stress field is dependent on the temperature distribution but the inverse does not apply (e.g., Pilipenko 2001, Chang and Lee 2009 and Jin et al. 2011). Another indispensable part of the modelling approach was the application of the element “Birth and Death” technique (Brickstad et al. 1998). This technique constitutes the foundation of the welding simulation since it enables the gradual construction and insertion in the model of each weld bead, one after the other, based on the welding pass sequence. The model undergoes changes as “material” is added with the insertion of every weld bead to realistically simulate the welding process.

In the following sections, a detailed description of the welding procedure, geometry and meshing is presented, as well as the FE modelling technique used and the heat transfer and stress analysis process and results using, initially, expected and, subsequently, measured material properties from the testing program (Chapter 3). This Chapter is an extension of recent work presented in the 3rd Specialty Conference on Material Engineering & Applied Mechanics (Nikolaidou et al. 2013).

4.2 Welded Column Assembly Geometry and FE Meshing

Two 25mm thick, 286x1332mm doubler plates were welded to the web of a W360x237 (W14x159) column section at the beam-to-column connection location as discussed in Chapter 3 (Section 3.1, Figure 3.1). Figure 4.1 illustrates an isometric drawing of the welded column assembly. The welding process on each side of the web consisted of two 13-pass complete joint penetration (CJP) flare bevel groove welds with weld angle 30° performed at the k-areas and two 6-pass plug welds at the middle, as shown in Figure 4.2.

The welding sequence typically used in practice, and simulated in this thesis, involves completion of all welding passes on the one side of the web of the W-shape, both plug and flare bevel welds. The column is then flipped and the welds on the other side of the web are performed. Table 4.2 in Subsection 4.5.1 contains detailed information about all the parameters of the welding sequence. Based on this process, the finite element modelling consisted of a heat transfer and stress analysis performed for one side of the web for the welding of one doubler plate. The same analyses with the exact same steps were then repeated for the other side of the column web for the welding of the second doubler plate. An additional step was inserted at the beginning for the simulation of the welding of the second side of the web where the results from the first two analyses were inserted as initial conditions for the next two analyses. A detailed description of the heat transfer and stress analysis modelling procedure is presented in Section 4.5 and 4.6.

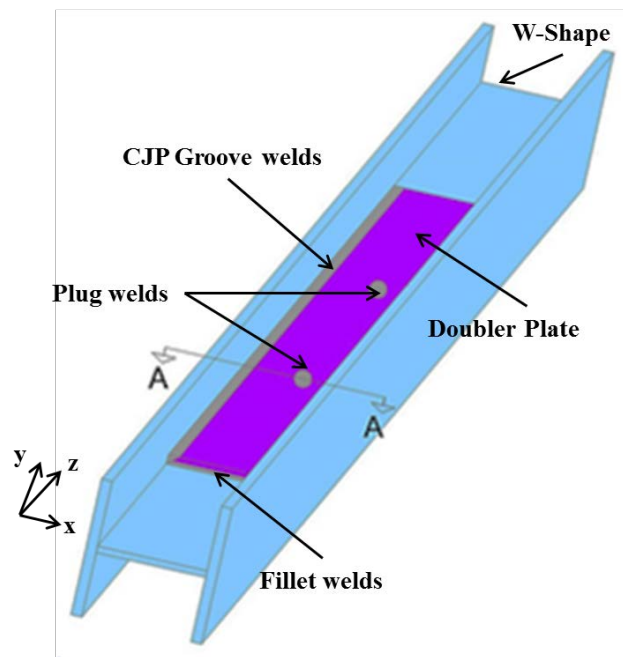


Figure 4.1: Isometric drawing of welded column assembly

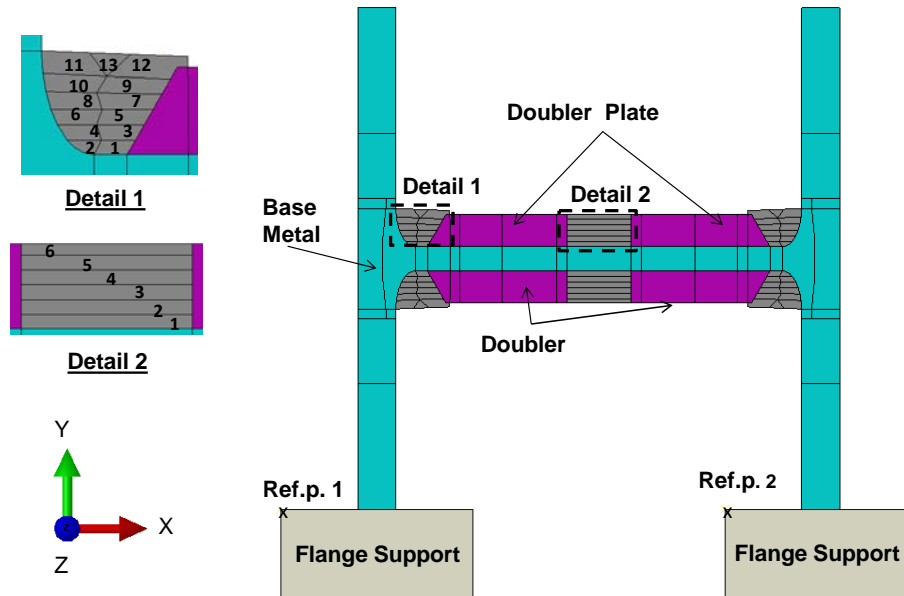


Figure 4.2: 2D model geometry of the welded column assembly (Cross-section A-A)

The numerical model consisted of four parts; (1) the W-shape with the welds; (2) the upper doubler plate; (3) the lower doubler plate; and (4) the flange supports (ref.p.1 and ref.p.2 refer to reference points added in the model as part of the rigid body constraints; the reference points were transferred to the centre of the mass of the rigid bodies during the stress analysis). Constraints and boundary conditions were applied to the numerical model because adequate stiffness and numerical stability of the model is an indispensable factor when referring to the convergence of a stress analysis. For this reason, a tie constraint was applied to all contact surfaces of independent parts of the welded column assembly. In addition, a rigid body constraint was used in the model since in the fabrication shop welding is typically performed while a column is positioned on top of steel supports, placed at certain intervals. The rigid body constraints were applied at the rigid body parts as shown in Figure 4.2; fixed boundary conditions were applied at their

reference points. Between the flange tips and the rigid bodies, surface-to-surface contact interaction was applied and tangential behaviour was chosen with a penalty friction formulation and a friction coefficient 0.2. For the normal behaviour, a hard contact and the penalty method were chosen for the linear contact stiffness behaviour. Clearance was 1mm and slip tolerance was 0.01, given the dimensions of the W-shape in question.

Flux cored arc welding (FCAW) was used to conduct the welds with a CO₂ shielding gas (see Section 2.2, Figure 2.1). The amperage used was 300A, the voltage 29V, the wire feed speed 7620mm (300in)/min while the electrode weld speed was 300mm (12in)/min. The electrode type was E71-T1, size 1.6mm (1/16in) while the wire type was H16 (or less). The heat input was 2kj/mm (47kj/in).

The doubler plates were also welded along the other two edges perpendicular to the length of the column with 1-pass fillet welds using the same welding process (FCAW) and parameters as for the CJP and plug welds (Figure 4.1). However, the model simulated a cross section through the fabricated column therefore these welds were not included and, thus, they are not shown in Figure 4.2. The same applies for the second plug weld. Nonetheless, the corresponding construction time for these welds was taken into account as explained in Section 4.5.1.

The FE meshing arrangement of the 2D cross-section is shown in Figure 4.3. Two types of finite elements are required in order to perform the uncoupled heat transfer and stress analyses; diffusive heat transfer and plain strain elements. Diffusive heat transfer elements have only temperature as a degree of freedom; the nodal temperature values are saved as output and inserted as input in the stress analysis. These elements have the

ability of thermal storage and thermal conduction. Some of the output variables are magnitude of the heat flux vector and integration point temperatures. Plain strain elements are stress/displacement elements with translational nodal degrees of freedom. For those elements, the out-of-plane strain is considered zero. These elements are appropriate for modelling associated with material and geometric nonlinearities, contact simulation and large deformations. The same elements can be used as a subsequent element type in a thermal-stress analysis after the thermal analysis is conducted with diffusive elements (Abaqus FEA/CAE 2011, Version 6.11-3). Plane strain elements are suitable for a 2D stress analysis where residual stresses (out-of-plane stresses) and in-plane strain distributions are of interest. The basic element type selected was continuum (solid) elements based on the geometry of the model and the fact that this family of elements supports both diffusive heat transfer and plain strain elements.

Furthermore, quadratic elements were selected. Quadratic solid elements are second order 8-node elements for a 2D model in Abaqus. Gaussian integration is used for second order elements. Full integration was chosen for these elements after hourglassing modes were observed in some elements when using, initially, reduced integration. By selecting full integration quadratic elements, the possible influence of effects such as hourglassing and shear locking on the accuracy of the results was minimized. In addition, it is recommended to select second order elements when referring to a heat transfer analysis that does not involve latent effects (as explained in Section 4.5) and it is underlined that these elements provide more accurate results when used in a meshing arrangement with elements of the same number of nodes (Abaqus FEA/CAE 2011, Version 6.11-3).

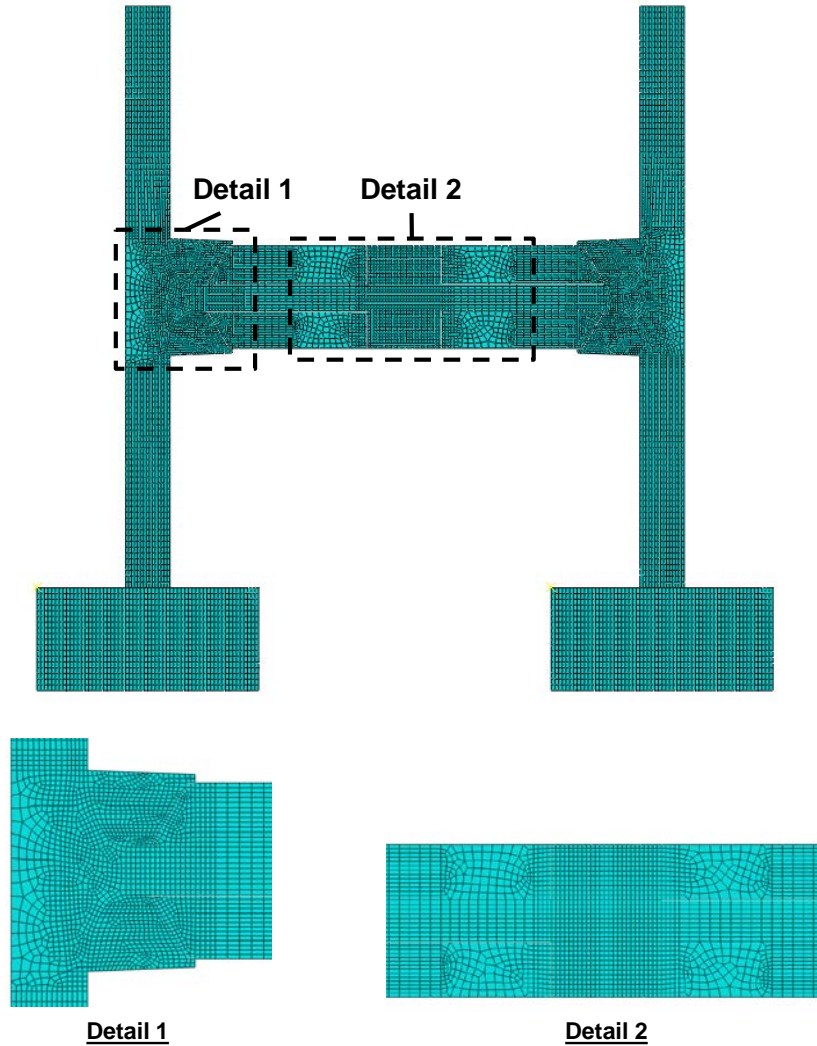


Figure 4.3: FE mesh of the W-shape, the doubler plates and the welds

Abaqus (Abaqus FEA/CAE 2011) provides sizing controls that involve a minimum size factor and a curvature control based on the geometry and dimensions of the part chosen to be meshed. The user can clarify whether the automatically generated mesh for a specific region will be based on a specific number or size of the elements. Given the challenging geometries of the welded column assembly shown in Figure 4.2, free meshing was more suitable in order to mesh the model effectively and avoid distorted element shapes. In certain locations, such as the k-area regions of the W-shape, the number and size of

elements had to be chosen manually so that distorted elements shapes could be avoided. Based on the above choices the minimum element size was found to be 2mm for the denser regions with an approximate general element size of 4mm. Moreover, after several trials, quadrilateral elements were deemed more suitable than the combination of triangular and quadrilateral elements for the geometry in question (Figure 4.1) so that distorted element shapes and sharp angles could be avoided. Thus, heat transfer and plane strain 8-node quadratic quadrilateral elements were implemented for the heat transfer and stress analysis, respectively.

For the element meshing arrangement, it was of great importance, that it remained exactly the same for both analyses (heat transfer and stress analysis). The reason was that the elements carrying the nodal temperature values needed to remain in the same position in the model. The meshing for the surface of the flange tip was chosen to be denser than the body of the flange in general but not entirely different from the surface of the rigid body, given that the latter is the master surface and penetration errors needed to be avoided. The geometry of the welds and the number of weld passes shown in Figure 4.2 was based on information from the industry. Each weld was designed as a whole and then separated with partitions in a number of passes. The weld bead of each pass was then meshed based on its geometry and the minimum element size selected.

The width of the heat-affected zone (HAZ) was assumed to be 8mm near the weld and 16mm under the weld based on feedback from the industry and previous studies (Gunaraj & Murugan 2002, Aloraier et al. 2006, Aloraiera et al. 2010, Lee et al. 2007, Mark et al. 2012). The effect on the material properties of the base metal of the heat input associated with depositing weld beads for different welding processes was examined using

micrography. From these studies, the heat-affected zone was found to be from 4 to 6mm under the weld and 2mm near the weld (Chapter 2). In the HAZ regions the meshing was denser than in the area of the model between the CJP and plug welds and the CJP and the tips of the flanges, as shown in Figure 4.3. It should be noted that the flanges had an equal mesh density to the HAZ, but this was due to the contact elements inserted between the flange tips and their rigid supports.

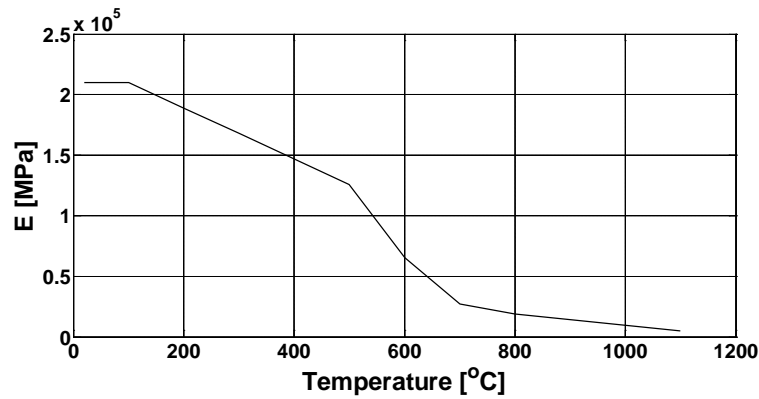
4.3 Material Properties

The material properties inserted in the finite element model are described in detail, referring to properties characterizing the material tensile behaviour, as well as characterising the behaviour of the material when exposed to elevated temperatures.

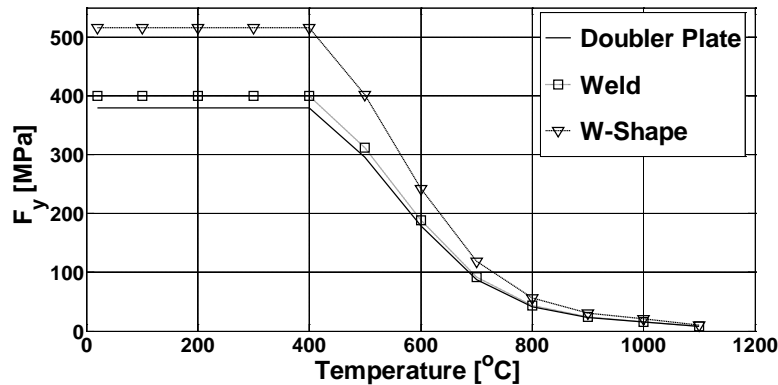
4.3.1 Expected Material Properties

The W-shape and doubler plates were fabricated from ASTM A913 Gr. 65 and A572 Gr. 50 steel, respectively. In the initial FE models, conducted before completion of the testing program described in Chapter 3, expected material properties were relied on to define the behaviour of the steel and welds. In order to simulate the nonlinear behaviour of the steel materials, a bilinear model was employed with 3% strain hardening. Only for the A913 Gr. 65 steel, the yield stress at 15°C (ambient temperature, shop conditions) was assumed to be 516MPa based on mill tests provided from our industry partner for the particular steel material, as shown in Chapter 3. Similarly, for the A572 Gr. 50 steel, the yield stress was assumed to be 380MPa (expected yield stress with 1.1 factor per CSA S16 2009). An expected value of 400MPa (Funderburk 1999) and was chosen as the yield stress of the weld metal for an E480MPa (70ksi) electrode at room temperature. The reduction of the

yield stress and Young's modulus as a function of the temperature increase was taken into account based on Eurocode 3, Design of steel structures Part 1-2 (Eurocode-3, 2005) (Figure 4.4a and b). Note that at temperatures above 1000°C the material has practically zero yield stress and axial rigidity.



(a) Young's modulus vs. temperature

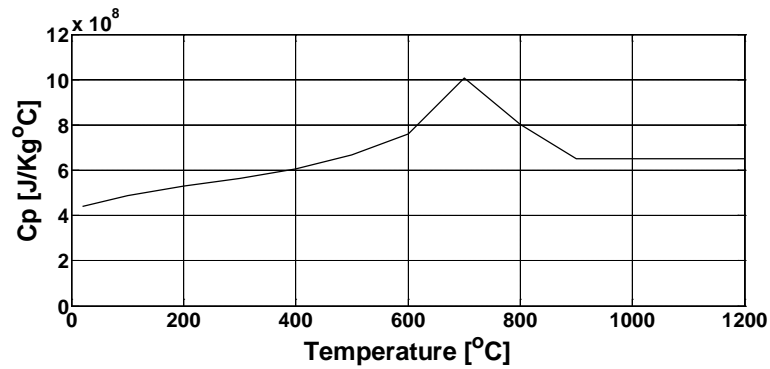


(b) Yield stress vs. temperature

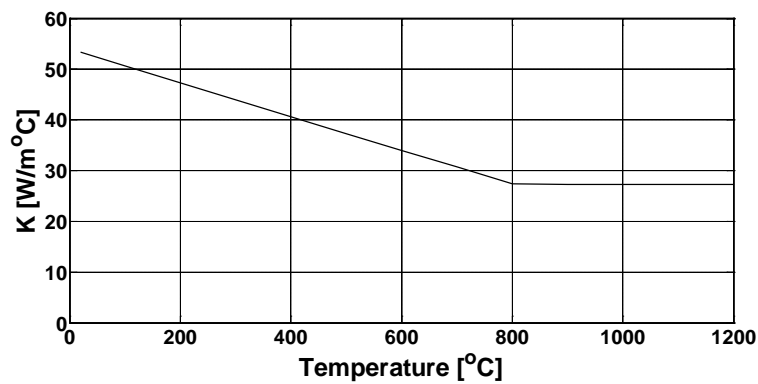
Figure 4.4: Material properties variation with temperature (Eurocode 3 2005)

Other parameters describing the behaviour of the material with the increase of temperature as defined in Chapter 2, such as thermal conductivity (fully isotropic), thermal expansion and specific heat coefficient, also vary with temperature based on the factors provided by Eurocode 3, Design of steel structures Part 1-2 (2005), as shown in

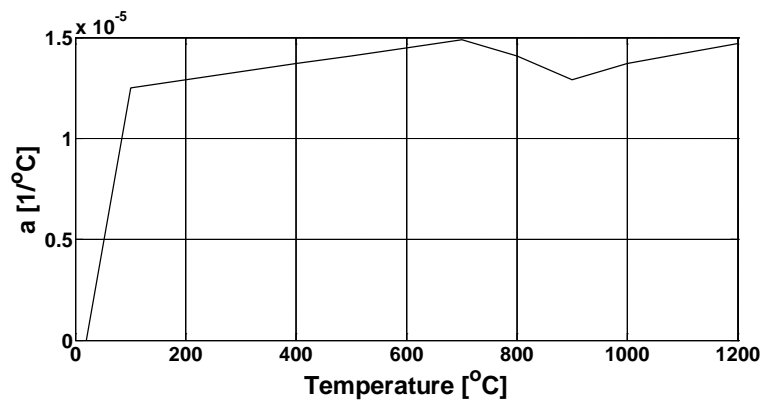
Figure 4.4c, d and e. The phase transformation of metal (at 723°C) was taken into account in these graphs.



(c) Specific heat coefficient vs. temperature



(d) Thermal conductivity vs. temperature



(e) Coefficient of thermal expansion vs. temperature

Figure 4.4 (Continued): Material properties variation with temperature (Eurocode 3 2005)

It should be mentioned that AISC 360 (2010a) and CSA S16 (2009) offer similar reduction factors as Eurocode 3 (2005). Using factors from either of the codes would provide the exact same reduction in the values. However, in Section 4.3.2 experimental reduction factors are introduced based on Outinen et al. (2000); in their study the experimental factors were compared with those listed in Eurocode 3 (2005), as explained in Chapter 2, Section 2.2.6.1

The density of steel was defined having a constant value of $\rho = 7.85\text{E-}009\text{Mg/mm}^3$. According to Eurocode 3 (2005) this value does not vary with the increase of temperature. Additional material values defined in the model were the Stefan-Boltzmann constant = $5.67\text{E-}11\text{ N/mm}^2\text{C}$ and the absolute zero temperature = -273°C , where the Stefan-Boltzmann constant is “a proportional constant, which refers to the amount of energy per unit area that gets radiated from a black body based on its temperature” (Cengel 2007). These values are required for the case of a heat transfer analysis in order to incorporate surface emissivity and radiation conditions in the model.

4.3.2 Measured Material Properties

After the completion of the materials testing program the finite element model was updated. In particular, the behaviour of the representative elements in the FE model was redefined based on the measured tensile material properties for different parts of the W-shape columns. Following the information given in Chapter 3 (Section 3.4.2), the measured material properties (true stress-strain curves deduced from measured engineering stress-strain curves) were applicable in four locations; flange edge, flange up, k-area and web. The average values of each group of standard coupons for each region

(Chapter 3) were used for the Young's modulus, the yield (from the 0.02% offset method), the strain hardening and the ultimate point, as well as the Ramberg-Osgood equation (Equation 4.1) to approximate the engineering stress-strain curve (Table 4.1) in the inelastic range from the strain hardening point until the ultimate point.

Table 4.1: Average values for the measured engineering stress-strain curves

Locations	E (MPa)	F _y (MPa)	ε _{sh} (mm/mm)	ε _u (mm/mm)	F _u (MPa)	n	ε _y (mm/mm)
k-area	205305	480	0.0222	0.1358	570	13	0.0153
Flange-up	205305	496	0.0188	0.1215	559	27	0.0042
Flange-edge	203441	496	0.0150	0.1166	565	34	0.0046
Web	203846	472	0.0233	0.1229	546	30	0.0042

The curves were then converted to true stress-strain curves (Equation 4.2 & 4.3).

$$\varepsilon_e = \frac{\sigma_e}{E} + \alpha \frac{\sigma_o}{E} \left(\frac{\sigma_e}{\sigma_o} \right)^n \quad (4.1)$$

where ε_e is the engineering strain, σ_e is the engineering stress, σ_o is the yield stress, E is the Young's modulus and α and n are factors based on the material considered (Ramberg and Osgood 1943). The $\alpha(\sigma_o/E)$ is the yield offset and its typical value is 0.002.

$$\sigma_t = \sigma_e (1 + \varepsilon_e) \quad (4.2)$$

$$\varepsilon_t = \ln(1 + \varepsilon_e) \quad (4.3)$$

where σ_t and ε_t are the true stress and strain, respectively (Roylance 2001). The true stress- plastic strain curves required for the FE model are illustrated in Figure 4.5 for the ambient temperature. The elastic region of the graphs is taken into account by defining the Young's modulus values, separately in Abaqus, for each location.

The measured curves have a yield stress close to the expected (max difference 4%) but they demonstrate a strain hardening of nearly 0.7% which is low compared to the 3%

assumed initially, given also that the Young's modulus value was assumed 210GPa and the measured was found to be 205GPa for the W-shape. Therefore, the expected curve varies in the inelastic range from the experimental one.

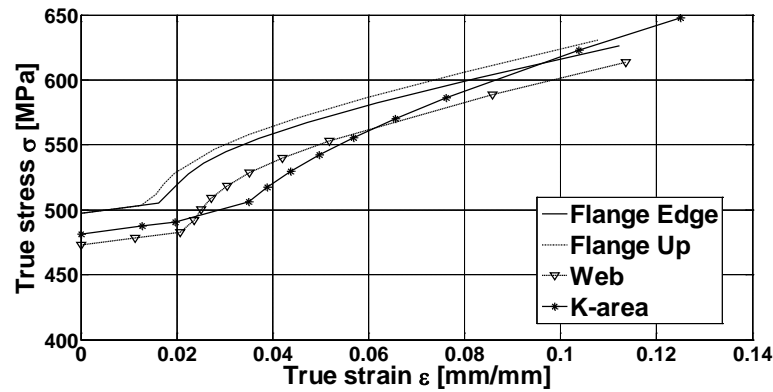
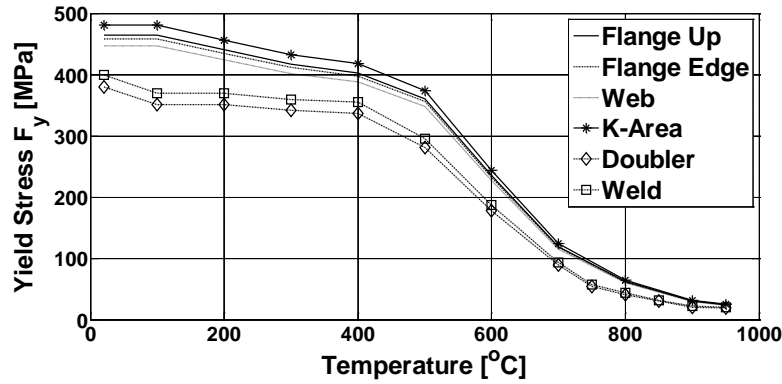
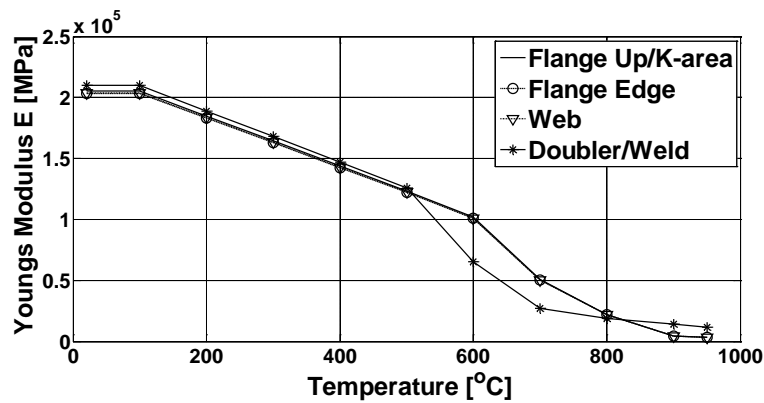


Figure 4.5: True stress-strain curves based on measured material properties

Moreover, apart from inserting the measured material properties in the FE model, the reduction factors based on Outinen et al. (2000) were also used to obtain the true stress-strain curves as the temperature increases, as explained in Chapter 2. These factors refer only to the high strength steel W-shape for better accuracy in the results and not the doubler plate or weld because the main focus of this thesis for potential fracture is the W-shape. The doubler plate is not considered critical for fracture; thus for the doubler plate and the weld, Eurocode 3 (2005) reduction factors were used. Figures 4.6a and b illustrate the reduction of the yield stress and Young's modulus for the different W-shape regions, the doubler plates and the weld.



(a) Yield stress variation with temperature



(b) Young's modulus variation with temperature

Figure 4.6: Measured material properties vs. temperature

4.4 Element Birth and Death Technique

The ability to remove and add parts of the FE model in Abaqus is referred to as the element “Birth and Death” technique (Brickstad et al. 1998). Essentially parts of the model are not removed, but rather deactivated (death) using the “Model Change” interaction and they can be reactivated (birth) in a following analysis step. In order for this to be achieved at the beginning of the analysis the model must be complete with all its parts active. For the heat transfer elements, the deactivation of a part sets the thermal conductivity of the corresponding elements to zero, while at the reactivation of the part

the thermal conductivity is ramped up from zero over the step. This technique allows the simulation of a welding process where weld beads are conducted or activated, in modelling terms, one after the other. The use of this technique differed in terms of how it was applied for the heat transfer and the stress analyses. In the heat transfer analysis all weld beads were deactivated at the beginning and reactivated at the appropriate step according to the welding sequence followed. In contrast, in the stress analysis all weld beads were not removed simultaneously at one analysis step. Each bead remained activated in the model throughout the welding process and was only instantaneously deactivated and activated in between its welding and its cooling step. The main reason is that, unlike the heat transfer analysis, in a stress analysis the model experiences deformations as the welding is being conducted. If the weld beads were all deactivated from the start (as in the heat transfer) then at the point of activation numerical errors would be introduced to the model since the “walls” of the base metal would be already deformed; thus the element nodes of the weld bead would no longer coincide with those of the base metal. Artificial stresses would have to be introduced in an effort to adjust the nodes which would influence the accuracy of the results. In addition, in order to ensure that the pre-existing weld beads in the stress analysis did not take any stress and, thus, did not influence the resulting stress output, a temperature of 1500°C was applied to them, until they were “born” based on the welding sequence. As shown in Section 4.3, the stiffness and yield strength of steel becomes practically zero at a temperature near 1000°C and higher.

4.5 Heat Transfer Analysis

A transient heat transfer analysis was conducted as part of the developed FE model. As mentioned in Section 4.1, this type of analysis includes conduction, boundary convection and boundary radiation, which enable the transfer and exchange of temperature between surfaces in contact and with the environment. Latent heat effects (between phase changes) were not included, given the small volume (weld bead and small area around it) that changes phase during the welding process.

The temperature boundaries chosen, based on feedback from the industry, were 15°C low temperature (ambient temperature) and 1500°C high temperature (temperature during welding).

The boundary conditions of the FE model included a prescribed temperature, surface heat flux and volumetric heat flux with surface convection given by Equation 4.4 and radiation by Equation 4.5.

$$q = h(\theta - \theta_o) \quad (4.4)$$

where $h = h(x, t)$ is the film coefficient and $\theta_o = \theta_o(x, t)$ is the sink temperature (15°C).

$$q = A((\theta - \theta_z)^4 - (\theta_o - \theta_z)^4) \quad (4.5)$$

where A is the radiation constant (emissivity with a constant value of 0.625 from Eurocode 3 2005) times the Stefan-Boltzman constant and θ_z is the value of absolute zero.

4.5.1 Welding Sequence and Modelling Parameters

As mentioned, the welding sequence performed for the connection of one doubler plate to the web of the W-shape consisted of two plug welds in the middle of the web and two edge CJP flare bevel groove welds (Figure 4.2). In the 2D model only one plug weld in the middle is shown but the construction time for both plug welds was taken into account as part of the simulation process. The welding process is fully described in Table 4.2. Based on industry feedback, first a sealing pass was performed around the doubler plate (pass 1 of weld bead at each edge shown in Figure 4.2). The welds in the other dimension of the doubler plate are not shown in the 2D model, as explained in Section 4.2, but the time of their construction was also taken into account. At this point it should be noted that the construction time, for the welds that are not shown in Figure 4.2 and were not part of the model, was considered. The reason was that an accurate cooling time between the passes that were simulated must be inserted in the model, given that during this cooling period tensile stresses develop in the adjacent parts of the weld bead that are undergoing shrinkage. The duration of the welding passes that were not included in the model constitutes an additional cooling time for the weld beads in the model that were already conducted. Following the first sealing pass, the 6 passes of the plug welds were completed and, subsequently, the rest of the passes of the edge welds. Specifically, after the second pass of the left edge weld was completed a second pass of the right weld followed, then the third pass of the left weld, the third pass of the right weld and so on. This process was simulated in Abaqus with a total of 99 steps. In the initial step, predefined fields were inserted indicating 15°C as the base metal initial temperature (ambient temperature) and 1500°C as the weld metal initial temperature, referring

essentially to the molten metal deposited at the base metal surface during each pass. In the next step, all weld beads and the doubler plate on the other side of the web (the side where no welding was taking place) were removed instantaneously using a “Model Change” interaction provided in Abaqus in order to be added again later on according to the welding sequence. Subsequently, preheat was applied to the surfaces that were going to be welded through a temperature boundary condition added in the preheat step. The preheat temperature chosen was 66°C (150°F) based on information from the industrial partner of this project, although the AWS D1.1 (2010) welding procedures do not require preheat for A913 Gr. 65 steel (Table 3.2 of AWS D1.1 2010). Preheat was applied for 900sec assuming ramp linear behaviour over a step. These values were chosen based on feedback from professional in practice welders. At every step, if a surface was not heated, film condition and surface radiation interactions were applied ensuring the interaction of each surface with the surroundings.

After preheat, the first sealing pass was performed. Every welding pass was simulated using three analysis steps. The first step involved the heating of the surfaces where the molten metal was to be deposited. This was achieved by gradually applying a temperature boundary condition of 1500°C to the relative surfaces over the time of the step. The second step involved the reactivation of the weld bead in question in its solid form and the third step replicated the time between passes when weld and base metal were allowed to cool before the next welding pass. The cooling time also included removing the flux coating from the previously conducted pass (120sec to remove flux from one pass of the CJP welds and 90sec for one layer of the plug welds respectively). All time steps were based on the actual time needed for welders to complete this type of weld. The

characteristic time for the completion of one pass of an edge weld was 300sec, whereas the cooling time was set at 900sec, while for the plug welds 45sec and 225sec, respectively, were used for modelling. During this time the electrode travel speed, the doubler plate dimensions and the time needed to move the equipment were all taken into account. The maximum number of increments was set to 100, 1000 or 10000 with maximum increment size equal to the time period and initial and minimum increment size defined manually depending on the sizes required for the analysis to be completed in a successful manner. In several cases, the initial step had to be reduced so that the loading would be applied more gradually; this would enable the smooth continuation of the numerical analysis.

After the completion of all the steps for the one side of the web, referring to the first heat transfer analysis (HT1), a period of 1800sec (30min) was considered in order for the column to be flipped. Then, the second side welding commenced. Thus, the final step of the HT1 had a cooling time of 1800sec. The conditions (temperatures) of that step were then inserted as initial condition to the second heat transfer analysis (HT2) and the same 99 steps were then repeated for the welds on the other side of the web. The final step of the HT2 had a cooling time of 18000sec since the column is typically allowed to cool down for 5 hours before the welding of the shear tabs is conducted. Based on Table 4.2, Figure 4.7 shows a time-based graph illustrating the relative duration for the basic processes taking place in the welded column assembly. The time periods are shown for the CJP and plug weld pass as described in Table 4.2.

Table 4.2: Welding sequence and procedures


Steps	Time(sec)	Time(min)
Remove welding and the doubler plate on other side of the web	Instantly	Instantly
Preheat*	900	15
Start Left CJP Welding Pass1	300	5
Birth of Left CJP Welding Pass1	Instantly	Instantly
Cooling after Left CJP Welding Pass1**	900	15
Start Right CJP Welding Pass 1	300	5
Birth Right CJP Welding Pass 1	Instantly	Instantly
Cooling after Right CJP Welding Pass 1	630	10.5
Start Plug Weld Pass1 (one of the two Plugs)	45	1
Birth of Plug Weld Pass1 (one of the two Plugs)	Instantly	Instantly
Cooling after Plug Weld Pass1 (one of the two Plugs)***	225	4
The same process for the other 5 Passes of the one web side plug welds respectively		
Cooling after Plug Weld Pass 6****	345	6
Start Left CJP Welding Pass2	300	5
Birth of Left CJP Welding Pass2	Instantly	Instantly
Cooling after Left CJP Welding Pass2	750	12.5
Start Right CJP Welding Pass2	300	5
Birth of Right CJP Welding Pass2	Instantly	Instantly
Cooling after Right CJP Welding Pass2	750	12.5
Respectively for the 11 remaining passes of the two CJP welds		
Cooling after Top Right CJP Welding of the 13th Pass	2160	36
Initial conditions for welding on the other side of the web	Instantly	Instantly
Preheat of all doubler plates and W shape	900	15
Start Bottom Right CJP Welding Pass 1	300	5
Respectively for the remaining passes for the CJP and Plug welds for the other side of the weld*****		
Cooling after final CJP Welding Pass	18000	300
Welding of shear tabs		
Comments		
Flip of column symbol 		
*Preheat for one web side doubler plate and W-shape in 3in distance in all directions near the welds		
**Cooling time before the weld pass of the opposite side starts.		
***Cooling time before the second layer of the second plug weld starts.		
****Cooling time before the construction of the two CJP welds continues.		
***** After preheating again --> sealing first pass around the other doubler plate, including the fillet welds --> construction of the other two plug welds --> continuing with the other CJP welds.		

Table 4.2(Continued): Welding sequence and procedures

Time (min)	Explanation of time periods used
15	6 min remove flux from this pass + 1min fillet weld pass +1.5min remove flux of fillet weld pass+6.5min move equipment throughout the process
10.5	6min remove flux from this pass+ 1min fillet weld pass+ 1.5min remove flux from fillet weld pass + 2min move equipment
4	1.5min remove flux from this first plug weld pass + 45sec for the first layer in the second plug weld + 1.5min remove flux from that layer
6	1.5min remove flux from this plug weld pass + 45sec for the last layer in the second plug weld + 1.5min remove flux from that layer +2min move equipment
12.5	12.5 to remove flux and move equipment to the opposite side to do the second pass on the right other CJP weld

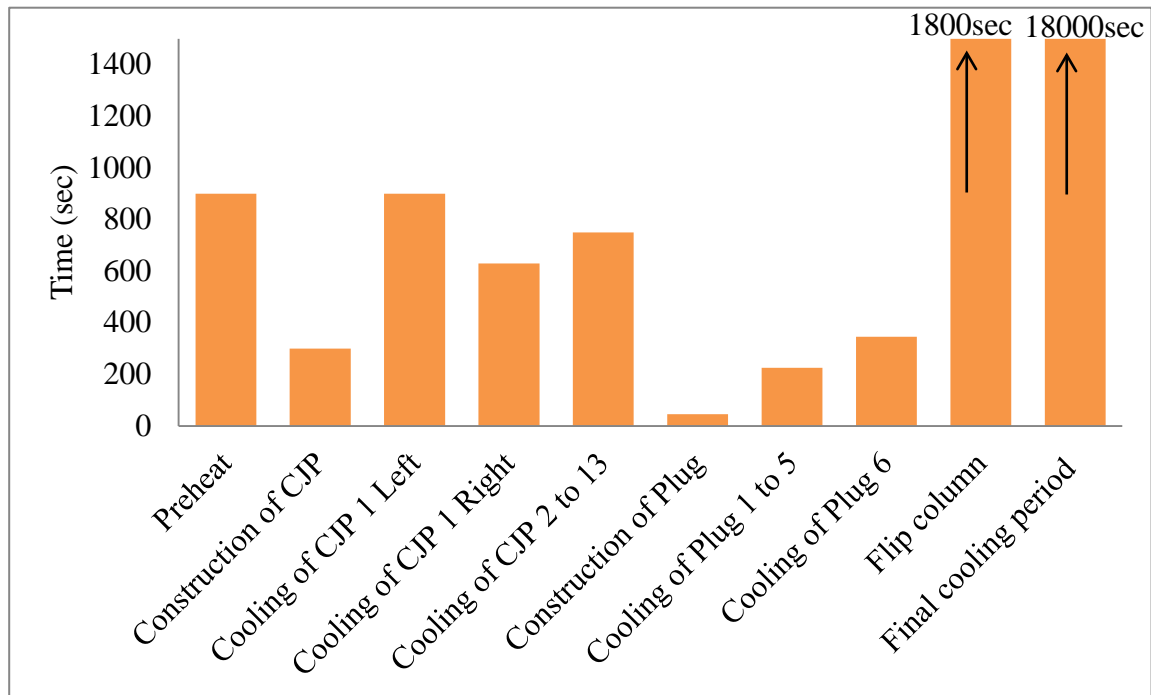


Figure 4.7: Time periods of basic welding procedures

From Figure 4.7, it is clearly shown that the construction and cooling times for each case differ. As explained in Table 4.2, the difference is based on the duration of each pass (with electrode speed 300mm/min), the equipment that needs to be moved each time in order to conduct the pass at a certain location in the column and the process used (FCAW). Therefore, the welding realised at the welded column assembly in question is

not a continuous process. Practical issues need to be taken into account when considering construction and, mostly, cooling time of each part of the welding procedure, since it has a great influence on the resulting residual stress field.

4.6 Stress Analysis

After the heat transfer analysis had been completed, the stress analysis corresponding to the same parts welded in the heat transfer analysis was performed. A nonlinear static analysis was conducted that considered geometric nonlinearities. The plasticity model was not strain-rate dependent, meaning that the rate with which the material was strained did not influence the response of the model under investigation.

For the FE analysis the classical metal plasticity model was used to describe the inelastic behaviour of the material, which involves in this case the von Mises yield surfaces and isotropic hardening. Furthermore, the default direct sparse solver of Abaqus was used, which uses a sparse, direct, Gauss elimination method and the full Newton solution technique.

4.6.1 Modelling Parameters

The same FE model used in the heat transfer analysis was then used in the stress analysis by means of changing the element type from heat transfer to plane strain. An additional step involved adding the constraints and boundary conditions described in Section 4.2. In order to facilitate the activation of the contact, an extra step was inserted in the analysis, in which only the self-weight of the welded column assembly was linearly applied over the time of the step to the initially existing parts of the model. The self-weight of every part added at each step was also taken into account throughout the analysis. The contact

interaction applied between the flange tips and the rigid bodies was also applied between the web of the W-shape (master surface) and the doubler so that the doubler plate would follow the deformation of the web. It also took into account the pressure exerted between the two surfaces during the welding process. In the stress analysis the previously obtained temperature distributions were inserted as loads in the form of stresses. In particular, each welding pass was simulated with a total of four analysis steps describing the pass construction, deactivation and reactivation and the cooling time before the beginning of the next pass. In the first and last step the temperature distributions corresponding to the construction of the pass and cooling time were inserted as predefined fields, respectively. The time periods of these steps were the same as those used in the corresponding steps of the heat transfer analysis. Thus, results from HT1 were inserted in the first stress analysis (SA1), referring to the one side of the web, and HT2 results were inserted in the second stress analysis (SA2) for the other side of the web of the high strength steel column under examination.

Due to convergence issues that were directly related to the flexural and tensile stiffness of the model, the SA1 analysis was conducted without the presence of the doubler plate and welds on the other side of the web, which was not being welded at this stage. Those parts (that were not present in real life conditions) were not simply deactivated as explained in Section 4.5.1, but they were entirely deleted from the model in order for the analysis to run successfully. The two basic reasons for this assumption are summarized as follows:

- 1) Model parts in a stress analysis cannot be deactivated at the beginning for the numerical stability to be maintained; thus, the stiffness of those parts had to be reduced by applying to them an initial condition high temperature; so those parts would not

“attract” any stress, 2) By applying no. 1, the final model consisted of parts with very low and high stiffness interacting with each other, which constitutes possible cause for non-convergence during the analysis. One limitation of these assumptions involved the displacement distribution. After the completion of SA1, the stress distribution of the final step was inserted as initial conditions to the SA2. It was observed that the resulting deformation and displacements in the SA2 due to these stresses in the initial step were smaller than those at the final step of the SA1. This was attributed to the fact that in the SA2 all parts were now present with full stiffness at the beginning of the analysis. Thus, the model exhibited higher resistance to the applied stresses. However, the stress distribution, which is primarily of interest based on the objective of this research, was obtained accurately, as it will be shown in the Section 4.7. A stabilisation factor may also need to be implemented in some analysis steps to facilitate convergence but with a very small value to avoid influencing the results (i.e. 0.0001).

4.7 Summary of the Results

Results for the heat transfer and stress analysis during and after welding of the doubler plate on the A913 Gr. 65 steel column are presented in this section. The emphasis is placed on the temperature and stress distributions.

4.7.1 Heat Transfer Analysis Results

The heat transfer analysis provided the expected temperatures at each step of the welding process at each location of the FE model. These values were inserted in the stress analysis as loads so that the residual stresses and deformations of the structure due to the welding process could be obtained. In Figure 4.8a, the numerical model of the steel column with

the doubler plates is depicted at the initial step of the analysis when the welds and the lower doubler plate were deactivated. During the welding simulation, each pass on the upper side of the web was activated and the temperature was distributed as expected without influencing the lower deactivated parts or the upper welding passes that were still deactivated. This can be seen in Figures 4.8b and 4.8c in which snapshots of the activation of welding passes at the plug welds and CJP are shown. The welding pass being conducted is indicated with red. The parts adjacent to the weld that mostly experienced the highest temperatures due to welding are highlighted with green and yellow. Figure 4.9 shows the temperature distribution immediately after the completion of pass 1 of the left CJP weld and of the first pass at the plug weld. The distance x in Figure 4.9a is measured from the edge of bead 1 of the CJP weld to the edge of the first bead at the plug welds while in Figure 4.9b from the edge of the first bead at the plug weld to the edge of the bead 1 of the CJP weld (the weld bead dimensions are not included in the distance, only the length of the doubler plate between them).

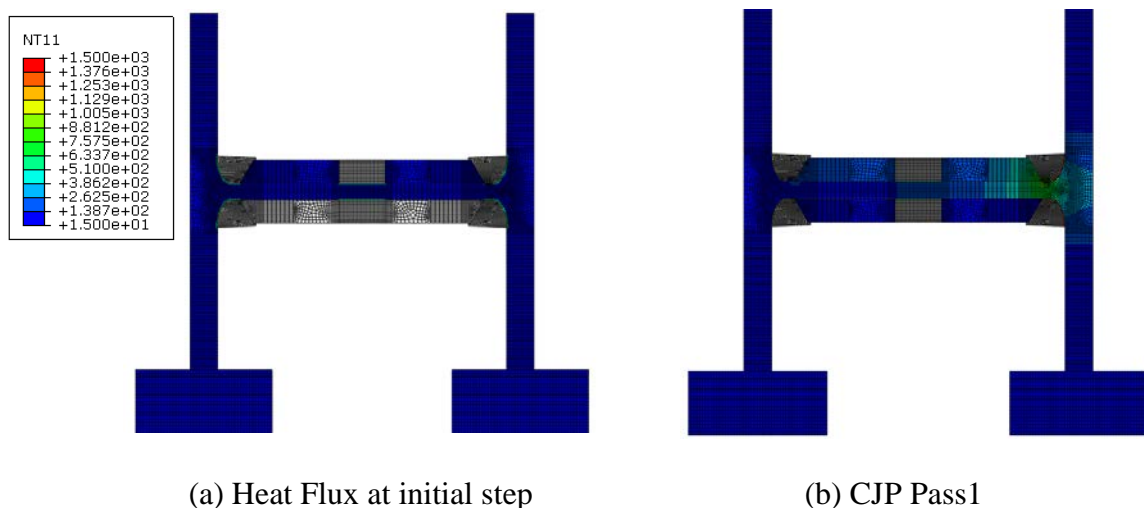
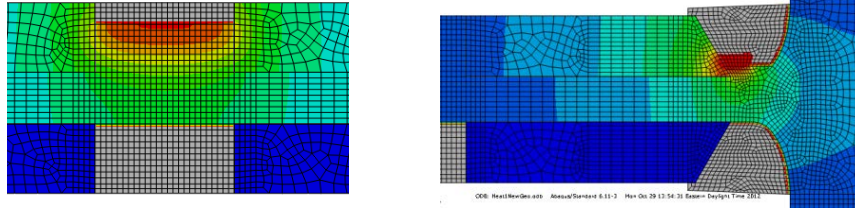


Figure 4.8: Snapshots of the activation of welding beads from heat transfer analysis ($^{\circ}\text{C}$)



(c) Welding Beads

Figure 4.8 (Continued): Snapshots of the activation of welding beads from heat transfer analysis ($^{\circ}\text{C}$)

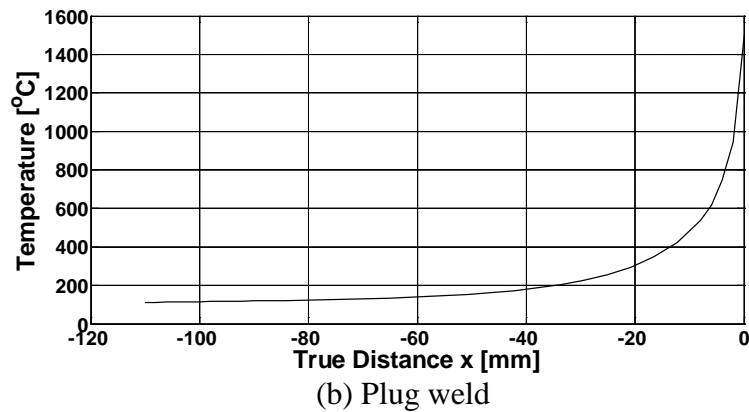
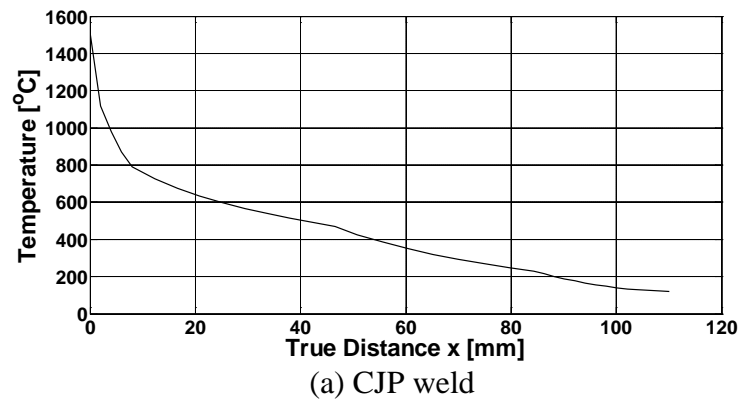


Figure 4.9: Temperature distribution in two different analysis phases

From Figure 4.9, at least 16mm of base metal adjacent to the weld was subjected to high temperature (nearly 600°C); an indication that the assumption for the width of the HAZ was reasonable (Section 4.2). The model demonstrated that each welding pass introduced

high temperatures in the W-shape and thus suggested the appearance of considerable stresses upon cooling.

4.7.2 Stress Analysis Results

Stresses and deformations of the model are presented as they were obtained from the final stress analysis (SA2), where all welding processes on both sides of the column web were completed. Figures 4.10a and b illustrate the deformation in the x axis of the W-shape as the welding was being performed for the 5th left CJP weld pass, while Figures 4.11a and b depict the accompanying stresses, referring to the measured material properties model. The deformation shown (Figures 4.10 and 4.11) has a magnification factor of 3. In addition, the grey shape in the background is the initial model shape that has not experienced any deformation. Both figures demonstrate how the column flange is expected to deform during the welding of the fifth pass (Figures 4.10a, 4.11a) and how it resumes its position during the cooling time (Figures 4.10b, 4.11b). The locally heated location expands and then contracts to its previous state when it is allowed to cool.

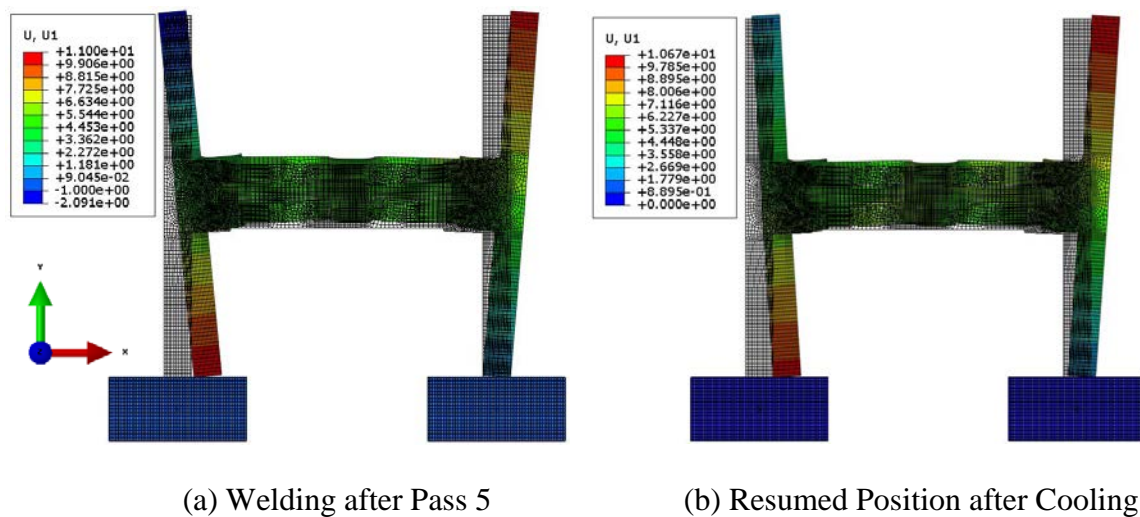


Figure 4.10: Snapshots from stress analysis results for Ux displacements (mm)

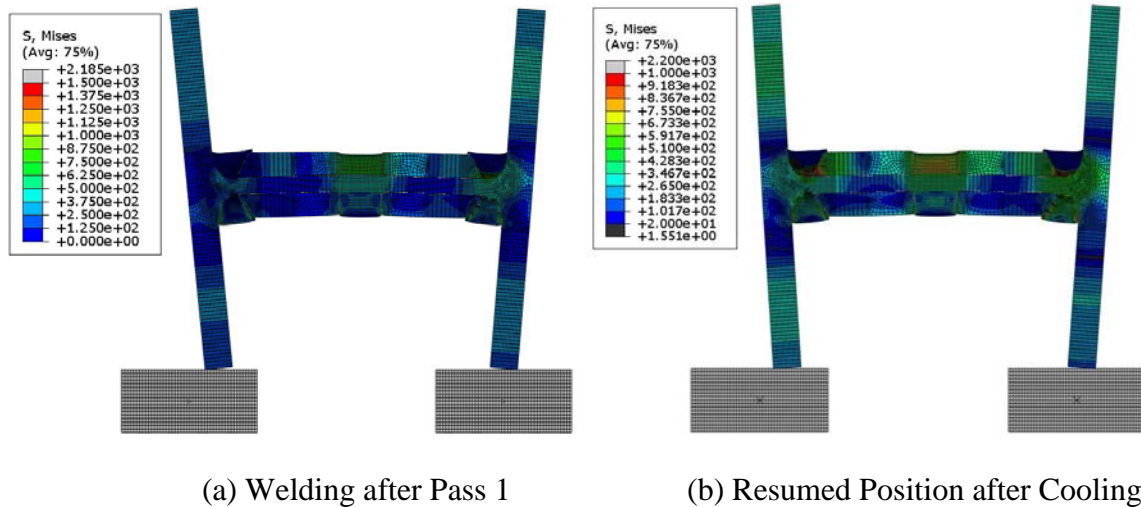
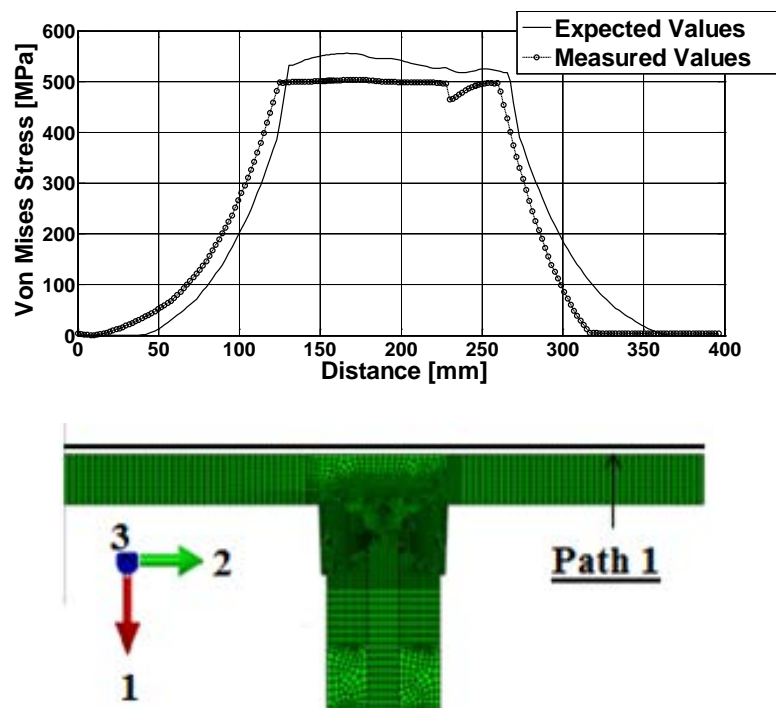


Figure 4.11: Snapshots from stress analysis results for von Mises stresses (MPa)

With each welding pass conducted, due to contact elements inserted, the flange tips are free to translate and rotate with respect to the end supports and the movement of each flange in total involves a rotation with respect to the k-area location where the weld is being performed. When the flange tip from the side being welded expands and moves to the left, the flange tip in the other side moves to the right (referring to one flange). However, the displacement of the flange tips for each flange is not equal leading to tensile and compression stresses developing in the region of the flange on top of the k-area.

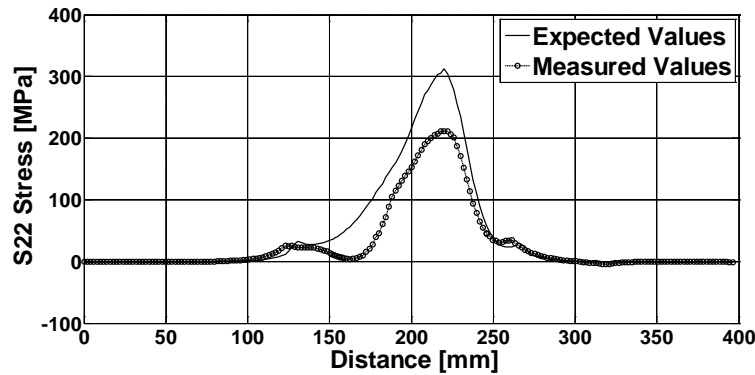
Moreover, from the deformed shapes, it is shown that the contact elements between the web and the doubler plates are activated since the doubler plates are following the deformation of the web. Contact is successfully applied between the rigid bodies and the flange tips too as the welded column assembly deforms on top of the supports. Figures 4.12a, b and c illustrate the von Mises, S22 and S33 stresses in the final step of the SA2 for the top flange region (path) that is the main focus of this research. Results are presented for both the expected and the measured material properties case.

The final step of this analysis exhibited the highest von Mises stresses, which are shown in Figure 4.12a. For all stress types, Figures 4.12a, b and c clearly depict that the difference in the obtained stresses is small when the expected and measured material properties are employed in the FE model of the welded steel assembly. In particular, for the S33 stresses the difference is nearly 8%. For S22 stresses within this analysis step the difference is around 30%. The higher stress values when the expected material properties are used are attributed to the fact that the measured material properties F_y and E inserted were smaller than the expected ones (a difference of 4% for the F_y and 2% for the Young's modulus).

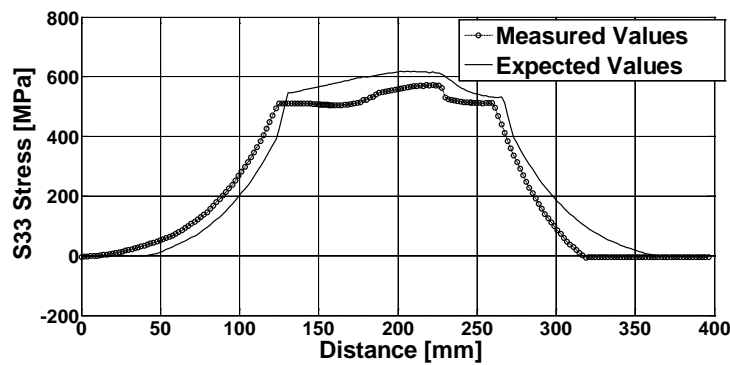


(a) Von Mises stresses of top flange path

Figure 4.12: Results from final step of the stress analysis



(b) S22 stresses of top flange path



(c) S33 stresses of top flange path

Figure 4.12 (Continued): Results from final step of the stress analysis

In Section 4.3 it was indicated that the expected material values and the measured differ in the inelastic region; however the model with the thermal loading applied reaches a maximum strain value of 0.009mm/mm which indicates that the strains did not exceed by much the yield strain. Thus, in Figure 4.12 the differences in stress are based on the difference between the expected (assumed) versus the measured E . If the strains were in the post-yielding region there would be significant difference between the two material cases in the results. In Figure 4.12, the von Mises stresses reach a maximum value of 500MPa to 550MPa, the S22 a value of 200MPa to 300MPa while the S33 stresses reach a maximum value of 600MPa. It should be noted that after the 5 hour cooling period the

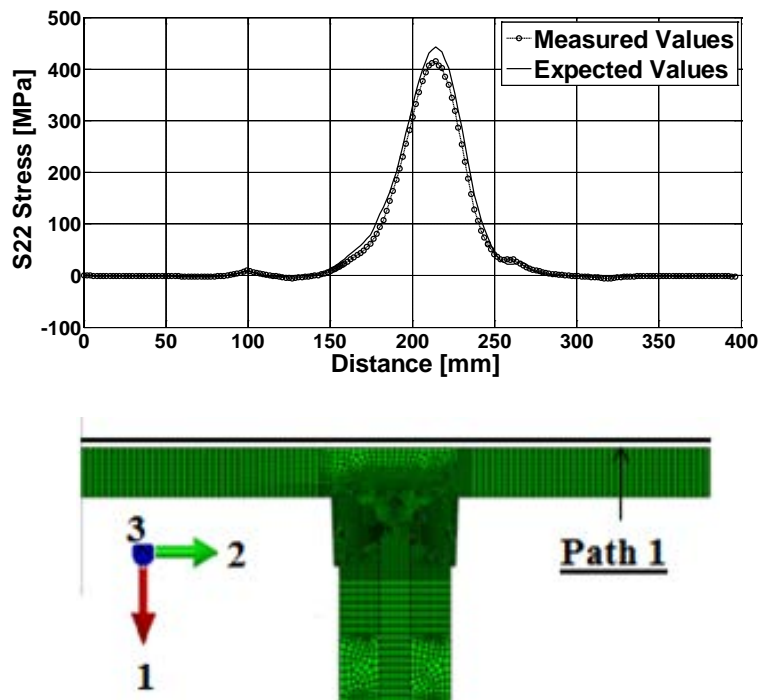
column has reached a room temperature of 15 °C to 20°C; thus, increasing the cooling period would not affect the final stresses indicated in Figure 4.12. This is also verified by the fact that in 2.5hours of cooling time the flange region has already cooled to a temperature of 31°C and the von Mises stresses have a maximum value of 500MPa, as shown after 5hours in Figure 4.12a. Stresses obtained during in-between steps of the analysis are not influenced by the final cooling period. The most important parameter is the intermediate temperature between the conduction of the welding passes. By changing the heat input (meaning the volume of the weld bead) the stresses can vary significantly, as the heat input influences the cooling rate (CWB 2006).

The stresses that constitute the focal point of this thesis are the S22 stresses in the y-y direction. These represent the stress field in the direction perpendicular to the crack found at the top of the flanges. In Figure 4.12b, it is shown that the peak of the S22 stress distribution is at the exact location where the shear tab was welded (at a location approximately 11mm away from the centre of the flange width). This is the location where the crack was detected. Thus, this is a first indication that the residual stresses caused by the welding sequence and process could have led to the crack initiation at this location. This also confirms that the crack likely existed prior to the welding of the shear tabs. The maximum values for the S22 stresses were found in the preheat step of the SA2. Figures 4.13a and b depict the maximum S22 stress distribution in two paths, one along the width at the top of the flange and one through the thickness of the flange.

From Figure 4.13, it is depicted that both FE models produce almost the same S22 stress distribution in this step of the analysis with a small difference at the peak values of 6%.

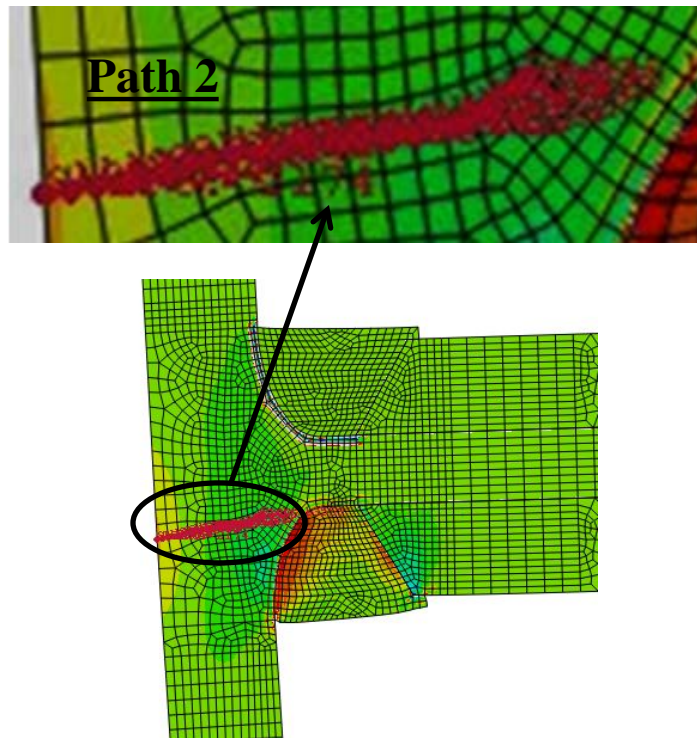
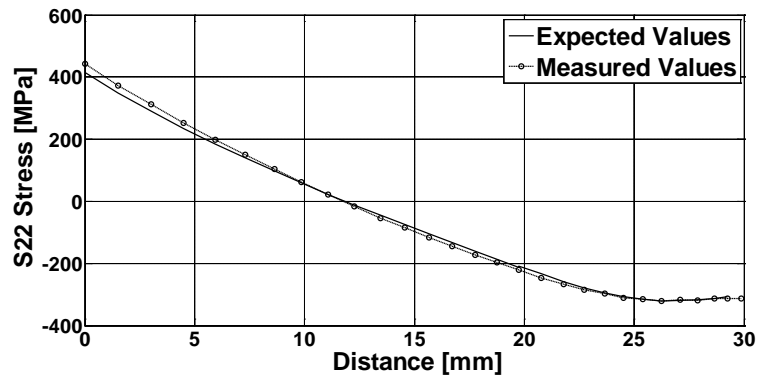
Figure 4.13a illustrates that the S22 stress has an average maximum value for the two

nodes of the first element of path 2, 408MPa when the expected material properties are used in the FE model. The same S22 stress becomes 382MPa when the measured material properties are employed in the FE model. The peak stresses are 443MPa and 415MPa for the two cases, respectively. As already mentioned, this high stress level is located near the location where the shear tab was welded and load path 2 follows approximately the crack path detected in that location (Figure 4.13b).



(a) Maximum S22 stresses along the flange width

Figure 4.13: Maximum S22 stress diagrams in the critical crack region

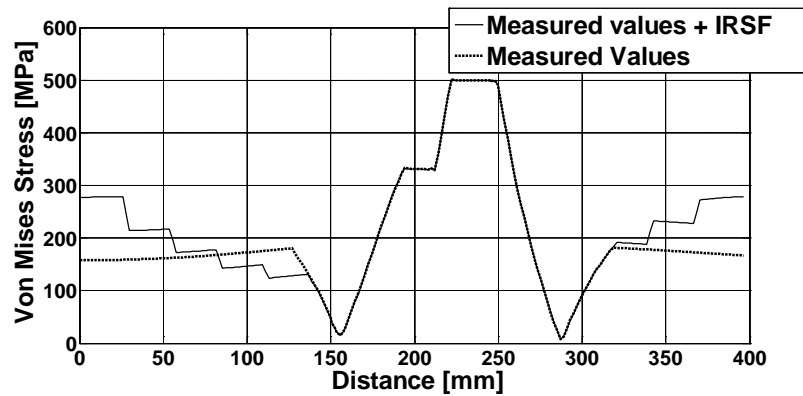


(b) Maximum S22 stresses through the flange thickness

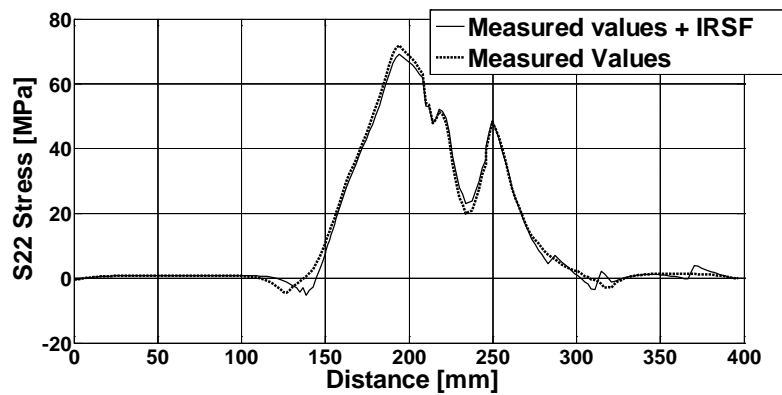
Figure 4.13 (Continued): Maximum S22 stress diagrams in the critical crack region

An important observation concerning this research is the necessity to include the initial residual stresses from member fabrication in the FE model. In the results presented in Figures 4.10 to 4.13, initial residual stresses from rolling of the W-shape column were neglected. However, after the successful completion of the analyses the typical residual stresses were subsequently included in the FE model to examine their level of influence

on the results. In Abaqus, the stresses had to be inserted manually in the input file by assigning average stress values to previously defined element groups. The residual stress distributions were based on past studies discussed in Chapter 2 (Figure 2.15 parabolic distribution by Szalai et al. 2005 and 2.16 by Hubert 1956). Figures 4.14a and b illustrate the S22 and von Mises stresses in the final step of the SA1 with and without the integration of initial residual stresses from fabrication for the experimental material properties case.



(a) Von Mises stress distribution at final step of SA1



(b) S22 stress distribution at final step of SA1

Figure 4.14: Comparison of results for SA1 with and without initial residual stresses from fabrication

The stress distributions shown refer to path 1, as depicted in Figures 4.12 and 4.13. In Figure 4.14a, it is illustrated that the von Mises stresses in the flange region that is of interest for this research were not influenced by the insertion of initial residual stresses from fabrication. The same applies for the S22 stress distribution depicted in Figure 4.13b referring in this case to the whole width of the flange. Therefore, for the particular case of this W-shape section initial stresses from roll forming can be neglected. However, it should be noted that the von Mises stress distribution changes towards the tips of the flange with a maximum difference of 50% of the experimental values without initial residual stresses from fabrication compared to the model case where these stresses were implemented. To this end, if the flange-tips are of interest initial residual stresses from fabrication (IRSF in Figure 4.14) should be included in the modelling process.

4.8 Critical Crack Length

Having obtained all the information concerning the residual S22 stresses caused by the welding procedure, linear elastic fracture mechanics was employed in order to investigate the possibility of crack initiating in the peak S22 stresses location of the welded column assembly. To this end, for the FE model that employed the expected and measured material properties, the critical crack length a_{cr} was calculated as discussed in Section 2.2.6.3.

In particular, based on the crack location the stress intensity factor K_I was calculated using the single notch edge equations (Equation 2.10 and 2.11, Zehnder 2012, Rooke and Cartwright 1976, Tada et al. 2000). The fracture toughness K_{Ic} was calculated using Equations 2.14, 2.15 and 2.19 for the upper and lower shelf energies while the

relationship for in-between temperatures was linear. Calculations were performed for both the expected and measured material properties cases. The average maximum nodal values 408MPa and 382MPa for the elements with the peak stresses were used, as mentioned in Section 4.6.2, Figure 4.13. These high stresses appear in a region of 4 elements around the point where the shear tab was welded (as mentioned in Section 4.7.2). Moreover, the CVN values chosen in order to calculate K_{Ic} refer to 0°C and 21°C temperature based on the shop conditions under which the welding was performed. Tables 4.3 and 4.4 include the results for the a_{cr} for the two material cases.

Table 4.3: Expected material properties case, a_{cr} calculation

Average max stress (MPa)	Temperature (°C)	a_{cr} (mm)
408	0	9
	21	12

Table 4.4: Measured material properties case, a_{cr} calculation

Average max stress (MPa)	Temperature (°C)	a_{cr} (mm)
382	0	9
	21	13

For both material cases, the a_{cr} calculated for 0°C was 9mm while for 21°C was 12mm and 13mm, which indicates that a crack found with minimum crack length 9mm or 12/13mm, for the two temperatures discussed, can lead to fracture. As mentioned in Chapter 3, the depth of the crack found was 12.7mm. Therefore, it is demonstrated that fracture is likely to occur for the welded column assembly. The reason is that at 15°C (i.e., temperature at the fabrication shop during welding) the a_{cr} is less than 12.7mm.

4.9 Summary

In this chapter the FE modelling approach developed in this research in order to evaluate the current welding sequence used in practice for high strength steel sections was presented. The welding procedures that took place on the beam-to-column connection location were simulated through the conduction of heat transfer and stress analysis. Stress distributions were obtained for the critical flange region with emphasis on the S22 stresses, as the stress field being perpendicular to the crack found. Linear elastic fracture mechanics was employed to calculate the critical crack length based on the S22 stresses in order to examine the possibility for fracture. From the results, the following points should be highlighted:

- The uncoupled heat transfer and stress analysis can successfully simulate the welding procedures of the welded column assembly discussed in this thesis.
- The initially assumed expected stress-strain curve was found to vary significantly from the measured ones in the inelastic region (expected strain hardening 3% versus measured 0.7%). However, the finite element modelling approach proposed in this thesis with the use of expected material properties led to stress distributions similar with those obtained with the measured material properties. This is because the finite element model exhibited strains that did not exceed much the yield strain. The use of a more realistic initial expected material curve (i.e. with a strain hardening of 1%) could provide stresses close to those obtained using measured properties even in the case of strains in the post-yielding region.
- The S22 stress distributions obtained from the FE model indicate that the maximum stresses are concentrated in the critical flange region where the cracks were found.

Calculation of the critical crack length a_{cr} using linear elastic fracture mechanics confirmed that fracture due to welding procedures is likely to occur in the welded column assembly.

- Initial residual stresses from rolling fabrication of the W-shape column have little influence on the stress distribution resulting from the welding procedure for the flange region under investigation.

CHAPTER 5

Summary and Conclusions

The primary goal of this thesis was to evaluate the applicability of the current welding codes (AWS 2005, D1.8/D1.8M 2009, D1.1/D1.1M 2010 and CSA W59-03 2008) and welding techniques used in practice for steel subassemblies composed of 450 MPA (65 ksi) grade steel columns. To this end, a finite element (FE) model was developed capable of simulating these welding procedures in order to investigate their influence on the formation of cracks. A case study was examined, which involved cracking that occurred during the fabrication of prequalified beam-to-column connections built with welded doubler plates on A913 Gr. 65 (i.e., nominal yield stress, $F_y = 450\text{MPa}$) W-shape steel columns. Cracks were found in the flanges of the steel column near the flange to web junction, after misplaced shear tabs had been removed. Based on a subsequent evaluation using the FE model, recommendations for future work are provided so that cracking related to the welding induced residual stresses during fabrication of similar subassemblies can be avoided in the future.

5.1 Material Characterisation: Testing Program

An extended material characterisation program was conducted involving Charpy V-Notch (CVN) testing, coupon tensile testing and scanning electron microscopy (SEM) of the case study W-shape column provided by the industrial partner of this project.

➤ **Charpy V-Notch Tests**

A total of 138 CVN samples from the W-Shape column were tested based on the ASTM A370 (2007a) Standard guidelines. The results were evaluated using the impact energy versus temperature theoretical curve developed for the specific material of the column under investigation. In addition, the empirical approach discussed in the ASTM A370 (2007a) Standard for shear surface percentage and lateral expansion calculation was used in the fracture surface of each specimen. The findings were categorized based on the CVN samples representing different location, thickness and orientation in the W-Shape section over a range of temperatures.

➤ **Scanning Electron Microscopy**

Scanning electron microscopy, including secondary electrons (SE), backscattered electrons (BSE) and energy dispersive spectroscopy (EDS) examination techniques, was used to further describe the steel material of the W-Shape column. With the first two methods (SE and BSE) the fully brittle and fully ductile fracture surface of two CVN specimens was examined, while EDS was used on a prepared and polished surface in order to verify the chemical composition of the steel.

➤ **Tensile Coupon Tests**

Tensile coupon testing was performed for 22 standard coupons, 23 small coupons and 3 special k-area coupons taken from the W-shape column. The small and standard coupons were obtained from different locations, thicknesses and orientations in the column, and were designed based on the specimen dimensions of the ASTM A370 (2007a) Standard. The special k-area coupons were cut from the grain-long orientation of the steel column.

The main conclusions from the testing program are summarized as follows:

- The ASTM A913 (2007a) Standard provides a CVN value of 54 Joules (40 ft.lb) at 21°C requirement for the 450 MPa steel. The measured CVN values for the long orientation samples, which are of interest for this research, were above this value; therefore the material under investigation met this Standard's requirement. In addition, the CVN values of the long orientation samples followed the theoretical curve constructed based on prior research studies.
- Through the use of the EDS method, the chemical composition of the material was verified, emphasizing the low carbon content (0.06wt.% carbon content). Examination of the fracture surface with SE and BSE revealed transgranular fracture with cleavage facets and purely dimpled fracture surface for the fully brittle and fully ductile fractured CVN specimens, respectively.
- The tensile tests showed acceptable stress, strain and Young's modulus values for the high strength steel in question, based on the nominal values given in the ASTM A913 (2007b) Standard.
- The W-shape column material satisfied the ASTM A913 requirements. Therefore, it was considered not to be the cause of the cracking in the particular case study under investigation. This implies that the welding process during fabrication was the main cause for the observed cracks in the steel column.

5.2 Finite Element Modelling of Welding Procedures on High Strength Steel W-shape Columns

An advanced FE modelling approach capable of simulating welding procedures performed on high strength steel W-shape columns was developed. Complete joint penetration and plug welds were conducted on the web of a column section, connecting it to a thick doubler plate as part of a prequalified connection. The input modelling parameters of the finite element model were based on the welding sequence currently used in practice. This information was obtained from the industrial partner of this project. Initially, the expected material properties of the steel material of the W-shape column, the weld and the doubler plates were incorporated in the FE model. The change of material properties with the increase of temperature was defined according to Eurocode 3 (2005). However, after the completion of the testing program, the input modeling parameters related to the steel material of the W-shape column were updated using the measured material properties. The temperature dependent material properties of the steel were also updated based on research of Outinen et al. (2000). The main findings are summarized as follows:

- The uncoupled heat transfer and stress analysis described in this thesis can successfully simulate the welding procedures under consideration.
- The expected material stress-strain curve initially inserted in the FE model described in this thesis was close to the measured one in the elastic region but exhibited significant difference in the inelastic region. However, the strain values found did not exceed much the yield strain; thus the model provided similar results for the two

material cases. A better initial selection of strain hardening for the expected stress-strain curve (i.e. 1%) could lead to close results for the expected and measured material properties in the case of severe post-yielding strains. This indicates that, assuming that the steel material meets the AWS/ASTM requirements, “simple” finite element models with only expected material properties may be used for simulation of welding procedures of high strength steel W-shapes.

- Initial residual stresses from rolling fabrication of the column itself had little influence on the stress distribution due to the welding procedure for the flange region that was investigated.
- The stress distributions obtained from the FE model indicate that the maximum stresses are concentrated in the critical flange region where the cracks were found. Calculation of the critical crack length using linear elastic fracture mechanics confirmed that the likelihood of crack initiation in the location where the shear tabs were welded is large. Thus, the welding sequence and the current welding techniques used were likely the source of the cracking for the case study under investigation. This result underlines the necessity to improve the current welding techniques and make recommendations so that this type of fabrication failure can be avoided.

5.3 Suggestions for Future Work

This research raised important questions regarding the welding techniques used today in steel subassemblies that utilize high strength steel columns. The following projects emerge from the findings of this research:

- Investigation of an alternative welding sequence, which allows the even distribution of residual stresses between both sides of the web during the conduction of the weld, as this can prove to be the key in avoiding crack initiation.
- Conduction of a parametric study in order to assess the influence of the material used for the separate components of the high strength steel subassembly and of every welding parameter on the resulting residual stresses.
- Development of a more advanced modelling approach that explicitly simulates fracture for the case of fairly small crack lengths.
- Accordingly, for every welding process, the development of a 3D model should be employed, if necessary in order to take into consideration the welding length effect.

List of References

ABAQUS FEA/CAE (2011), (2010), Dassault Systemes Simulia Corp., Providence, RI, USA, @ Dassault Systèmes, Version 6.11-3.

Allen, N. P., Rees, W. P., et al. (1953), “Tensile and impact properties of high purity iron-carbon and iron-carbon- manganese alloys of low carbon content,” *Journal of Iron and Steel Institute*, 174: 108-120.

Aloraiera, A.S., Joshib, S., Asadic, M., Alenac, R.G. and Goldakd, J.A. (2010), “Microstructural and hardness modeling: Effect of multiple bead deposition in temper bead welding technique,” *International Journal of Energy & Technology*, 2(16): 1-11.

Aloraier, A., Ibrahim, R. and Thomson P. (2006), “FCAW process to avoid the use of post weld heat treatment,” *International Journal of Pressure Vessels and Piping*, 83: 394-398.

Alpsten, G.A. (1968), “Thermal residual stresses in hot rolled steel members” Fritz Engineering Laboratory *Report No. 337.3*, University of Lehigh, Bethlehem, Pennsylvania.

AISC (2010a), “Specification for structural steel buildings”, AISC 360-10, American Institute of Steel Construction, Chicago, Illinois.

AISC (2010b), “Prequalified Connections for Special and Intermediate Steel Moment Frames for Seismic Applications, incl. Supplement No. 1”, AISC 358-10, American Institute of Steel Construction, Chicago, Illinois.

API (2010), “Welding processes, inspection and metallurgy,” American Petroleum Institute.

ASTM (2007a), “A370 – 07a Standard test methods and definitions for mechanical testing of steel products,” American Society for Testing and Materials, West Conshohocken, PA.

ASTM (2009a), “A514/A514M-05 Standard specification for high-yield-strength, quenched and tempered alloy steel plate, suitable for welding,” American Society for Testing and Materials, West Conshohocken, PA.

ASTM (2010), “A517 Standard specification for pressure vessel plates, alloy steel, high-strength, quenched, tempered,” American Society for Testing and Materials, West Conshohocken, PA.

ASTM (2009b), “A709/709M Specification for structural steel for bridges,” American Society for Testing and Materials, West Conshohocken, PA.

ASTM (2008), “A63/A36M Standard specification for carbon structural steel,” American Society for Testing and Materials, West Conshohocken, PA.

ASTM (2007b), “A913/A913M Specification for high-strength low-alloy steel shapes of structural quality, produced by quenching and self-tempering process (QST),” American Society for Testing and Materials, West Conshohocken, PA.

ASTM (2007c), “A572 Specification for high-strength low-alloy columbium-vanadium structural steel,” American Society for Testing and Materials, West Conshohocken, PA.

ASTM (2006a), “A992 Specification for structural steel shapes,” American Society for Testing and Materials, West Conshohocken, PA.

AWS (2010), “D1.1/D1.1M Structural welding code-Steel,” American Welding Society, Miami, FL.

AWS (2009), “D1.8/D1.8M Structural welding code-Seismic supplement,” American Welding Society, Miami, FL.

AWS (2005), “A5.20 Specification for carbon steel electrodes for flux cored arc welding,” American Welding Society, Miami, FL.

Banerjee, K. (2013), “Role of base metal microstructure on tensile properties and weldability of simulated of simulated annealed advanced high strength steels,” *International Journal of Metallurgical Engineering* 2(1): 100-110.

Barsom, J.M. and Rolfe, S.T. (1970), “Correlations between KIC and Charpy V-Notch test results in the transition-temperature range,” *Impact Testing of Metals*, ASTM STP 466, American Society for Testing and Materials, Philadelphia, 281-302.

Barsom, J.M. and Rolfe, S.T. (1987), “*Fracture and fatigue control in structures: Applications of fracture mechanics*,” Prentice-Hall, Englewood Cliffs, N.J., XX: 628.

Bletzacker, R.W. (1966), “Effect of structural restraint on the fire resistance of protected steel beam floor and roof assemblies,” Building Research Laboratory *Report EES 246/266*, Engineering Experiment Station, Ohio State University, Columbus, Ohio.

Blodgett, O.W., Funderbur, R.S., Miller, D.K. and Quintana, M. (1999), “Fabricator’s and Erector’s guide to welded steel construction,” The James F. Lincoln Arc Welding Foundation, USA.

Bjorhovde, R. (1988), “Columns: from theory to practice,” *Engineering Journal*, American Institute of Steel Construction AISC 25(1): 21–34.

Bjorhovde, R. (2006), “Cold bending of wide-flange shapes for construction,” *Engineering Journal*, American Institute of Steel Construction AISC 43(4): 271–286.

Brickstad, B. and Josefson, B.I. (1998), “A parametric study of residual stresses in multi-pass butt welded stainless steel pipes,” *Journal of Pressure Vessel and Piping* 75: 11-25.

Brockenbrough, R. L. (1992), “Material Behavior,” *Constructional steel design: An international guide*, (P. J. Dowling, J. E. Harding, and R. Bjorhovde, eds.), Elsevier Applied Science, London, Chaps. 1.1 and 1.2.

Brockenbrough, R. L. and Merritt, F.S. (1999), “Properties of structural steels and effects of steelmaking and fabrication,” *Structural Steel Designer’s Handbook*, New York: McGraw-Hill.

Brozzetti, J., Alpsten, G.A., and Tall, L. (1970a), “Residual stresses in a heavy rolled shape 14WF730,” Fritz Eng. Lab. *Rep. No. 337.1*, Lehigh University, Bethlehem, PA, Jan.

Brozzetti, J., Alpsten, G.A., and Tall, L. (1970b), "Welding parameters, thick plates and column strength," Fritz Eng. Lab. *Rep. No. 337.21*, Lehigh University, Bethlehem, PA, Feb.

BS EN (1993), "Charpy impact test on metallic materials - Part 2: Method for the verification of impact testing machines," London.

Burns, K. W. and Pickering, F. B. (1964), "Deformation and fracture of ferrite-pearlite structures," *Journal of Iron and Steel Institute* 202: 899-906.

Cengel, Yunus A. (2007), "Heat & mass transfer: a practical approach," Tata McGraw-Hill Education.

Chandel, R. S. (1990), "Electrode melting and plate melting efficiencies of submerged arc welding and gas metal arc welding," *Materials Science and Technology*, 6: 772-777.

Chang, K. and Lee, C. (2009), "Finite element analysis of the residual stresses in T-joint fillet welds made of similar and dissimilar steels," *The International Journal of Advanced Manufacturing Technology*, 41: 250-258.

Coffey, J.M. and Whittle, M.J. (1981), "Non-destructive testing: its relation to fracture mechanics and component design," *Philosophical Transactions of the Royal Society*, London A 299: 93-110.

CSA (2008), "W59-03 Welded steel construction (Metal Arc Welding)", Canadian Standards Association, Mississauga, Ontario.

CSA (2009), "S16 Design of steel structures," Canadian Standards Association, Mississauga (Ontario, Canada).

CWB (2006), "Welding for design engineers," Canadian Welding Bureau, Mississauga, ON.

DVN (2012), "Non-destructive testing," *Classification Notes No. 7*, Det Norske Veritas AS.

Eurocode 3 (2005), “Design of steel structures Part 1-2: General rules — Structural fire design”.

Fisher, J.W. and Penser, A.W. (1987), “Experience with use of heavy W-shapes in tension,” *Engineering Journal*, AISC 24 (2): 63-77.

Funderburk, R.S. (1999), “Key concepts in welding engineering,” *Welding Innovation* XIV(2).

Gunaraj, V. and Murugan, N. (2002), “Prediction of heat-affected zone characteristics in submerged arc welding of structural steel pipes,” *Welding Journal*, NY, 81(3): 45-s.

Hubert, A.W. (1956), “Summary of important findings on residual stress and compressive properties of rolled WF columns,” Fritz Engineering Laboratory, *Report No. 220A.23*, University of Lehigh.

James, M.N. (2010), “Residual stress influences in mechanical engineering,” *XVIII Congreso Nacional de Ingeniería Mecánica*, Ciudad Real, Spain.

Jefferson, T.B. and Woods, G. (1990), “Metals and how to weld them,” The James F. Lincoln Arc Welding Foundation, Ohio.

Jefferson’s welding encyclopedia, (1997). 18th edition, American Welding Society.

Jin, J., King, L.C., Ping, C.S. and Shan, Z.M. (2011), “Numerical modelling of the residual stress distributions in high strength steel plate-to-plate T and Y joint,” *7th International Conference on Steel & Aluminium Structures*, Kuching, Sarawak, Malaysia.

Johnson, A.A. and Storey, R.J. (2008), “The effect of carbon on the Charpy V-Notch ductile brittle transition curves,” *ICASI & CCATM’2008 International Conference and Exhibition on Analysis & Testing of Materials*, Beijing, China.

Klopper, J.J., Laubscher, R.F., Steuwer, A. and James, M.N., (2011), “An investigation into the effect of weld technique on the residual stress distribution of 3CR12 (DIN 1.4003) built-up structural sections,” *Proceedings of the Institution of Mechanical Engineers, Part L: Journal of Materials Design and Applications* SAGE 225:123.

Lee, C.S., Chandel, R.S. and Seow, H.P. (2007), “Effect of welding parameters on the size of heat affected zone of submerged arc welding,” *Materials and Manufacturing Processes*, Taylor & Francis, London, England.

Ma, N.X., Ueda, Y., Murakawa, H. and Madea, H. (1995), “FEM analysis of 3D welding residual stresses and angular distortion in T-type fillet welds,” *Transactions of the Japan Welding Research Institute*, 24(2): 115–122.

Maddox, S.J. (1994), “Applying fitness-for-purpose concepts to the fatigue assessment of welded joints,” *The International Conference on Fatigue*, Toronto, Ontario, Canada, 72–81.

Mark, A.F., Francis, J.A., Dai, H., Turski, M., Hurrell, P.R., Bate, S.K., Kornmeier, J.R. and Withers, P.J. (2012), “On the evolution of local material properties and residual stress in a three-pass SA508 steel weld,” *SciVerse Science Direct*, 60: 3268-3278.

Nikolaidou, V., Rogers, C.A. and Lignos, D.G. (2013), “Finite element modeling of welding procedures in high strength W-shapes,” *Proceedings Canadian Society of Civil Engineering (CSCE), 3rd Specialty Conference on Material Engineering and Applied Mechanics*, Montreal, Quebec, 80.

Nyashin, Y.I. (1982), “Examination of residual stresses in hot-rolled flange beams and their effect on beam stability,” *Problemy Prochnosti*, Plenum Publishing Corporation, 2: 111-114.

Okazaki, T., Fukami, H., Ohata, M. and Nakashima, M. (2011), “Japanese research on super-high strength structural steel,” *North American Steel Construction Conference*, Proceedings, Pittsburgh, Pennsylvania, N12.

Outinen, J., and Mäkeläinen, P. (2004), “Mechanical properties of structural steel at elevated temperatures and after cooling down,” *Fire and materials* 28(2-4):237-251.

Outinen, J., Kaitila, O., Mäkeläinen, P. (2000), “A study for the development of the design of steel structures in fire conditions,” *1st International Workshop of Structures in Fire*, Proceedings, Copenhagen, Denmark, 267-281.

Pilipenko, A. (2001), “Computer simulation of residual stress and distortion of thick plates in multi electrode submerged arc welding. Their mitigation techniques,” *Ph.D. Thesis*, Department of Machine Design and Materials Technology Norwegian University of Science and Technology, N-7491 Trondheim, Norway.

Ramberg, W., and Osgood, W. R. (1943), “Description of stress-strain curves by three parameters,” *Technical Note No. 902*, National Advisory Committee for Aeronautics, Washington DC.

Rooke, D.P. and Cartwright, D.J. (1976), “*Compendium of stress intensity factors*,” HMSO Ministry of Defence. Procurement Executive, London, 1:12.

Roylance, D. (2001), “Stress-strain curves,” Department of Materials Science and Engineering, Massachusetts Institute of Technology study, Cambridge, MA 02139.

Siddique, M., Abid, M., Junejo, H.F. and Mufti, R.A. (2005), “3-D finite element simulation of welding residual stresses in pipe-flange joints: effect of welding parameters,” *Materials Science Forum*, 490–491:79–84.

Standard SFS-EN 10 113-3 (1993), “Hot rolled products in weldable fine grade structural steels. Delivery conditions for thermomechanical rolled steels,” (in Finnish), Helsinki.

Standard SFS-EN 10 025 (1993), “Hot-rolled products of non-alloy structural steel,” (in Finnish), Helsinki.

Standard SFS-EN 10 147 (1992), “Continuously hot-dip zinc coated structural steel sheet and strip. Technical delivery conditions,” (in Finnish), Helsinki.

Standard SFS-EN 10219-1 (1998), “Cold formed welded structural hollow sections of non-alloy and fine grain steels. Parts 1-2,” (in Finnish), Helsinki.

Suwan, S. (2002), “Analysis of structural plate mechanical properties: Statistical variability and implications in structural reliability,” *M.Sc. Thesis*, University of Texas, Austin.

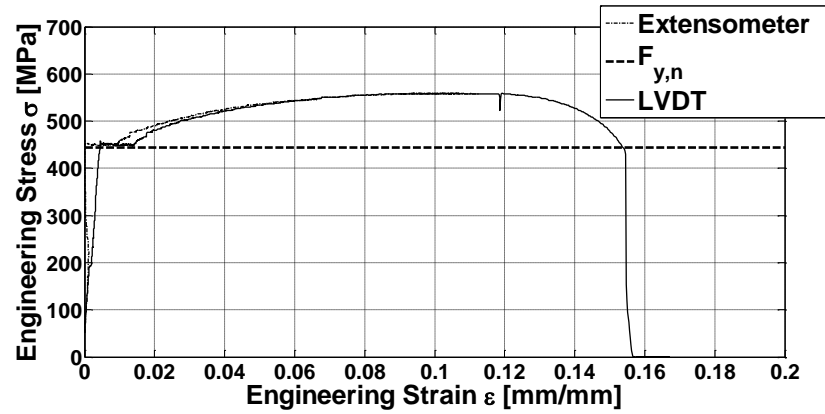
- Szalai, J. and Papp, F. (2005), "A new residual stress distribution for hot-rolled I-shaped sections," *Journal of Constructional Steel Research*, 61: 845–861.
- Tada, H., Paris, P.C., Irwin, G.R. and Tada, H. (2000), "The stress analysis of cracks handbook," American Society of Mechanical Engineers press, NY, 130.
- Tall, L. (1964), "Recent developments in the study of column behavior," *Journal of Institute of Engineers Australia*, 36(12): 319–333.
- Teng, T.L., Fung, C.P., Chang, P.H. and Yang, W.C. (2001), "Analysis of residual stresses and distortions in T-joint fillet welds," *International Journal of Pressure Vessel and Piping*, 78: 523-538.
- U.S. Army Corps of Engineers (2001), "Chapter 7 - Examples and material standards," *Engineering and Design Inspection, Evaluation and Repair of Hydraulic Steel Structures*, Washington, DC 20314-1000.
- Vakili-Tahami, F., Zehsaz, M., Saeimi-Sadigh, M. and Seyedreihani (2010), "Finite element analysis of the in-service-welding of T joint pipe connections," *European Journal of Scientific Research*, ISSN, 1450-216X, 40(4): 557-568.
- Vakili-Tahami, F., Daei-Sorkhabi, A.H., Saeimi-S, M.A. and Homayounfar, A. (2008), "3D finite element analysis of the residual stresses in butt-welded plates with modeling of the electrode-movement," *Journal of Zhejiang University Science A*, 10(1): 37-43.
- Vander Voort, G.F. (1984), "Metallography: principles and practice," American Society for Metals (ASM International).
- Whittaker, V.N. (1972), "How to use fracture mechanics to assist in drawing up realistic acceptance standards," *Fracture mechanics series 5, Non-Destructive Testing*, Department of Metallurgy, University of Aston, Birmingham, UK.
- Zehnder, A.T. (2012), "Fracture mechanics," Springer London Dordrecht Heidelberg New York.

Ziemian (2009), “Centrally loaded columns,” *Guide to stability design criteria for metal structures*, John Wiley & Sons, Hoboken, New Jersey, USA, 23-128.

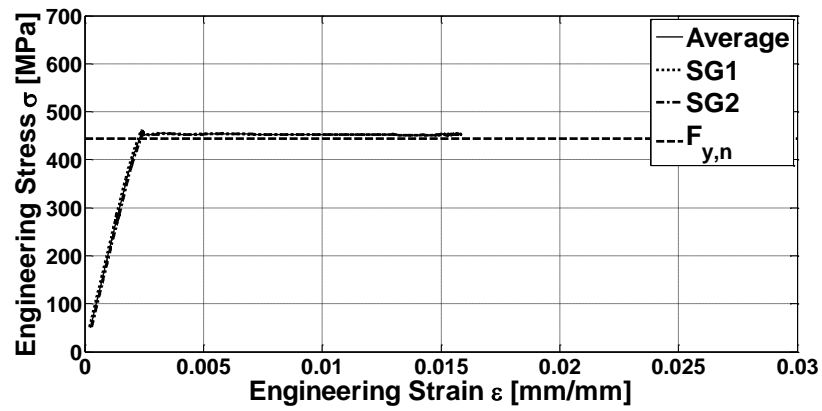
APPENDIX A

Summary of Tensile Coupon Testing Results

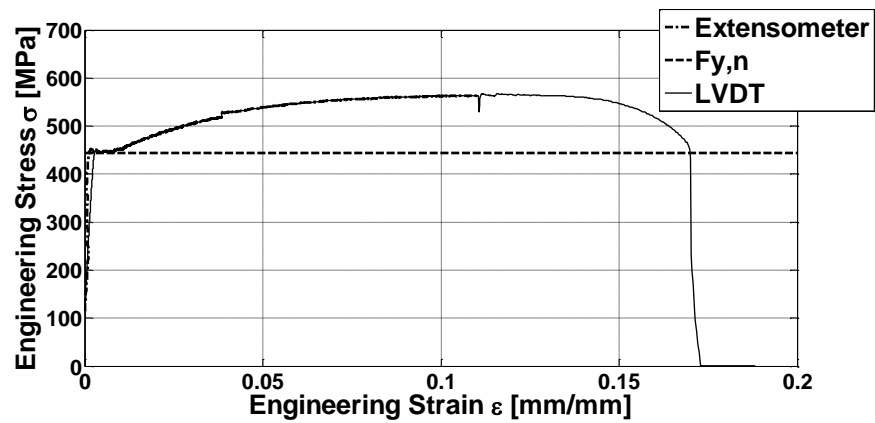
This appendix includes the results obtained from the tensile coupon testing of 22 standard, 23 small and 3 k-area coupons discussed in Chapter 3 of this thesis. Engineering stress-strain curves are included that give information about the mechanical properties of the steel material of the A913 Gr. 65 steel column (Chapter 3). An extensive discussion and evaluation of the results is presented in Chapters 3. Tables 3.7, 3.8 and 3.9 include all the information about the coupon names and locations. Figures 3.21, 3.22 and 3.23 illustrate the coupon locations in the column section and plan view while Figure 3.20 shows the coupon dimensions. Figure A.1, A.2 and A.3 illustrate the engineering stress-strain graphs for the standard, k-area and small coupons, respectively. Tables A.1, A.2 and A.3 summarize all the values obtained from the engineering stress-strain curves for all the specimens. In the stress-strain curves shown SG1 and SG2 refer to the strain gauge measurements. The average value from the two strain gauges is also shown in these figures. The nominal yield stress $F_{y,n}$ of A913 Gr. 65 material (ASTM A931 2007b) is superimposed in the same figures for comparison purposes. Graphs depicting strain gauge values are included for the 1st specimen of each group as mentioned in Chapter 3.



(a) Specimen F11

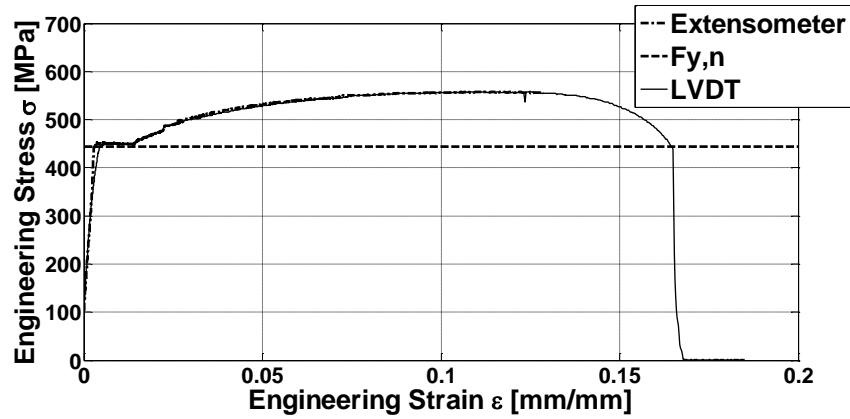


(b) Specimen F11: strain gauge measurements

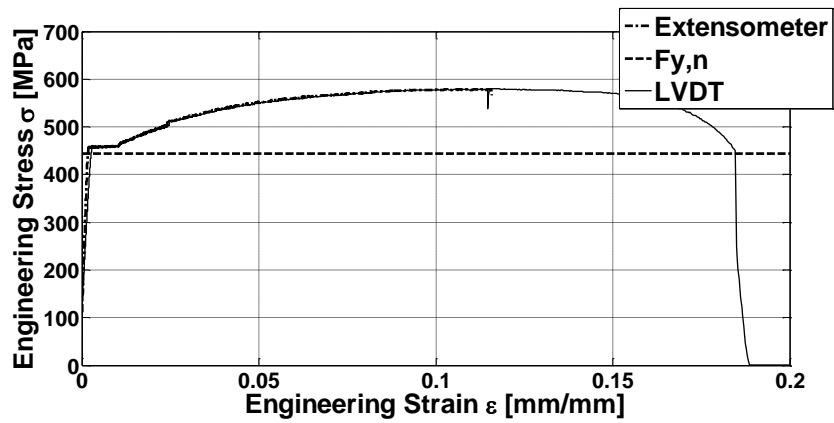


(c) Specimen F12

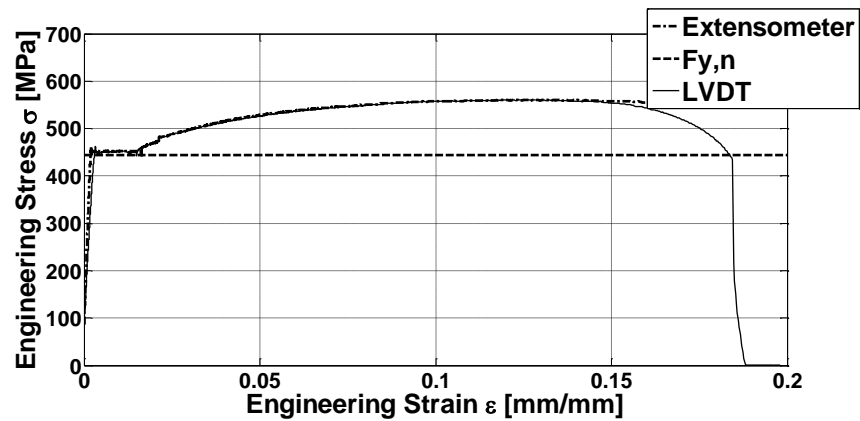
Figure A.1: Standard coupon test results



(d) Specimen F13

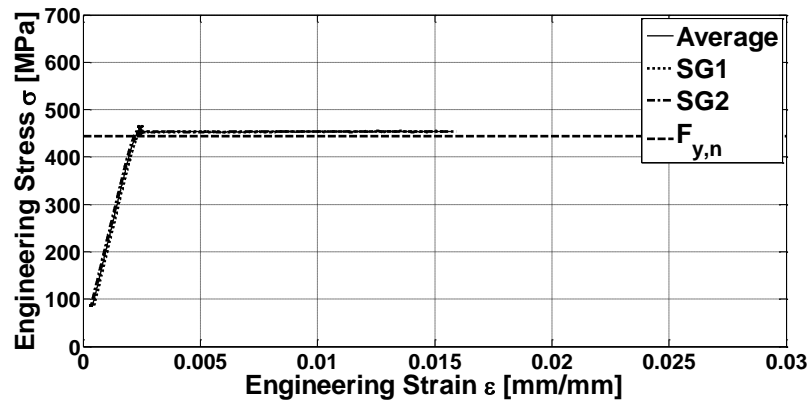


(e) Specimen F14

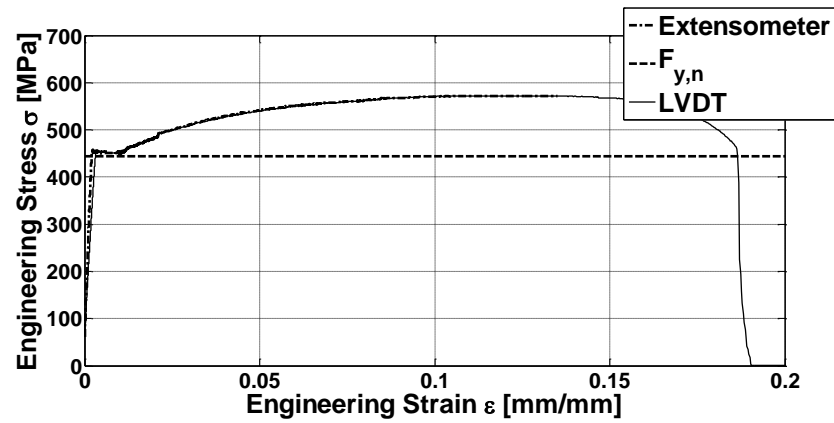


(f) Specimen F21

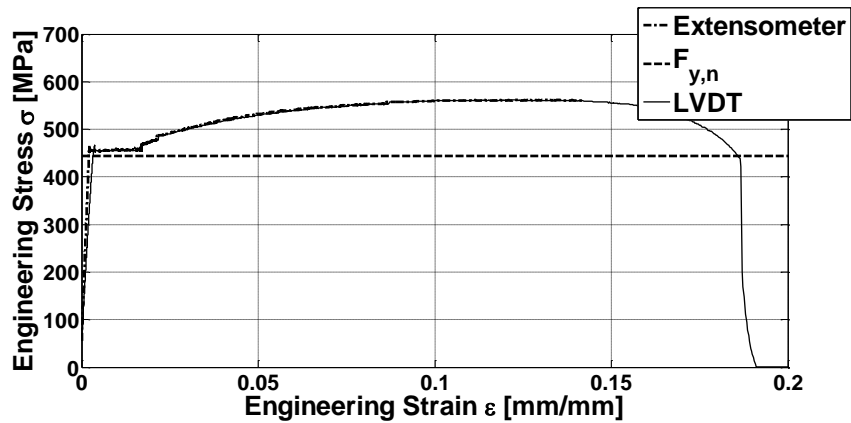
Figure A.1 (Continued): Standard coupon test results



(g) Specimen F21: strain gauge measurements

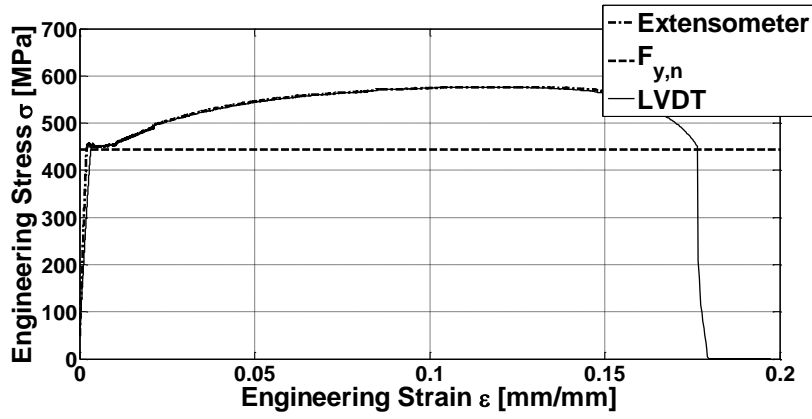


(h) Specimen F22

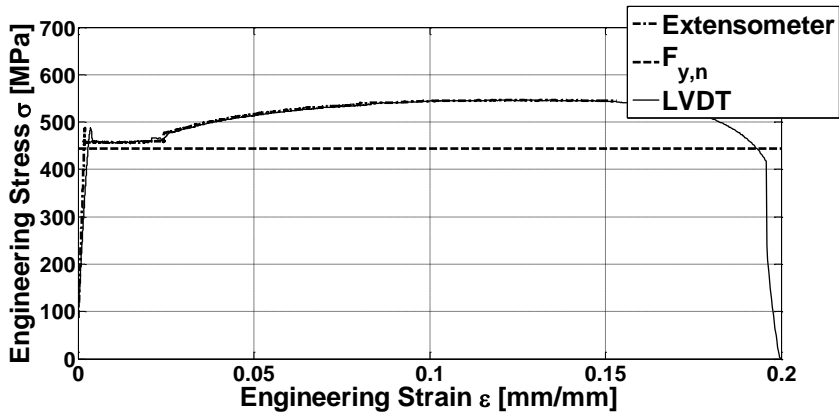


(i) Specimen F23

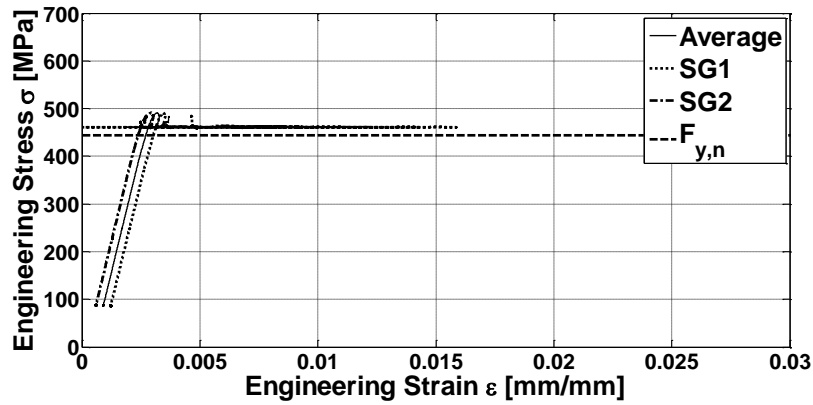
Figure A.1 (Continued): Standard coupon test results



(j) Specimen F24

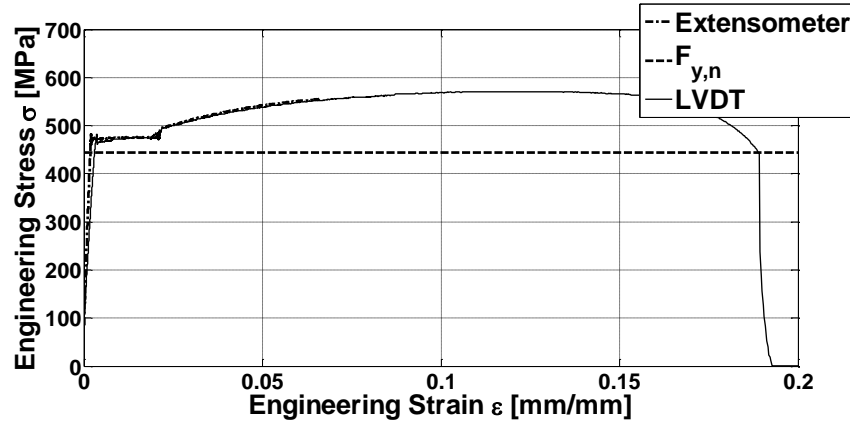


(k) Specimen F31

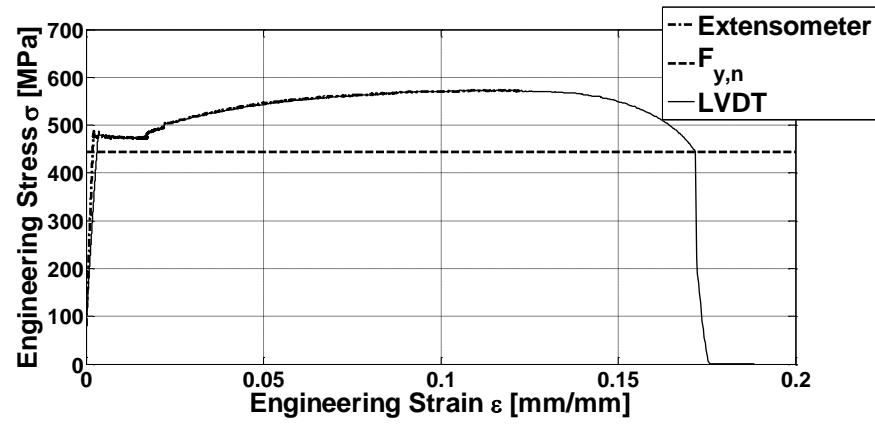


(l) Specimen F31: strain gauge measurements

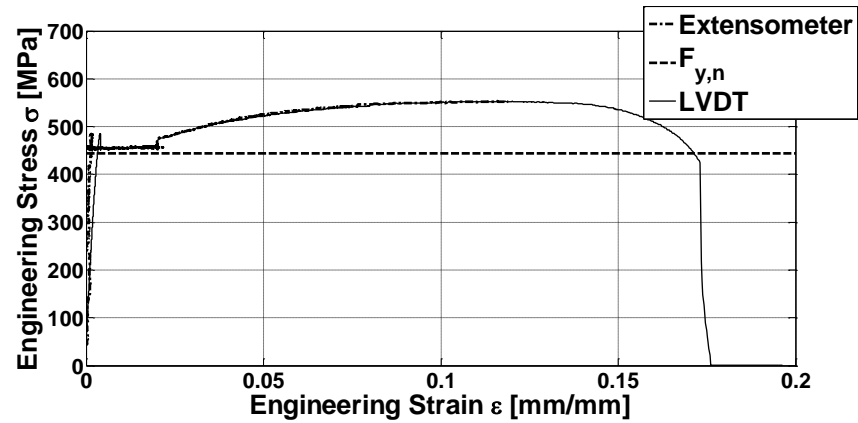
Figure A.1 (Continued): Standard coupon test results



(m) Specimen F32

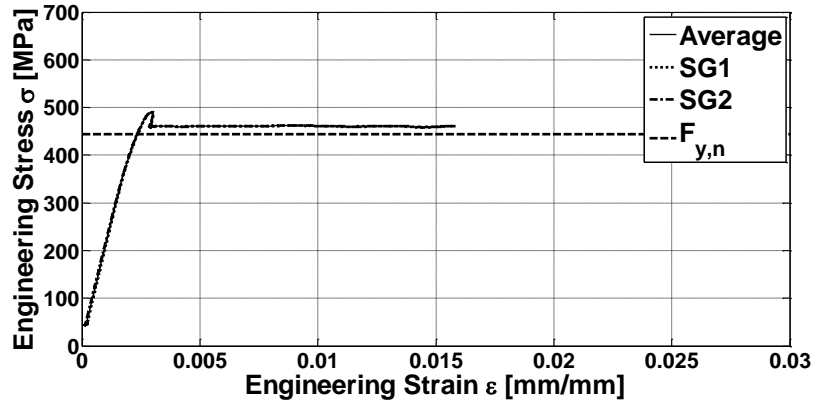


(n) Specimen F33

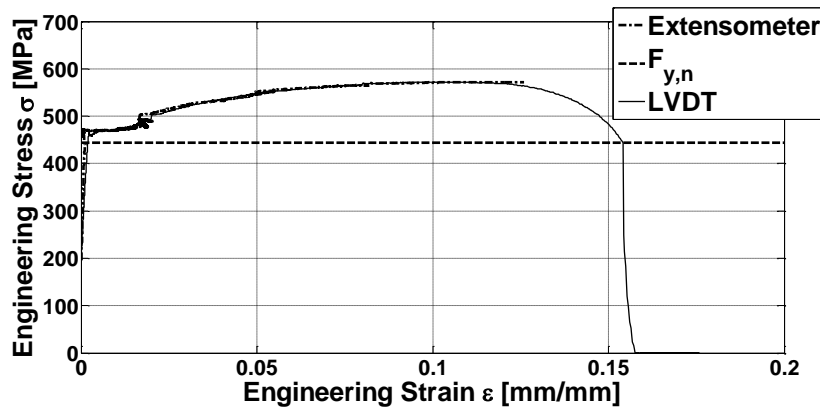


(o) Specimen F41

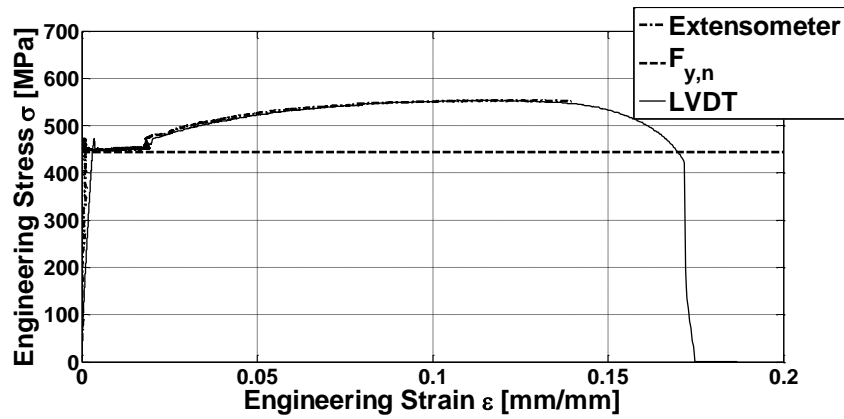
Figure A.1 (Continued): Standard coupon test results



(p) Specimen F41: strain gauge measurements

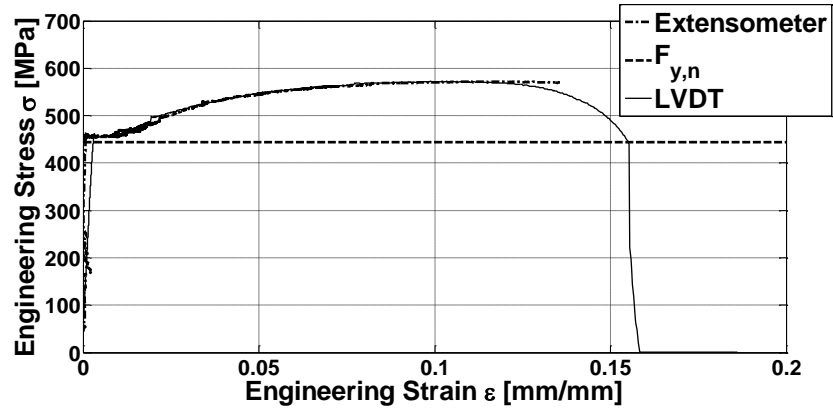


(q) Specimen F42

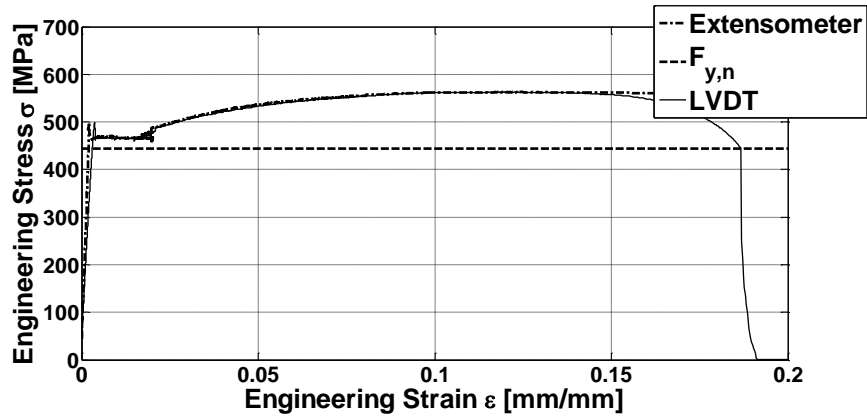


(r) Specimen F43

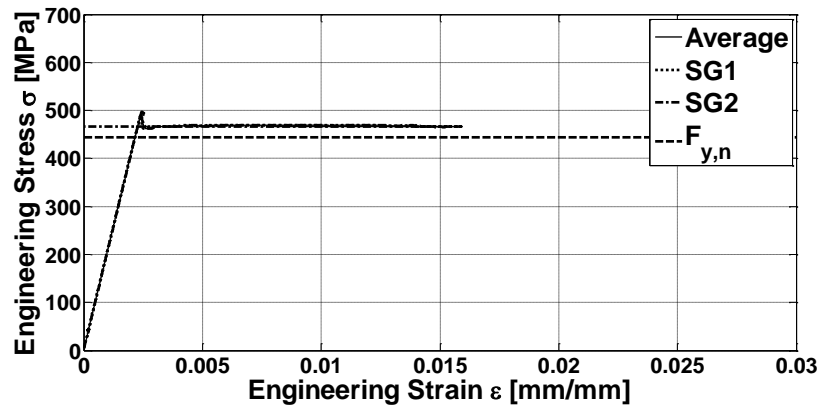
Figure A.1 (Continued): Standard coupon test results



(s) Specimen F44

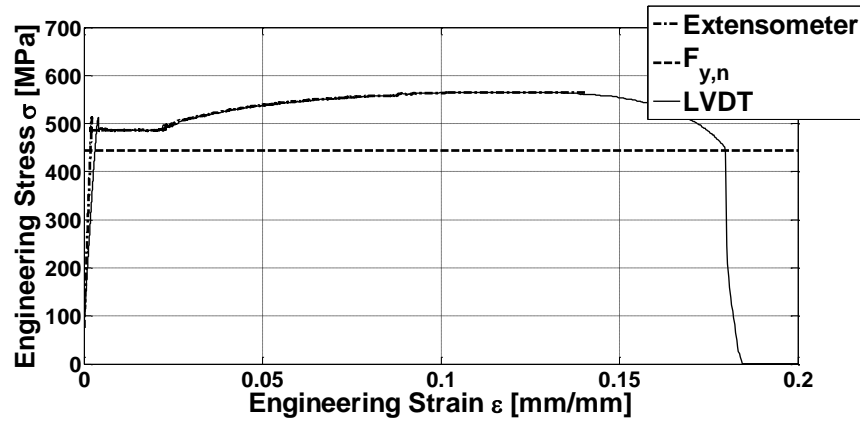


(t) Specimen K21

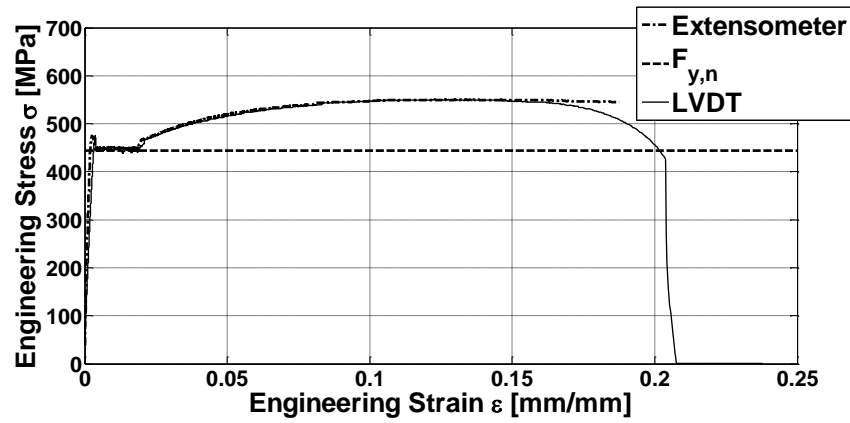


(u) Specimen K21: strain gauge measurements

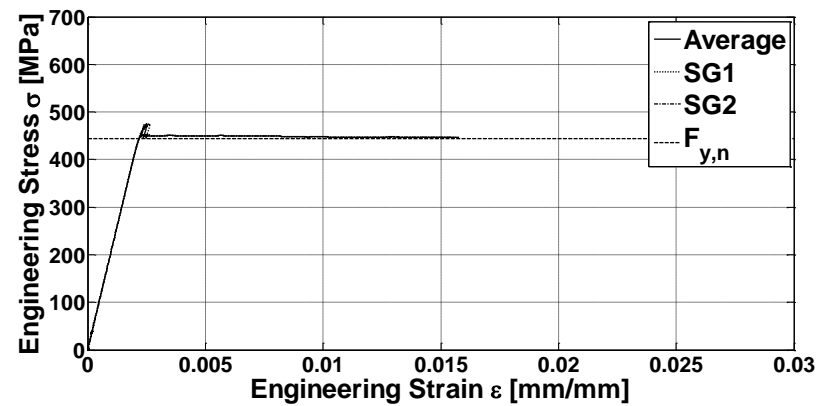
Figure A.1 (Continued): Standard coupon test results



(v) Specimen K22

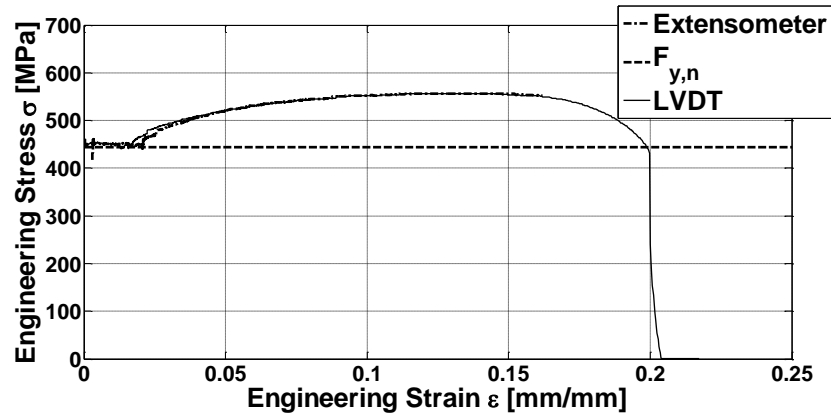


(w) Specimen K41

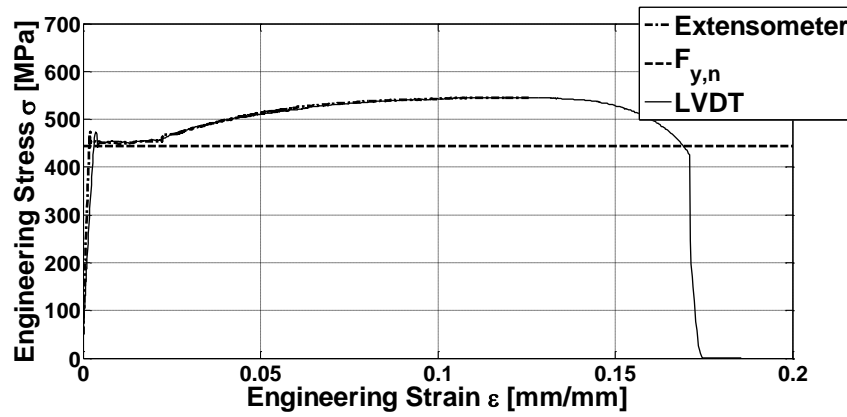


(x) Specimen K41: strain gauge measurements

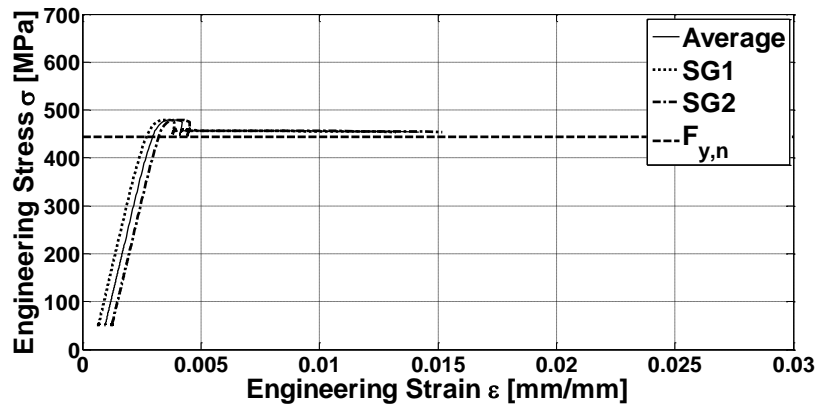
Figure A.1 (Continued): Standard coupon test results



(y) Specimen K42

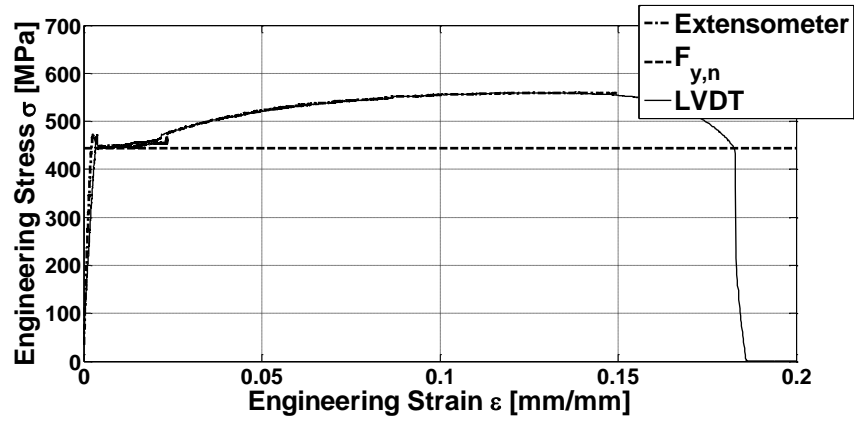


(z) Specimen W31

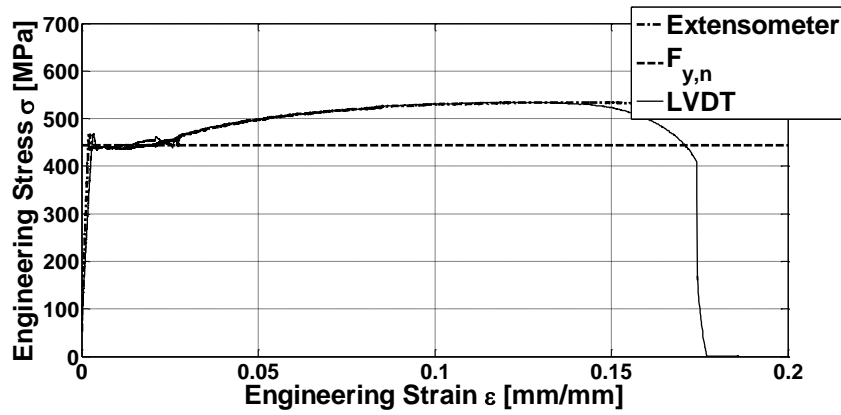


(a') Specimen W31: strain gauge measurements

Figure A.1 (Continued): Standard coupon test results

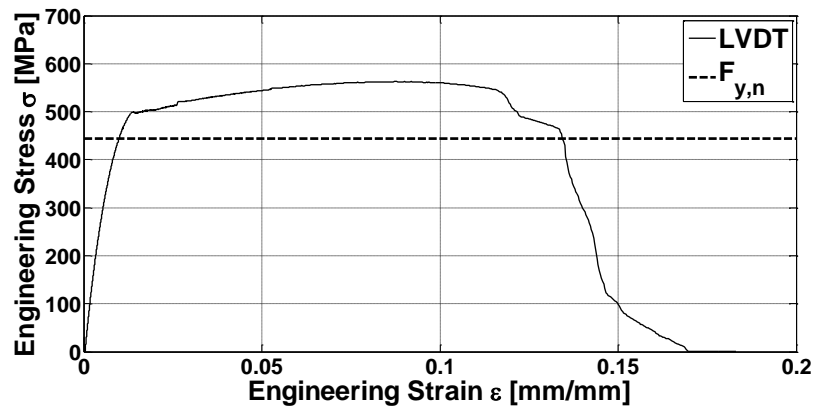


(b') Specimen W32



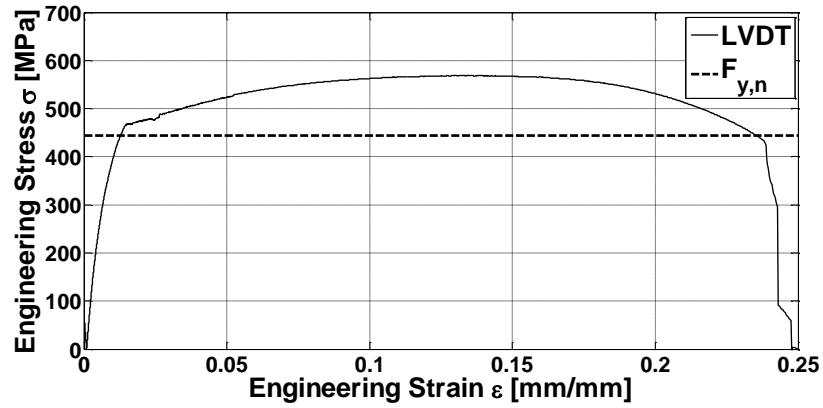
(c') Specimen W33

Figure A.1 (Continued): Standard coupon results

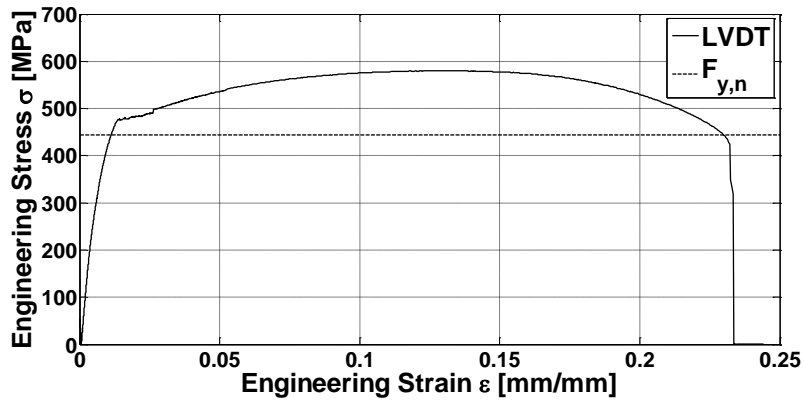


(a) Specimen K11

Figure A.2: K-area coupon test results

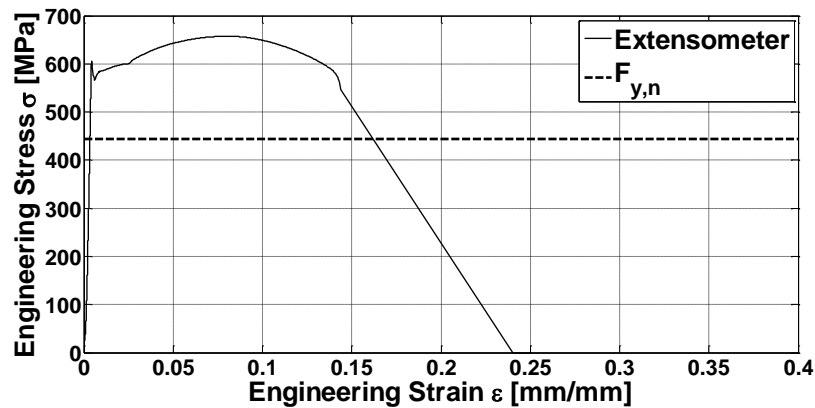


(b) Specimen K31



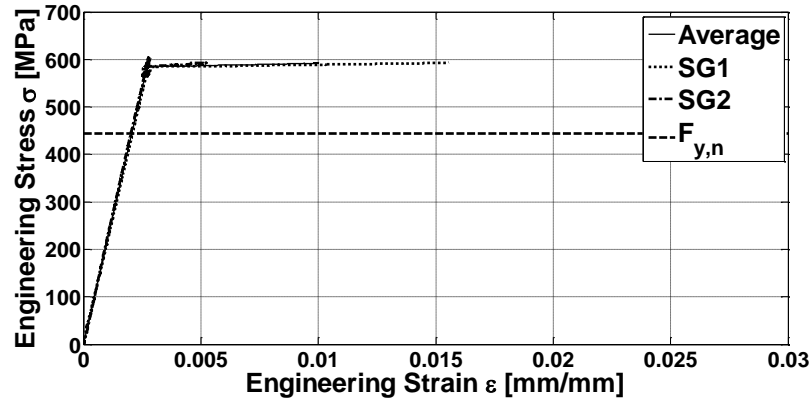
(c) Specimen K33

Figure A.2 (Continued): K-area coupon test results

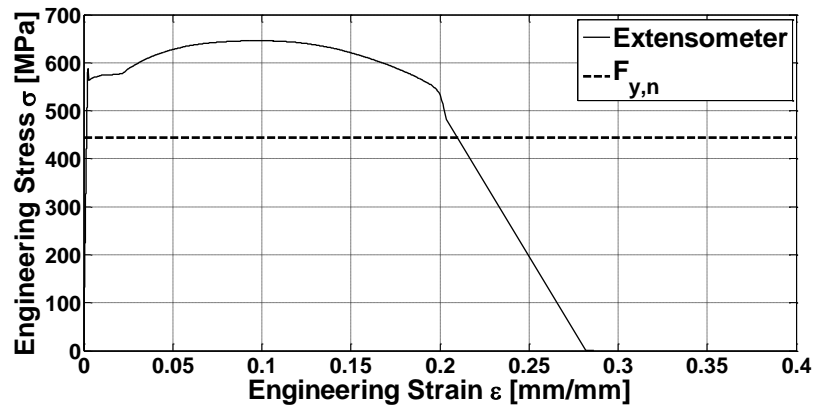


(a) Specimen F51

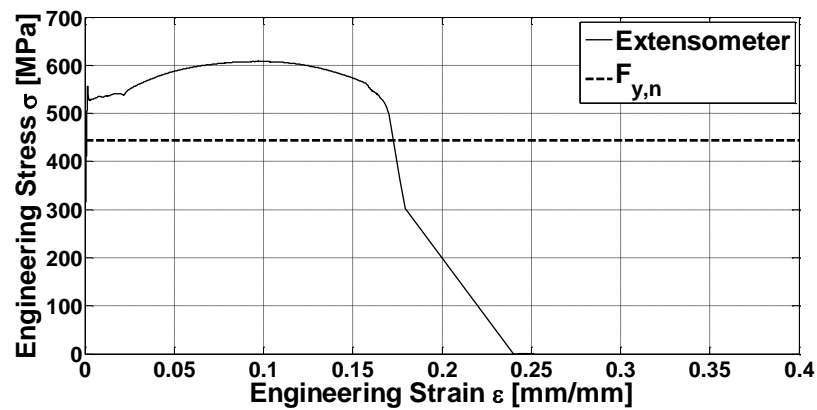
Figure A.3: Small coupon test results



(b) Specimen F51: strain gauge measurements

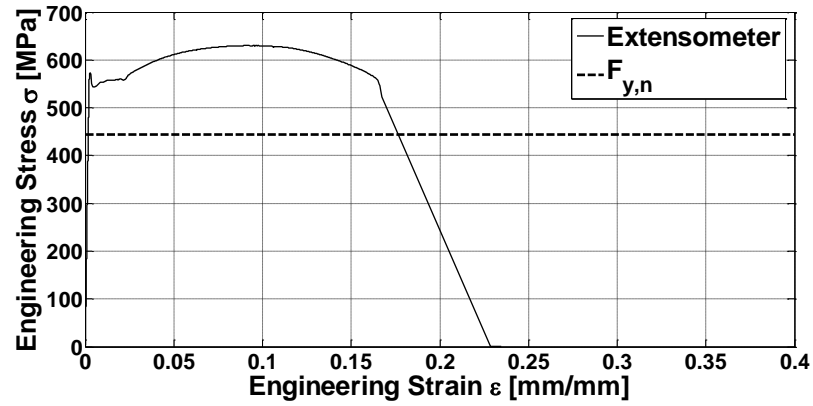


(c) Specimen F52

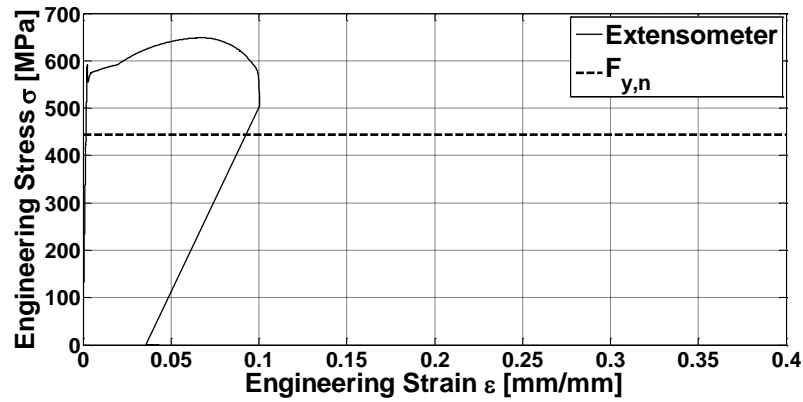


d) Specimen F53

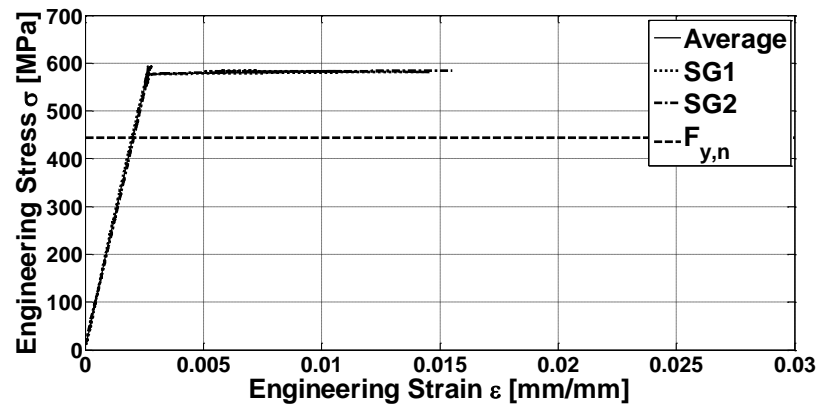
Figure A.3 (Continued): Small coupon test results



e) Specimen F54

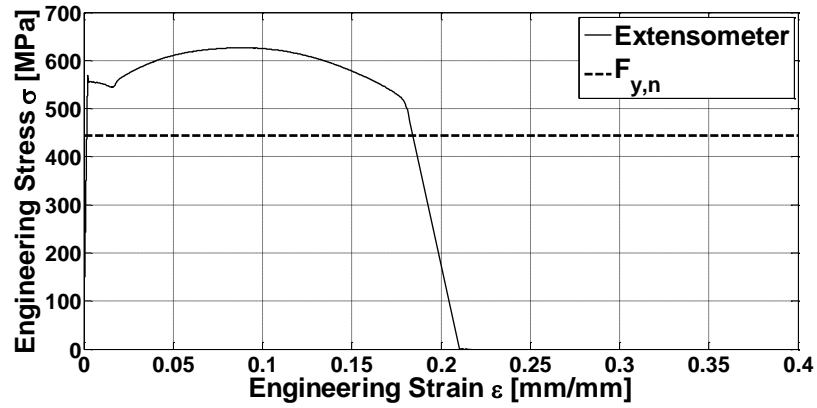


f) Specimen F61

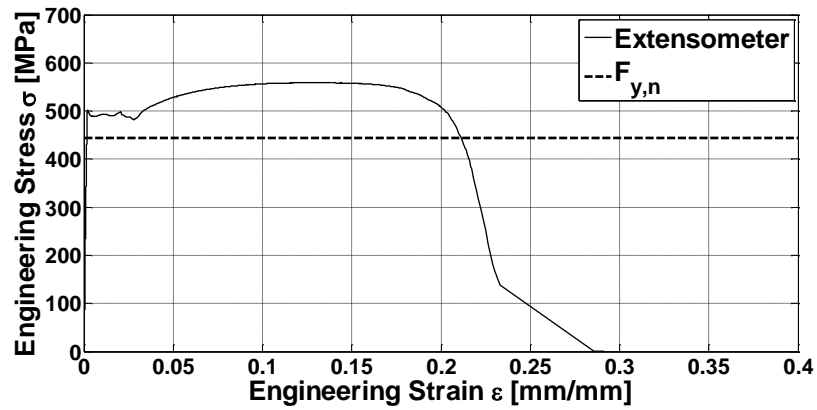


(g) Specimen F61: strain gauge measurements

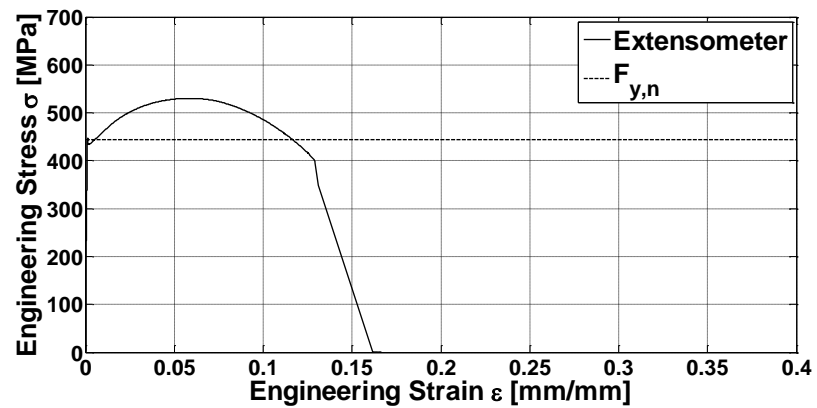
Figure A.3 (Continued): Small coupon test results



h) Specimen F62

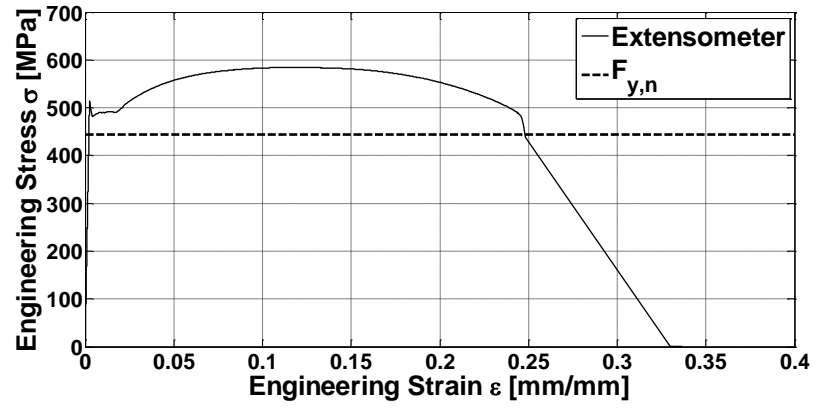


(i) Specimen F63

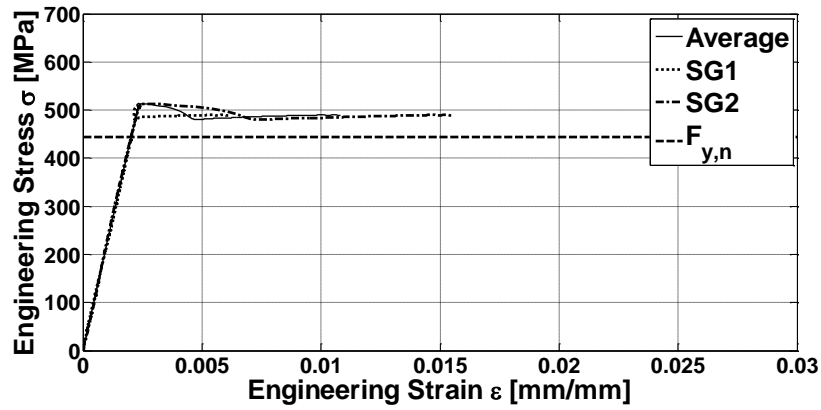


(j) Specimen F64

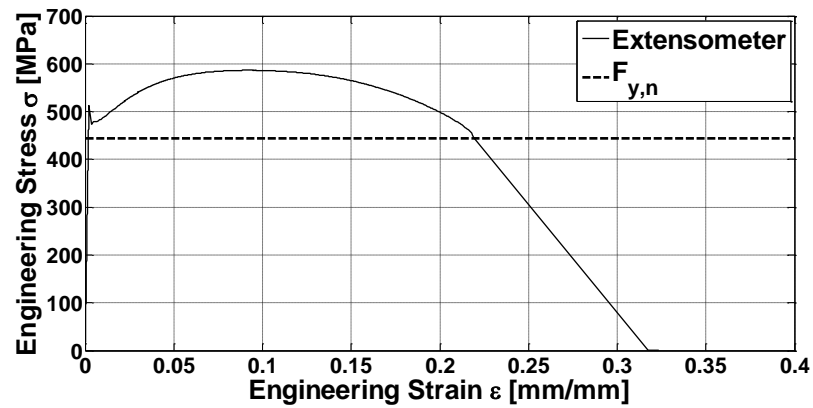
Figure A.3 (Continued): Small coupon test results



(k) Specimen R11

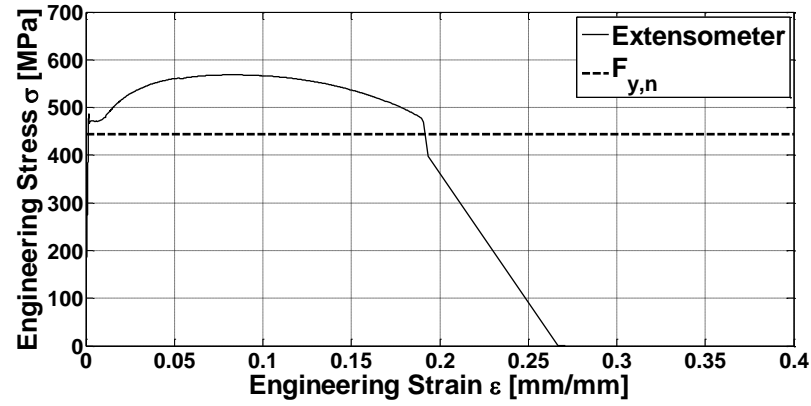


(l) Specimen R11: strain gauge measurements

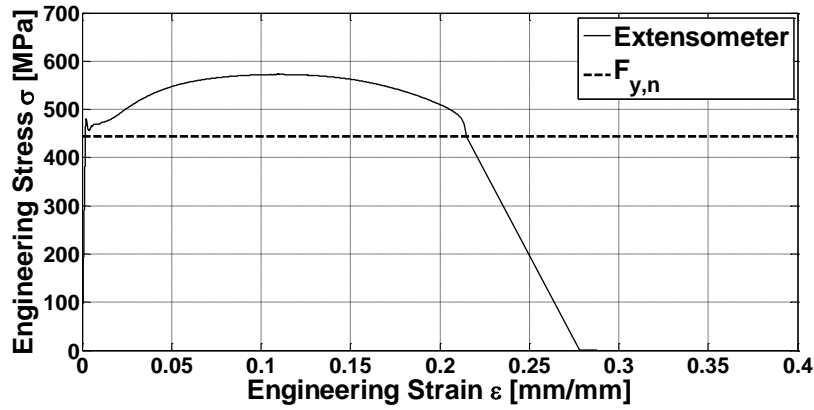


(m) Specimen R12

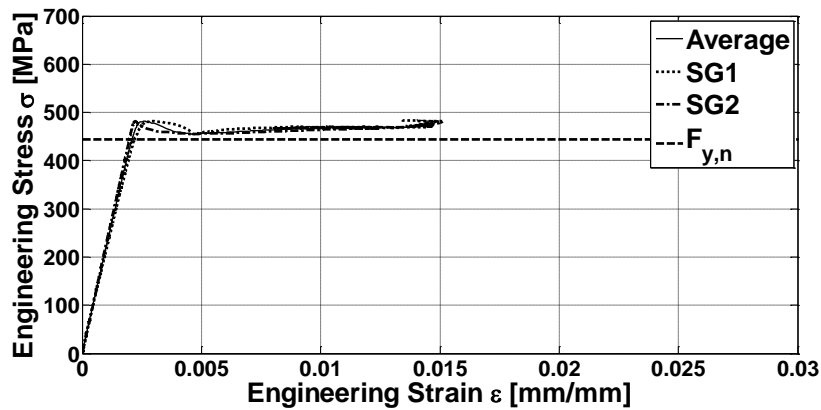
Figure A.3 (Continued): Small coupon test results



(n) Specimen R13

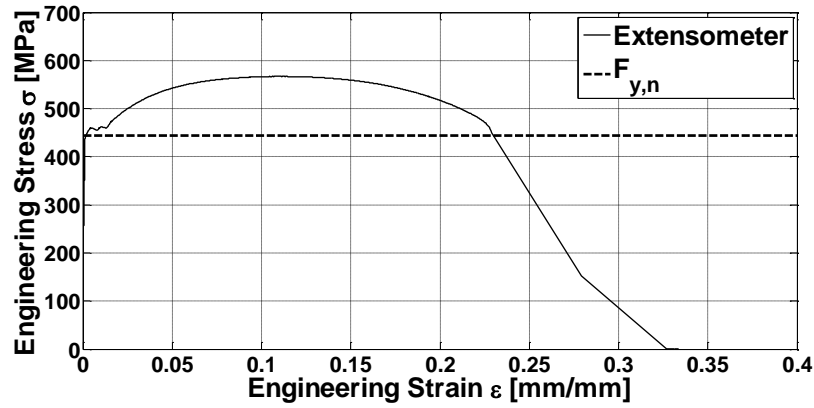


(o) Specimen R21

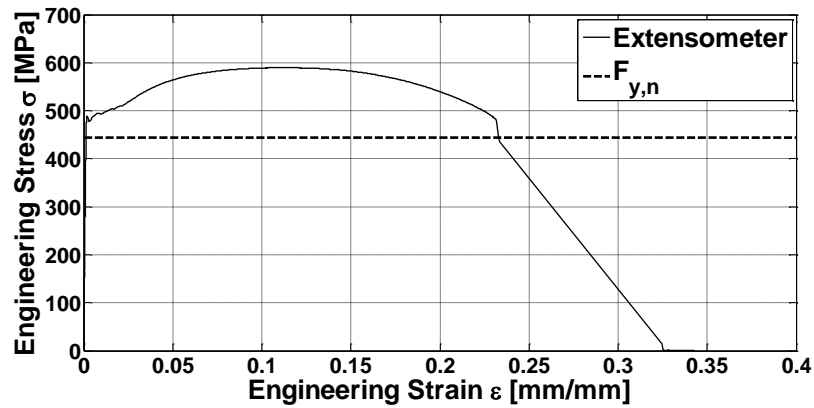


(p) Specimen R21: strain gauge measurements

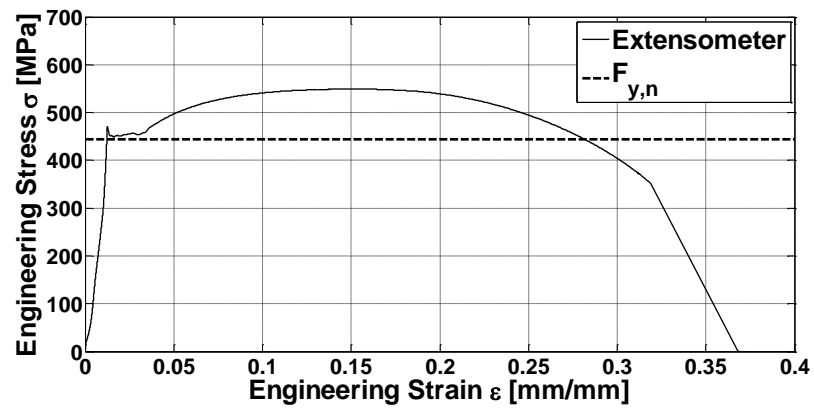
Figure A.3 (Continued): Small coupon test results



(q) Specimen R22

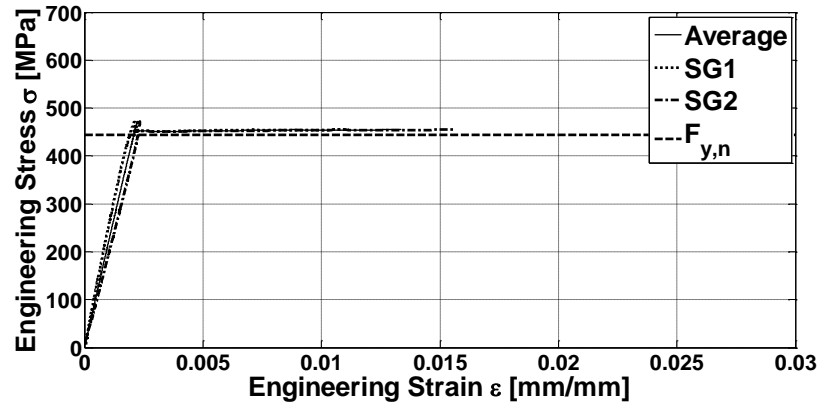


(r) Specimen R23

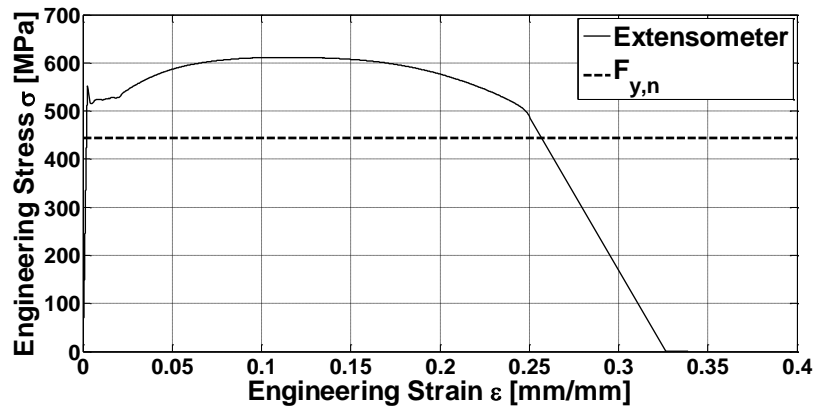


(s) Specimen U41

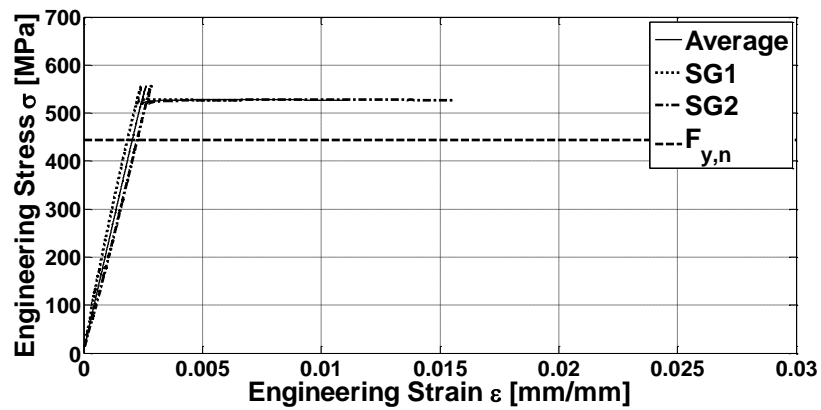
Figure A.3 (Continued): Small coupon test results



(t) Specimen U41: strain gauge measurements

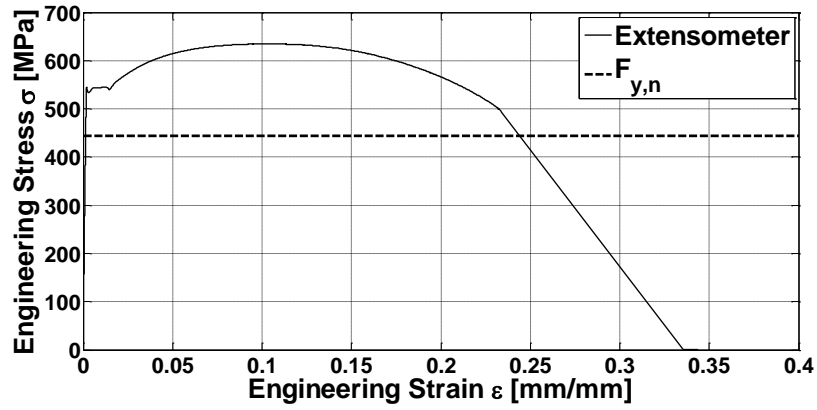


(u) Specimen W11

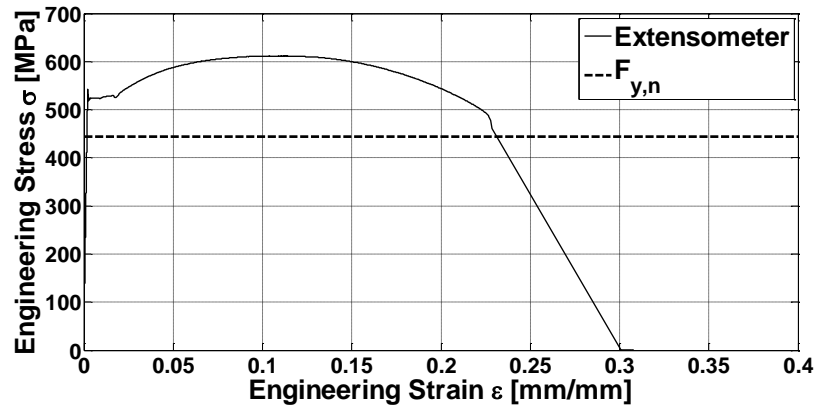


(v) Specimen W11: strain gauge measurements

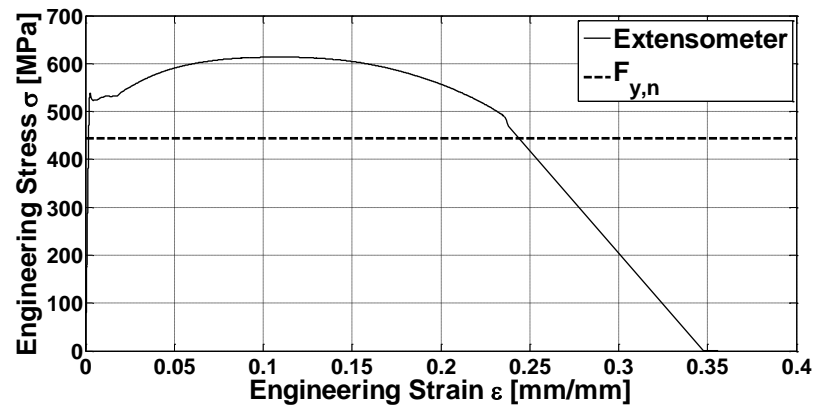
Figure A.3 (Continued): Small coupon test results



(w) SpecimenW12

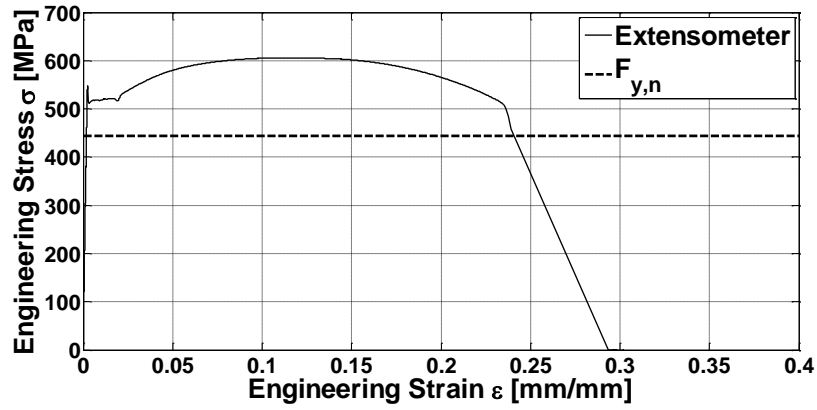


(x) SpecimenW13

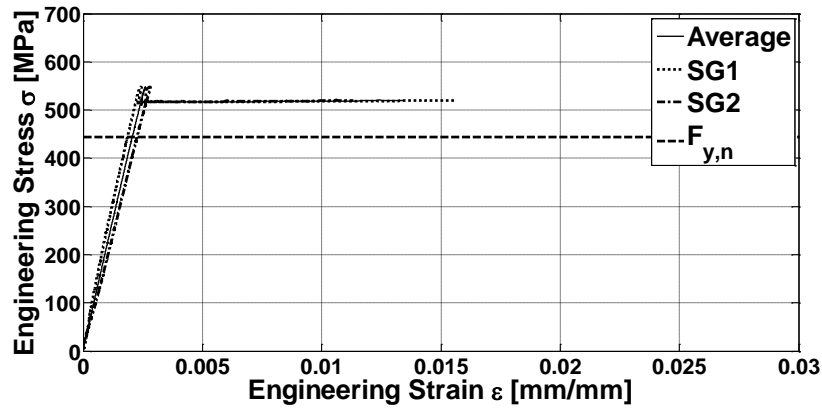


(y) SpecimenW14

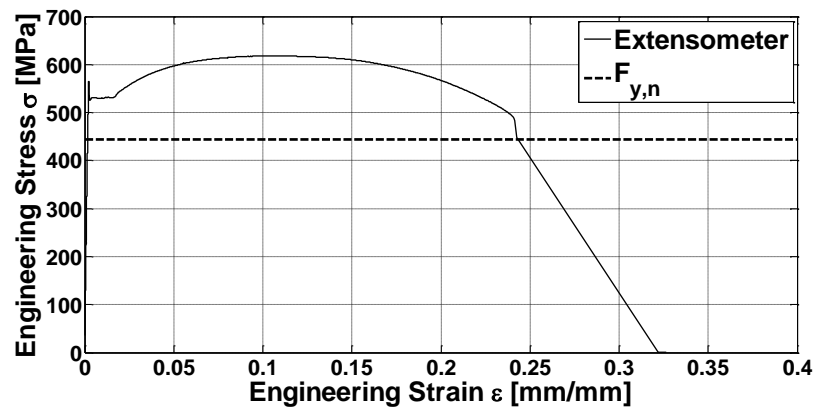
Figure A.3 (Continued): Small coupon test results



(z) SpecimenW21

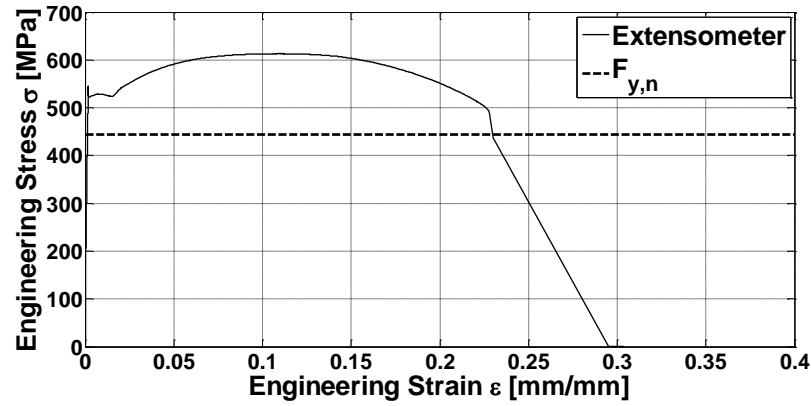


(a') Specimen W21: strain gauge measurements

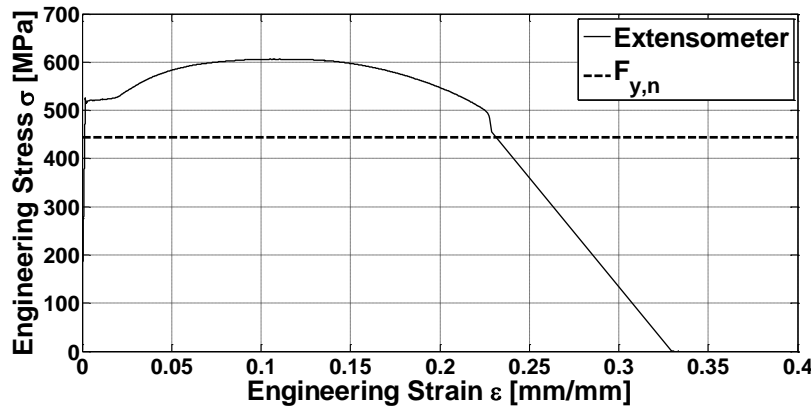


(b') SpecimenW22

Figure A.3 (Continued): Small coupon test results



(b') SpecimenW23



(c') SpecimenW24

Figure A.3 (Continued): Small coupon test results

Table A.1, A.2 and A.3 summarize the results for the standard, the k-area and the small coupon tests, respectively. In these tables t is the thickness of the coupon web, b is the coupon width, b_m is the average width out of two or three measurements and t_m is the average thickness. Moreover, F_u and ϵ_u refer to the ultimate tensile stress point, F_y and ϵ_y to the yielding point while F_r and ϵ_r values refer to the fracture point. Lastly, in Table A.2 A is the area measured for the k-area profile of the coupons while b' includes the measurements of three different width locations of the k-area special coupon.

Table A.1: Standard coupon test results

Specimen	b (mm)	b _m (mm)	t (mm)	t _m (mm)	F _y at 0.2% strain (MPa)	ε _y (mm/mm)	F _u (MPa)	ε _u (mm/mm)	E (MPa)	F _r (MPa)	ε _r (mm/mm)
F1-1	40.08	40.12	8.02	7.97	453	0.0056	559	0.1192	203159	431	0.1545
	40.07		7.96								
	40.21		7.94								
F1-2	40.13	40.12	8.10	8.10	445	0.0054	567	0.1159	-	459	0.1695
	40.11		8.09								
	40.11		8.10								
F1-3	40.08	40.08	8.09	8.08	451	0.0063	558	0.1244	-	439	0.1650
	40.07		8.10								
	40.08		8.05								
F1-4	40.00	39.98	7.96	7.98	458	0.0042	581	0.1162	-	449	0.1847
	39.92		7.98								
	40.01		7.99								
F2-1	40.01	40.01	8.07	8.07	452	0.0042	561	0.1240	204246	435	0.1845
F2-2	40.09	40.09	7.96	8.00	451	0.0043	572	0.1188	-	466	0.1858
	40.08		8.07								
	40.09		7.96								
F2-3	40.08	40.05	8.09	8.06	456	0.0044	562	0.1245	-	443	0.1859
	40.04		8.05								
	40.03		8.05								
F2-4	40.07	40.10	7.97	7.94	449	0.0042	576	0.1190	-	454	0.1762
	40.09		7.93								
	40.13		7.93								
F3-2	40.06	40.06	8.08	8.06	474	0.0043	571	0.1217	-	442	0.1891
	40.07		8.07								
	40.06		8.04								
F3-3	40.07	40.06	8.2	8.05	476	0.0044	573	0.1156	-	448	0.1715
	40.06		8.03								
	40.06		7.93								

Table A.1 (Continued): Standard coupon test results

Specimen	b (mm)	b _m (mm)	t (mm)	t _m (mm)	F _y at 0.2% strain (MPa)	ε _y (mm/mm)	F _u (MPa)	ε _u (mm/mm)	E (MPa)	F _r (MPa)	ε _r (mm/mm)
W3-2	40.10	40.11	7.92	7.94	443	0.0041	560	0.1317	-	432	0.1829
	40.10		7.95								
	40.12		7.96								
W3-3	40.07	40.21	8.07	8.13	438	0.0042	534	0.1122	-	410	0.1741
	40.28		8.09								
	40.28		8.22								
K2-2	40.01	40.12	7.95	7.95	487	0.0044	565	0.1178	-	451	0.1795
	40.01		7.96								
	40.35		7.94								
K4-2	40.12	40.08	7.95	7.93	460	0.0040	556	0.1222	-	431	0.1997
	40.06		7.93								
	40.05		7.92								
F4-2	40.07	40.08	8.01	7.98	469	0.0046	572	0.0968	-	444	0.1541
	40.09		7.98								
	40.08		7.95								
F4-3	40.01	39.97	8.05	8.02	450	0.0041	553	0.1158	-	426	0.1716
	39.94		8.01								
	39.97		8.01								
F4-4	39.95	40.01	7.97	7.98	456	0.0051	572	0.0988	-	443	0.1551
	40.10		7.96								
	39.99		8.00								
F4-1	40.00	40.03	8.03	8.04	460	0.0040	553	0.1131	202812	430	0.1726
	40.05		8.05								
	40.05		8.05								
W3-1	40.13	40.09	8.10	8.05	458	0.0044	546	0.1248	207923	425	0.1709
	40.09		8.03								
	40.06		8.02								
F3-1	40.10	40.09	8.01	7.99	457	0.0043	547	0.1248	203546	417	0.1957
	40.10		8.02								
	40.08		7.95								

Table A.1 (Continued): Standard coupon test results

Specimen	b (mm)	b _m (mm)	t (mm)	t _m (mm)	F _y at 0.2% strain (MPa)	ε _y (mm/mm)	F _u (MPa)	ε _u (mm/mm)	E (MPa)	F _r (MPa)	ε _r (mm/mm)
K2-1	40.13	40.11	8.04	7.99	467	0.0041	564	0.1205	203846	445	0.1867
	40.08		7.95								
	40.11		7.98								
K4-1	40.03	40.04	7.99	7.99	450	0.0042	550	0.1254	206764	428	0.2035
	40.02		7.96								
	40.07		8.02								

Table A.2: K-area coupon test results

Specimen	b' (mm)	A (mm ²)	t (mm)	F _y at 0.2% strain (MPa)	ε _y (mm/mm)	F _u (MPa)	ε _u (mm/mm)	F _r (MPa)	ε _r (mm/mm)
K3-1	80.08	1134	7.96	469	0.0167	568	0.1377	424	0.2387
	20.00								
	23.05								
K3-3	79.95	1137	7.95	475	0.0146	580	0.1339	425	0.2321
	19.87								
	23.22								
K1-1	80.20	1229	9.97	497	0.0145	563	0.0872	-	-
	20.05								
	23.07								

Table A.3: Small coupon test results

Specimen	b (mm)	b _m (mm)	t (mm)	t _m (mm)	F _y at 0.2% strain (MPa)	ε _y (mm/mm)	F _u (MPa)	ε _u (mm/mm)	E (MPa)	F _r (MPa)	ε _r (mm/mm)
R1-1	6.28	6.28	7.96	7.96	483	0.0047	585	0.1411	220523	439	0.2483
	-				497	0.0041					
	-										
R1-2	5.67	5.67	8.00	8.00	478	0.0043	586	0.1137	-	446	0.2191
	-										
	-										
R1-3	6.26	6.26	7.88	7.91	472	0.0039	569	0.1011	-	469	0.1908
	6.23		7.91								
	6.29		7.95								
R2-1	6.27	6.28	7.95	7.96	459	0.0042	573	0.1297	216412	443	0.2150
	6.29		7.96		459	0.0041					
	-										
R2-2	6.25	6.21	7.99	7.93	456	0.0033	567	0.1318	-	450	0.2291
	6.20		7.89								
	6.18		7.90								
R2-3	6.12	6.14	7.92	7.90	478	0.0033	590	0.1374	-	481	0.2314
	6.15		7.89								
	6.16		7.89								
W1-1	6.22	6.24	7.97	7.98	515	0.0047	612	0.1405	215656	484	0.2504
	6.24		7.98		527	0.0041					
	6.27		7.98								
W1-2	6.11	6.10	7.84	7.84	536	0.0039	635	0.1224	-	496	0.2333
	6.10		7.85								
	6.10		7.82								
W1-3	6.15	6.15	7.98	7.98	524	0.0043	612	0.1349	-	461	0.2284
	-										
	-										
W1-4	6.25	6.25	7.95	7.94	523	0.0044	614	0.1281	-	469	0.2379
	6.25		7.93								
	6.25		7.93								

Table A.3 (Continued): Small coupon test results

Specimen	b (mm)	b _m (mm)	t (mm)	t _m (mm)	F _y at 0.2% strain (MPa)	ε _y (mm/mm)	F _u (MPa)	ε _u (mm/mm)	E (MPa)	F _r (MPa)	ε _r (mm/mm)
W2-1	6.24	6.26	7.93	7.95	516	0.0046	606	0.1419	216146	457	0.2392
	6.28		7.92		517	0.0041					
	-		8.01								
W2-2	6.27	6.27	7.92	7.93	531	0.0044	618	0.1250	-	448	0.2427
	6.28		7.95								
	6.26		7.93								
W2-3	6.24	6.24	7.95	7.95	525	0.0035	613	0.1326	-	436	0.2300
	6.25		7.96								
	6.23		7.95								
W2-4	6.24	6.26	7.98	7.96	520	0.0037	606	0.1335	-	455	0.2288
	6.26		7.96								
	6.28		7.93								
U4-1	6.40	6.42	7.99	7.97	450	0.0165	549	0.1723	215552	351	0.3187
	6.33		7.96		451	0.0038					
	6.54		7.97								
F5-1	6.26	6.25	7.95	7.94	574	0.0044	657	0.0976	216666	546	0.1438
	6.24		7.92		589	0.0043					
	-		7.94								
F5-2	6.26	6.26	7.97	7.96	567	0.0044	646	0.1203	-	482	0.2034
	6.26		7.96								
	6.26		7.96								
F5-3	6.23	6.23	7.93	7.93	530	0.0042	608	0.1202	-	303	0.1794
	6.23		7.93								
	6.23		7.93								
F5-4	6.26	6.26	7.96	7.96	544	0.0045	630	0.1095	-	523	0.1673
	6.26		7.95								
	6.27		7.97								

Table A.3 (Continued): Small coupon test results

Specimen	b (mm)	b _m (mm)	t (mm)	t _m (mm)	F _y at 0.2% strain (MPa)	ε _y (mm/mm)	F _u (MPa)	ε _u (mm/mm)	E (MPa)	F _r (MPa)	ε _r (mm/mm)
F6-2	6.24	6.24	8.00	8.00	555	0.0046	627	0.1049	-	474	0.1823
	6.25		8.02								
	6.22		7.99								
F6-3	6.27	6.28	7.99	7.97	490	0.0041	559	0.1534	-	139	0.2331
	6.29		7.96								
	6.28		7.97								
F6-4	6.26	6.26	7.98	7.98	440	0.0040	530	0.0729	-	349	0.1310
	6.26		7.99								
	6.26		7.97								